A Study of Immiscible Liquids, Liquid Behavior at Zero Gravity, and Dynamic Contact Lines and Angles

Thesis by

Gregory Todd Smedley

In Partial Fulfillment
of the Requirements for the Degree of
Doctor of Philosophy

California Institute of Technology
Pasadena, California

1990
(Submitted March 9, 1990)

To my family

ACKNOWLEDGMENTS

I have thoroughly enjoyed my stay at GALCIT. I would like to thank all of my friends for their encouragement and understanding, especially during this past year.

My advisor Donald Coles has been very generous with his time and advice. His extensive knowledge of experimental design and technique is a treasure that I am fortunate to have sampled. I know that what I have learned from him will benefit me eternally.

Most of all, I would like to thank my wife, Keyue Smedley, for her love, encouragement, advice, and electronic consulting. There is nothing better than support at home when completing a Ph.D.

ABSTRACT

The work reported here covers three topics that were investigated as part of preparation for a space based experiment. The intention of the proposed experiment was to study the relationship between container geometry and interface geometry for a free liquid surface at zero gravity.

A mathematical theory proposed by Paul Concus and Robert Finn in 1974 and recently developed by Finn yields explicit geometrical criteria for the position of the free surface of a liquid at zero gravity in a cylindrical container of specified cross section. It is possible to find geometrical criteria that promise a particular liquid location. A unified graphical presentation of four geometries is given that can be used directly for the design of containments for liquids at zero gravity. As one application of these design curves, a container was built and tested in a series of 2 second drop-tower experiments at NASA Lewis Research Center.

It was apparent that the space based experiment would require use of sophisticated optical instrumentation that would be most effective if a pair of immiscible liquids were used rather than a single liquid under its vapor. This work identifies 121 transparent immiscible liquid pairs that have properties compatible with optical instrumentation based on laser-induced fluorescence. Physical data such as specific gravity, index of refraction, viscosity, flash point, and toxicity were found in the literature. Compatibility with plexiglas (PMMA), contact angles of the internal meniscus on glass and PMMA, meniscus formation times, and clearing times were measured. A useful non-invasive technique for determining interfacial tensions is explained and used.

The contact angle is a critical parameter in the consideration of liquid behavior at zero gravity, therefore, a technique, based on laser light refraction, was developed to objectively measure it. Dynamic contact line experiments were conducted at various velocities, both advancing and receding, using one of the 121 immiscible liquid pairs (nonane/formamide) in contact with glass.

TABLE OF CONTENTS

LIST OF FIGURES

LIST OF TABLES

Chapter I

1 Introduction

The general problem considered in this research is liquid containment at zero gravity. The specific problem is the effect of container geometry on the static and dynamic behavior of liquid free surfaces that are controlled primarily by surface-tension forces. Research on this problem at Caltech has been carried out from 1979 to 1990, with some interruptions. Because no other coherent and accessible record exists, a short account of the entire effort is given here, using material extracted from proposals and contract reports submitted by Caltech to NASA.

The foundations of the research were laid about 1974 by two mathematicians, Paul Concus (U.C. Berkeley/Lawrence Berkeley Laboratory) and Robert Finn (Stanford University). Their mathematical investigations (Concus and Finn 1974, Finn 1983) have led to several novel and important ideas about the configuration of static interfaces at zero gravity. In 1979, when NASA offered a prospect of space experiments, Concus and Finn enlisted Donald Coles (California Institute of Technology) as co-investigator to assist in design of a practical experiment. In 1981, when it became apparent that sophisticated optical instrumentation would play a central role in such an experiment, Lambertus Hesselink (Stanford University) became the fourth co-investigator. The research was supported through NASA Lewis Research Center as part of a program called Physics and Chemistry Experiments in space (PACE). This program was administered by the Office of Aeronautics and Space Technology (OAST) until 1984, when it was transferred to the Microgravity Science Applications Division in the Office of Space Science and Applications (OSSA).

The planning of a space experiment has several aspects that can interact strongly. First, a suitable geometry is required that embodies the critical mathematical conditions for existence or

non-existence of a bounded solution surface. Second, the working liquid or liquids must be acceptable in terms of toxicity and flammability and also in terms of reproducibility of physical properties, especially contact angle. Third, some means is required for observing and measuring the position of the meniscus in three space dimensions and time. A rough division of responsibility was agreed on for the proposed space experiment. Geometry was primarily the responsibility of Concus and Finn. Materials were primarily the responsibility of Coles, aided by Frederick Fowkes (Lehigh University) as a consultant on questions of physical and surface chemistry. Instrumentation was primarily the responsibility of Hesselink.

2 Geometry

Some of the more recent work by Concus and Finn is outlined in chapter 4. This work considers a limited part of the general problem of liquid containment at zero gravity. The container is taken to be a cylinder of infinite length, and the liquid and its interface are taken to be at rest. The non-linear equation describing the interface position, and its boundary condition, are then well understood. A variational method is used to determine whether a static interface exists, in the sense that it occupies a finite length along the cylinder, or does not exist, in the sense that it extends to infinity. The cylinder cross-sectional shapes chosen for study all have one plane of symmetry and are all defined by two geometric parameters. Examples, in chronological order, are the trapezoid, the bathtub (a trapezoid with rounded ends) and the keyhole. They all show a discontinuous dependence of the shape of the interface on the boundary data, but not necessarily in a simple way. The trapezoid, in particular, has two acute corners and two obtuse corners, and it is possible for the interface to extend to infinity in the corners if the condition $\alpha + \gamma \leq \pi/2$ is satisfied (Concus and Finn 1974), where α is the half angle of the corner and γ is the contact angle. This mechanism acts for arbitrary values of gravity and is discussed pragmatically in the next section. However, at zero gravity the interface can also extend to infinity, when the local condition just stated is not satisfied, by responding to a quite different and more general global minimum-energy mechanism.

In general, the existence of a bounded interface depends critically on the contact angle and in a non-evident way on subtle variations in the shape of the container cross section. The liquid

tends to occupy regions of higher wall curvature, with a sharp corner as a separate case. In fact, the recent development at UCB/Stanford of simple rules for existence or non-existence of a bounded capillary surface in a general cylindrical geometry was motivated in part by the observation at Caltech that contact angles greater than 45° are very difficult to achieve. For almost all of the liquid pairs studied so far, the internal contact angle is in the range from 7° to 20° . This finding essentially disqualifies the trapezoid geometry, because the corners will fill with liquid and interfere with observation of the global criterion for unboundedness. A difficulty with the bathtub geometry, given the contact angles just mentioned, is that only a small fraction of the cross sectional area, at most 5 to 10 percent, will be associated with the region of unbounded displacement. Hence only a small part of the finite test volume is associated with equilibrium configurations for the heavier fluid, and difficulties can be expected at the ends of the container when the critical state is passed. The question of geometry is to some extent still open.

For engineering and design purposes, some quantitative values for the critical condition to be satisfied for the three shapes already mentioned have been worked out in detail, as described in chapter 4. One issue that has evaded resolution is the need to vary the container geometry in flight, or to provide an array of containers covering a range of parameters on both sides of the critical configuration. A fourth shape, the eccentric cylinders, is therefore also studied because it allows at least one of the two geometric parameters to be varied continuously.

As one application of these design curves, a drop-tower test was carried out in 1986 in the 2-second tower at NASA Lewis Research Center. The geometry studied was a bathtub shape whose geometry was chosen to exceed the critical condition for small contact angles (23 degrees for 50% ethanol in water under air) and not to exceed it for large contact angles (56 degrees for 10% ethanol in water). The test was complicated by the poor quality of instrumentation supplied with the drop carriage, but led to some useful results that are described in chapter 3.

3 Materials

The shape of a capillary surface depends on container geometry, liquid density, apparent gravity, surface tension, and contact angle. The contact angle, which enters through the boundary condition for the governing equation, is usually assumed to be a property only of the materials involved. The contact angle is known to be sensitive to many factors, including temperature, surface roughness, composition of the third phase, contamination of the solid surface or the liquid volume, and direction of approach; i.e., whether the contact line is advancing, stationary, or receding. Hence it is not surprising that there is a substantial lack of agreement among various measured values for particular combinations of materials.

Even a brief study of the literature on contact angles (e.g., Fowkes 1964, Bikerman 1970, Dussan 1979) is discouraging. An initial effort at Caltech in 1980 therefore undertook development of a technique that is capable in principle of measuring contact angle accurately. This technique is not new, except that the instrumentation uses the refractive rather than the reflective properties of a free liquid surface and is nearly equivalent to the shadowgraph method commonly used in gas dynamics. The apparatus constructed for this purpose consisted of a glass-bottomed tank having a volume of about one liter, a means of partially submerging a glass plate at a known angle, and a source of parallel monochromatic light directed vertically downward on the contact region. The contact line was stationary, and a moving light detector under the tank recorded the pattern of refracted light in a direction normal to the contact line. The contact angle is measured as the rotation angle of the glass plate (from the horizontal) for which the refracted light has uniform intensity, indicating a flat liquid surface. The apparatus can be used with almost any combination of liquid and solid materials as long as both are transparent.

Figure 1 is the only available record of work with this original apparatus. The light source was a short-arc mercury lamp without reflector. An optical interference filter was used to isolate the green line at 0.5461 μm, and a lens and front-surface mirror were used to produce a parallel beam of light normal to the fluid surface. The liquid used in obtaining the figure was acetone, and the solid surface was a glass plate rotated about an axis near the contact line. No special precautions were taken to avoid contamination. The light detector was a laser power

meter whose sensing element was masked to a pinhole aperture of diameter 0.02 cm and was traversed along a line below the glass bottom of the tank, about 10 cm below the contact line. The traverse was motorized and was equipped with a potentiometer to provide position information for the abscissa of figure 1. The total travel of the detector in the figure is 1.0 cm. The lowest trace in the figure is for the glass plate at 16.6 degrees from the horizontal. The other traces (slightly displaced for clarity) are for decrements of 1 degree from 16.6 to 1.6 degrees. Minor irregularities are caused by an unintended variation of traverse speed along the various traces. The contact angle is estimated to be about 7 degrees. The potential sensitivity of the method is probably a small fraction of a degree, although this sensitivity has by no means been achieved.

The report to NASA of this work says

> "The results so far amount mostly to proof of principle. On the experimental side, several elements of the apparatus need improvement. A better approximation to a monochromatic high-density point light source is required. The spatial resolution at the detector could be improved by an order of magnitude by using a stationary photo-conducting array (such as a Reticon array), with the further advantage that an essentially instantaneous trace could be recorded over an interval in x of about 2 cm, thus allowing dynamic measurements of contact angle as a function of rate and direction of displacement for the contact line. For this purpose rotation of the glass plate needs to be automated and instrumented. Finally, it is desirable to minimize mechanical vibration, which causes annoying waves in the liquid surface. For best results, the apparatus should be mounted on a vibration-isolated table."

Implementation of these proposed improvements has taken ten years. The improved apparatus and some results are described in chapter 5.

Since the contact angle is a critical parameter in the present research, Concus and Finn in 1981 asked Coles to look at the feasibility of using their corner criterion (Concus and Finn 1974) to measure the contact angle. The corner criterion, valid with or without gravity, states that the height of an interface in a corner will be bounded or unbounded accordingly as

$$\alpha + \gamma > \frac{\pi}{2} \quad \text{or} \quad \alpha + \gamma \leq \frac{\pi}{2} \tag{1}$$

where α is half of the interior angle, as indicated in the first sketch, and γ is the contact angle measured in the liquid.

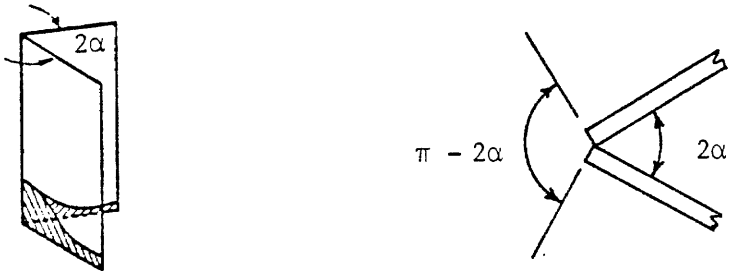

A Caltech undergraduate student, Minami Yoda, worked on this task during the summer of 1983 under the Caltech Summer Undergraduate Research Fellowship (SURF) program. Much of what follows is taken from her SURF report. The technique was to hold two microscope slides in contact at their corners, to insert one end of the slides in a petri dish containing the liquids, and to vary the angle between the slides while observing the meniscus. A mechanism for holding and rotating the slides about their line of contact was designed and constructed by Coles and functioned well. Two photographs of this mechanism are shown in figure 2. The angle between the two slides can be smoothly changed from 180° to about 20° ; i.e., contact angles from 0° to about 80° can be measured. The slides were placed with their lower ends in a petri dish (60 mm diameter, 15 mm deep) containing about ten ml of liquid. The view of the meniscus in the corner was typically magnified about thirty times by a binocular microscope.

All experiments were conducted in a fume hood to avoid contact with harmful vapors. Various methods were tried for cleaning the glass slides and were rated by the reproducibility of

the contact-angle measurements. The method finally chosen was a three-minute ultrasonic bath in Freon 113 (1,1,2-trichloro-1,2,2-trifluoroethane). Similar trials were made for plexiglas, and the method chosen was washing in MS-260 (65% water, 5% 2-butoxyethanol, 30% various alcohols and additives).

About 100 liquids were tested. Hysteresis for advancing and receding contact lines was highly variable, ranging from 1° (1-bromobutane, several esters) to 25° (1-octanol), with most values in the range from 3° to 8° . Most liquids had mean contact angles on glass in the range from 5° to 15° . The observed contact angle for water on glass was about 35° . Some correlation was found between contact angle and chemical structure. Among the straight-chain alcohols (ethanol, 1-propanol, 1-butanol, 1-pentanol, 1-hexanol, 1-octanol) and the straight-chain aldehydes (butanal, pentanal, heptanal), the contact angle both on glass and on plexiglas tended to increase with the number of carbon atoms in the chain. The contact angles on glass for the straight-chain ketones (2-propanone, 2-butanone, 3-pentanone, 2-octanone) were all in the range from 5.7° to 8.2° ± 20%. The glycols as a family had larger contact angles (10° to 27° on glass, 37° to 67° on plexiglas).

As with most new methods, this method had some problems. There was a conspicuous discontinuity in meniscus shape only for water, dibromomethane, benzyl formate, and butyl benzoate. The meniscus was hard to see for many liquids, no matter what lighting was tried, because the indices of refraction were close to those of glass or plexiglas. Some of the liquids, especially the glycols, are known to be hygroscopic. Their contact angles tended to decrease with time as the liquid absorbed more and more water. Some liquids were very viscous, and would not drain off the slides; examples are glycerin and triethylene glycol on glass. In fact, none of the liquids could be said to drain completely. The contact angle of a liquid could decrease significantly between the first and second readings because of wetting. The contact line was often very ragged, making it difficult to classify the profile. It was particularly difficult to estimate the contact angle for liquids with low boiling points, such as acetone or ethanol. As soon as the surface developed a sharp tip, it evaporated away. Many of the more volatile liquids would evaporate, condense on the slides a few millimeters above the contact line, and drip back down.

In view of these problems, the corner-angle method is considered at present to be a marginally usable method for measuring the contact angle. A measurement takes about ten minutes and requires about 10 ml of liquid, the solid material need not be transparent, and the method works best with liquids having a high index of refraction and a high boiling point. An apparently irreducible disadvantage of the geometry, illustrated in the second sketch, is that the criterion $\alpha + \gamma \leq \pi/2$ will always be exceeded for the rear corner before it is exceeded for the front corner, unless $\gamma > 45°$. Ideally, the two corners should be isolated by a seal, but no practical sealing method has been found. The technique is probably most useful for quick comparative tests such as determining the effect of impurities such as fluorescent dyes or the effect of a particular cleaning procedure. To improve the technique, the apparatus should be enclosed in a sealed enclosure, perhaps a glove box, so that evaporation and contamination can be controlled.

Another important interaction between the co-investigators occurred when preliminary work at Stanford on instrumentation of the proposed experiment suggested that there are important advantages in working with an internal meniscus between two liquids. A search was therefore made at Caltech to identify suitable immiscible transparent liquid pairs. No particular chemical expertise was on hand at the time, so a simplistic assumption was made that one liquid should be hydrophilic (examples are formamide and several glycols) and the other liquid should be hydrophobic (examples are brominated hydrocarbons, numerous esters, and a few alcohols and ketones).

The search, particularly for pairs that are compatible with plexiglas and perhaps other optical plastics, has also taken into account various other desirable physical and optical properties. These include low toxicity, optical clarity, chemical stability, closely matched refractive indices, low viscosity, compatibility with dye, and absence of permanent deposition of either liquid as droplets on the wall under the other liquid. Altogether, 110 candidate liquid pairs were identified, 76 of which are compatible with plexiglas. Several dozen pairs were found showing a close match in index of refraction, and a few pairs were found showing a close match in specific gravity. Two pairs had a good match in both (1,3-propanediol/diethyl maleate, and glycerol tributanoate/ethylene glycol). An optical estimate of internal contact

angle on glass showed that this quantity was usually in the range from 8 to 15 degrees. Contact angles on plexiglas, where these could be measured, were usually considerably larger and were usually inverted; i.e., the interface was concave in the opposite sense to that found for glass. Details and results of this search are given in chapter 2.

4 Instrumentation

Work on optical instrumentation at Stanford began in 1982. Hesselink made a preliminary study of the relative complexity and sensitivity of various optical methods, including shadowgraphy, Schlieren photography, holography, direct or holographic interferometry, scattering, refraction, reflection, and laser-induced fluorescence. A corollary consideration was the recording means, whether photographic or electronic. Some elegant optical processing techniques were investigated for holographic records, and holographic images of a test cell were produced, but this method was eventually judged to be impractical. In the event, the method recommended in 1984 for further development was laser-induced fluorescence, using one or more sheets of laser light scanned through the volume of the fluid. Images viewed along the axis of the container were to be recorded electronically. On-board data processing, if used, would be limited to reduction of data volume by edge-detection algorithms. This method was shown to be capable of a resolution of about 0.01 cm in all three space dimensions, and thus capable in principle of determining the surface curvature and the contact angle as part of the experiment. The method could also be applied to dynamic measurements.

One consequence of these developments, as already mentioned, was almost to require use of an immiscible liquid pair rather than a single liquid in equilibrium with its vapor. Even for a two-liquid system, serious optical distortions can occur inside the container if the refractive indices are not well matched. For example, if the difference in refractive index is 0.01, total reflection will occur whenever light traveling through the optically denser liquid encounters the interface at a relative angle smaller than about 7° . There is therefore a conflict between the need for a close match in index for the flight experiment and the need for a sufficient mismatch in index so that the contact angle can be measured in the laboratory. Another consideration was that a suitable fluorescent dye should be soluble in one liquid of the pair but not in the other. A

suitable dye was defined to be one capable of being excited by light from a solid-state laser diode, for obvious reasons of reliability of the optical instrumentation. In practice, this last consideration was found not to be a problem.

Other contributions to the research, mostly coming from Hesselink at Stanford, included ideas about the mechanical design of the flight apparatus. Small contact angles generally require containers of large aspect ratio if a substantial fraction of the fluid volume is to be associated with the critical region for which displacement is theoretically unbounded. The difficulty of managing stretched or distorted geometries needs to be weighed against the disadvantage of using liquids having larger contact angles but having less desirable and perhaps less reproducible physical and chemical properties. In order to operate on both sides of a critical condition, the geometry should be variable or the container should be tapered, either literally or figuratively (perhaps by a programmed change in temperature). In either event, the experiment must initially define one direction to be down. One method in space might be to mount several containers on a carousel to produce artificial gravity that can be slowly and carefully reduced to zero after the container is filled and the liquids are separated. A side benefit would be the opportunity to experiment over a wide range of Bond number. A disadvantage is potential conflict between the need for rotation and the needs imposed by whatever technique is chosen for optical instrumentation.

Several possible configurations for the apparatus have been explored to achieve the objectives of the experiment. The major differences are in the placement of the optical and electronic instrumentation. Maximum flexibility is achieved by placing the optical diagnostics on the carousel and by providing an independent scan mechanism. This flexibility is achieved at the expense of complexity. A mechanically simpler system would place the optical diagnostics on a stationary platform and use the rotation of the carousel to scan the liquid volume inside the container. However, the observation period is then slaved to the spin rate of the carousel. The scan rate is slowest when the body forces are small and the interface behavior is most interesting. Other problems concern the amount of data processing to be performed in space or on the ground after the flight, the influence of the space-vehicle environment on the design, and the probable effects of launch on the apparatus. None of these problems seems to

be particularly difficult.

5 Other Interactions

Peer review of this research was part of several contract renewals. These reviews more than once raised the point that a space experiment might not be necessary if a liquid pair could be found with a sufficiently close match in specific gravity. Examination of the tables in chapter 2 suggests that a suitable pair might be, for example, glycerol tributanoate (specific gravity 1.035) and 1,2-propanediol (1.036), with the specific gravity of either adjustable by dilution with small amounts of a third liquid.

The existing theory stipulates a value of zero for the Bond number B, defined as

$$B = \frac{g \Delta \rho L^2}{\sigma} = \frac{g}{g_0} \frac{\Delta \rho}{\rho_0} \left[\frac{g_0 \rho_0 L^2}{\sigma} \right] \tag{2}$$

where g is apparent gravity, $\Delta\rho$ is difference in density, L is a characteristic scale of the apparatus, σ is surface tension, and the subscript 0 refers to terrestrial values. For a terrestrial experiment with a single liquid under its vapor, g/g_0 is unity and $\Delta\rho/\rho_0$ is close to unity. For a space experiment, g/g_0 can presumably be reduced to $O(10^{-4})$. To reach the same small Bond number on the ground, other things being equal, $\Delta\rho/\rho_0$ would have to be reduced to $O(10^{-4})$ by use of a suitable liquid pair. This value is beyond the ordinary limit of resolution in measurement of density for either liquid, and it implies that the temperature has to be very precisely controlled. Moreover, no method suggests itself for varying the Bond number substantially during such a terrestrial experiment. Small changes in Bond number, even including a change in sign, might be achieved if the temperature is controlled and the two liquids have sensibly different volume coefficients of expansion (whether or not this is the case for the liquid pair named above, or for other candidate liquid pairs, is not known at present). Because the characteristic thermal diffusion time will be of the order of minutes to hours, it is likely for any terrestrial experiment in which temperature is an independent variable that the same difficulties with density inhomogeneities and slow convection currents will be encountered that characterize several other experiments in the PACE program, particularly experiments

aimed at quantitative study of critical-point phenomena. Experiments on earth might well turn out to be as complex and as expensive as experiments in space.

From the experimental point of view, it is another difficulty in the theory that the geometry and the contact angle are the primary data. In practice, it is the apparent gravity g that is at the disposal of the experimenter. Available evidence from recent numerical computations suggests that the striking surface behavior predicted for critical configurations can be observed even if the Bond number is not strictly zero. In order to achieve a more precise understanding of physical phenomena observed in a real apparatus, therefore, it was proposed to conduct the experiments with one or more systems that are demonstrably well behaved for non-zero Bond number but approach the limiting singular behavior as the Bond number approaches zero. This objective can be best achieved in space by control of g/g_0 through programmed imposition and removal of a body force associated with rotation. This procedure also provides an opportunity to observe any hysteresis as the direction of motion of the interface is reversed. The direction of rotation can itself be reversed if there is any reason to believe that the effects of angular acceleration are not negligible, or cannot be adequately compensated for by programming the orientation of the container.

In 1986, after the Challenger accident, a PACE science review board consisting almost entirely of physicists recommended that the present proposed experiment be dropped from the program. One of the reasons given was that the static mathematical theory is sound and also sufficiently complete so that space experiments are not needed. The investigators disagree sharply. They thought and still think that space experiments should be designed to produce accurate quantitative data on dynamic configurations of the internal interface. The analytical results at present are based on a static theory. They predict conditions under which a global change in the surface configuration must occur. The theory thus provides essential guidance on the question of geometry. However, presently available analytical results do not predict the dynamic nature of this change, and no such complete description is currently in sight. The equations considered so far amount to a boundary condition of constant surface curvature and constant contact angle for much more complex non-linear dynamic equations that apply when the fluid is moving. Moreover, the contact-angle boundary condition is then highly uncertain,

since there exists no acceptable theory for conditions near a moving contact line. Even if no attempt is made in an experiment to observe the internal motion of the liquid, dynamic data on surface configuration can therefore provide a challenge to theory for a long time to come. In fact, the existence of such dynamic data at the end of a space experiment can be taken as a direct measure of success or failure. A corollary conclusion is that flight experiments in simulated free fall, or experiments in a drop tower, are unlikely to be successful in the sense just defined, because the necessary instrumentation probably could not be accommodated.

References

Bikerman, J. J. (1970) *Physical Surfaces*, Academic Press, New York.

Concus, P. and Finn, R. (1974) On capillary free surfaces in the absence of gravity. Acta Mathematica **132**, 178-198.

Dussan, E. B. (1979) On the spreading of liquids on solid surfaces: Static and dynamic contact lines. In: *Annual Reviews of Fluid Mechanics* **11**, 371-400.

Finn, R. (1983) Existence criteria for capillary free surfaces without gravity. Indiana University Math Journal **32**(3), 439-460.

Fowkes, F. M. (ed.) (1964) *Contact Angle, Wettability, and Adhesion*, Adv. in Chem. Series **43**, Am. Chem. Soc., Washington, D.C.

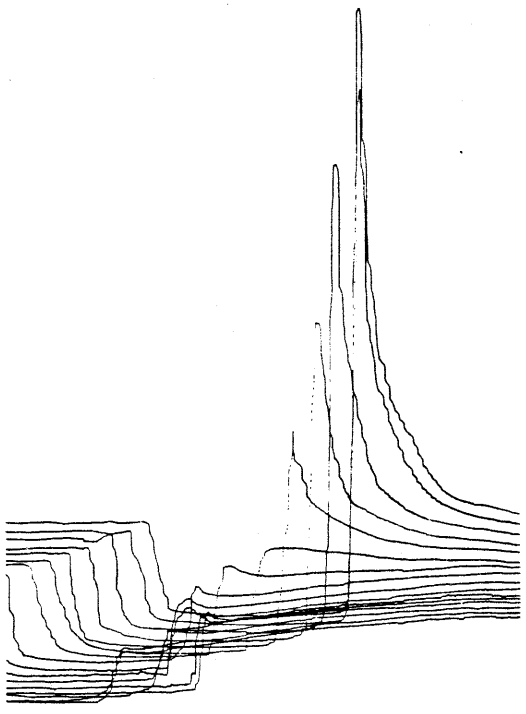

Figure 1. Measurement of the static contact angle of acetone on a glass plate by the refraction method. Horizontal coordinate is space; vertical coordinate is light intensity. Plate angle varies from 1.6 degrees (top trail) to 16.6 degrees (bottom trail).

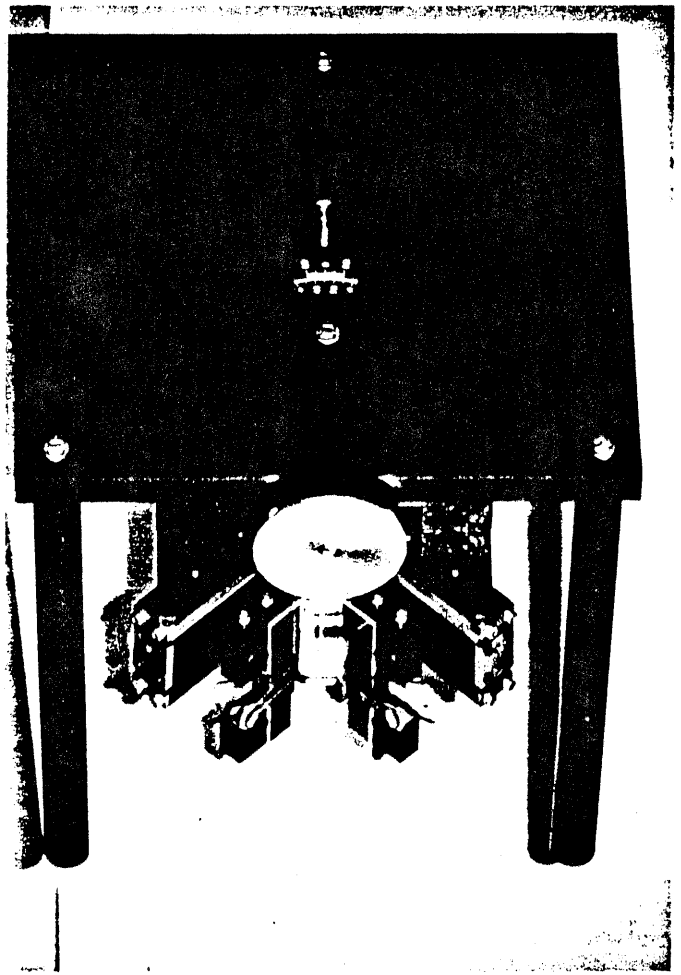

Front/top view

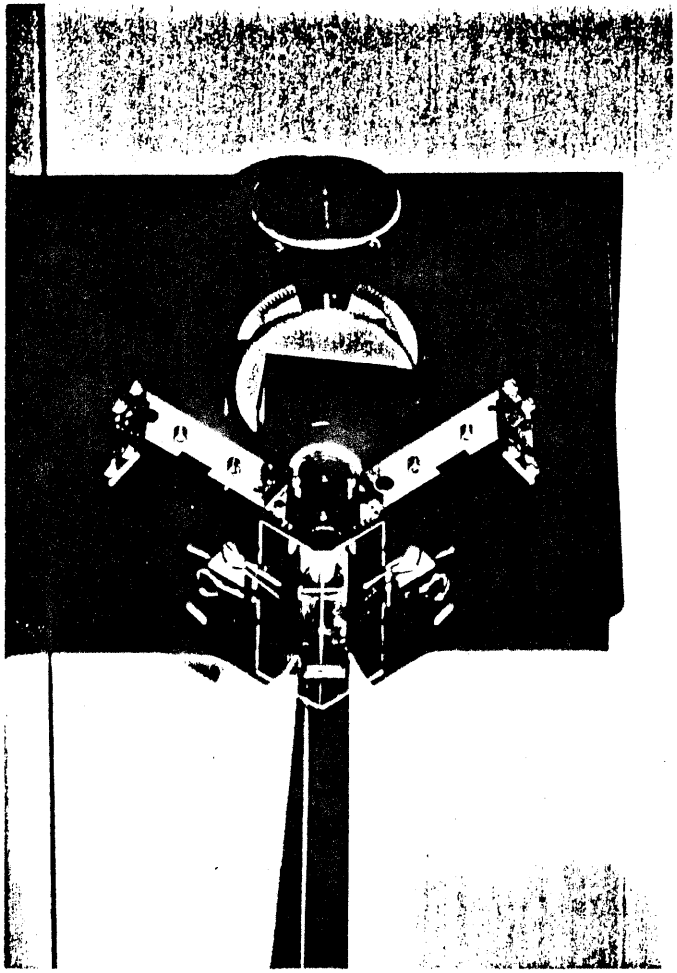

Front/bottom view

Figure 2. Two views of the apparatus used to measure contact angle by application of the corner criterion of Concus and Finn (1974). (M. Yoda, private communication).

Chapter II

Some transparent immiscible liquid pairs

short running title: Transparent immiscible liquid pairs

(To appear in the Journal of Colloid and Interface Science)

Gregory Smedley and Donald Coles
Graduate Aeronautical Laboratory
California Institute of Technology
Mail code: 205-45
Pasadena, California 91125
U.S.A.

Abstract

This report identifies 121 transparent immiscible liquid pairs that have properties compatible with optical instrumentation based on laser-induced fluorescence. Physical data such as specific gravity, index of refraction, viscosity, flash point, and toxicity were found in the literature. Compatibility with plexiglas (PMMA), contact angles of the internal meniscus on glass and PMMA, meniscus formation times, and clearing times were measured. A useful non-invasive technique for determining interfacial tensions is explained and used. Some dependence of interfacial tension on molecular structure is found.

1 Introduction

The work reported here was undertaken as part of preparation for a proposed space experiment to study the relationship between container geometry and interface geometry for a free liquid surface at zero gravity. The research has involved a search for immiscible liquid pairs having properties compatible with optical instrumentation based on laser-induced fluorescence. The research was also guided by the peculiar requirements of space flight, including especially the prospect that any experiment will be highly automated and will be carried out only once.

In general, the capillary behavior of a liquid-vapor-solid system can be expected to be very sensitive to thermal effects. If the system is not closed or is not in thermodynamic equilibrium, evaporation and condensation at the liquid surface can change the temperature locally. Even in the absence of gravity, temperature inhomogeneities can affect the interfacial tension and thus lead to convective motions in both the liquid and the vapor. Condensation of vapor on the solid surface near a contact line can also produce an anomalous surface condition and thus affect the capillary behavior.

Although these difficulties are reduced in a closed system whose temperature is closely regulated, some means is still required to observe the shape of the capillary surface, including perhaps the static or dynamic contact angle. Either reflective or refractive properties of the interface are normally used for this purpose. However, total light reflection will occur at near-grazing angles of incidence if there is an appreciable discontinuity in index of refraction at the interface or at the container wall. One solution for this total-reflection problem is use of two immiscible liquids with closely matched indices of refraction. For detection of the interface, it is proposed to dissolve a fluorescent dye in one of the liquids and to use a laser light sheet to probe the meniscus by exciting the dye. Preliminary work suggests that this technique is feasible.

In section 2 of this paper, the methods used to select suitable liquids are outlined, and a table is provided of numerous transparent liquids with some of their physical properties. The main content of the paper is an associated table in section 2 of immiscible liquid pairs suitable

for research of the kind contemplated here, and perhaps for other purposes as well, such as experiments with stratified flow. Some approximate measurements of internal contact angle on glass and plexiglas are described in section 3. A non-intrusive technique, used to estimate Bond number and interfacial tension, is outlined in section 4. Some observed trends in the data are related to molecular structure in section 5, and a few comments are made about the reliability of the tables.

2 Liquid Properties

The primitive strategy of the initial search was first to generate lists of transparent liquids that can be classified either as strongly hydrophilic or as strongly hydrophobic, according to their solubility or lack of solubility in water. The hydrophilic group originally consisted of ten liquids, of which two (water and glycerol) were eliminated for reasons stated in the next paragraph. The hydrophobic group originally consisted of 130 liquids, of which 65 survived to be included in the final tables. A number of other hydrophobic liquids were considered but were disqualified on grounds of unsuitable freezing or boiling point, low flash point, lack of optical clarity, known toxicity, or other unattractive properties. It is possible that some of the accepted liquids, particularly formamide and several brominated hydrocarbons, have toxic properties that may eventually disqualify them when they are examined more carefully. In any event, the list of liquid pairs presented here is not claimed to be definitive.

Each liquid of one group was tested for miscibility with each liquid of the other group. The miscibility test consisted of placing approximately one milliliter of each liquid of a pair in a pyrex culture tube with a teflon-lined screw cap (VWR Scientific Catalog (1): Kimble: 45066A). The liquids remained in contact for a year or more, and were repeatedly mixed (emulsified) by vigorous shaking. There were several grounds for rejection of a liquid pair:

mutual solubility estimated as more than a few percent (some mutual solubility may be desirable);

chemical reaction, including discoloration (rare);

failure to de-emulsify or clear in a reasonable time (including especially persistence of a frost-like emulsion on the wall near the internal contact line);

permanent deposition of droplets of either liquid on the tube wall under the other liquid (water and glycerol were rejected on this ground).

Table I summarizes some physical properties of the 8 hydrophilic and 65 hydrophobic liquids, listed in each case in order of increasing specific gravity. In almost all cases the name assigned to a chemical is the popular name. An official identification number taken from the Chemical Abstracts Service register is also listed. The specific gravity (usually measured at 20°C) and the index of refraction (usually measured at 20°C for the sodium D line) are weighted in favor of values listed in the CRC Handbook of Chemistry and Physics (2). Default values are from the current Aldrich catalog (3) or from the Merck Index (4). The code for toxic hazard is from Sax (5). Values for flash point are taken from the Aldrich catalog (3) or from Sax (5). The property that is least certain in the table is the viscosity (measured or interpolated at 20°C except where noted). In some cases, no value for viscosity could be found in the literature even after a diligent computer search.

Of the 1300 pairs tested, 121 were found to be acceptable according to the criteria already mentioned. These pairs are listed in Table II in order of increasing nominal difference in index of refraction. Observations or estimates are provided for several other properties, including meniscus formation time and clearing time, and contact angle on glass and plexiglas. Estimates of interfacial tension, determined from measurements of meniscus height and contact angle, are also provided.

3 Measurements

In Table I, the entry for compatibility with plexiglas or poly(methylmethacrylate) or PMMA is the result of a test in which small strips of this material were partially immersed in each liquid for several months. This test was motivated by the fact that plexiglas is a popular material in some experimental work where these liquids may be used. The approximate meaning of the entries is:

good -- no readily apparent effect;

fair -- some swelling or softening and/or very slow crazing;

poor -- severe crazing; partial or complete solubility; occasional gel formation.

All of the hydrophilic liquids, and about half of the hydrophobic liquids, are judged to be compatible with PMMA. These combine to provide 66 compatible liquid pairs.

In Table II, the entries for meniscus formation time represent the time required for the two liquids to form a smooth, well-defined meniscus after vigorous shaking. The clearing time represents the additional time required for both liquids to become essentially clear. A clearing time of zero means that no emulsion was present after the meniscus was fully formed.

Direct measurements were made, using a cathetometer with a rotating angular eyepiece, of the height and the contact angle on borosilicate culture-tube glass of the internal meniscus for each liquid pair. These measurements are used in section 4 to estimate the interfacial tension. If the meniscus was concave upward, the contact angle refers to the lower liquid. If the meniscus was concave downward, the contact angle refers to the upper liquid and is enclosed in parentheses in Table II. It is worth noting that the hydrophilic liquid is always on the convex side of the interface in all the liquid pairs considered here. To remove distortion caused by refraction at the glass-air interface of the cylindrical culture tube, the tube was mounted in a square glass cell, and the intervening space was filled with a mixture of methanol and methyl benzoate whose composition was adjusted until the index of refraction closely matched that of the culture tube. Various modes of lighting were tried for observation of the meniscus, and diffuse polychromatic light was finally judged to be more effective than parallel and/or monochromatic light. Fig. 1 is a photograph of the culture-tube wall and a portion of the interface and contact region for 1-chlorohexane over formamide. The index of the matching solution has been deliberately detuned to show the location of the outer culture-tube wall.

There is a systematic distortion of the meniscus in Fig. 1. To analyze this distortion at a rudimentary level, assume that the culture tube is lighted from the rear by a diffuse light source and is viewed from a large distance using telescopic optics. The meniscus is convex to one of

the liquids, whose index of refraction n_i is assumed to be smaller than the index n_o of the culture tube and cell (this is the case for all of the liquid pairs in Table II). Fig. 2 shows a light ray that touches the interface and emerges from the cell along the line of sight. The geometry of the figure yields immediately the series of proportionalities

$$\frac{n_i}{n_o} = \frac{\sin\theta_o}{\sin\theta_i} = \frac{r'/L}{r/L} = \frac{r'}{r} \qquad [1]$$

of which the first is Snell's law of refraction. Thus the apparent radial position r' of the meniscus is related to the real position r by the affine transformation $r' = r\,\frac{n_i}{n_o} < r$, and the real contact angle γ is related to the apparent angle γ' by

$$\gamma = \tan^{-1}\left[\frac{n_o}{n_i}\tan\gamma'\right] \qquad [2]$$

This correction was applied to all of the measured contact angles. In most cases, the correction was less than 0.5 degrees, which is well within the estimated accuracy of ±2 degrees for the measurement.

To obtain a rough estimate of the internal contact angle on PMMA, strips of this plastic were inserted into the culture tubes containing the 66 compatible pairs. The new contact region was viewed edge on, as in the photograph in Fig. 3, which shows diethyl diethylmalonate over formamide. The measured contact angles were in general larger and covered a wider range than those for glass. The inflection of the interface in the figure (the inversion of the contact angle) is typical for all but a few of the liquid pairs. Examination of the whole of the data suggests that the inversion is a result of stronger bonding of the hydrophilic liquid to glass compared with bonding of the hydrophobic liquid. In the few cases where inversion of the interface did not occur; the contact angle increased, but not past the 90 degrees required for inversion.

4 Non-intrusive Determination of Interfacial Tension

The dimensionless number that is characteristic of capillary phenomena is the Bond number, which is essentially the ratio of gravitational force to surface-tension force;

$$B = \frac{\Delta\rho\, g\, L^2}{\sigma} \qquad [3]$$

In this equation $\Delta\rho$ is the difference in density for two liquids separated by an interface, g is the acceleration of gravity, L is a characteristic length (here taken as the radius of the culture tube, 0.57 cm), and σ is the interfacial tension.

In the present context, all of the quantities in Eqn. [3] are known except B and σ. If the Bond number can be estimated, a value for the interfacial tension follows. The necessary estimate can be obtained from an analysis carried out by P. Concus (6) to determine the geometry of an equilibrium capillary surface inside a vertical cylinder of circular cross section. Along a diameter, the interface elevation $z(r)$ is determined by the capillary equation

$$\frac{1}{r}\frac{d}{dr}\left[\frac{r\, dz/dr}{[1+(dz/dr)^2]^{1/2}}\right] - Bz - \lambda = 0 \qquad [4]$$

where λ is a constant equal to twice the radius of curvature of the interface on the axis, where $r = z = 0$. All lengths are made dimensionless with L. The boundary conditions are

$$z = 0, \quad \frac{dz}{dr} = 0 \quad \text{at} \quad r = 0 \qquad [5]$$

$$z = h, \quad \frac{dz}{dr} = \cot\gamma \quad \text{at} \quad r = 1 \qquad [6]$$

where h is the meniscus height and γ is the contact angle. Concus used a shooting method to integrate Eqn. [4] and provided plots of h and λ as functions of B for fixed contact angles of 0 (10) 80 degrees. In the present work, the quantities h and γ are assumed to be known from the optical measurements. The same numerical methods used by Concus were applied to implement a two-parameter search for the quantities B and λ. Concus's plots

established a suitable starting point, given the measured contact angle and meniscus height. The values inferred for σ from Eqn. [3], using values of $\Delta\rho$ derived from Table I, are included in Table II.

5 Discussion and Conclusions

The properties listed in Tables I and II for the various liquids and liquid pairs should not be accepted uncritically. The culture tubes were not cleaned but were used as received, because the primary objective at the outset of the work was to identify acceptable liquid pairs. The manufacturer (Kimble; division of Owens, Illinois) states that the screw-top culture tubes were annealed at high temperature, hot enough to burn off organic deposits, before being packaged in sealed cardboard boxes. On arrival, the tubes were found to be clean, except for the occasional occurrence of fibers. The chemicals were purchased in small quantities, were not tested for purity, and in a few cases were labelled as "tech" or "pract" grade. Due to the large number of chemicals used and the small volume of each, custom purification of each liquid considered was simply out of the question. Handbook values for specific gravity or index of refraction were sometimes found to be inconsistent from one authority to another. For example, the four best visible matches in index of refraction, as judged by eye in terms of a weak color band as a vestigial indicator of interface position, are marked by asterisks in Table II. In one case, a pair having a difference in nominal index of 0.009 appeared to the eye to be much more closely matched than pairs having identical nominal indices. Nevertheless, the tables should be useful in making a preliminary choice of liquid pairs whose properties can then be established more rigorously for a particular application. The tables should also be useful in suggesting combinations (of pairs) that might be used to allow close control over either the difference in specific gravity or the difference in index of refraction or both.

Statements about compatibility of the various liquids with PMMA should also be treated as preliminary. Impurities in the various liquids may be a factor, and there are numerous formulations of PMMA. Considerable care may be required in fabrication of PMMA containers, including stress-relieving during and after machining to minimize crazing.

The measured contact angle itself may be in error by as much as two degrees in either direction. A more serious uncertainty in the measurement of contact angle arises from lack of control over the purity of the chemicals. One or two experiences with a second measurement of contact angle for a given liquid pair, but with one or both chemicals obtained from different vendors, showed discrepancies amounting to several degrees. More precise work aimed at a particular application therefore implies suitable care in specifying the purity of the liquids and the cleanliness of the container.

Errors in the measurements of contact angle γ and meniscus height h must be considered before determining the overall accuracy to which the Bond number is known. For an error of two degrees in contact angle, the error in Bond number varies from 28 percent to 5 percent as the Bond number varies from 1 to 60. It is important to note that the error in Bond number is also dependent upon the size of the angle being measured. A $\pm 2°$ error in a larger contact angle yields a larger error in the Bond number; this is demonstrated in Fig. 4 by the convergence of the Bond number curves as the contact angle approaches 90°. Therefore, the largest errors in Bond number occur for large contact angles and small Bond numbers. An error of 0.004 cm in the measurement of the meniscus height produces an error in Bond number of 10 percent to 7 percent over the same range. For Bond numbers greater than 10, the error due to contact angle measurement is less than 7 percent, while the error due to meniscus height measurement is also less than 7 percent. Note that these two errors are independent. The relative error in σ is the same as the error in B. For the test case, described in the following paragraphs, the Bond number was approximately 4. The estimated error in B computed for the average contact angle and meniscus height was approximately 22 percent, which is consistent with the observed spread in the data reported in Table III and displayed in Fig. 4.

A reviewer suggested that contact angles and therefore interfacial-tension measurements would be very sensitive to the cleanliness of the glass. The method described in this paper was therefore tested for a few liquid pairs for which interfacial tensions have been found in the literature. These liquid pairs were organic liquids; namely, heptanol, nonanol, decanol, benzene, ethyl ether, and carbon tetrachloride, all paired with water. The interfacial tensions quoted in the literature are for mutually saturated liquids, and the liquid pairs used in this test

were therefore emulsified several times to ensure mutual saturation. However, only carbon tetrachloride with water was found to be even marginally suitable for the technique used here. This liquid pair would have been rejected according to the specifications listed in section 2. The three alcohols were rejected because of the persistence of a frost-like emulsion on the wall near the contact line. Benzene and ethyl ether were rejected because their meniscus heights were of the order of the measurement resolution. The pair carbon tetrachloride and water tended to deposit droplets of either liquid on the tube wall under the other liquid. However, by rotating the inclined tube slowly, these droplets could be reduced in size and number, so that contact-angle and meniscus-height measurements could be performed with reasonable satisfaction. The method used was the same as for all the other measurements reported here.

This test also included a comparison of interfacial-tension values obtained from carefully cleaned tubes and tubes that were used as received. For this purpose, one tube was cleaned according to procedure 'C' as specified by Scientific Specialties Service (7). The tube was washed in biodegradable laboratory glassware cleaner, rinsed thoroughly with tap water, rinsed with 1:1 nitric acid, rinsed with triple distilled deionized water, air dried, and assembled in an organic-free environment. One milliliter of spectro-photometric grade carbon tetrachloride and one milliliter of triple-distilled deionized water were added to each tube. Measurements at ten circumferential locations were made of each interface after the liquids had been in contact for more than two weeks and had been shaken several times. The results of these measurements, given in Table III, indicate that cleaning of the tube reduces the dispersion in the data from 28 percent to 23 percent, and also yields an interfacial tension that is closer to the value interpolated from Harkins and Cheng (8). Nevertheless, the results obtained indicate that a reasonable estimate of the interfacial tension can be achieved by this method without first cleaning the tube.

Determination of the interfacial tension using the technique described here depends on measurement of both the contact angle γ and the meniscus height h. In calculations using the method of Concus (6), the Bond number is assumed fixed, although its value has to be determined. The Bond number is a dimensionless indicator of meniscus shape. Therefore, h and γ have a well-defined (nearly linear) relationship for fixed Bond number. This same

relationship turned out to be satisfied by the observed values of h and γ in the test just described. Fig. 4 shows the observed values of h and γ and the curves of constant Bond number for B = 5.06, 4.15, and 3.24 from bottom to top. These curves were calculated by fixing γ and B and shooting λ to find the meniscus height at the tube wall. The Bond number used to compute the solid curve, was found by a line fit to all the data. The dotted curves represent the estimated error in the Bond number caused by the uncertainty in the contact-angle and meniscus-height measurements. Note that the observed contact angle for the water/carbon tetrachloride pair in the cleaned culture tube varied from 19° to 48° at the ten points around the circumference, and from 26° to 63° for the tube used as received. However, in the main body of experiments reported in Table II, two contact-angle measurements were made 180° apart, and these contact angles rarely differed by more than the estimated accuracy of ±2° about the mean value. The eight cases where the contact angle difference was larger than ±2° but not more than ±4° are indicated by daggers † in Table II. Therefore the estimates of interfacial tension reported in Table II are dependable to the stated accuracy, unless indicated by daggers.

The interfacial tensions found for the 121 liquid pairs in Table II cover a broad range of values. The value of the interfacial tension for a particular liquid pair is a measure of the relative strength of intra-fluid attractions and inter-fluid attractions. A useful parameter is the hydrophilicity index (Table IV), which is the ratio of the number of OH groups to the number of carbon atoms in the molecule. A higher hydrophilicity index implies greater intra-fluid attraction and higher interfacial tension when paired with hydrophobic liquids. Indeed, this general trend was found, as recorded in Tables V and VI. Esters and ketones tended to have lower interfacial tensions than saturated hydrocarbons when paired with the same hydrophilic liquids. This observation indicates that inter-fluid forces are stronger between hydrophilic liquids paired with esters or ketones than they are for the same hydrophilic liquids paired with saturated hydrocarbons, probably because of oxygen-to-hydrogen attraction across the interface. The position of the OH groups on the hydrophilic molecules was also found to be important, as recorded in Table VII. When the OH groups are located on the first and second carbons, as for 1,2-propanediol, rather than the first and third, as for 1,3-propanediol, the interfacial tension is decreased dramatically. Note that dipropylene glycol was omitted from these tables, since it formed only one acceptable immiscible pair. Formamide was also omitted, because although it

formed many successful liquid pairs, its structure is very different from the other hydrophilic liquids and therefore does not lend itself well to comparison. A final note is that the three alcohols, octanol, nonanol, and decanol, formed acceptable immiscible pairs only with formamide. Alcohols have non-zero hydrophilicity indexes and stronger inter-fluid attraction when paired with hydrophilic liquids; hence greater solubility.

In summary, 121 suitable liquid pairs have been found. They exhibit a wide range of contact angles, interfacial tensions, and viscosities. In addition, 66 of these pairs are compatible with plexiglas. Suggested relationships between molecular structure and interfacial tension may aid in the extension of Table II and in the choice of a liquid pair best suited to a specific application. The method described here for determination of the interfacial tension may be adequate if other more intrusive techniques are not feasible.

This material is based upon work supported by the U.S. National Aeronautics and Space Administration and the University of California. The opinions, findings, conclusions and recommendations are those of the authors and not necessarily of the U.S. National Aeronautics and Space Administration or the University of California.

References

1. VWR Scientific Catalog 84/85, p 1551.

2. Weast, R.C. (ed.), "CRC Handbook of Chemistry and Physics (59th edition)". CRC Press, West Palm Beach, Florida, 1978.

3. "Aldrich Catalog Handbook of Fine Chemicals (1984-1985)". Aldrich Chemical Co., Milwaukee, Wisconsin, 1984.

4. Windholz, M. (ed.), "The Merck Index (9th edition)". Merck and Co., Rahway, New Jersey, 1976.

5. Sax, N., "Dangerous Properties of Industrial Chemicals (6th edition)". Van Nostrand Reinhold, New York, 1984.

6. Concus, P., *J. Fluid Mech.* **34**, 481-495 (1968).

7. Scientific Specialties Service Inc. Randallstown, MD 21133. Pre-Cleaned Bottle Book 1988, p 16.

8. Harkins, W.D. and Cheng, Y.C., *J. Amer. Chem. Soc.* **43**, 35-53 (1923).

Figure Captions

Figure 1 Internal meniscus against borosilicate glass culture tube (1-chlorohexane over formamide).

Figure 2 Ray trace diagram of affine contraction.

Figure 3 Internal meniscus inversion from borosilicate glass culture-tube wall to PMMA blade (diethyl diethylmalonate over formamide).

Figure 4 Meniscus height versus contact angle for water/carbon tetrachloride. (Contact angle measured in upper liquid) Bond number = 5.06, 4.15, and 3.24 from bottom to top.

Table I
Collected physical properties of some transparent liquids

[ ]	=	Chemical Abstracts Service identification number.
SG	=	specific gravity, usually measured at 20 °C and referred to water at 4 °C.
IR	=	index of refraction, usually measured at 20 °C for the yellow D line of sodium.
ν	=	kinematic viscosity, usually at 20 °C, in stokes (cm^2/sec). (ν^*, computed from formulas, usually with reference to experimental data; ν^{25}, viscosity at different temperature, usually 25 °C; ν^+, extrapolated or interpolated from experimental data.)
Toxic hazard	=	symbol from Sax (4). Usually refers to 50-percent lethal dose in laboratory animals ("3" means 0.04-0.4 g/kg: "2" means 0.4-4 g/kg: "1" means 4-40 g/kg). More than one code means that the chemical is more toxic to some species of laboratory animals than to others.
Flash point	=	usually closed cup in °F, from Aldrich catalog (2) where possible.
Compat PMMA	=	compatibility with unstressed plexiglas = poly(methylmethacrylate). ("good", no easily visible effect; i.e., the chemical can be stored in a PMMA container; "fair", noticeable crazing, swelling, or softening; "poor", severe interaction, often in a period of minutes.)

Name [CAS number]	SG	IR	ν cm^2/sec	Toxic hazard	Flash point °F	Compat PMMA
			HYDROPHILIC LIQUIDS			
1,5-pentanediol [111-29-5]	0.992	1.449	1.290	1	265	good
dipropylene glycol [106-62-7]	1.021	1.440	0.746^{25}	1	280	good
1,2-propanediol [57-55-6]	1.036	1.432	0.541	3-2-1	225	good
1,3-propanediol [504-63-2]	1.060	1.440	0.440	1	175	good
ethylene glycol [107-21-1]	1.109	1.432	0.179	2-1	230	good
diethylene glycol [111-46-6]	1.116	1.447	0.320	3	290	good
triethylene glycol [112-27-6]	1.124	1.453	0.436	3-1	330	good
formamide [75-12-7]	1.133	1.447	0.034	3	310	good
			HYDROPHOBIC LIQUIDS			
octane [111-65-9]	0.703	1.397	0.008	1	60	good
nonane [111-84-2]	0.718	1.405	0.010	3	88	good
decane [124-18-5]	0.730	1.410	0.012	3	115	good
1-decene [872-05-9]	0.741	1.422	0.011	--	118	good

1-octyne [629-05-0]	0.746	1.416	0.008^{25}	--	64	fair
4-octyne [1942-45-6]	0.751	1.425	--	--	68	good
dihexyl ether [112-58-3]	0.794	1.420	0.016^{*}	1	170	good
2,6-dimethyl-4-heptanone [108-83-8]	0.805	1.413	0.012	2-1	120	good
squalane [111-01-3]	0.808	1.453	0.467	--	424	good
2-heptanone [110-43-0]	0.811	1.409	0.010	2-1	117	poor
4-heptanone [123-19-3]	0.817	1.407	0.009	2	120	poor
3-heptanone [106-35-4]	0.818	1.406	--	2	106	poor
2-octanol [123-96-6]	0.819	1.420	0.098	3	160	good
2-octanone [111-13-7]	0.820	1.415	0.013^{+}	2	145	poor
5-nonanone [502-56-7]	0.822	1.420	0.016	2	141	good
3-octanone [106-68-3]	0.822	1.415	--	3	115	fair
4-decanone [624-16-8]	0.824	1.424	--	--	160	good
1-nonanol [143-08-8]	0.827	1.433	0.135	2-1	168	good
1-decanol [112-30-1]	0.830	1.437	0.172	3	180	good
isopropyl myristate [110-27-0]	0.853	1.435	0.066	3	--	good
isobutyl isobutyrate [97-85-8]	0.854	1.400	0.010^{25}	2-1	111	good

ethyl laurate [106-33-2]	0.862	1.431	0.039	--	234	good
isopropylbenzene [98-82-8]	0.862	1.492	0.009	2	115	poor
ethyl caprate [110-38-3]	0.865	1.426	0.027[+]	1	216	good
ethyl isovalerate [108-64-5]	0.866	1.396	--	2-1	80	poor
ethyl caprylate [106-32-1]	0.869	1.418	0.018	1	167	good
methyl laurate [111-82-0]	0.870	1.432	0.036	--	235	good
butyl butyrate [109-21-7]	0.871	1.408	0.012	2-1	128	good
2-ethylhexyl acetate [103-09-3]	0.872	1.420	0.017	2	187	good
methyl caprylate [111-11-5]	0.878	1.417	0.026	1	163	good
1-chlorohexane [544-10-5]	0.879	1.420	0.008	--	80	good
ethyl butyrate [105-54-4]	0.879	1.400	0.008	1	67	poor
methyl caproate [106-70-7]	0.885	1.405	0.010	--	113	poor
butyl acrylate [141-32-2]	0.890	1.419	0.010[*]	2	103	poor
bis(2-ethylhexyl) adipate [103-23-1]	0.922[25]	1.447	0.140[+]	--	380	good
dibutyl carbonate [542-52-9]	0.925	1.412	0.019[25]	--	--	fair
dibutyl sebacate [109-43-3]	0.937	1.442	0.096	1	353	good
dibutyl adipate [105-99-7]	0.962	1.437	0.037[38]	1	--	good

dipropyl adipate [106-19-4]	0.979	1.431	--	--	--	poor
diethyl diethylmalonate [77-25-8]	0.988	1.424	0.038	--	202	good
diethyl pimelate [2050-20-6]	0.994	1.431	0.040	--	235	poor
dipropyl succinate [925-15-5]	1.002	1.425	--	3-1	--	poor
diethyl adipate [141-28-6]	1.008	1.427	0.035	2	235	poor
dimethyl azelate [1732-10-1]	1.008	1.437	0.050	--	--	poor
butyl benzoate [136-60-7]	1.010	1.496	0.021^{38}	2-1	225	fair
dipentyl phthalate [131-18-0]	1.024	1.489	0.321^{+}	--	245	good
glycerol tributanoate [60-01-5]	1.035	1.436	0.112	3	345	good
ethyl benzoate [93-89-0]	1.047	1.501	0.021	2-1	184	poor
dimethyl adipate [627-93-0]	1.060	1.428	0.031	--	225	poor
diethyl maleate [141-05-9]	1.066	1.442	0.033	2	200	poor
1-bromodecane [112-29-8]	1.070	1.456	0.024^{+}	--	202	good
2-phenylethyl acetate [103-45-7]	1.088	1.517	0.022^{25}	3	230	poor
methyl benzoate [93-58-3]	1.089	1.516	0.019	2-1	181	poor
glycerol tripropanoate [139-45-7]	1.098	1.432^{19}	0.130	2	--	poor
1,5-dichloropentane [628-76-2]	1.101	1.456	0.016	3	80	poor

1-bromooctane [111-83-1]	1.112	1.452	0.015	1	173	good
1-bromohexane [111-25-1]	1.174	1.448	0.009	--	135	good
1-bromo-3-methylbutane [107-82-4]	1.207	1.442	0.006^{+}	--	90	fair
2-bromopentane [107-81-3]	1.208	1.441	--	3	69	fair
1-bromopentane [110-53-2]	1.218	1.445	0.007	3	88	poor
2-bromobutane [78-76-2]	1.259	1.437	0.005^{+}	3	70	poor
1-bromobutane [109-65-9]	1.276	1.440	0.005	1	75	poor
bromocyclohexane [108-85-0]	1.336	1.496	0.017	--	145	good
1-bromopropane [106-94-5]	1.354	1.434	0.004	1	78	poor
1,1,2-trichlorotrifluoro-ethane [76-13-1]	1.575	1.358	0.005	2	high	good

Table II
Capillary properties of some immiscible liquid pairs

CA	=	internal contact angle on borosilicate glass or on poly(methylmethacrylate), degrees.
Men. form	=	time required for formation of internal meniscus, minutes.
$\sigma_{int.}$	=	interfacial tension of internal meniscus, dynes/cm (see section 4).
Clear	=	time required for liquid pair to become clear after meniscus is formed, minutes.
SG	=	specific gravity, upper liquid/lower liquid (usually measured at 20°C and referred to water at 4°C).
IR	=	index of refraction, upper liquid/lower liquid (usually measured at 20°C for the yellow D line of sodium).

LIQUID PAIRS

NAMES	CA glass (deg)	CA PMMA (deg)	Men. form. (min)	$\sigma_{int.}$ dyne/cm	Clear (min)	SG	IR
glycerol tripropanoate / ethylene glycol	15	-	2.3	0.9	0	1.098 / 1.109	1.432 / 1.432
bis (2–ethylhexyl) adipate / formamide	13	(70)	3.0	14.4	80	0.922 / 1.133	1.447 / 1.447 *
1,3–propanediol / 1–bromobutane	(13)	-	4.8	9.7	60	1.060 / 1.276	1.440 / 1.440
methyl laurate / ethylene glycol	10	(37)	1.2	10.8	60	0.870 / 1.109	1.432 / 1.432
methyl laurate / 1,2–propanediol	11	(24)	3.0	4.1	0	0.870 / 1.036	1.432 / 1.432
1,3–propanediol / 2–bromopentane	9	-	4.0	9.7	120	1.060 / 1.208	1.440 / 1.441
ethyl laurate / ethylene glycol	15	(44)	1.0	10.1	0	0.862 / 1.109	1.431 / 1.432
dipropyl adipate / ethylene glycol	16	-	1.4	7.0	0	0.979 / 1.109	1.431 / 1.432
1,5–pentanediol / 1–bromohexane	(8)	28	5.3	3.7	240	0.992 / 1.174	1.449 / 1.448
ethyl laurate / 1,2–propanediol	13	(59)	6.7	3.9	0	0.862 / 1.036	1.431 / 1.432
dipropyl adipate / 1,2–propanediol	29	-	4.4	0.3	18	0.979 / 1.036	1.431 / 1.432
diethylene glycol / 1–bromohexane	(7)	44	6.0	5.5	120	1.116 / 1.174	1.447 / 1.448
diethyl pimelate / ethylene glycol	27	-	1.9	1.7†	0	0.994 / 1.109	1.431 / 1.432
1,3–propanediol / 1–bromo –3–methylbutane	(10)	-	5.0	9.6†	60	1.060 / 1.207	1.440 / 1.442
1,3–propanediol / diethyl maleate	(15)	-	6.9	2.1	0	1.060 / 1.066	1.440 / 1.442

diethylene glycol / 1–bromopentane	(7)	-	2.0	4.9	180	1.116 / 1.218	1.447 / 1.445
bis (2–ethylhexyl) adipate / 1,5–pentanediol	9	(43)	8.5	5.3	180	0.922 / 0.992	1.447 / 1.449
dibutyl sebacate / 1,3–propanediol	30	(33)	6.0	14.1	0	0.937 / 1.060	1.442 / 1.440
ethylene glycol / 1–bromopropane	(18)	-	4.8	10.1	0	1.109 / 1.354	1.432 / 1.434
1–bromodecane / triethylene glycol	11	86	8.2	6.1	60	1.070 / 1.124	1.456 / 1.453
1,5–pentanediol / 1–bromooctane	(12)	54	5.0	7.0	0	0.992 / 1.112	1.449 / 1.452 *
dimethyl azelate / 1,3–propanediol	13	-	2.7	5.0	120	1.008 / 1.060	1.437 / 1.440
dimethyl adipate / ethylene glycol	11	-	2.1	2.1	12	1.060 / 1.109	1.428 / 1.432
glycerol tributanoate / ethylene glycol	13	(18)	1.6	8.4	12	1.035 / 1.109	1.436 / 1.432
1,5–pentanediol / 1–bromopentane	(8)	-	1.6	5.8	180	0.992 / 1.218	1.449 / 1.445
glycerol tributanoate / 1,2–propanediol	8	(8)	11.5	0.3	1680	1.035 / 1.036	1.436 / 1.432
1,3–propanediol / 1–bromopentane	(12)	-	4.6	8.9	60	1.060 / 1.218	1.440 / 1.445
diethyl adipate / ethylene glycol	16	-	2.0	3.6	0	1.008 / 1.109	1.427 / 1.432
1,2–propanediol / 2–bromobutane	(49)	-	1.1	2.9†	60	1.036 / 1.259	1.432 / 1.437
diethylene glycol / 1–bromo –3–methylbutane	(5)	-	3.2	5.8	240	1.116 / 1.207	1.447 / 1.442
dimethyl azelate / ethylene glycol	9	-	1.5	5.2	120	1.008 / 1.109	1.437 / 1.432
isopropyl myristate / dipropylene glycol	23	13	3.5	1.7	60	0.853 / 1.021	1.435 / 1.440
1–bromooctane / formamide	9	(59)	5.8	13.6	180	1.112 / 1.133	1.452 / 1.447 *

squalane / formamide	16	(35)	60.0	14.1	120	0.808 / 1.133	1.453 / 1.447
1,3–propanediol / 1–bromopropane	(17)	-	0.8	7.9	120	1.060 / 1.354	1.440 / 1.434
ethyl caprate / 1,2–propanediol	18	(57)	3.1	4.2	60	0.865 / 1.036	1.426 / 1.432
bis (2–ethylhexyl) adipate / triethylene glycol	12	(89)	1.8	6.4	80	0.922 / 1.124	1.447 / 1.453
dipropyl succinate / ethylene glycol	26	-	2.2	0.1†	60	1.002 / 1.109	1.425 / 1.432
4–octyne / ethylene glycol	18	(27)	3.1	6.7	16	0.751 / 1.109	1.425 / 1.432
diethylene glycol / 1–bromobutane	(19)	-	2.5	3.5	120	1.116 / 1.276	1.447 / 1.440
1,5–pentanediol / 1,5–dichloropentane	(5)	-	4.4	5.7	120	0.992 / 1.101	1.449 / 1.456
1,5–pentanediol / 1–bromo –3–methylbutane	(9)	-	2.2	8.7	240	0.992 / 1.207	1.449 / 1.442
formamide / 1–bromobutane	(6)	-	5.8	41.4	120	1.133 / 1.276	1.447 / 1.440
bis (2–ethylhexyl) adipate / 1,3 propanediol	10	(50)	9.1	10.5	180	0.922 / 1.060	1.447 / 1.440
1,5–pentanediol / 1–bromodecane	(8)	63	8.0	8.3	120	0.992 / 1.070	1.449 / 1.456
1,2–propanediol / 1–bromobutane	(15)	-	2.1	5.4	18	1.036 / 1.276	1.432 / 1.440
4–decanone / ethylene glycol	11	(38)	0.8	9.3	0	0.824 / 1.109	1.424 / 1.432
1,3–propanediol / 1–bromohexane	(10)	31	5.0	10.8	120	1.060 / 1.174	1.440 / 1.448
ethylene glycol / 1–bromobutane	(9)	-	4.1	14.9	18	1.109 / 1.276	1.432 / 1.440
4–decanone / 1,2–propanediol	20	(42)	2.3	2.7	0	0.824 / 1.036	1.424 / 1.432
diethyl diethylmalonate / ethylene glycol	10	(16)	1.0	7.8	180	0.988 / 1.109	1.424 / 1.432

1,5–dichloropentane / formamide	11	-	4.6	large	120	1.101 / 1.133	1.456 / 1.447
1,2–propanediol / 2–bromopentane	49	-	1.3	4.6	60	1.036 / 1.208	1.432 / 1.441 *
ethylene glycol / 2–bromopentane	(6)	-	3.8	19.8	20	1.109 / 1.208	1.432 / 1.441
ethyl laurate / 1,3–propanediol	13	(37)	2.3	7.2	180	0.862 / 1.060	1.431 / 1.440
1,5–pentanediol / 1–bromobutane	(8)	-	2.3	5.6	180	0.992 / 1.276	1.449 / 1.440
diethyl maleate / ethylene glycol	14	-	1.9	3.8	12	1.066 / 1.109	1.442 / 1.432
1,2–propanediol / 1–bromo –3–methylbutane	24	-	3.4	4.8	120	1.036 / 1.207	1.432 / 1.442
ethylene glycol / 1–bromo –3–methylbutane	(8)	-	3.7	16.6	60	1.109 / 1.207	1.432 / 1.442
1–decanol / formamide	12	(54)	1.7	5.5	20	0.830 / 1.133	1.437 / 1.447
dibutyl sebacate / 1,2–propanediol	14	(42)	3.0	3.9	180	0.937 / 1.036	1.442 / 1.432
dibutyl adipate / formamide	15	(28)	1.7	6.7	80	0.962 / 1.133	1.437 / 1.447
dimethyl azelate / formamide	14	-	1.0	3.2	0	1.008 / 1.133	1.437 / 1.447
glycerol tributanoate / diethylene glycol	14	(25)	3.9	2.4	120	1.035 / 1.116	1.436 / 1.447
glycerol tributanoate / formamide	12	(15)	4.8	7.2	12	1.035 / 1.133	1.436 / 1.447
1–chlorohexane / ethylene glycol	15	(24)	1.5	5.7	60	0.879 / 1.109	1.420 / 1.432
5–nonanone / ethylene glycol	18	(28)	1.2	9.8	13	0.822 / 1.109	1.420 / 1.432
2–ethylhexyl acetate / ethylene glycol	10	(25)	1.2	7.1	120	0.872 / 1.109	1.420 / 1.432
1,3–propanediol / dimethyl adipate	(8)	-	8.7	0.1	1680	1.060 / 1.060	1.440 / 1.428

2–ethylhexyl acetate / 1,2–propanediol	14	(19)	2.2	1.4	360	0.872 / 1.036	1.420 / 1.432
1,5 pentanediol / 2–bromobutane	(67)	-	0.7	5.2†	180	0.992 / 1.259	1.449 / 1.437
1,2–propanediol / 1–bromopentane	(11)	-	1.8	4.2†	120	1.036 / 1.218	1.432 / 1.445
ethylene glycol / 1–bromopentane	(4)	-	3.8	11.7	120	1.109 / 1.218	1.432 / 1.445
isopropyl myristate / diethylene glycol	12	(49)	2.9	9.7	60	0.853 / 1.116	1.433 / 1.447
ethyl caprylate / 1,2–propanediol	14	(45)	1.8	2.9	270	0.869 / 1.036	1.418 / 1.432
1–nonanol / formamide	9	(58)	1.0	4.9	60	0.827 / 1.133	1.433 / 1.447
bis (2–ethylhexyl) adipate / 1,2–propanediol	8	(69)	2.5	4.9	120	0.922 / 1.036	1.447 / 1.432
1–octyne / ethylene glycol	17	-	0.9	7.1	15	0.746 / 1.109	1.416 / 1.432
ethyl laurate / diethylene glycol	10	(73)	5.2	5.0	60	0.862 / 1.116	1.431 / 1.447
2–octanone / ethylene glycol	9	-	0.6	7.3†	120	0.820 / 1.109	1.415 / 1.432
dihexyl ether / dipropylene glycol	13	14	2.5	1.5†	120	0.794 / 1.021	1.420 / 1.440
dibutyl carbonate / 1,2–propanediol	19	-	1.3	3.3	1440	0.925 / 1.036	1.412 / 1.432
2–heptanone / ethylene glycol	12	-	0.7	7.1	60	0.811 / 1.109	1.409 / 1.432
4–decanone / diethylene glycol	19	(50)	1.1	4.2	60	0.824 / 1.116	1.424 / 1.447
diethyl diethylmalonate / diethylene glycol	12	(15)	4.6	2.5	120	0.988 / 1.116	1.424 / 1.447
4–decanone / formamide	9	(61)	0.3	3.8	0	0.824 / 1.133	1.424 / 1.447
diethyl diethylmalonate / formamide	9	(29)	0.3	7.1	20	0.988 / 1.133	1.424 / 1.447

1–decene / formamide	10	(50)	3.5	8.3	60	0.741 / 1.133	1.422 / 1.447
3–heptanone / ethylene glycol	10	-	0.9	8.0	12	0.818 / 1.109	1.406 / 1.432
2–octanol / formamide	13	(47)	1.5	4.2	120	0.819 / 1.133	1.420 / 1.447
dihexyl ether / formamide	8	90	0.3	19.4	60	0.794 / 1.133	1.420 / 1.447
1–chlorohexane / formamide	8	(68)	1.6	20.9	60	0.879 / 1.133	1.420 / 1.447
2–ethylhexyl acetate / formamide	12	(27)	0.4	7.9	20	0.872 / 1.133	1.420 / 1.447
butyl acrylate / formamide	13	-	0.2	10.0	12	0.890 / 1.133	1.419 / 1.447
ethyl caprylate / formamide	9	(54)	0.4	12.8	240	0.869 / 1.133	1.418 / 1.447
4–decanone / triethylene glycol	13	(52)	1.4	3.8	18	0.824 / 1.124	1.424 / 1.453
methyl caprylate / formamide	12	(39)	0.7	10.6	240	0.878 / 1.133	1.417 / 1.447
2–octanone / formamide	11	-	0.3	5.8	12	0.820 / 1.133	1.415 / 1.447
3–octanone / formamide	18	-	0.3	9.7	13	0.822 / 1.133	1.415 / 1.447
2–ethylhexyl acetate / triethylene glycol	12	(49)	1.3	2.6	120	0.872 / 1.124	1.420 / 1.453
2,6–dimethyl–4–heptanone / formamide	12	(54)	0.7	10.8	12	0.805 / 1.133	1.413 / 1.447
decane / diethylene glycol	11	72	5.5	12.8	1440	0.730 / 1.116	1.410 / 1.447
butyl butyrate / formamide	12	(44)	0.8	10.9	1440	0.871 / 1.133	1.408 / 1.447
4–heptanone / formamide	17	-	0.2	7.2	18	0.817 / 1.133	1.407 / 1.447
2,6–dimethyl–4–heptanone / triethylene glycol	13	(49)	2.0	3.5	270	0.805 / 1.124	1.413 / 1.453

dipentyl phthalate / diethylene glycol	10	(26)	5.5	2.9	240	1.024 / 1.116	1.487 / 1.447
methyl caproate / formamide	9	-	0.5	6.2	12	0.885 / 1.133	1.405 / 1.447
nonane / formamide	8	(89)	2.2	28.3	120	0.718 / 1.133	1.405 / 1.447
dipentyl phthalate / formamide	14	(41)	8.2	12.9	180	1.024 / 1.133	1.489 / 1.447
octane / 1,3–propanediol	10	(88)	2.7	13.2	60	0.703 / 1.060	1.397 / 1.440
decane / triethylene glycol	12	61	4.0	13.1	180	0.730 / 1.124	1.410 / 1.453
isopropylbenzene / formamide	12	-	2.6	19.3	120	0.862 / 1.133	1.492 / 1.447
ethyl butyrate / formamide	12	-	0.5	5.5	0	0.879 / 1.133	1.400 / 1.447
formamide / bromocyclohexane	(13)	34	0.6	21.6	12	1.133 / 1.336	1.447 / 1.496
butyl benzoate / formamide	10	-	15.0	13.8	180	1.010 / 1.133	1.496 / 1.447
ethyl isovalerate / formamide	12	-	0.2	9.5	12	0.866 / 1.133	1.396 / 1.447
isobutyl isobutyrate / triethylene glycol	20	(58)	2.2	3.1	80	0.854 / 1.124	1.400 / 1.453
ethyl benzoate / formamide	14	-	0.9	7.9	120	1.047 / 1.133	1.501 / 1.447
methyl benzoate / formamide	13	-	2.1	9.5	0	1.089 / 1.133	1.516 / 1.447
2–phenylethyl acetate / formamide	10	-	2.0	3.4	20	1.088 / 1.133	1.517 / 1.447
triethylene glycol / Freon 113	(15)	(74)	1.9	4.5	60	1.124 / 1.575	1.453 / 1.358

* Freon 113 = 1,2,2-trifloro-1,1,2-trichloroethane

Culture tube	σ estimated (28^{o}C) (dynes/cm)	Error from published* value: 44.2 dynes/cm
as received	49.7 ± 14.0	12%
cleaned	46.0 ± 10.7	4%

*(interpolated from Harkins and Cheng (8))

Table III

Interfacial tension measurements for water/CCl_4

	Hydrophilicity Index $\left(\frac{\#\ OH}{\#Carbon}\right)$
ethylene glycol	1.00
1,3 propanediol	0.67
1,2 propanediol	0.67
diethylene glycol	0.50
1,5 pentanediol	0.40
dipropylene glycol	0.33
triethylene glycol	0.33
formamide	0.00

Table IV

Hydrophilicity index of hydrophilic compounds

	Hydrophilicity Index (# OH / # Carbon)	Esters				Ketone	Saturated Hydrocarbons			
		2-ethylhexyl acetate	glycerol tributanoate	ethyl laurate	diethyl diethyl malonate	4-decanone	1-bromobutane	1-bromo-3-methyl butane	1-bromopentane	decane
ethylene glycol	1.00	7.1	8.4	10.1	7.8	9.3	14.9	16.6	11.7	---
diethylene glycol	0.50	---	2.4	5.0	2.5	4.2	3.5	5.8	4.9	12.8
triethylene glycol	0.33	2.6	---	---	---	3.8	---	---	---	13.1

Table V

Decrease of interfacial tension (dyne/cm) with decreasing hydrophilicity

	Hydrophilicity Index (# OH / # Carbon)	Esters					Saturated Hydrocarbons					
		dimethyl adipate	diethyl maleate	dimethyl azelate	ethyl laurate	bis (2-ethylhexyl) adipate	1-bromopropane	1-bromobutane	1-bromo-3-methyl butane	1-bromopentane	2-bromopentane	1-bromohexane
ethylene glycol	1.00	2.1	3.8	5.2	10.1	---	10.1	14.9	16.6	11.7	19.8	---
1,3-propanediol	0.67	0.1	2.1	5.0	7.2	10.5	7.9	9.7	9.6	8.9	9.7	10.8
1,5-pentanediol	0.40	---	---	---	---	5.3	---	5.6	8.7	5.8	---	3.7

Table VI

Decrease of interfacial tension (dyne/cm) with decreasing hydrophilicity

	Hydrophilicity Index (# OH/ # Carbon)	Esters			Sat. Hydrocarbons			
		ethyl laurate	dibutyl sebacate	bis (2-ethylhexyl) adipate	1-bromobutane	1-bromo-3-methyl butane	1-bromopentane	2-bromopentane
1,3-propanediol	0.67	7.2	14.1	10.5	9.7	9.6	8.9	9.7
1,2-propanediol	0.67	3.9	3.9	4.9	5.4	4.8	4.2	4.6

Table VII

Dependence of interfacial tension (dyne/cm) on OH placement

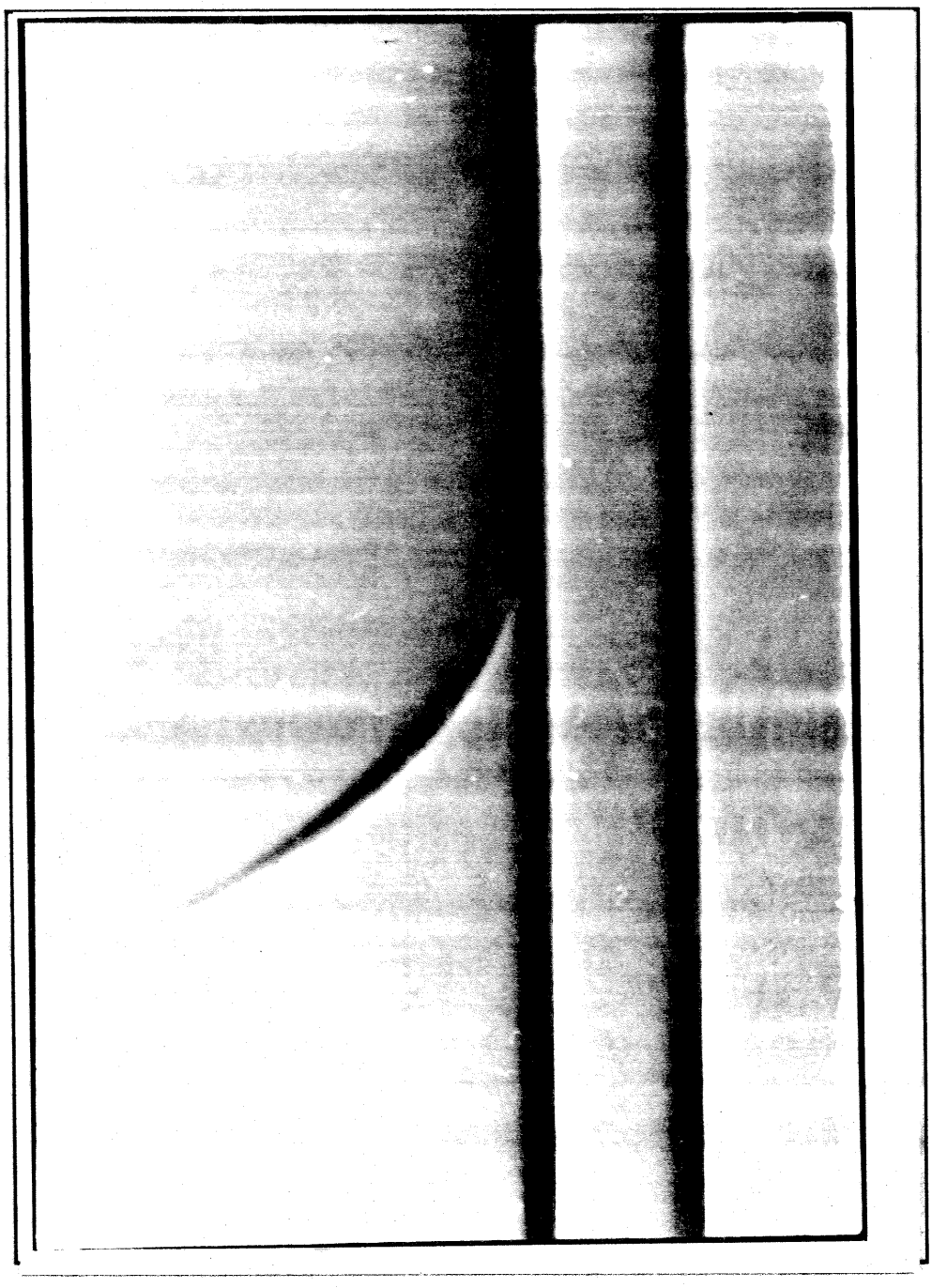

Figure 1

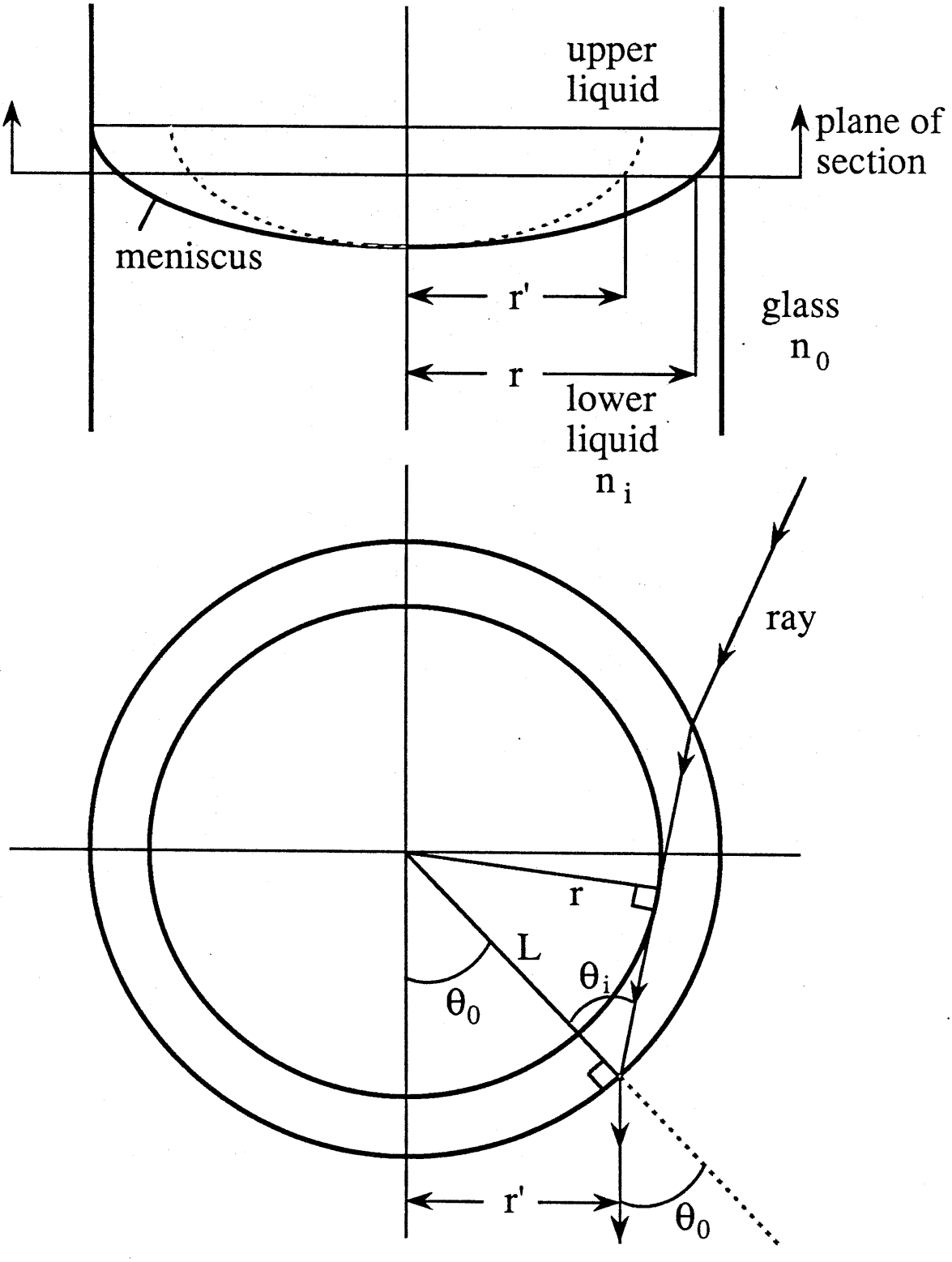

Figure 2 Ray-trace diagram of affine contraction

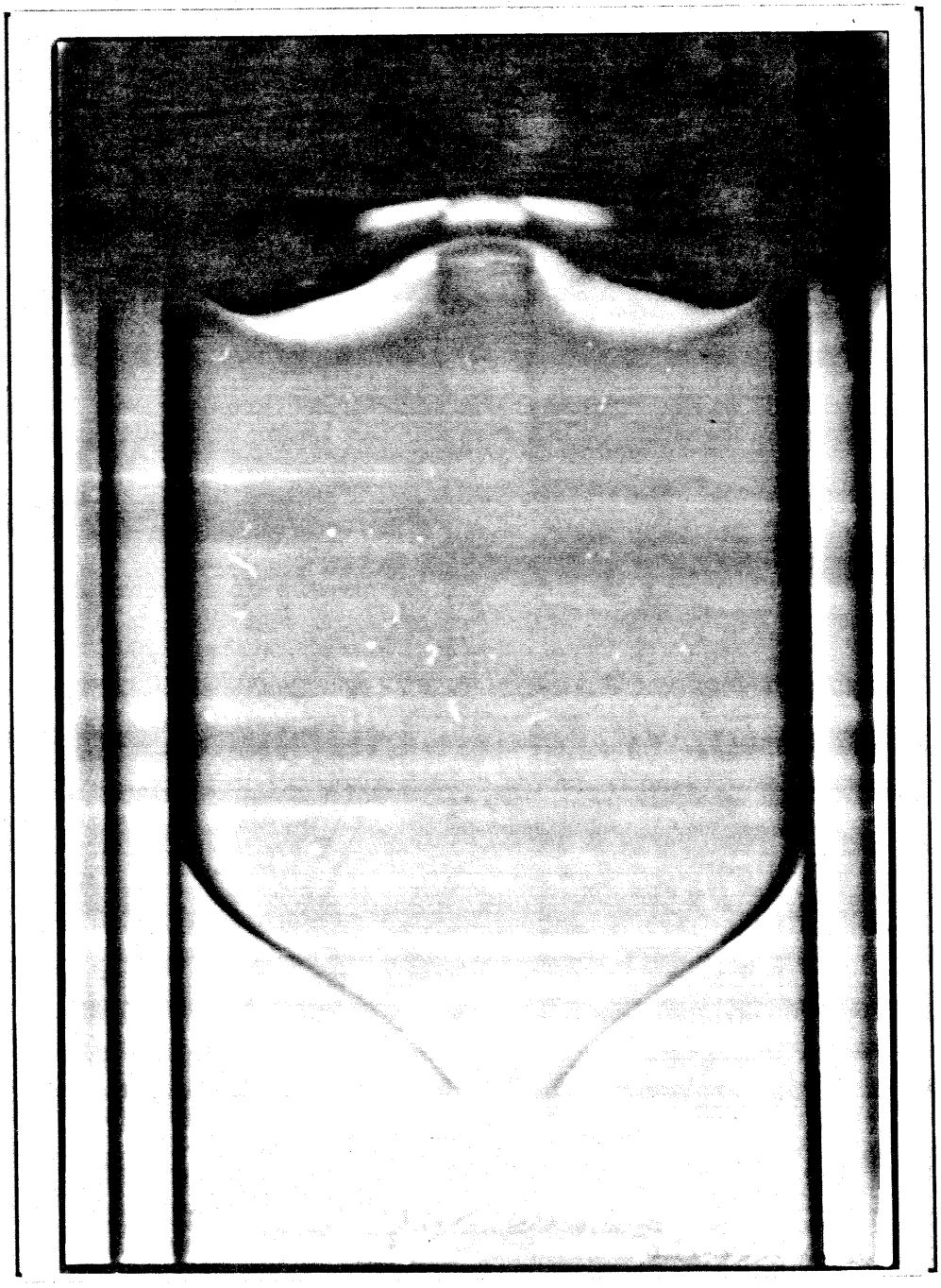

Figure 3

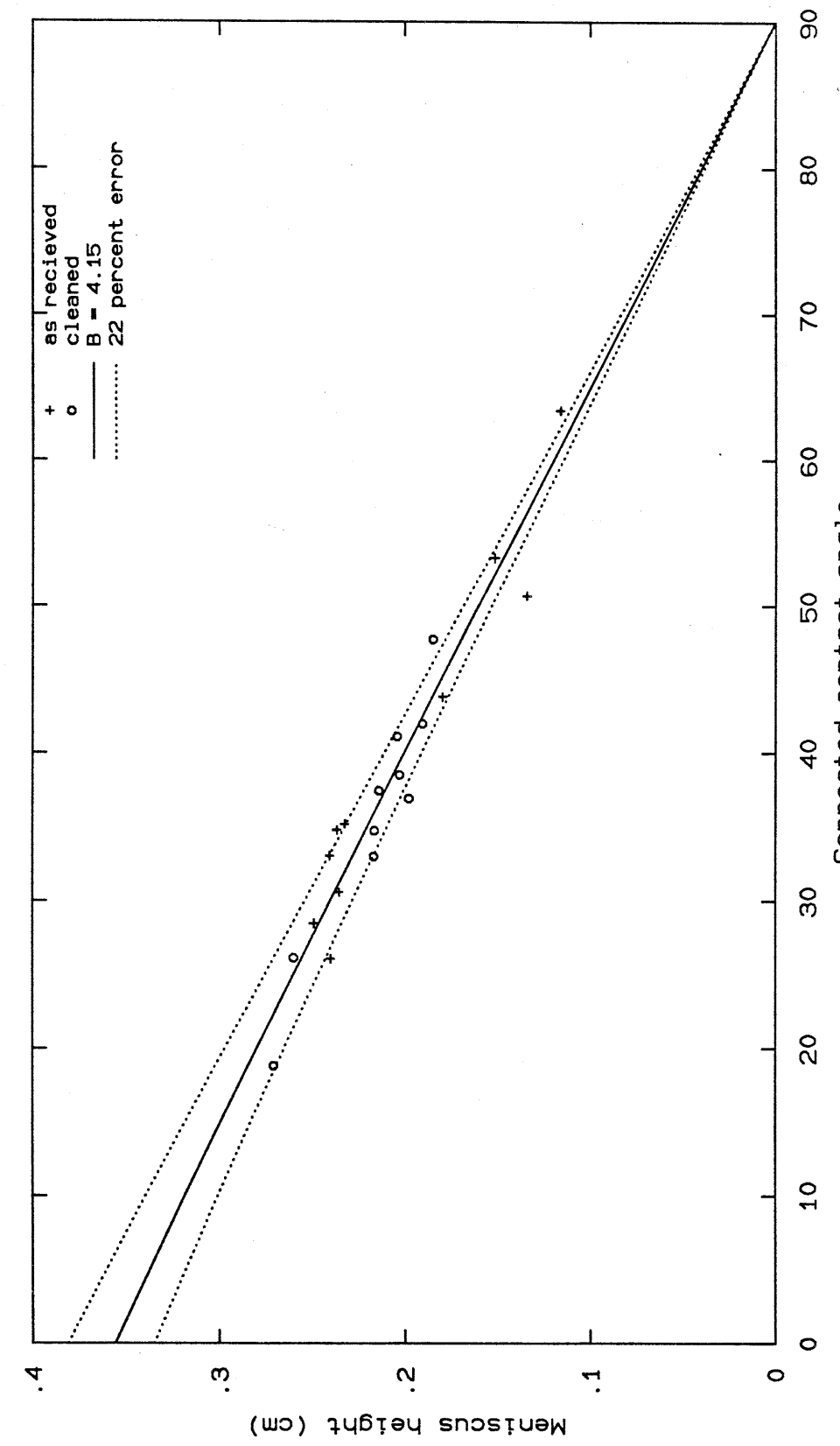

Figure 4 Meniscus height vs. contact angle for water/carbon tetrachloride
Bond number = 5.06, 4.15, and 3.24 from bottom to top

Chapter III

Preliminary drop-tower experiments on liquid-interface geometry in partially filled containers at zero gravity.

(In Experiments in Fluids **8**, *312-318(1990))*

G. Smedley
Graduate Aeronautical Laboratory
California Institute of Technology
Mail code: 205-45
Pasadena, CA 91125
U.S.A.

Abstract

Plexiglas containers with rounded trapezoidal cross sections were designed and built to test the validity of Concus and Finn's existence theorem (1974,1983) for a bounded free liquid surface at zero gravity. Experiments were carried out at the NASA Lewis two-second drop tower. Dyed ethanol-water solutions and three immiscible liquid pairs, with one liquid dyed, were tested. High-speed movies were used to record the liquid motion. Liquid rose to the top of the smaller end of the containers when the contact angle was small enough, in agreement with the theory. Liquid interface motion demonstrated a strong dependence on physical properties, including surface roughness and contamination.

1 Introduction

For a partially filled container in a zero-gravity environment, the location of the liquid is not known a priori. This fact poses several practical problems in areas such as the management of spacecraft fuel and the use of multi-phase heat pipes. Concus and Finn (1974) and Finn (1983) developed a theorem that addresses the static problem of existence for a bounded liquid free surface at zero gravity in a cylinder of arbitrary cross section. Given the geometry of the container and the contact angle between the liquid and solid, the theory, outlined in section 2 below, predicts whether the equilibrium shape of the liquid free surface at zero gravity is bounded or goes to infinity. Because the behavior of moving contact lines is not understood, the solution of the corresponding dynamic problem is still far beyond the reach of theory and numerical computation. Nevertheless, a valid static theory can be very useful for design of a dynamic experiment. If the liquid moves as the static theory suggests it should, confidence in use of the theory to design containers for measurement of dynamic surface behavior would be increased. To test the static theory in this sense, several experiments were carried out in the NASA Lewis two-second drop tower. Six mixtures of ethanol and water under air, and three immiscible liquid pairs, were dropped in plexiglas containers designed according to the static theory. The experiments are described in sections 3 and 4.

2 Theory

The following description of the theory is a general outline of the theory presented in Finn (1983); a more detailed analytical and numerical application of this theory to several different cylinder cross-sections will be reported in another paper. A standard variational technique is used to minimize an expression for the free energy of a liquid in a container at zero gravity (Fig. 1). The free energy includes the free surface energy ($E_S = \sigma S$) and the wetting energy ($E_{S^*} = -\lambda_0 \sigma S^*$), where σ is the surface tension, S and S^* are the free surface area and the wetted surface area, respectively, and λ_0 is a constant of proportionality. The total volume of the liquid is held constant as a constraint ($\lambda_1 V$). Thus

$$E(S) = S - \lambda_0 S^* + \frac{\lambda_1}{\sigma} V \tag{1}$$

Minimization of the free energy (Eq. 1) yields the Laplace-Young equation for a static liquid free surface in a cylinder of arbitrary cross section at zero gravity;

$$\text{div } \mathbf{T}(h) = \frac{\Sigma \cos\gamma}{\Omega} \tag{2a}$$

$$\nu \cdot \mathbf{T}(h) = \cos\gamma = \lambda_0 \tag{2b}$$

where ν is the unit outward normal, Σ and Ω are the perimeter and area of the cross section; γ is the contact angle, measured in the liquid; $h = h(x,y)$ is the height of the free surface; and

$$\mathbf{T}(h) = \frac{\nabla h}{(1 + |\nabla h|^2)^{1/2}} \tag{2c}$$

Consider a cross section of the container, normal to the axis (Fig. 2). The free surface intersects the cross section along a curve Γ. Integration of equation (2a) over this section yields an energy per unit length (Eq. 3), which is a two-dimensional analog to the three-dimensional energy (Eq. 1). There is a close analogy between the free surface area (S), the wetted surface area (S^*), and the liquid volume (V) in equation (1) and the length of the curve (Γ), the length of the wetted boundary (Σ^*), and the liquid area (Ω^*) in equation (3).

$$\Phi(\Gamma) = \Gamma - (\cos\gamma)\Sigma^* + \left[\frac{\Sigma \cos\gamma}{\Omega}\right] \Omega^* \tag{3}$$

If $\Phi \leq 0$, the free surface appears in the cross section. Thus a configuration of minimum energy requires the presence of liquid between the container wall and the convex side of the curve Γ. Minimization of equation (3) shows that Γ is a circular arc of radius $R_\gamma = \frac{\Omega}{\Sigma \cos\gamma}$. If $\Phi > 0$, however, the free surface does not appear in the cross section. Therefore, the functional Φ enables us to characterize the expected equilibrium interface in a particular geometry at zero gravity.

The theory predicts that liquid rises to infinity on some part of the wall of a two-dimensional container if $\Phi \leq 0$. However, the theory does not indicate how high the liquid will rise, if at all, for $\Phi > 0$. To determine the height of the equilibrium free surface, in this case, it is necessary to solve the static problem (2) for the specific cylinder of interest. Such a solution h(x,y) is available for a particular rounded trapezoid (Bainton, 1986). The shape was chosen, using the static theory, to have a critical contact angle of 30°. Free-surface solutions along the longer axis of symmetry of the cross section are shown in Fig. 3 for $\gamma = 30.6°$, 40°, 50°, and 80°. The difference between the maximum and minimum of each curve is extracted as a function of γ in Fig. 4. No solution was possible for $\gamma \leq 30°$, as predicted by the theory. The Newton's method used for these calculations did not converge for $\gamma < 30.6°$. There is a smooth but rapid trend in the rise of the liquid toward infinity as the predicted critical contact angle is approached.

3 Experiment

A cylindrical container with rounded trapezoid cross section was designed using the same geometry considered by Bainton (Fig. 5). The functional Φ (Eq. 3) depends only on the parameters α, β, and γ, where $\alpha \leq 90°$ is the half angle of the extended sides, $0 \leq \beta \leq 1$ is the ratio of the radii, and γ is the contact angle. One geometry can therefore be used to exhibit behavior for both $\Phi > 0$ and $\Phi \leq 0$ by changing the liquid, thereby changing γ. For a liquid with $\gamma > \gamma_{crit}$ (supercritical), $\Phi > 0$, and the liquid is expected to rise to a finite height in the narrow end of the container at zero gravity (Fig. 4). For $\gamma \leq \gamma_{crit}$ (subcritical), $\Phi \leq 0$. According to Concus and Finn's static theory, the liquid is expected to rise to an infinite height (Fig. 4). In a container of finite height, the top of the container (Fig. 4) interferes with the theoretical behavior. Numerically computed heights greater than 6.25 cannot be discerned from infinite heights with the containers used in this work.

Three containers were machined from solid blocks of plexiglas using a computer-controlled milling machine with an accuracy of 0.0002" and a repeatability of 0.0005". The nominal dimensions of the plexiglas containers are shown in Fig. 6. Two of the containers were designed for $\Phi = 0$ at $\gamma = 30°$ (the critical contact angle). One of these (A) was polished using

1000-grit grinding polish, the other (B) was polished using 400-grit. The third container (C) was inadvertently cut oversize with larger radii and was left unpolished, with $\gamma_{crit} \approx 28°$. This container provided some data regarding the effect of roughness on the predictions of the static theory.

The liquids that were used in the experiments fell into two groups. The first group consisted of mixtures, in various proportions, of ethanol and water under air. This group allowed us to vary the contact angle by varying the concentration of ethanol (0% to 50% in steps of 10%) and thus to determine whether the static theory correctly predicted the critical contact angle for the geometry in question. The second group of liquids consisted of three immiscible liquid pairs, intended to show the effects of liquid properties, particularly viscosity, on the time scale of the liquid motion at zero gravity. Since the dominant factors determining this time scale are not known, the three liquid pairs were chosen to have very different physical properties to cover a wide range of behavior (Table 1). The three pairs were: (1) glycerol tributanoate over ethylene glycol, (2) diethyl diethyl malonate over formamide, and (3) 1-chlorohexane over formamide. Liquid pairs 1 and 2 were chosen because both had subcritical contact angles with PMMA and pair 1 was three to five times more viscous than pair 2. Pair 3 was chosen because of its supercritical contact angle. In addition, liquid pairs have the advantage that the difference in index of refraction of the liquids is small. The total internal reflection that results from a lack of index match between the gas and the liquid in the ethanol-water samples causes the interface to appear as a dark band (Fig. 7a-7g), thereby preventing accurate measurement of its position as a surface in two dimensions.

The experiments were carried out in the two-second drop tower at NASA Lewis Research Center. Before each drop, the containers were cleaned in an ultrasonic bath of Freon 113 (1,2,2-trifloro-1,1,2-trichloroethane) for about five minutes and allowed to air dry. They were filled approximately one-third full (20ml) with various mixtures of ethanol and water containing a small amount of blue vegetable dye. The container lids were sealed quickly to prevent evaporative loss of ethanol, which would reduce the ethanol concentration. The vapor/liquid system was then allowed to come to equilibrium before the drop. Complete filling of containers with immiscible liquid pairs was achieved by assembling them while fully submerged. In all

cases, the upper liquid was expected to move down the narrow end of the container because the smaller contact angle existed between the upper liquid and the container walls. It was therefore necessary to have the container approximately one-third full of the upper liquid and two-thirds full of the lower one (Fig. 7h). Dying of the lower liquid was easily achieved, using a blue vegetable dye that was not soluble in the upper liquid.

High-speed movies were taken with a 1962 D. B. Milikan camera (DBM 4) set to run at 400 frames per second. The camera was focused on the long side of the containers with the narrow end of the rounded trapezoid cross section on the left. Back lighting of the containers and liquids was provided by a diffuse back-lighted screen. A digital clock display, stated to be accurate to 0.001 seconds, was also mounted on the test rig and was recorded on the film.

4 Results

The instrumentation supplied for the drop-tower tests was not always adequate. This fact together with limited time at the facility prevented a full evaluation of the many experimental questions posed in the preceding sections. As a result, the data obtained represent an incomplete set. In the following discussion, the results obtained for 50% ethanol and for liquid pair 1 are emphasized, while the results from the rest of the liquids are briefly mentioned.

Quantitative measurements from the high-speed films required a knowledge of the actual framing rate of the camera. The first decision to be made was whether to trust the camera setting (400 fps) or the digital clock, since these did not agree. The camera was started and allowed to accelerate for two seconds prior to the drop, and the clock was started at the instant the experimental package was released. Provided that the batteries were in good condition, it was probably safe to assume that the camera ran at the same equilibrium speed for the full duration of the two-second drop. Except for the first test, the batteries in the test rig were new and nearly fully charged, so that the voltage should not have varied much throughout the drop duration. With this assumption, the clock readout was accepted as accurate, provided that it could be deciphered. The clock did not hold numbers on its four-digit display until they changed; instead each of the four numbers was turned on and off in sequence whether it had changed or not. The clock readout looked reasonable to the unaided eye, but to the high speed

camera only one or two digits were visible during a single frame. During the worst asynchrony of clock and camera, particular clock digits would not be seen for four or five consecutive frames. Although the clock read out to 0.001 second, the accuracy of determining the frame time was not better than 0.005 second. To determine the framing rate of the camera, film frames were counted while using the clock as a time reference. The film speed was found to be fairly constant (278 fps ± 2%) for the 50% ethanol case, but differed from the specified 400 fps by 30%. This measured framing rate was used to interpolate the elapsed time for a given film frame.

The experiments involved the use of three containers. The results are very scattered and exhibit a wide range of behavior. Still photographs taken from the high-speed films are shown in Figs. 7a-7h. The dimensions of the liquid/vapor containment area shown in these figures are approximately 2.5" by 2.5" (Fig. 6). Water (0% ethanol) in container A and 10% ethanol in container C were the only liquid mixtures that reached equilibrium and did not reach the roof of the containers (Fig. 7a,7b). The 10% ethanol mixture started its rise very erratically, with many notches in the contact line and waves on the surface (Fig 7b). These effects were probably caused by jerky movement of the contact line due to the roughness of the container walls. The experiment involving 20% ethanol in container A was very inconclusive. Waves were observed on the surface of the liquid throughout the entire drop and the liquid did not rise (Fig. 7c), perhaps indicating that the drop package was bumped as it was dropped. Neither 30% ethanol in container C nor 40% ethanol in container B (Fig. 7d, 7f) achieved equilibrium during the two seconds of drop time. The liquid in container C exhibited the same notched contact line that moved erratically up the walls of the container as in the 10%-ethanol case. The 40% ethanol moved up the polished walls of container B very smoothly. Measurements were made from projected film images of the liquid rise (Fig. 8a). Qualitatively, the results obtained compare quite well with the results obtained for 50% ethanol in the same container (Fig. 8b). There was one notable difference between the two cases; the 40% ethanol contact line moved approximately 20% slower (average ≈ 3.07 cm/sec) up the left side and 30% slower (≈ 1.41 cm/sec) across the roof than the 50% ethanol contact line (Fig. 8a, 8b). One or both of these discrepancies may be caused by some type of contamination that increased the contact angle (compare photos 7e-7g), thereby slowing the progress of the contact line. This

observation indicates that the contact angle is an important contributor to the velocity of the contact line at zero gravity; the larger the angle, the slower the motion, despite the fact that the surface tension is higher.

Figure 7g shows a sequence of frames from a high-speed movie of the experiment using a mixture of equal parts by volume of water and ethanol under air, for which the contact angle on plexiglas is about 23°. The smaller radius is at the left, and the two dashed lines in the initial frame are the projection of the critical arc Γ for this geometry. When the body force due to gravity is first removed, and again when the rising liquid at the left first reaches the top of the container, rapid dynamic movement of the contact line is manifested mainly by necking; i.e., by withdrawal of liquid from the near vicinity of the contact region rather than from the distant bulk of the liquid. Note also that the contact line at the right is advancing during the first half of the experiment and receding during the second half, with some visual evidence of a dependence of contact angle on the direction of the velocity.

Measurements of liquid interface positions for 50% ethanol in container B were made directly from projected film images and non-dimensionalized with the larger radius of the container cross section. The results are shown in Fig. 8b. The measurements include the height of the free-surface minimum, the height of the right and left contact lines, and the distance traveled across the top of the container. Note that initially the liquid moves very quickly at both ends at about the same rate and the minimum decreases at a comparable rate, as the interface moves from a nominally plane configuration toward one of much higher curvature. The presence of free-surface motion during the first half-second of the drop, indicated by the initial necking down, is accompanied by oscillation in the height of the surface minimum. The advance and retreat of the right contact line are easily seen. Note that the retreat of the right contact line and the reduction in the surface minimum occur at fairly constant rates after approximately one second. When the left contact line reaches the top of the container, the velocity of retreat of the right contact line and the minimum of the free surface change; the surface minimum decreases more quickly and the right contact line height recedes more slowly. This behavior seems to indicate a withdrawal of liquid from the bulk rather than from the vicinity of the contact line, contrary to the condition that existed during the earlier part of the

drop. Also notice that as the left contact line climbs, its velocity decreases (average $\approx$ 3.87 cm/sec). Upon reaching the top, experimental error caused by lack of index match across the interface introduces an artificial jump in the contact-line position. The liquid then proceeds across the top of the container at a nearly constant rate ($\approx$ 2.04 cm/sec). Given more time, we might have been able to see the bottom of the container become uncovered, since the surface minimum can be extrapolated to zero after roughly another two seconds.

The three experiments involving liquid pairs exhibited similar behavior on a much longer time scale. The interface moved very slowly in all three cases. The final state for pair 1 is shown in Fig. 7h. Corresponding figures for pairs 2 and 3 are not given since their final appearance is very similar to Fig. 7h. It was not possible to determine the difference between supercritical and subcritical behavior with only two seconds of zero gravity. Evidence for differences in time scale is provided by differences in the advancing velocity of the left contact line (Table 1). Interfacial tensions and contact angles were found by Smedley and Coles (1989). Note that the pair 1, with the smallest contact angle, had the highest contact-line velocity despite the fact that it was the most viscous, again indicating the importance of contact angle in determining contact-line velocity. A careful study of the table suggests that the relative magnitudes of the contact line velocities are determined by the product of the surface tension and the cosine of the contact angle. The data also seem to indicate a dependence on the degree of criticality of the contact angle; subcritical angles yield higher contact-line velocities than supercritical angles for similar values of $\sigma\cos\gamma$ (compare pair 1 and pair 3 in table 1). Also, pair 1, which has a more subcritical contact angle than pair 2, moves at a rate three times higher than pair 2 despite their similar interfacial tensions. The interfaces of the liquid pairs advanced at the following average rates: pair 1 $\approx$ 0.28 cm/sec, pair 2 $\approx$ 0.09 cm/sec, pair 3 $\approx$ 0.13 cm/sec. These velocities of advance were nearly constant over the entire duration of the drop. The results depicted in Fig. 8c for pair 1 are typical for these three liquid pairs.

The measured liquid interface positions for liquid pair (1) (Fig. 8c) changed much less dramatically than those for 50% ethanol. The interface moves from the top down, and measurements are given as distances from the top of the container. This liquid pair reacts much more slowly to the sudden removal of the gravitational body force. A region of very quick

motion does not exist near the beginning of the drop; however, some necking is still indicated by the photographs and by the behavior of the minimum height of the interface. The oscillation in the surface minimum of this liquid pair is smaller by about a factor of two than the corresponding one for 50% ethanol. The left and right contact lines advance at monotonic rates that are similar in magnitude, with the left contact line moving slightly faster. According to the measurements of contact angle, this particular liquid pair was subcritical; therefore, the liquid interface should go to infinity or to the bottom of the container (Fig. 7h). But, since the interface minimum was moving approximately seven times slower than for 50% ethanol, and had farther to go, it would not have reached the bottom until roughly another sixteen seconds had elapsed.

5 Discussion and Conclusions

All nine of the experiments discussed above are compared to the theory in Fig. 4. As previously mentioned, at the end of section 2 and the beginning of section 3, Fig. 4 contains the theoretical and numerical results for the case $\gamma_{crit} = 30°$. This plot also contains symbols representing the difference between the measured maximum and minimum heights of the final state, of each liquid surface or interface, of the nine experiments reported here. The heights are nondimensionalized with the large radius of the cross section and plotted against the measured contact angle.

The symbols labeled 1 through 6 are the results for the various ethanol solutions 0%(10%)50% respectively. The symbols labeled 7 through 9 are the results for liquid pairs 1 through 3 respectively. Consider first the ethanol solutions compared to the dotted numerical curve. There is a substantial scatter; however, the trend is correct: as the contact angle decreases toward the critical value (30°), the liquid rises to greater heights. Some scatter can be attributed to the fact that contact angles were measured in the lab rather than on-site, since appropriate equipment for these measurements was not available on-site. In the lab, contact angles for the ethanol and water solutions were measured for a sessile drop on plexiglas using a cathetometer. Contact angles for the three immiscible liquid pairs were measured against a blade of plexiglas inserted into a test tube containing the liquid pair (Smedley and Coles, 1989).

The 30%, 40%, and 50% ethanol solutions (symbols 4, 5, and 6) all reached the roof of their containers (Fig. 7d, 7f, and 7g). The upper limits of the containers are shown as dashed lines on the plot (Fig. 4). The symbols 5 and 6, however, are not located on the upper dashed line, since the plotted height is the difference between the maximum and minimum of the liquid surface. A symbol would only rest on the dashed line if the bottom of the container was bare of liquid. If less liquid had been used in these cases, this may have happened. Limited time at the facility did not allow this adjustment of the experiment to be made. The same is true for symbol 4 (30% ethanol), which does not lie on the lower dashed line. Symbol 3 (20% ethanol) represents the case that may have been bumped and therefore never realized zero gravity (see section 4). Symbol 2 (10% ethanol) is a large distance from the numerical results. This might be accounted for by an error in the contact angle, measured in the lab rather than site, and/or by the roughness of the wall perhaps wicking the liquid to a higher than expected height. The location of symbol 1 (0% ethanol) is reasonably close to the numerical results.

The final rise heights for the three liquid pairs (symbols 7, 8, and 9) were small compared to the results for the ethanol solutions. Note that the upper dashed line represents the bottom of the container when considering the three liquid pairs, since the upper liquid moved down toward the bottom of the container (see section 3). Despite the fact that pairs 1 and 2 (symbols 7 and 8) had sub-critical contact angles, symbols 7 and 8 did not come close to the bottom of the container. These pairs did not reach equilibrium in the two seconds of zero gravity. The velocities of the moving interfaces were too slow (Table 1). Symbol 9 (liquid pair 3) is reasonably close to the numerical curve despite the fact that it also had not reached equilibrium in two seconds.

The theory, combined with numerical solutions, appears to be an adequate tool for the design of containers that incorporate strong dynamic free-surface behavior when zero gravity is suddenly imposed. This fact provides support for the use of the static theory as a means to design containers to study dynamic free surface behavior at zero gravity. The dynamic behavior of liquid interfaces demonstrates strong dependence on physical properties. However, the data presented here do not represent a large enough range to support conclusive statements regarding this dependence. Observations suggest that the dynamics of a liquid free surface or interface do

not depend on the contact angle and physical properties in a simple manner. Wall roughness appears to cause a notched, erratic motion of the contact line, whereas smooth walls lead to very smooth motion. Equilibrium states for liquid pairs were not attainable in two seconds of zero gravity. Further work is needed to determine dynamic time constants based on the physical properties of single liquids or liquid pairs.

This material is based upon work supported by the U.S. National Aeronautics and Space Administration and the University of California. The opinions, findings, conclusions and recommendations are those of the authors and not necessarily of the U.S. National Aeronautics and Space Administration or the University of California.

References

Bainton,M.C. 1986: Fluid interfaces in the absence of gravity (Masters Thesis). Lawr. Berk. Lab. U. of CA; Dept. of Math.

Concus,P. and Finn,R. 1974: On capillary free surfaces in the absence of gravity. Acta. Math., 132,177-198.

Finn,R. 1983: Existence criteria for capillary free surfaces without gravity. Ind. Univ. Math. J. 32(3), 439-460.

Smedley,G. and Coles,D. 1989: Some immiscible liquid pairs. Submitted to the Journal of Colloid and Interface Science.

Figure Captions

Figure 1: Generic cylinder partially filled with liquid.

Figure 2: Cross section of generic cylinder.

Figure 3: Computed equilibrium free surfaces for $\gamma = 30.6°, 40°, 50°$, and $80°$.

Figure 4: Liquid height (max - min) in rounded trapezoid. Symbols: (1)-(6) ethanol and water mixtures tabulated below, (7) glycerol tributanoate over ethylene glycol, (8) diethyl diethyl malonate over formamide, (9) 1-chlorohexane over formamide.

Symbol #	1	2	3	4	5	6	7	8	9
Container	A	C	A	C	B	B	A	B	B
Ethanol %	0	10	20	30	40	50	--	--	--

Figure 5: Rounded trapezoid cross section.
α = half angle of extended sides.
$\beta = \frac{b}{a}$ = radius parameter.

Figure 6: Nominal dimensions of constructed containers.
Containers A and B: $\alpha \approx 6.16°$; $\beta = \frac{0.2''}{0.4''} = 0.5$; $\gamma_{crit} = 30°$.
Container C: $\alpha \approx 6.73°$; $\beta = \frac{0.22''}{0.44''} = 0.5$; $\gamma_{crit} \approx 28°$.

Figure 7a: Water (0% ethanol) in container A at final time.

Figure 7b: 10% ethanol solution in container C at final time.

Figure 7c: 20% ethanol solution in container A at final time.

Figure 7d: 30% ethanol solution in container C at final time.

Figure 7e: 40% ethanol solution in container B at T = 0.5 seconds.

Figure 7f: 40% ethanol solution in container B at final time.

Figure 7g: 50% ethanol solution in container A at times shown.

Figure 7h: Glycerol tributanoate over ethylene glycol in container A at final time.

Figure 8a: Position of free surface of 40% ethanol solution at zero gravity.

Figure 8b: Position of free surface of 50% ethanol solution at zero gravity.

Figure 8c: Position of interface of glycerol tributanoate over ethylene glycol at zero gravity.

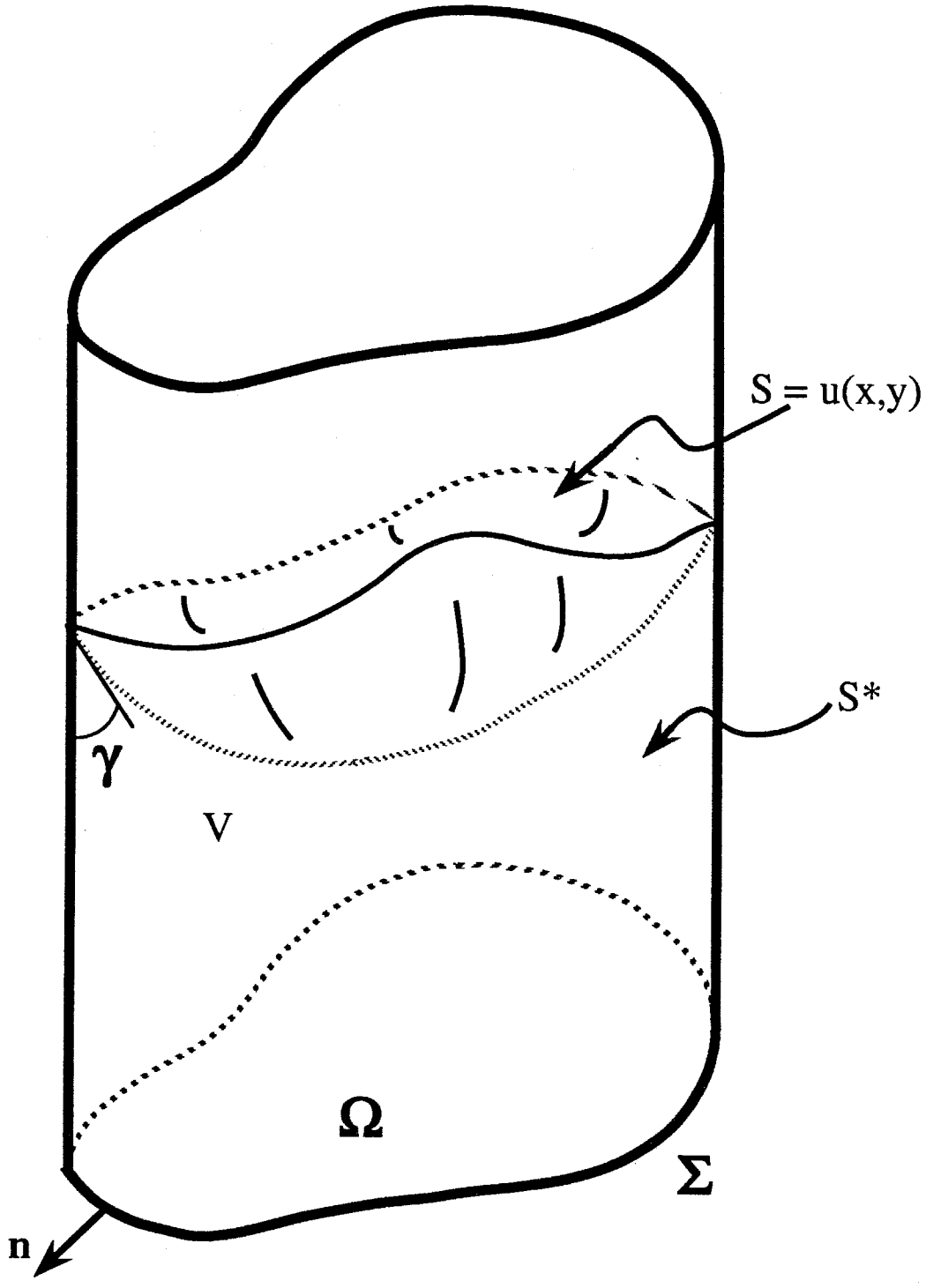

Figure 1 Generic cylinder partially filled with liquid

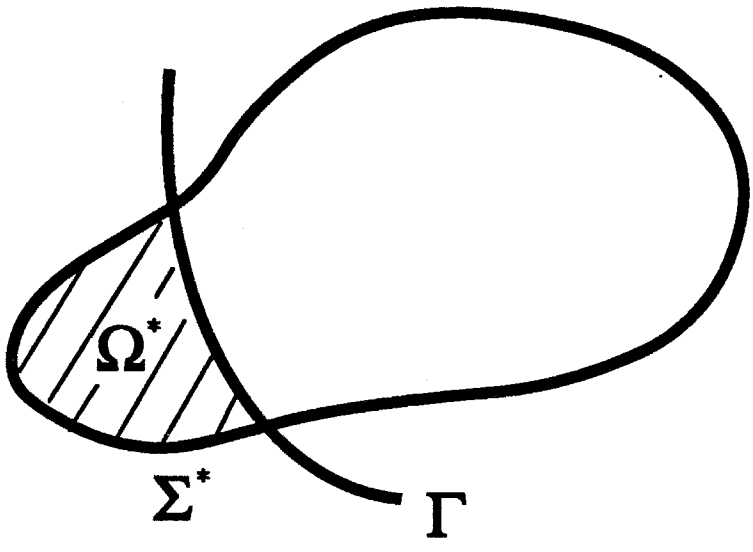

Figure 2 Cross section of generic cylinder

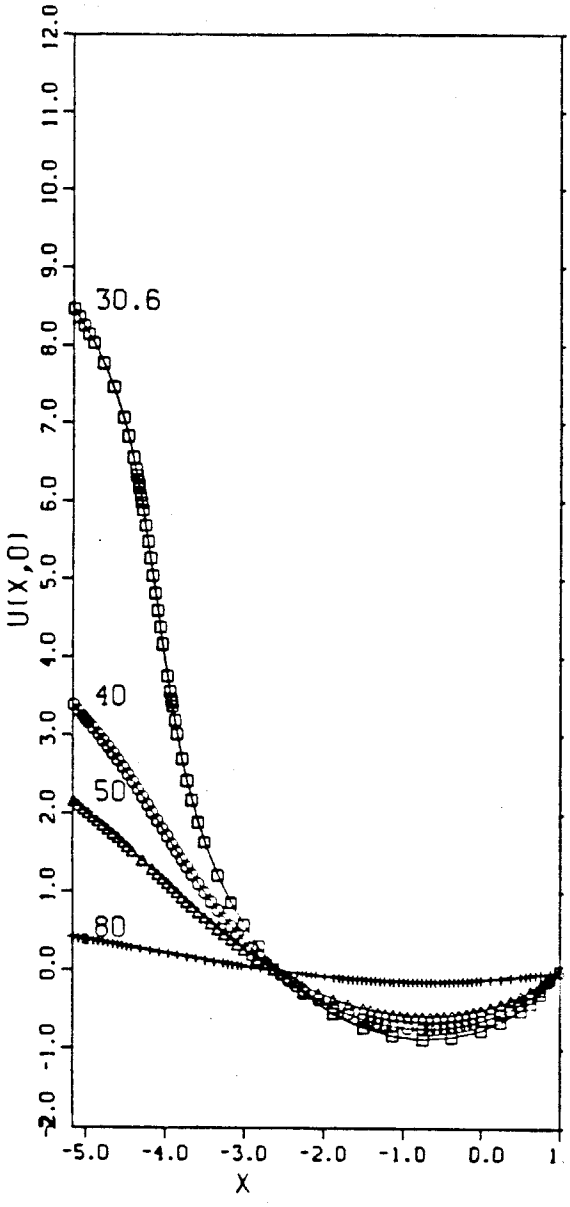
U(X,0)
X
30.6
40
50
80
12.0
11.0
10.0
9.0
8.0
7.0
6.0
5.0
4.0
3.0
2.0
1.0
0.0
-1.0
-2.0
-5.0
-4.0
-3.0
-2.0
-1.0
0.0

Figure 3

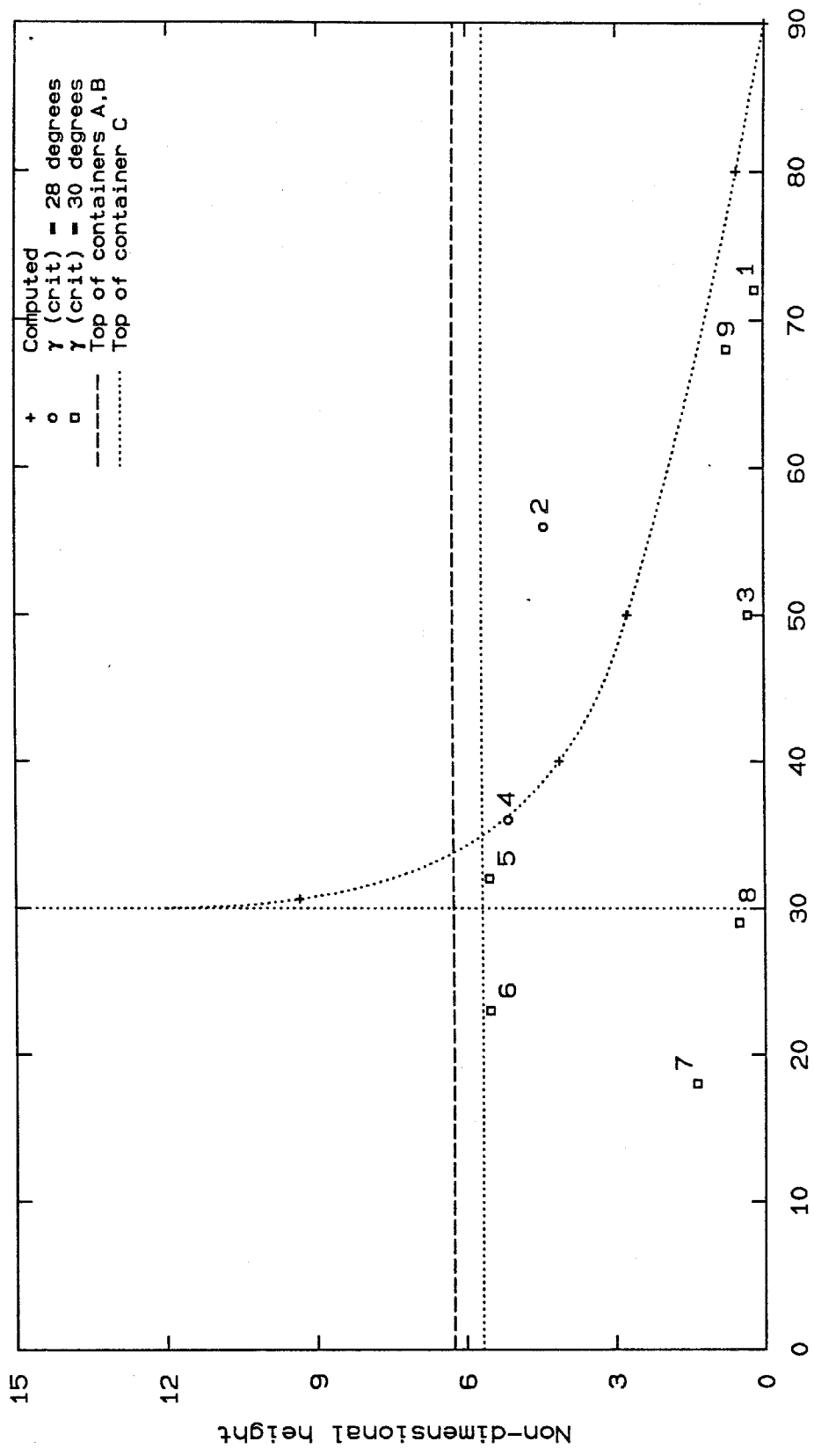

Figure 4 See figure caption

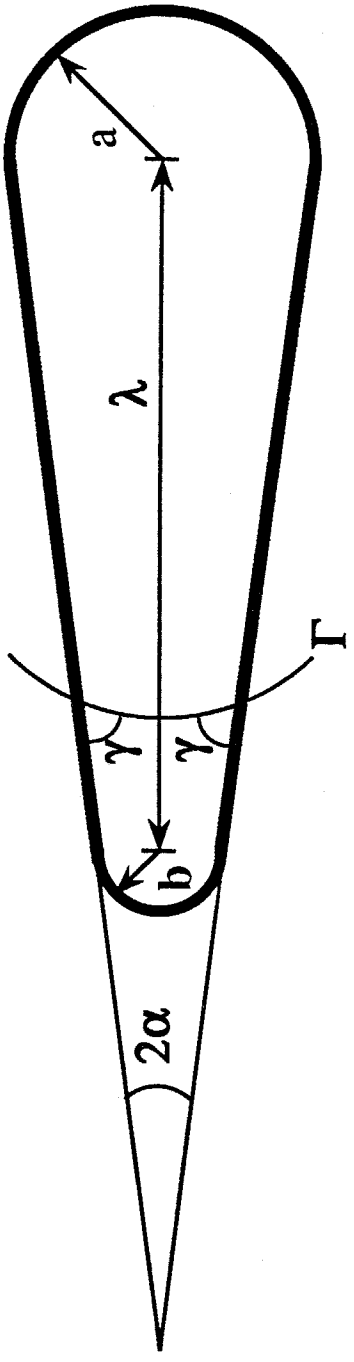

α = half angle of extended sides
β = b/a = radius parameter

Figure 5 Rounded trapezoid cross section

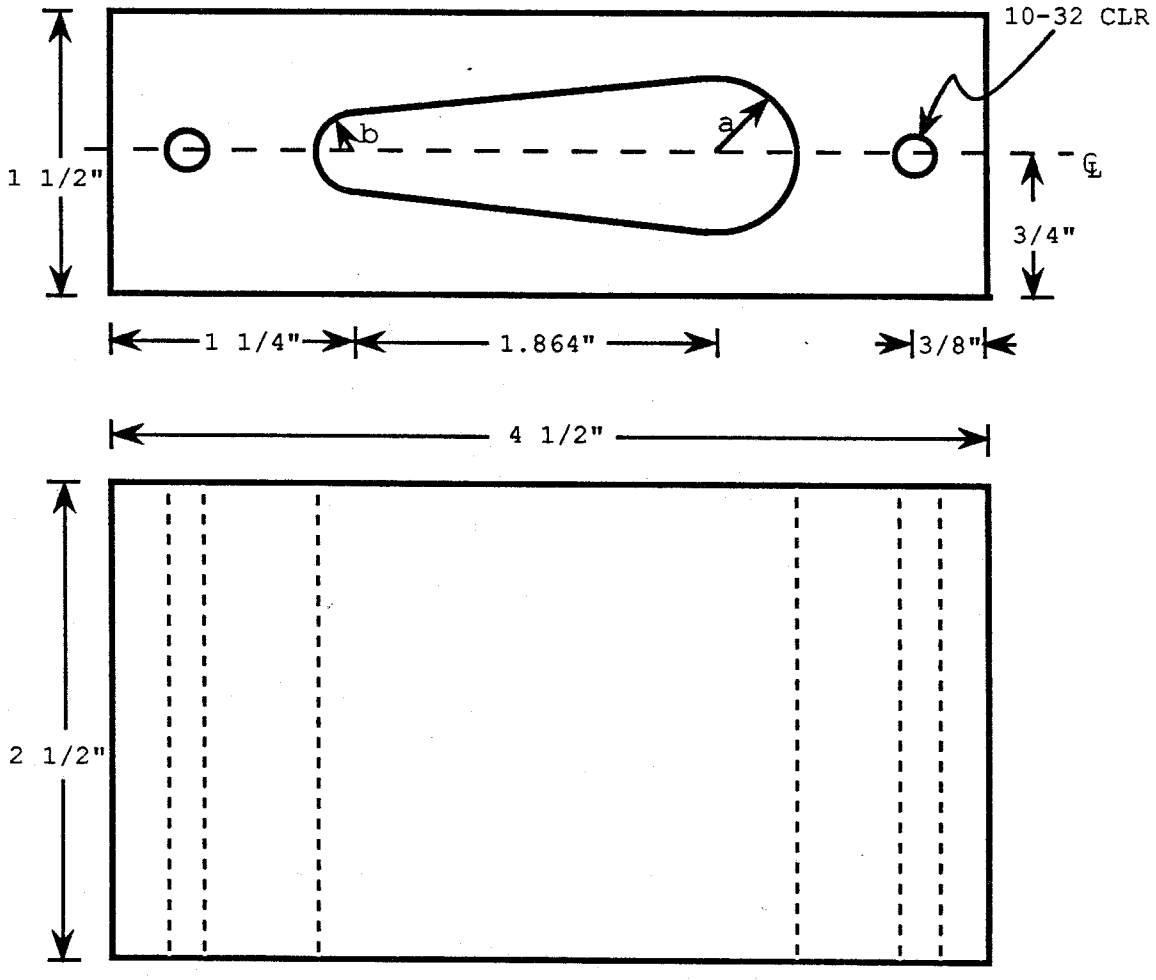

Containers A and B: $\alpha \cong 6.16$ degrees; $\beta = 0.2"/0.4" = 0.5$; $\gamma = 30$ degrees
Container C: $\alpha \cong 6.73$ degrees; $\beta = .22"/.44" = 0.5$; $\gamma \cong 28$ degrees

Figure 6 Nominal dimensions of constructed containers

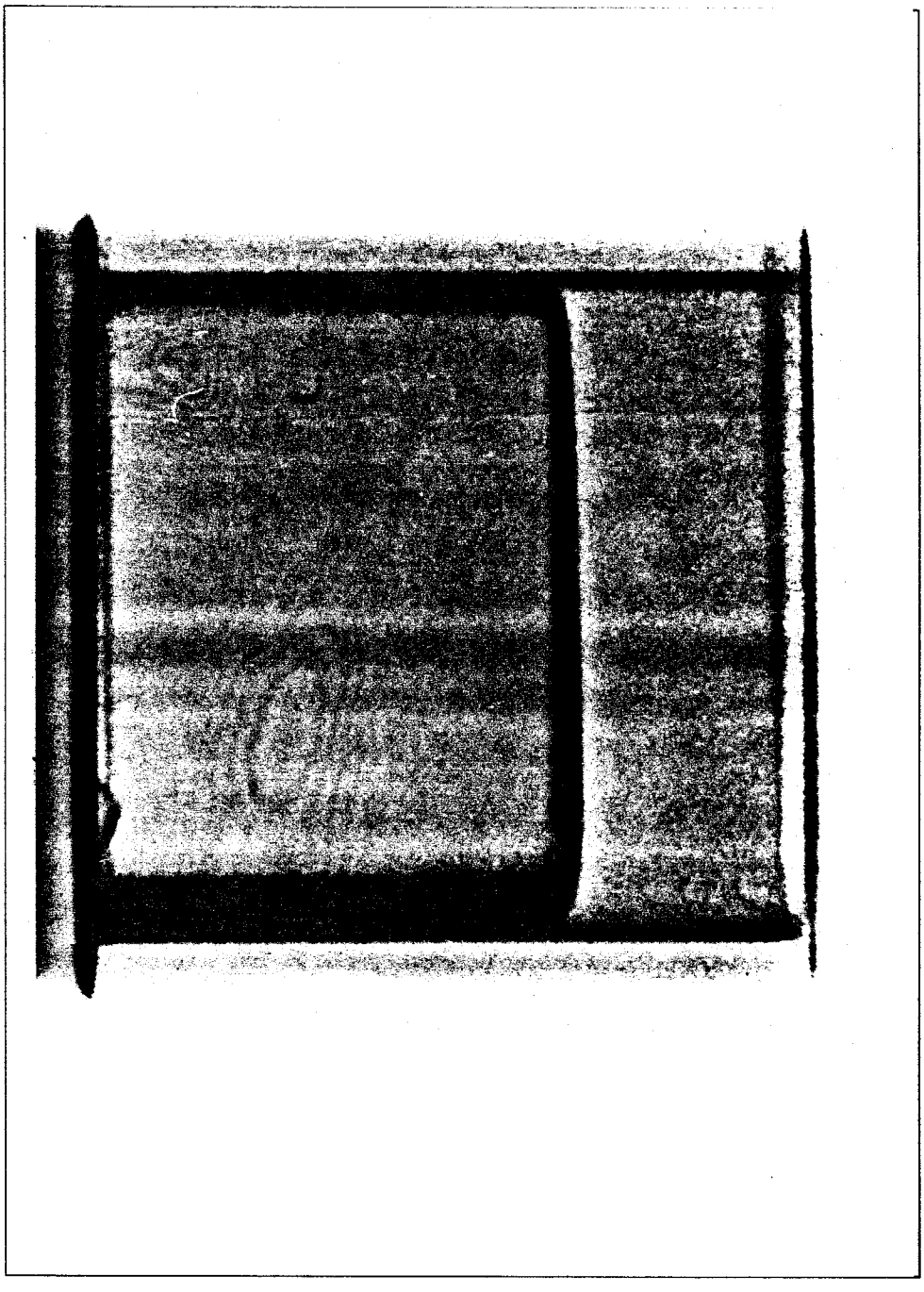

Figure 7a

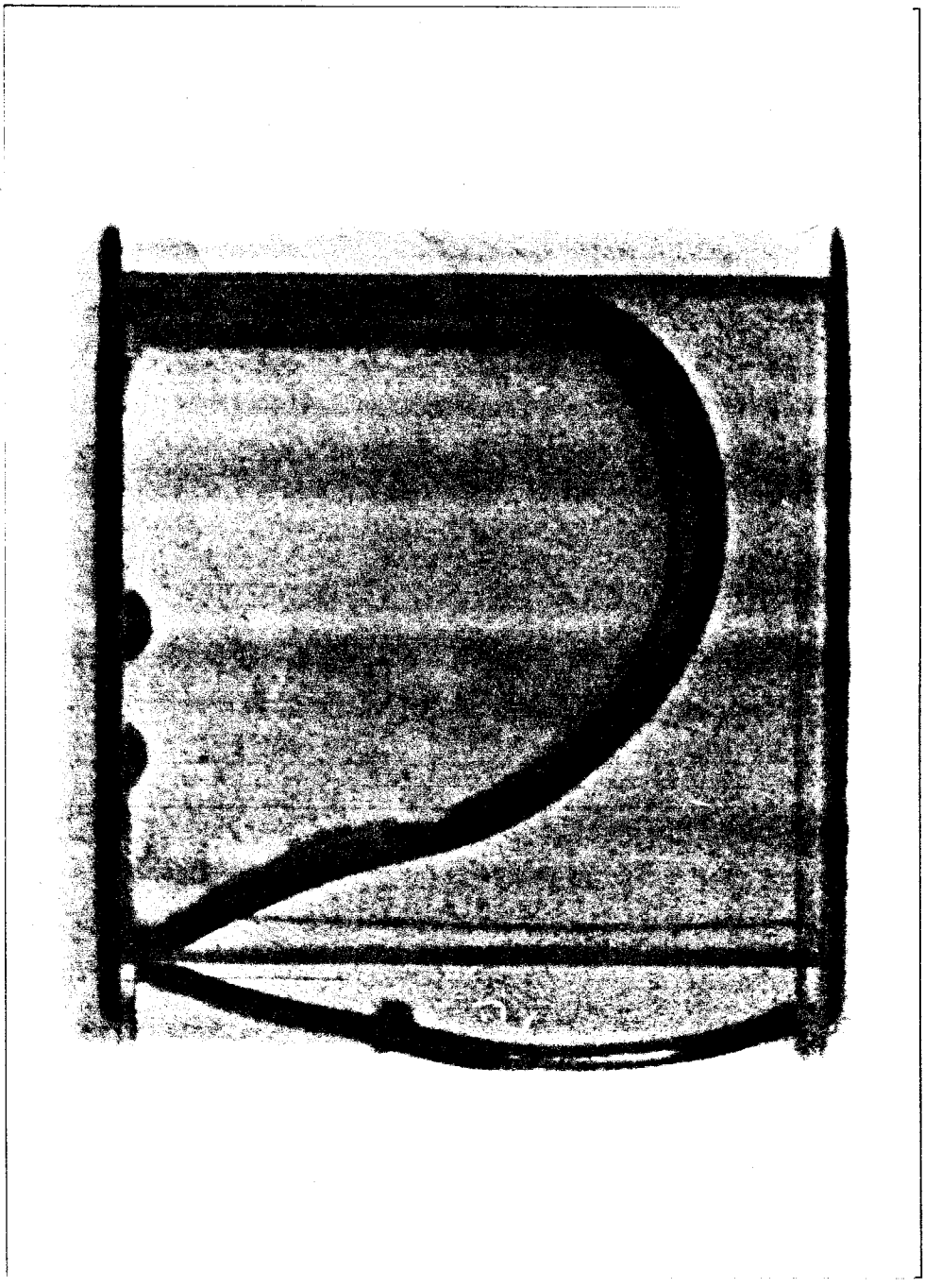

Figure 7b

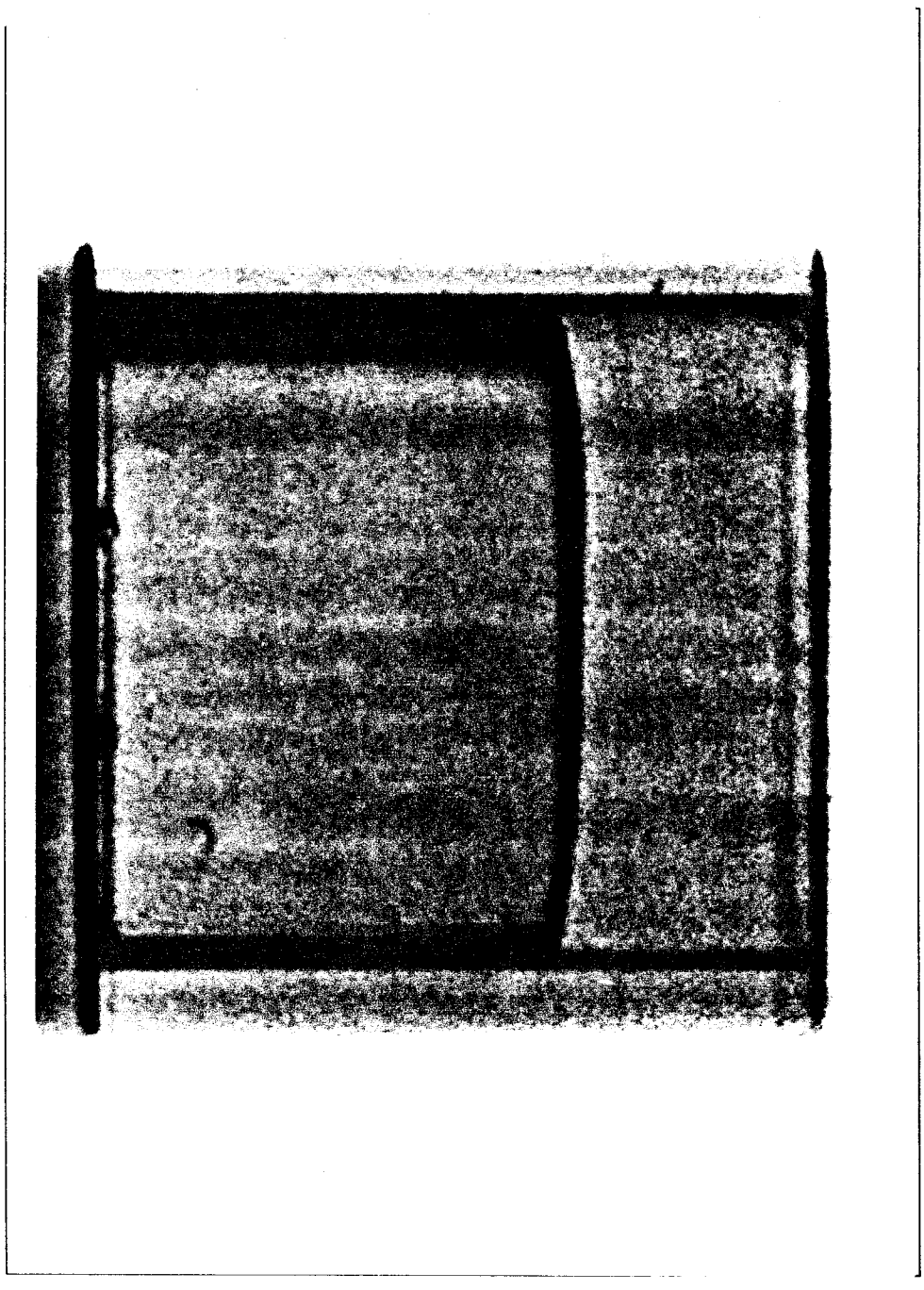

Figure 7c

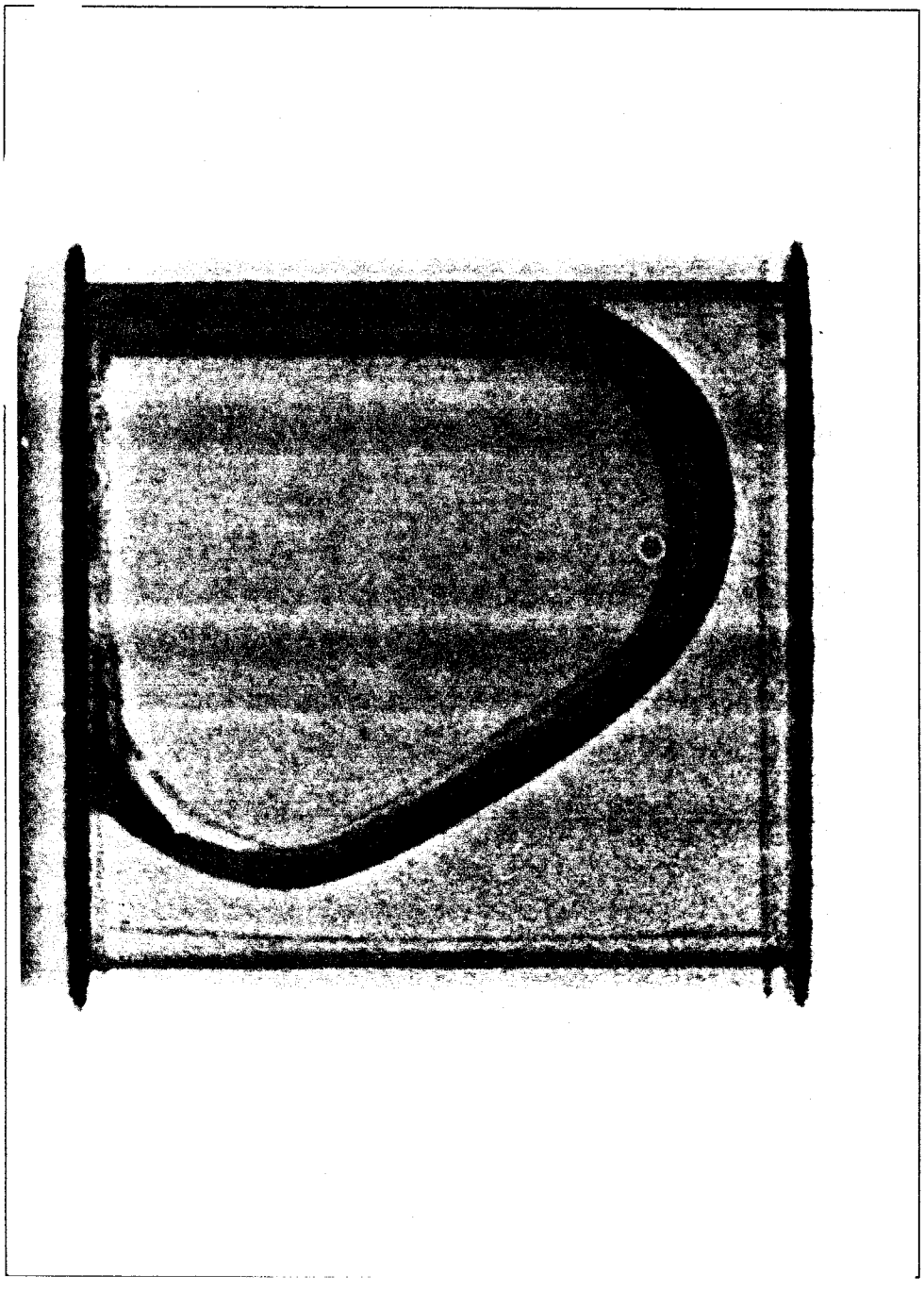

Figure 7d

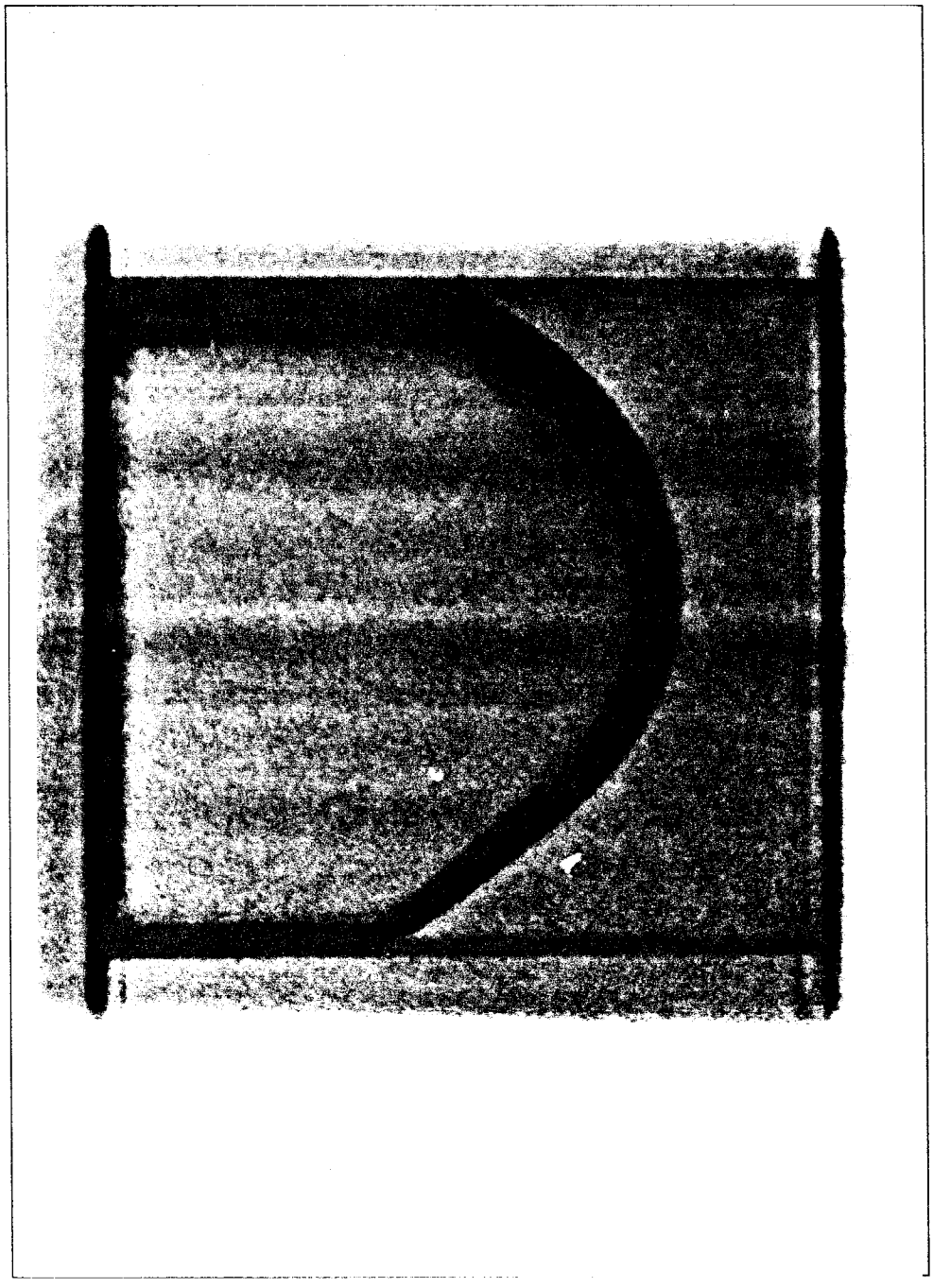

Figure 7e

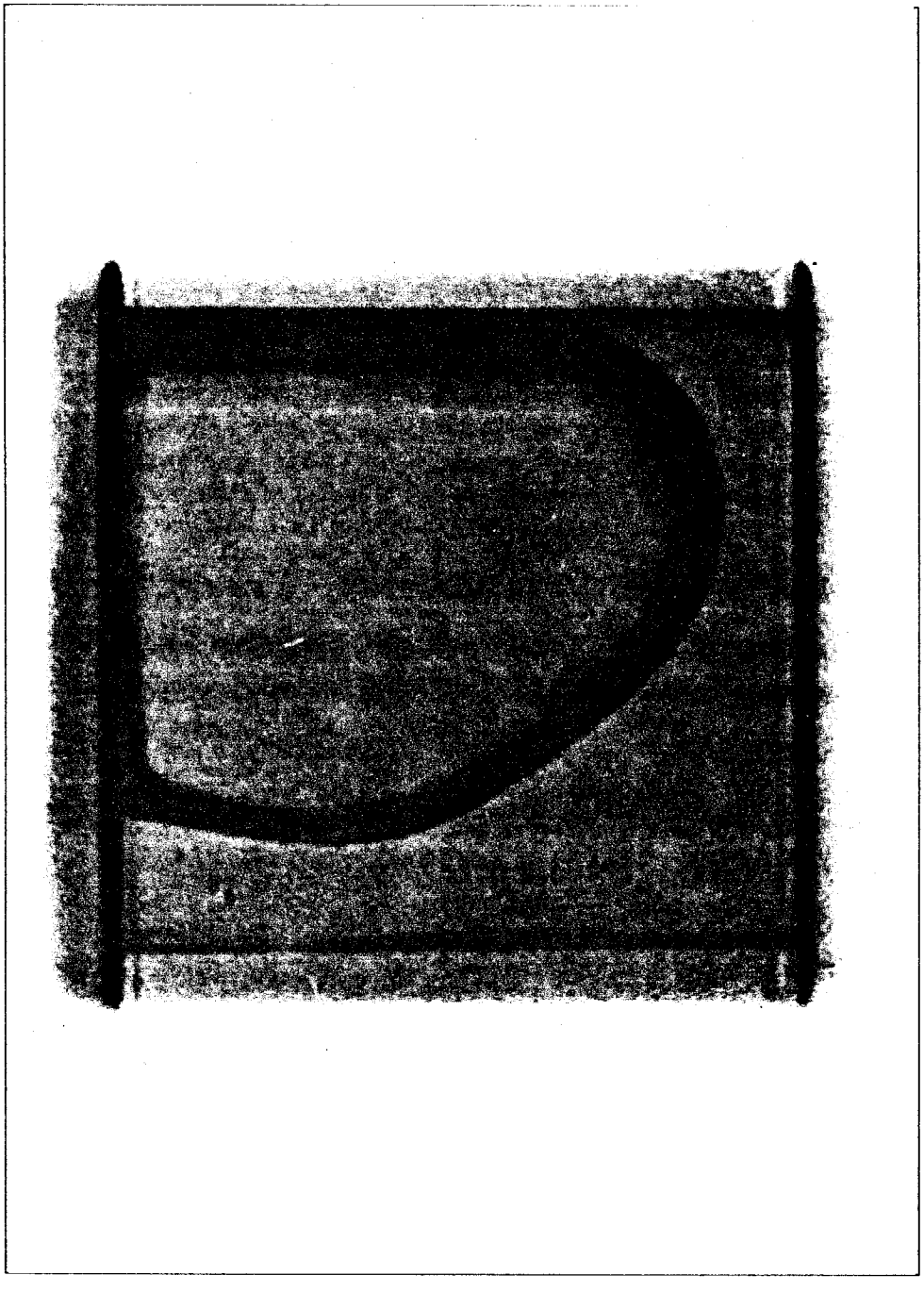

Figure 7f

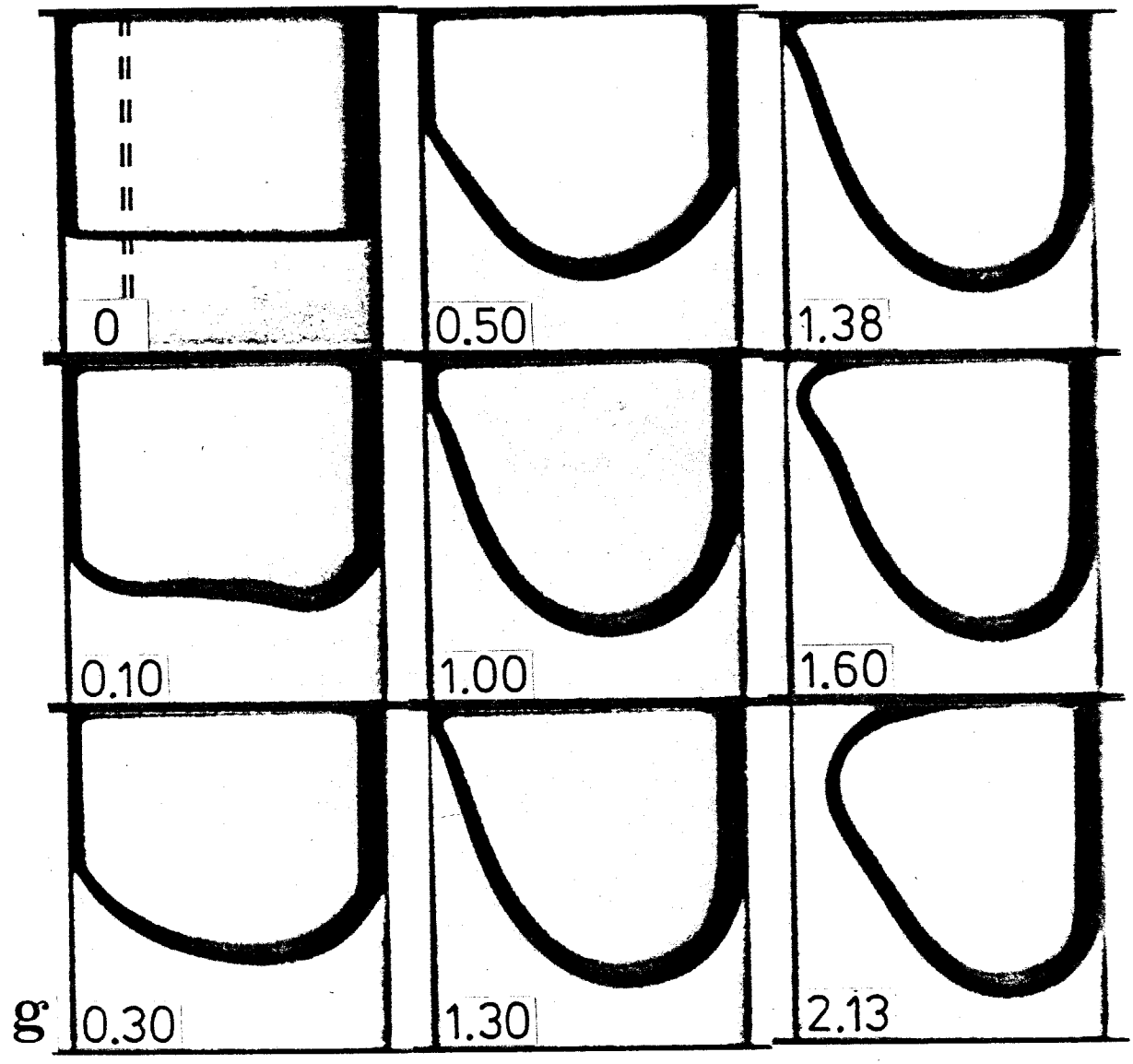

Figure 7g

Exp. Fluids 6U/2

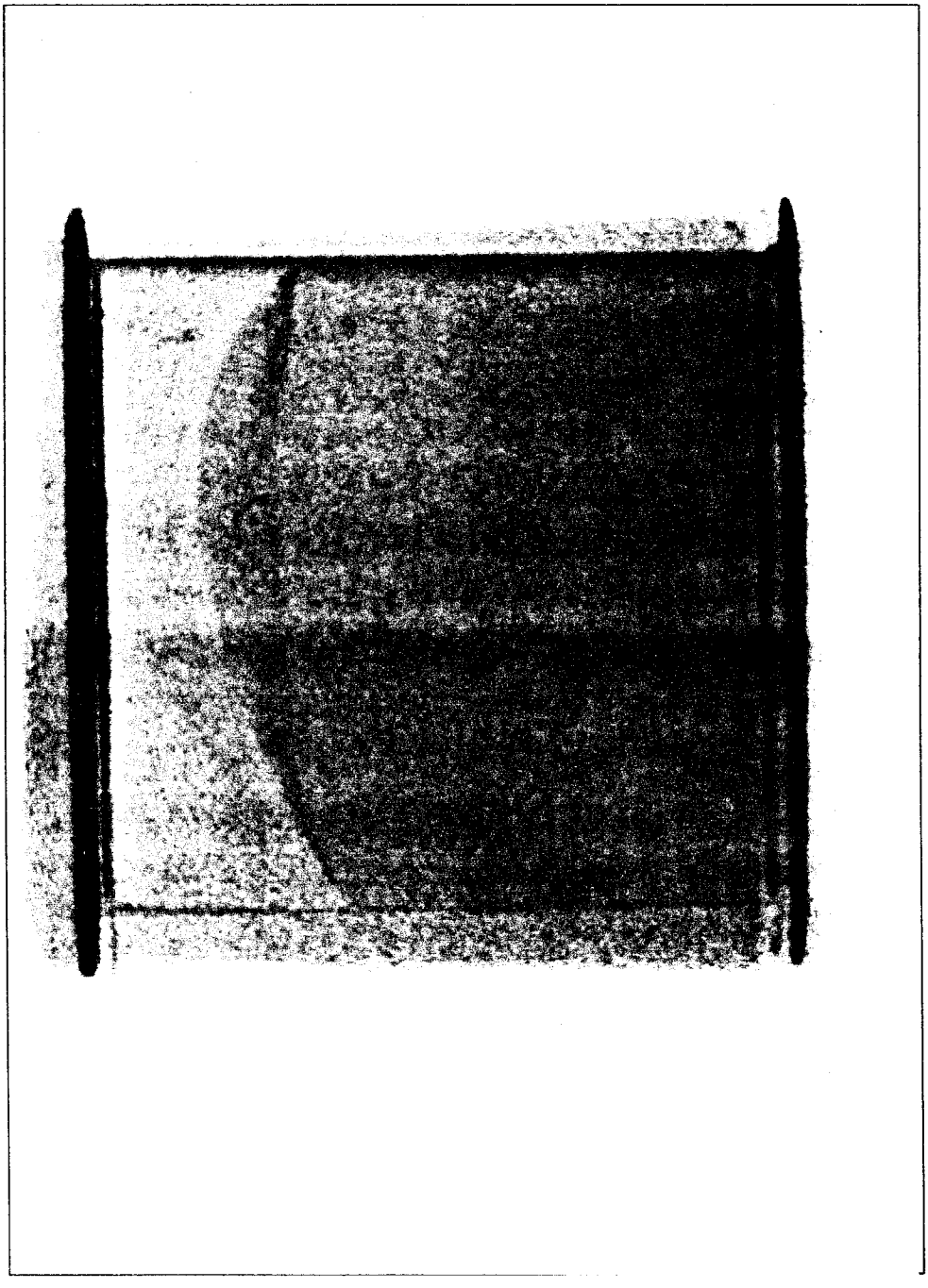

Figure 7h

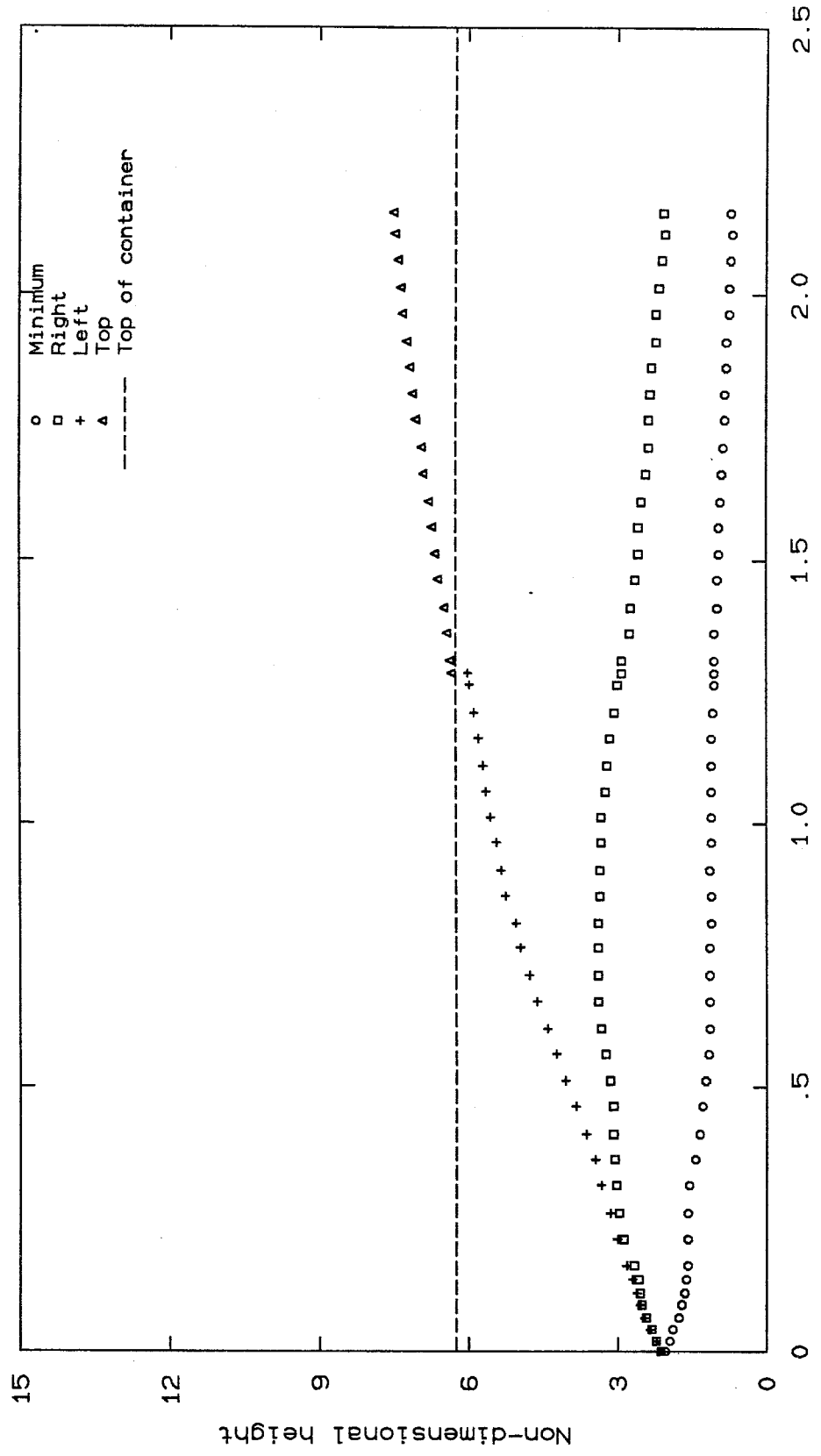

Figure 8a Position of free surface of 40 percent ethanol solution at zero gravity

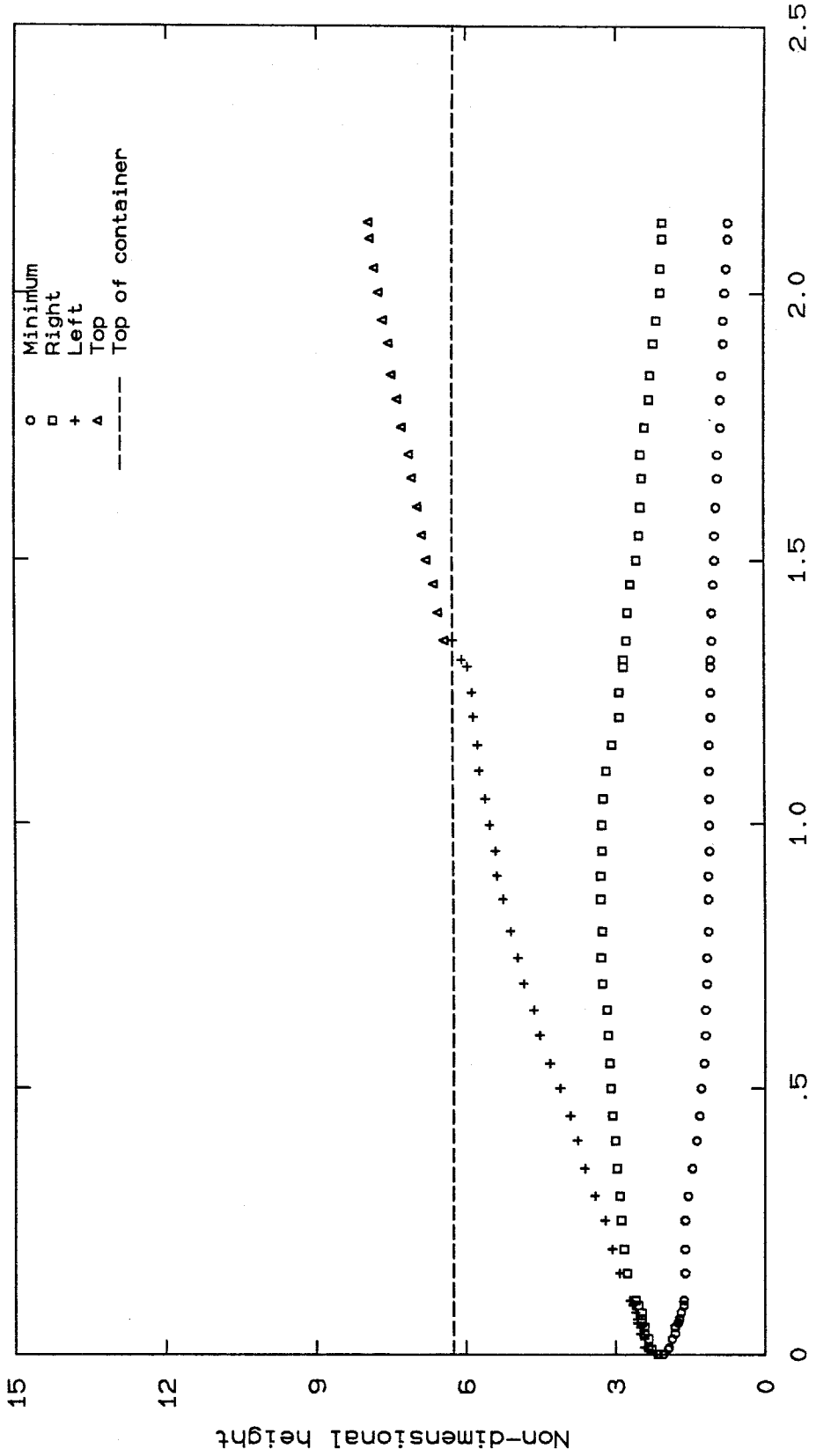

Figure 8b Position of free surface of 50 percent ethanol solution at zero gravity

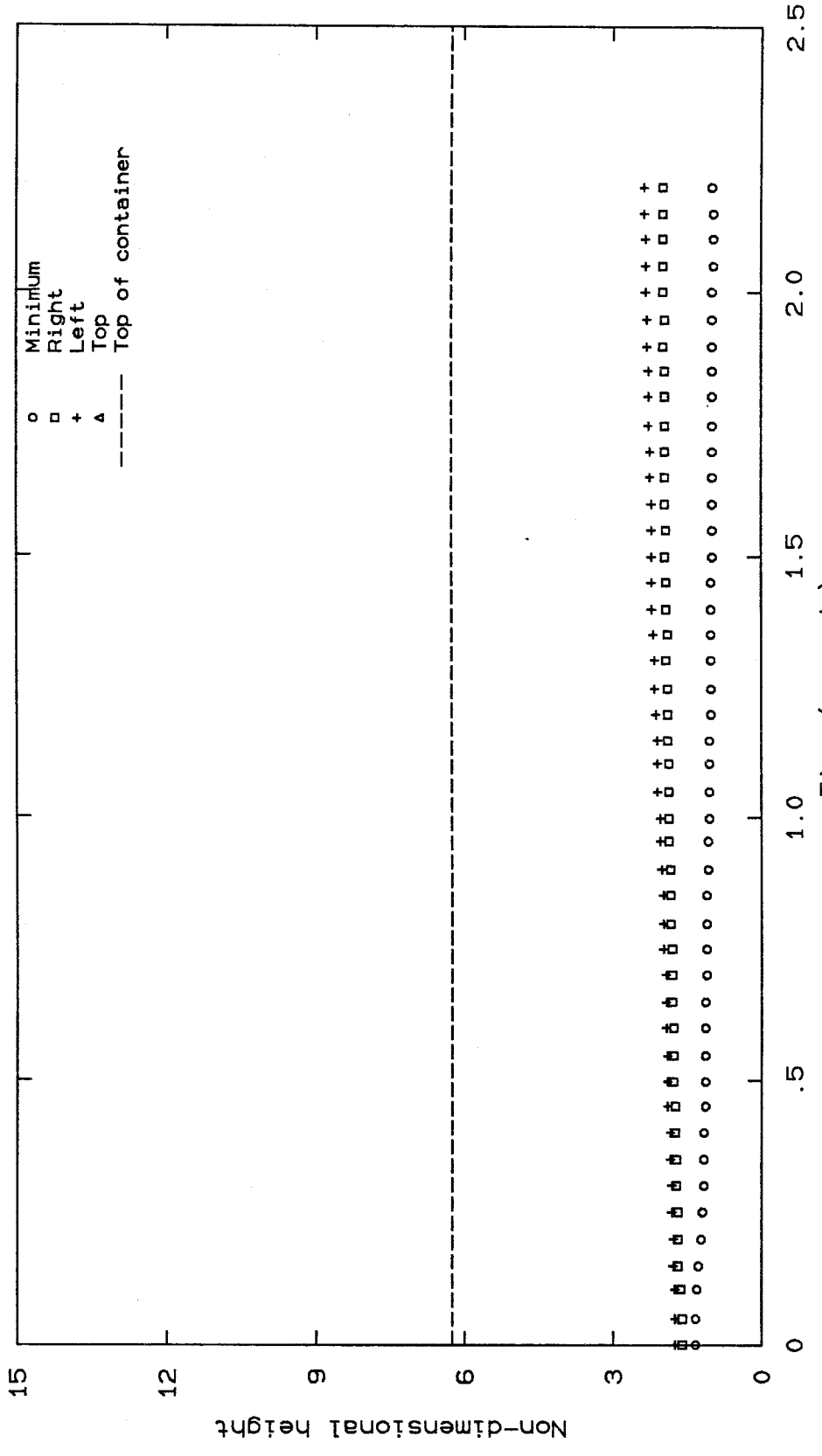

Figure 8c Position of free interface of glycerol tributanoate over ethylene glycol at zero gravity

Table 1: Liquid Pair Properties

Liquid Pair	Left Contact-Line Velocity ($\frac{cm}{sec}$)	σ $\left[\frac{dynes}{cm}\right]$	ρ (cP)	μ	γ	$\sigma \cos\gamma$
1	0.28	8.2	$\frac{1.035}{1.109}$	$\frac{11.6}{19.9}$	18°	7.80
2	0.09	7.1	$\frac{0.988}{1.133}$	$\frac{3.8}{4.5}$	29°	6.21
3	0.13	20.9	$\frac{0.879}{1.133}$	$\frac{0.8}{4.5}$	68°	7.83

Chapter IV

Containments for liquids at zero gravity.

(To appear in Applied Microgravity Technology)

G. Smeets
Graduate Aeronautical Laboratory
California Institute of Technology
Mail code: 205-45
Pasadena, CA 91125
U.S.A.

Abstract

A theory proposed by Concus and Finn in 1974 and recently developed by Finn yields explicit geometrical criteria for the position of the free surface of a liquid at zero gravity in a cylindrical container of specified cross section. These criteria were applied by Concus and Finn to three container geometries; the bathtub, the trapezoid, and the keyhole. It is possible to find geometrical criteria that promise a liquid interface of finite height, with the base still covered with liquid, or a liquid interface of infinite height, with the liquid wetting a well defined portion of the wall. In the present work, calculations are presented for a fourth geometry, the non-concentric cylinders. In addition, the earlier calculations of Concus and Finn are extended, and a unified graphical presentation of all four geometries is given that can be used directly for the design of containments for liquids at zero gravity.

1 Introduction

The work reported here was carried out in preparation for a proposed space experiment. The objective was to study the relationship between container geometry and interface geometry for a free liquid surface in equilibrium at zero gravity. The research has involved an analytical and numerical study of the four container geometries shown in Fig. 1. The intent was to determine the shapes of these four geometries for which the liquid location at zero gravity is qualitatively different from that found at non-zero gravity. Three of these configurations, the bathtub, the trapezoid, and the keyhole, were studied previously by Concus and Finn [1, 2] and are discussed here in somewhat more detail. The non-concentric-cylinder geometry was conceived by Coles [3]. Drop-tower experiments conducted to investigate the behavior of liquids in the bathtub geometry are reported in another paper [4]. The results of the experiments encouraged continuation of the analytical study. The results from all four geometries are displayed in a unified graphical representation that indicates different properties of these geometries in a zero-gravity environment.

The paper should be useful to designers of containers and pipes for use at zero-gravity. If the four geometries considered here are not adequate for a particular application, the user can extend the analysis to other geometries of interest. The static theory as developed by Finn [5] is quite general and applies to cylindrical containers of arbitrary cross-section. However, each case must be investigated individually. Dynamic liquid behavior caused by accelerating, emptying, filling, heating, or otherwise disturbing a static situation is not accounted for here. However, information regarding the static equilibrium position of a liquid at zero gravity provides a natural starting point for a study of dynamic behavior.

In general, the location of a liquid in a container at zero gravity is dependent upon the shape of the container and the contact angle γ between the chosen liquid and the container walls. Consider a cylinder of some arbitrary cross section Ω, partially filled with a liquid and standing upright in a normal gravity field, as shown in Fig. 2. A striking feature of the Concus-Finn [6] and Finn [1, 5] theories is the existence of a critical contact angle $\gamma_0(\Omega)$, with $0 \le \gamma_0 \le \frac{\pi}{2}$, such that when $\gamma_0 < \gamma \le \frac{\pi}{2}$ a large enough volume V of fluid will cover the base and yield an

interface of bounded height. When $0 \leq \gamma < \gamma_0$, however, every large enough volume of fluid will rise to the top of the container along a portion of the boundary walls, regardless of container height. If the liquid and the shape of the cross section are chosen appropriately, a liquid that resides on the base of the container in a one-gravity field may reside on a well-defined portion of the walls at zero gravity. The theory is based on a functional Φ, which is derived from the Laplace-Young equation and is described in Section 2. The application of this functional to the four geometries is described in Section 3. Results and conclusions are given in Sections 4 and 5. A detailed discussion of the topology of the graphical results is left to the appendix.

2 Theory

For greater detail on the theoretical background and derivations, the reader is referred to Finn [5]. The theory stated here is only what is necessary for the present discussion.

Let a standard variational technique be used to minimize an expression for the free energy of a liquid in a container at zero gravity. The free energy includes the free surface energy ($E_S = \sigma S$) and the wetting energy ($E_{S^*} = -k_0 \sigma S^*$), where σ is the surface tension, S and S^* are the free surface area of the interface and the wetted surface area of the container, respectively, and k_0 is a constant of proportionality. The total volume of the liquid is held constant as a constraint, represented by a term $k_1 V$. Thus

$$E(S) = S - k_0 S^* + \frac{k_1}{\sigma} V \tag{1}$$

Minimization of the free energy defined by Eqn. (1) yields the Laplace-Young equation for a static liquid free surface in a cylinder of arbitrary cross section at zero gravity;

$$\text{div } T(u) = \frac{\Sigma \cos \gamma}{\Omega} \tag{2}$$

$$\mathbf{n} \cdot \mathbf{T}(u) = \cos\gamma = k_0 \tag{3}$$

where $\mathbf{n}$ is the unit outward normal, Σ and Ω are the perimeter and area of the cross section, γ is the contact angle measured in the liquid, $u = u(x,y)$ is the height of the free surface, and

$$\mathbf{T}(u) = \frac{\nabla u}{(1 + |\nabla u|^2)^{1/2}} \tag{4}$$

Consider a cross section of the container, normal to the axis, as sketched in Fig. 3. Assume that the free surface intersects the cross section along a curve Γ. Integration of Eqn. (2) over this section yields an energy per unit length defined by

$$\Phi(\Gamma) = \Gamma - (\cos\gamma)\Sigma^* + \left[\frac{\Sigma\cos\gamma}{\Omega}\right]\Omega^* \tag{5}$$

which is a two-dimensional analog to the three-dimensional energy defined by Eqn. (1) [1]. There is a close analogy between the free surface area S, the wetted surface area S^*, and the liquid volume V in Eqn. (1) and the length of the curve Γ, the length of the wetted boundary Σ^*, and the liquid area Ω^* in Eqn. (5).

The cylinder has a flat bottom Ω and a smooth boundary Σ, while Γ is a circular arc of radius $R_\gamma = \frac{\Omega}{\Sigma\cos\gamma}$ for the entire range $0 \le \gamma \le \frac{\pi}{2}$. Under these circumstances, the liquid surface extends to a finite height inside the cylinder if and only if $\Phi > 0$ for every arc Γ that can be drawn in the cross section such that the arc meets the walls at the contact angle γ. In general, there are at most a finite number of these arcs that can be drawn; therefore, it is sufficient to evaluate Φ for only a finite number of cases. For the critical contact angle γ_0 introduced above, there will be at least one arc Γ such that $\Phi = 0$, with $\Phi \ge 0$ for all other arcs. In the present work, the aim is to determine these critical arcs Γ, since they separate the two types of behavior described below.

Whenever $\Phi > 0$ on all arcs Γ, the height of the liquid interface is bounded. To be precise, a solution $u(x,y)$ exists for the Laplace-Young equation (Eqns. (2)-(4)). The surface defined by $u(x,y)$ minimizes the mechanical energy among all possible surfaces satisfying the prescribed

volume constraint and meeting the bounding walls of the container at the contact angle γ.

Whenever $\Phi = 0$ for some arc Γ, a bounded solution cannot be found. The mechanical energy is then formally minimized by a generalized function that is positive infinite in Ω^* and finite in the rest of the domain, or finite in Ω^* and negative infinite in the rest of the domain. In the real case, this conclusion means infinite liquid rise (or rise to the top of the container) in Ω^* and possible uncovering of the base outside Ω^*, depending upon the volume of available liquid. It is this behavior that can be inferred from the graphical descriptions for the four cases discussed here.

3 Application of theory

Application of the Φ functional, described in section 2, to a particular geometry requires that all the terms in the functional be defined for that geometry. A position for the circular arc Γ must be specified in order to determine Σ^* and Ω^*. This circular arc represents the position of the free surface of the liquid in the cross section; therefore, the arc must meet the walls at the contact angle. Each geometry considered here requires special attention to details to determine the terms in Φ, which are listed in Figs. 4a-4e. It is useful to refer to the drawings of each geometry given in Figs. 5-8 for the following discussion.

Finn [1] presented a detailed account of the procedure used to find the location of the critical circular arc Γ for the trapezoid cross section. He considered all possible positions of Γ and found that $\Phi > 0$ for all except two of these. Fig. 6 shows that one of these arcs Γ is symmetrically located on the long-axis centerline, with the convex side of the arc toward the narrow end of the trapezoid. The other arc Γ is located in the corners of the trapezoid, with the convex side toward the corner, indicating the possibility of liquid rise to infinity there. Critical behavior of liquids in corners is considered again in the discussion of the bathtub and the trapezoid in the appendix.

The location of the arc Γ for the bathtub cross section shown in Fig. 5 was also determined by Finn [7]. A general rule appears to be that the liquid tends to rise in regions of higher curvature or in the narrower end of the container. When applied to the keyhole cross section,

this rule yields Γ as shown in Figs. 7a and 7b [8]. The cross section for the non-concentric cylinders is rather different from the other three, but application of the rule yields two circular arcs positioned as shown in Fig. 8a. Although this general rule is simple, finding critical solutions with $\Phi = 0$ is positive proof of correct arc placement. If the arc is not correctly placed, it is always found that $\Phi > 0$ [8].

When a general position for the arc Γ has been found, the geometric expressions for the terms of the Φ functional can be determined. The terms for each geometry include those listed in Figs. 4a-4e and the following equations, which are common to all four geometries:

$$R_\gamma = \frac{\Omega}{\Sigma \cos\gamma} \tag{6}$$

$$\Gamma = 2\theta R_\gamma \tag{7}$$

Eqn. (6) represents the radius of the circular arc Γ and Eqn. (7) represents its length. It is necessary to double the right-hand side of Eqn. (7) for the non-concentric cylinders, because there are two circular arcs. Each geometry is fully defined by two parameters α and β, which are shown in Fig. 1 for each geometry. The parameter α is defined as the half angle of the extended sides or tangents, with the exception of the non-concentric cylinders. For the latter, α is the angle between the axis of symmetry of the cross section and the line segment connecting the tops of the two circles. The parameter β is always defined as the ratio of the radii or sides, with the larger radius or half height defined to have unit length. These definitions for α and β allow the full range of possible shapes of each geometry to be represented by a finite range for each parameter, $0 \le \beta \le 1$ and $0° \le \alpha \le 90°$. The functional Φ depends only on geometry and contact angle. Therefore, $\Phi = \Phi(\alpha, \beta, \gamma)$.

In addition to choosing uniform geometric parameters to represent each geometry, the equations in Figs. 4a-4e have been written in a consistent form. For example, the total perimeter Σ is always written such that the first term represents the perimeter of the left portion or narrow end of the cross section. The second term represents the perimeter of the middle portion, and the last term represents the perimeter of the right portion. In the case of the

keyhole without parallel sides, pictured in Fig. 7b, and in the case of the non-concentric cylinders, pictured in Fig. 8a, there is no middle portion, but the left and right portions are represented in the standard way. The same is true for the organization of the rest of the expressions. The quantity θ always represents the half angle subtended by the arc Γ. The quantity ϕ is used for the keyhole with $h < 0$ in Fig. 7b and for the non-concentric cylinders in Fig. 8 to represent the angle of β from the center line to the intersection of the arc Γ with the cross section. The quantity λ represents the center-to-center distance in Figs. 5-8. For the bathtub in Fig. 5 and the trapezoid in Fig. 6, δ represents the distance of the circular arc Γ from the small end of the cross-section. The quantity h is introduced with the keyhole geometry in Figs. 7a and 7b to represent the length of the parallel sides. If no parallel sides are present, h is considered to be non-positive.

The terms for the bathtub and the trapezoid were determined by straightforward application of geometrical identities. These terms were given explicitly by Finn [1, 7]. The terms listed in Figs. 4a and 4b correspond exactly to Finn's notation; however, they are written in a form chosen for consistency among the four geometries considered here.

The keyhole geometry has two distinct shapes. Fig. 7a shows the case where the cross section contains parallel sides and Fig. 7b shows the case without parallel sides. The length of the parallel sides is defined as h. The keyhole terms for the case $h > 0$ are listed in Fig. 4c. The terms for the keyhole with $h < 0$, listed in Fig. 4d, are slightly more complicated. For the case $h = 0$, either set of equations can be used. The loss of the parallel sides requires the introduction of the point (X,Y), indicated in Fig. 7b, where the large circle intersects the smaller one. For the keyhole geometry, the arc Γ is located at the reentrant corners of the cross section, and does not change position with contact angle or container shape. However, the radius and the length of Γ still vary according to Eqn. (6) and (7). Theorem 1 of Finn [5] states that the arc Γ must intersect the reentrant corners and need not meet the walls at the contact angle γ; in fact, the angle between Γ and the parallel sides is $\geq \gamma$.

The terms for the non-concentric cylinders, shown in Fig. 4e, are the most complex among the four geometries. In this case, the two points of intersection, indicated in Fig. 8b, between Γ and the cross-section had to be numerically determined. X1 and X2 were iterated until the

circular arc Γ met the inner and outer cylinders at the contact angle γ. This additional complication yields the five-term expression for Ω^* given in Fig. 4e. The first term, Θ, is the area of the entire sector of the larger cylinder that contains the arcs Γ in Fig. 8a. The next four terms represent areas of the corresponding sections labeled 1 through 4 in Fig. 8b. Note that the areas in Fig. 8b must all be doubled to represent the areas on both sides of the dashed centerline.

The terms for Φ were inserted into computer programs for each geometry. The critical values $\Phi(\alpha, \beta, \gamma) = 0$ were found by straightforward application of binary search and secant-method zero-finding algorithms. The location of the arc Γ for the bathtub, the trapezoid, and the keyhole was found by straightforward analytical means once the contact angle γ was specified. The location of the arc Γ for the non-concentric cylinders, however, was found by iterating X1 and X2 (Figs. 4e, 8a). For all geometries, $\gamma = \gamma_0$ was chosen, β was fixed, and α was searched to find $\Phi(\alpha, \beta, \gamma_0) = 0$; then β was changed, and α was searched again. In every case, zeros of Φ were found to an accuracy of 10^{-12} or better using double-precision calculations.

4 Results

The results for each geometry are given in graphical form in Figs 9-12. The abscissa in every plot is $0° \le \alpha \le 90°$ and the ordinate is $0 \le \beta \le 1$, where α and β are the geometric parameters for each cross section. A particular geometry is fully defined by choosing a point (α, β). The first plot in each case, namely Figs. 9a, 10a, 11a, and 12a, depicts the critical curves $\Phi(\alpha, \beta, \gamma_0) = 0$ for γ_0 = constant. Any geometric point (α, β) lying on a particular curve $\Phi(\alpha, \beta, \gamma_0) = 0$ is critical for contact angles $\le \gamma_0$. That is, liquid rises to infinity on the convex side of the arc Γ at zero gravity. The second plot, namely Figs. 9b, 10b, 11b, and 12b, displays dotted curves of constant critical area ratio. For all the geometries except the non-concentric cylinders, the critical area ratio A_{crit} is defined as the ratio of cross sectional area occupied by liquid to the total available cross sectional area; i.e., $\frac{\Omega^*}{\Omega}$. For the non-concentric-cylinders case, $A_{crit} = \frac{\Omega^*}{\pi}$, where π is the area of the larger cylinder. If Ω is used rather than π,

$A_{crit} \approx$ 100 percent is found as $\beta \rightarrow 1$, yet almost no liquid is contained in the very small space between the two cylinders. The third plot, namely Figs. 9c, 10c, 11c, and 12c, depicts curves λ = constant. The quantity λ represents the center-to-center distance or, in the case of the trapezoid, the end-to-end distance. For all the geometries except the non-concentric cylinders, λ has a full range from zero to infinity. For the non-concentric cylinders case, λ is restricted to $0 \leq \lambda \leq 1$, otherwise the inner cylinder would protrude beyond the outer one. Note that all the curves in Figs. 9-12 are labeled from right to left except Fig. 12b, which is labeled in the reverse order.

For every plot shown, the computed points are connected by straight line segments. No curve fits were employed to smooth the computed data points; therefore, individual computed points are not shown. The computations yielded points (α, β) for a given γ_0 such that $\Phi(\alpha, \beta, \gamma_0) = 0$. Curves of A_{crit} = constant were determined by interpolating the A_{crit} results for each curve $\Phi(\alpha, \beta, \gamma_0) = 0$. For this purpose, various additional curves were computed for intermediate values of γ_0 in order to yield smooth critical area-ratio curves. Curves λ = constant were computed from the geometrical formulas shown in Figs. 4a-4e.

Each of the following four parts discusses the plots for a particular cross section. A number of prominent features that warrant close attention are discussed in the appendix.

Bathtub: The graphical results for the bathtub geometry are shown in Figs. 9a-9c. The design point for the container used in experiments at the NASA Lewis drop-tower facility [4] is indicated on each plot. As previously stated, the results of these experiments encouraged the continuation of this work.

Critical curves $\Phi = 0$ for $\gamma = 0°(5°)85°$ are shown in Fig. 9a. A similar plot for this geometry was presented by Concus and Finn [2], who plotted γ versus β with α constant. The points along each curve in Fig. 9a were found for a particular $\gamma = \gamma_0$ by first fixing β and then scanning the α range. This procedure yielded more than one zero for Φ; however, inspection revealed that $\delta < 0$ for all of these except one. The given formulas for Φ in Fig. 4a consider only the intersection of Γ with the non-parallel sides; therefore, $\delta < 0$ is not valid in this context. When the terms of Φ were written to include intersection of the curve Γ with the small

circular end, no zeros were found. The convergence of the curves $\Phi = 0$ to the point $\alpha = 0°$, $\beta = 1$, the α-intercepts, and the curve for $\gamma_0 = 0°$ are discussed in the appendix.

The curves are more easily understood by an application, in this case to the drop-tower experiments [4]. The plexiglas containers for these experiments were designed to have a critical contact angle of 30° with $\beta = 0.5$. Fig. 9a shows that the design point lies on the curve $\Phi = 0$ for $\gamma_0 = 30°$. The design point lies below and to the left of all critical curves for which $\gamma_0 < 30°$, and lies to the right and above all critical curves for which $\gamma_0 > 30°$. If a liquid partially filling this container has a contact angle of 30° or less, it will attempt to rise to infinity in the narrow end of the cross section. This behavior was seen in the experiments when 50% ethanol in water ($\gamma_0 \approx 23°$) was used. If the liquid has a contact angle greater than 30°, it rises to a finite height [6, 9]. This behavior was seen for water ($\gamma_0 \approx 72°$) and for 10% ethanol in water ($\gamma_0 \approx 55°$).

Plots of A_{crit} = constant and λ = constant for the bathtub geometry are shown in Figs. 9b and 9c respectively. The curves in Fig. 9b are bounded above by the curve $\gamma_0 = 0°$. The curves λ = constant depict how the center-to-center distance changes with the geometric parameters. The design point for the drop-tower tests had $A_{crit} \approx 12$ percent with $\lambda \approx 5$. For the design, it was important to have a sizeable percentage of the cross section filled with liquid while at the same time restricting the container to a reasonable length.

Trapezoid: The graphical results for the trapezoid geometry are shown in Figs. 10a-10d. Unlike the other three geometries, corners are always present in this cross section (Fig. 4b). The presence of corners complicates the explanation of the results. Basically, critical liquid rise in the corners is not as large-scale as it is in the narrow end of the container, and both can occur for the same contact angle and geometry. The curves $\Phi = 0$ in Fig. 10a are interpreted in the same manner as for the bathtub geometry. In this case, each scan of α for fixed β yielded only one zero for Φ. Some prominent physical features, such as the α-intercepts and the convergence of the curves $\Phi = 0$ to the point $\alpha = 0$, $\beta = 1$ were also seen for the bathtub geometry. The dotted and dashed curves in Fig. 10a, along with the fact that some of the curves $\Phi = 0$ end in mid-plot, are discussed in the appendix. The curves of A_{crit} = constant in Fig. 10b and λ = constant in Fig. 10c are once again easily understood. To obtain a higher

percentage of the cross section filled with liquid, it is necessary to consider longer lengths. The plot of curves $\delta = 0$ shown in Fig. 10d is discussed in the appendix.

Keyhole: The results for the keyhole geometry are shown in Figs. 11a-11c. The curves $\Phi = 0$ are interpreted in the same way as the previously discussed geometries. Only one zero was found for Φ for a given scan of α. The dashed curve in Fig. 11a indicates where $h = 0$. A different set of equations is used for the terms of the Φ functional for $h > 0$ and for $h < 0$ (Figs. 4c, 4d). The solutions join smoothly. The convergence of the curves $\Phi = 0$ to the point $\alpha = 90°$, $\beta = 0$, the β-intercepts, and the curve $\gamma_0 = 0°$ are discussed in the appendix. The interpretation of the curves A_{crit} = constant in Fig. 11b and the curves λ = constant in Fig. 11c is straightforward. The curves in Fig. 11b are bounded above by the curve for $\gamma_0 = 0°$ and bounded below by the curve for $\gamma_0 = 89.9°$. Note that critical area ratios larger than 30% are possible for reasonable values of λ and β.

Non-concentric cylinders: The graphical results for the non-concentric cylinders are given in Figs. 12a-12c. This set of plots differs markedly from the others considered here. The α range ($45° \le \alpha \le 90°$) is half of the α range seen for the three previous geometries. This limitation is a physical consequence of the geometry; at $\alpha = 45°$, the inner cylinder touches the wall of the outer cylinder. To allow α to go beyond this value would involve the consideration of crescent-shaped domains. The other distinguishing features are discussed in the appendix.

The curves $\Phi = 0$ in Fig. 12a are interpreted differently from the curves $\Phi = 0$ for the other geometries. If a point (α, β) lies to the right and below a particular $\gamma = \gamma_0$ curve, a liquid with a contact angle γ_0 would rise to a finite height in the container. However, if (α, β) lies on or above the curve, a liquid with that contact angle would rise to infinity. The technique used to find zeros for this geometry did not yield results for $\gamma_0 = 0°$. The curve for $\gamma_0 = 1°$ is plotted, and overlaps the curve for $\gamma_0 = 5°$. It is supposed that the curve for $\gamma_0 = 0°$ would also overlap. The curves A_{crit} = constant in Fig. 12b and the curves λ = constant in Fig. 12c are easily understood as before. The curves in Fig. 12b are bounded below by the curves for $\gamma_0 = 1°$.

5 Discussion and Conclusions

In the containers discussed above, the liquid tends toward the narrow ends or areas of high curvature at zero gravity. In the limit $\beta \rightarrow 0$ the small end of the bathtub or the trapezoid becomes a corner of angle 2α and the corner-condition [6] is satisfied by the curves $\Phi = 0$ (see the appendix). In the limit $\beta \rightarrow 1$ the sides of the bathtub and the trapezoid become parallel and all the curves $\Phi = 0$ converge to $\alpha = 0°$.

All of the plots in Figs. 9a, 10a, 11a, and 12a have empty regions. In Figs. 9a, 10a, and 11a, a geometry (α, β) effects finite liquid rise for a particular contact angle γ_0 if it is located above and to the right of the curve $\gamma = \gamma_0$. In Fig. 12a, a geometry (α, β) effects finite rise if it is located below and to the right of the curve. Therefore, any geometry (α, β) located in the blank region of a plot will not effect infinite rise for any contact angle. The results of Bainton [9] for the bathtub show that the farther the design point is above a curve $\Phi(\alpha, \beta, \gamma_0) = 0$, the smaller the finite rise height. For the keyhole, this blank region encompasses nearly the entire upper half of the plot. A designer of such a geometric shape for use in zero gravity might be disappointed with the results if β were chosen to be larger than 0.506 and large liquid rise was desired.

Another practical consideration for designing containers is the actual value of the contact angle. The contact angle depends on the liquid and the material chosen for the container. It also depends upon surface cleanliness, liquid purity, and other properties, such as surface roughness. Note that all the work presented here also applies to contact angles larger than 90° by using the supplement of the angle and considering the accompanying fluid as the one that is producing the movement. Consider vapor over a liquid with a contact angle of 120°. If the container is designed to have a critical angle of 60° or more, then the vapor would try to occupy the area of the container on the convex side of the arc Γ. In many applications, cleanliness and purity may not be fully controllable, or the contact angle may not be known. A conservative designer could choose a container shape that is critical for a large range of contact angles. For the bathtub, the trapezoid, and the keyhole, the designer might choose to design for a critical contact angle of 80°. This choice, although yielding a rather long cross section, will effect infinite liquid rise for liquids with contact angles less than or equal to 80°. For the non-

concentric cylinders, the designer need not know the contact angle. For example, with $\beta = 0.5$ and the inner and outer cylinder concentric ($\alpha = 90°$) small finite rise should occur for any liquid with $\gamma < 90°$. As the inner cylinder is moved radially ($\alpha \rightarrow 45°$), the liquid will rise to infinity as the appropriate critical curve is crossed. Used this way, the non-concentric cylinders could conceivably be used for measurement of the contact angle. This geometry also presents a means of causing fluid to move on demand, by merely moving the cylinder radially to effect liquid rise and then back toward the concentric position to cause the liquid to fall again. This geometry is the only one of the four considered here for which it is easy to visualize a continuous variation of the geometric parameters as part of an experiment in space.

If $\gamma_0 = 90°$, then the liquid has no component of surface tension along the solid surface of the container. Thus no liquid motion would be expected. All four geometries considered here demonstrate this rather vividly. Consider the bathtub. In the limit $\gamma_0 \rightarrow 90°$, Fig. 9a suggests that the curve $\Phi = 0$ approaches the left edge of the plot. In order for a geometry (α, β) to be critical, for $\gamma = \gamma_0$, it must be located below and to the left of the curve $\Phi(\alpha, \beta, \gamma_0) = 0$. However, this condition becomes increasingly difficult to satisfy as $\gamma_0 \rightarrow 90°$. At $\gamma_0 = 90°$, all the geometries in the plot are non-critical. This property is also seen in Figs. 10a, 11a, and 12a.

For other applications, the amount of liquid that rises may be important. For this purpose, the plots of A_{crit} = constant provide a useful guide. The user should be aware that these critical area-ratios are for the critical case only, that is to say that if the design point (α, β) is located on a curve $\gamma = \gamma_0$, then this area ratio is valid for a liquid with contact angle γ_0. These values of A_{crit} were interpolated from results for $\Phi = 0$ for many curves $\gamma = \gamma_0$. If a large region of liquid rise is desired, the designer should choose (α, β) within the highest A_{crit} contour on the curve $\gamma = \gamma_0$ of interest. It is worth noting that both the keyhole and non-concentric cylinders have finite A_{crit} values along their respective curves $\gamma_0 = 0°$, whereas $A_{crit} = 0$ along the curve $\gamma_0 = 0°$ for the bathtub geometry. Each of the containers considered here easily offers $A_{crit} \simeq 20$ percent for reasonable values of λ and β. Higher percentages can be realized with the keyhole geometry. However, this is simply a matter of making the parallel section longer so that it comprises a larger percentage of the cross sectional area. The result is a rather long container that may or may not be convenient for certain applications.

The results presented above provide a starting point for designers of containments for liquids at zero gravity. While these results do not settle dynamic questions, they do provide workable criteria in the four cases discussed, in order that statically stable configurations can be achieved. The theories of Concus and Finn [6] and of Finn [1, 5], on which the above work is based, can in principle be applied in analogous ways to cylindrical containers of arbitrary cross section.

This material is based upon work supported by the U.S. National Aeronautics and Space Administration and the University of California. I am indebted to D. Coles, P. Concus, and R. Finn for useful discussions. The opinions, findings, conclusions and recommendations are those of the authors and not necessarily of the U.S. National Aeronautics and Space Administration or the University of California.

Appendix

Some details regarding the topology of the plots in Figs. 9a, 10a, 11a, and 12a are presented below for each geometry. In addition, a discussion of the curves $\delta = 0$ in Fig. 10d is included in the trapezoid section.

Bathtub: All the curves $\gamma = \gamma_0$ shown in Fig. 9a intersect α-axis at $\alpha = 90° - \gamma_0$. The case $\gamma_0 = 0°$ is not so obvious and is discussed below. In addition, the slope of the curves $\Phi = 0$ at the intercepts is identically zero for all γ_0.

$$\frac{\partial \beta}{\partial \alpha} = \frac{1 - (\sin^2\gamma + \cos^2\gamma)}{4\cos\gamma\,(\sin\gamma - \gamma\cos\gamma)} \tag{8}$$

Explanation requires attention to the shape of the cross section as these intercepts are approached. In the limit $\beta \rightarrow 0$, the small end of the bathtub becomes a corner of angle 2α. Concus and Finn [6] determined that if $\alpha + \gamma < 90°$ the liquid free surface rises to infinity in the corner indicated in Fig. 13. Fig. 9a indicates that if $\beta = 0$ and $\alpha + \gamma_0 \leq 90°$ the liquid rises to infinity in the corner. Concus and Finn [6] also state that Γ is coincident with the corner. This is equivalent to $\delta = 0$, $R_\gamma = 0$ as found numerically.

The curve $\gamma_0 = 0°$ intersects the right side of the plot at $\alpha = 90°$, $\beta = 0.5$. This result seems curious when compared to the other curves on the plot. Analytically, setting $\gamma = 0°$ in the Φ terms listed in Fig. 4a and substituting them into Eqn. (5) with $\Phi = 0$ yields:

$$\Phi = \frac{(T - \beta)^2}{T}\left[\left(\frac{\pi}{2} - \alpha\right) - \cot\alpha\right] \tag{9}$$

where

$$T = \frac{R_\gamma \sin\left(\frac{\pi}{2} - \gamma - \alpha\right)}{\cos\alpha} = R_\gamma \tag{10}$$

since $\gamma = 0°$. Substitution of Eqn. (10) into Eqn. (9) yields:

$$\Phi = \frac{(R_\gamma - \beta)^2}{R_\gamma}[(\frac{\pi}{2} - \alpha) - \cot \alpha] \tag{11}$$

Thus $\Phi = 0$ implies $\cot \alpha = (\frac{\pi}{2} - \alpha)$ and/or $R_\gamma = \beta$. The first case yields $\alpha = \frac{\pi}{2}$, or the entire right side of the plot, since this result is not limited in β. The second case yields the equation

$$\cot \alpha = (\frac{\pi}{2} - \alpha) - \frac{\pi(1 - 2\beta)}{(1 - \beta)^2} \tag{12}$$

Note that at $\beta = 0.5$ this case reduces to the first one. Hence the intercept at $\alpha = 90°$, $\beta = 0.5$. The curve $\gamma_0 = 0°$ shown in Fig. 9a was computed using Eqn. (12). Note that because $T = R_\gamma = \beta$, and $\delta = 0$, the arc Γ is coincident with the circular arc of radius β.

All the curves $\Phi = 0$ converge at the point $\alpha = 0$, $\beta = 1$. The case $\beta = 1$ was studied by Concus and Finn [6] as a possible candidate for an "astronaut's bathtub". In the limit $\beta \rightarrow 1$, α necessarily goes to zero, since $\beta = 1$ requires parallel sides. This property was also discussed by Concus and Finn [2].

Trapezoid: All the curves $\gamma = \gamma_0$ shown in Fig. 10a intersect the α-axis at $\alpha = 90° - \gamma_0$, and at zero slope. This behavior was also exhibited by the curves for the bathtub in Fig. 9a. The explanation for this behavior is given above in the bathtub section of this appendix. The analytic expression for the slope at these points is:

$$\frac{\partial \beta}{\partial \alpha} = \frac{(1 - (\sin^2\gamma + \cos^2\gamma))^2}{2\sin 2\gamma} \tag{13}$$

The dotted curve in Fig. 10a indicates the point, along a given curve $\gamma = \gamma_0$, where the acute corners become critical. Define α_0 as the α at which the dotted curve crosses a particular curve $\gamma = \gamma_0$. Infinite liquid rise is expected to occur in the acute corners for $\alpha > \alpha_0$ along a particular curve $\gamma = \gamma_0$. Therefore, for $\gamma_0 \leq 45°$ the plot shows that the acute corners are critical for all α, and for $\gamma_0 > 60°$ the acute corners are not critical along the $\gamma = \gamma_0$ curves.

The dashed curve in Fig. 10a indicates the point, along the curve $\gamma = \gamma_0$, where the obtuse corners become critical. Once again define α_0 as the value of α at which the dashed curve

intersects a particular curve $\gamma = \gamma_0$. In this case, for all $\alpha < \alpha_0$ along a particular curve $\gamma = \gamma_0$, the liquid rises to infinity in the obtuse corners. For the critical curve $\gamma = 30°$, for example, this rise occurs for $\alpha \leq 30°$. If $\gamma > 45°$ then the obtuse corners do not become critical.

It is important to note that the dotted and dashed curves described above do not define regions of the (α, β) plot where the acute and obtuse corners become critical. They only act as indicators as to where these corners become critical along the curves $\gamma = \gamma_0$. General regions of corner criticality can be defined. However, these regions are bounded by vertical lines on an (α, β) plot. This corner condition is independent of β except for the case $\beta = 0$, where the two obtuse corners merge to become one corner of angle 2α. The acute corners are critical if $\alpha \geq (2\gamma - 90°)$, and the obtuse corners are critical if $\alpha \leq (90° - 2\gamma)$. Consider the acute corners first. If $\gamma = 45°$, then the acute corners are critical for all $\alpha \geq 0°$. If $\gamma < 45°$, then $\alpha \geq$ (negative value), but $0° \leq \alpha \leq 90°$. Therefore, the acute corners are critical for all valid α. For example, if $\gamma = 30°$, then $\alpha \geq -30°$, and the acute corners are critical for $-30° \leq \alpha \leq 90°$ and for $0 \leq \beta \leq 1$ as shown in Fig. 14a. If $\gamma > 45°$, then the area of criticality begins to shrink. For example, Fig 14b shows the critical region for $\gamma = 60°$. Critical liquid rise occurs in the acute corners when $(2\gamma - 90°) \leq \alpha \leq 90°$ for $0 \leq \beta \leq 1$.

Infinite liquid rise occurs in the obtuse corners when $0° \leq \alpha \leq (90° - 2\gamma)$ for $0 < \beta \leq 1$, as shown in Fig. 14c. Immediately noticeable is the fact that for $\gamma \geq 45°$ the obtuse corners are never critical. At $\beta = 0$ the obtuse corners no longer exist, and are replaced by one corner of angle 2α. If $\alpha + \gamma \leq 90°$, then infinite rise occurs in this corner. The region of the (α, β) plot that has infinite rise in the obtuse corners, and also in the corner 2α, is $0 \leq \alpha \leq (90° - 2\gamma)$ for $0 < \beta \leq 1$ and $0 \leq \alpha \leq (90° - \gamma)$ for $\beta = 0$ as shown in Fig. 14c. Fig. 14d demonstrates that all corners can be critical for some contact angles.

Some of the curves $\gamma = \gamma_0$ end in mid plot in Fig. 10a. Calculation of $\Phi = 0$ was stopped when $\delta = 0$. This is the point at which the circular arc Γ makes contact with the small side of the trapezoid (2β). Note that this endpoint always occurs at an α that is less than the critical α_0 for obtuse corners for that particular curve $\gamma = \gamma_0$. As α decreases and β increases along a curve $\gamma = \gamma_0$, the circular arc Γ moves closer to the small end of the trapezoid $(\delta \rightarrow 0)$. At some point (α_0) the obtuse corners, which are already filled with the liquid on the convex side of Γ, become

critical. Presumably nothing spectacular happens as α_0 is crossed. However, as α reaches $\alpha_{endpoint}$, the arc Γ touches the small end and it is no longer possible to draw this particular circular arc. This solution must therefore collapse and the liquid would remain trapped in the obtuse corners for any $\alpha < \alpha_{endpoint}$ for $0 \le \beta \le 1$. If β is decreased, as shown in Fig. 15, with $\alpha = \alpha_{endpoint}$, the arc Γ may reappear.

The plot of curves $\delta = 0$ is shown in Fig. 10d. These curves represent values of α and β, for a given $\gamma = \gamma_0$, for which the arc Γ touches the smaller end (2β) of the trapezoid. The curve $\delta = 0$, for a specific γ_0, intersects the curve $\Phi = 0$ for the same γ_0, at $\alpha = \alpha_{endpoint}$. Note that $\alpha_{endpoint} = 90°$ and $\beta = 0$ for $\gamma_0 = 0°$.

Keyhole: In the limit $\alpha \to 0°$, the curves $\Phi = 0$ in Fig. 11a meet the β-axis at well defined points. In the limit as $\alpha \to 0°$, $h \to \infty$. Therefore, a perturbation expansion of the Φ terms shown in Fig. 4c for large h yields (to leading $O(h^2)$):

$$\Phi = 4\beta^2(\theta + \sin\gamma\cos\gamma) + 4\cos^2\gamma[(\pi - \Theta)(2\beta - 1) - \beta\cos\Theta] \tag{14}$$

$$\theta = (\frac{\pi}{2} - \gamma) \quad ; \quad \Theta = \arcsin(\beta) \tag{15}$$

This set of equations was used to determine the values shown in Table 1 for the β-intercepts. Finn [8] reported a critical radius ratio for $\gamma = 0°$ of $\rho_0 = \frac{1}{\beta} = 1.974$ that is in agreement with the result quoted in Table 1.

All of the curves $\Phi = 0$ converge to $\alpha = 90°$ in the limit $\beta \to 0$. Unlike the two previous geometries, no corner is formed when $\beta \to 0$; therefore, no corner-condition α-intercepts are found. In the limit $\alpha \to 90°$, the cross-section becomes a circle; $h \to 0$ and $\beta \to 0$. The curve for $\gamma = 0°$ intersects the right side of the plot at $\beta = 0.5$. Unlike the other cases, the functional Φ did not cross zero for the case $\gamma = 0°$, instead Φ reached a maximum at $\Phi = 0$. The curve shown is flat from the β-intercept ($\alpha = 0°$), to the dashed $h = 0$ curve. From there, it drops off monotonically to the intercept on the right side of the plot. In the limit $\alpha \to 90°$ for $\gamma = 0°$, the shape of the cross section approaches a circle; therefore, Eqn. (6) yields $R_\gamma = 0.5$. In the limit

$R_\gamma \rightarrow 0.5$, with $\gamma = 0°$. $\beta \rightarrow 0.5$ so that the circular arc of radius β is coincident with the arc Γ.

Non-concentric cylinders: All the curves $\Phi = 0$ in Fig. 12a converge to $\alpha = 90°$ at $\beta = 1$ and to $\alpha = 45°$ at $\beta = 0$. As the inner cylinder radius approaches the outer one ($\beta \rightarrow 1$), no room is left to move the inner cylinder. Hence α must go to 90°. In the limit as $\alpha \rightarrow 45°$, the inner cylinder shrinks to zero radius at the wall of the outer cylinder.

References

[1] *Finn, R.:* Existence criteria for capillary free surfaces without gravity. Ind. Univ. Math. J. **32**(3), 439-460 (1983)

[2] *Concus, P., Finn, R.:* Continuous and discontinuous disappearance of capillary surfaces, in: Variational Methods for Free Surface Interfaces. *Concus, P., Finn, R.* (Eds.), Springer-Verlag, New York, Berlin, p. 197-204 (1987)

[3] *Coles, D.:* Private communication (1986)

[4] *Smedley, G.:* Preliminary drop tower experiments on liquid-interface geometry in partially filled containers at zero gravity. To appear in Experiments in Fluids **8** (1990)

[5] *Finn, R.:* A subsidiary variational problem and existence criteria for capillary surfaces. J. Reine Angew. Math. **353**, 196-214 (1984)

[6] *Concus, P., Finn, R.:* On capillary free surfaces in the absence of gravity. Acta Math. **132**, 177-198 (1974)

[7] *Finn, R.:* Private communication (1985)

[8] *Finn, R.:* Equilibrium capillary surfaces. Springer-Verlag, New York, Berlin, 1986

[9] *Bainton, M.C.:* Fluid interfaces in the absence of gravity. Masters Thesis, Department of Mathematics, Lawrence Berkeley Laboratory, University of California, (1986)

Figure Captions

Figure 1: Four container cross sections

Figure 2: Generic cylinder

Figure 3: Cross section of generic cylinder

Figure 4a: Φ terms: bathtub

Figure 4b: Φ terms: trapezoid

Figure 4c: Φ terms: keyhole, $h > 0$

Figure 4d: Φ terms: keyhole, $h < 0$

Figure 4e: Φ terms: non-concentric cylinders

Figure 5: Bathtub

Figure 6: Trapezoid

Figure 7a: Keyhole, $h > 0$

Figure 7b: Keyhole, $h < 0$

Figure 8a: Non-concentric cylinders

Figure 8b: Non-concentric cylinders: detail of Ω^*

Figure 9a: Critical curves: bathtub [$\gamma = 0°(5°)85°$]

Figure 9b: Critical area-ratio curves: bathtub [$A_{crit} = .01, .05(.05).30$]

Figure 9c: Curves of λ = constant: bathtub [$\lambda = .1, .5, 1(1)10$]

Figure 10a: Critical curves: trapezoid [$\gamma = 0°(5°)85°$]

Figure 10b: Critical area-ratio curves: trapezoid [$A_{crit} = .01, .05(.05).30$]

Figure 10c: Curves of λ = constant: trapezoid [$\lambda = .1, .5, 1(1)10$]

Figure 10d: Curves of $\delta = 0$: trapezoid [$\gamma = 0°(5°)85°$]

Figure 11a: Critical curves: keyhole [$\gamma = 0°(5°)85°$]

Figure 11b: Critical area-ratio curves: keyhole [$A_{crit} = .01, .05(.05).30$]

Figure 11c: Curves of λ = constant: keyhole [$\lambda = .1, .5, 1(1)10$]

Figure 12a: Critical curves: non-concentric cylinders [$\gamma = 1°, 5°(5°)85°$]

Figure 12b: Critical area-ratio curves: non-concentric cylinders [$A_{crit} = .01, .05(.05).20$]

Figure 12c: Curves of λ = constant: non-concentric cylinders [$\lambda = .1(.1).9$]

Figure 13: Generic corner.

Figure 14a: $\gamma = 30°$: acute corners critical.

Figure 14b: $\gamma = 60°$: acute corners critical.

Figure 14c: $\gamma = 30°$: obtuse corners critical.

Figure 14d: $\gamma = 30°$: all corners considered.

Figure 15: Decreasing β with α fixed: trapezoid.

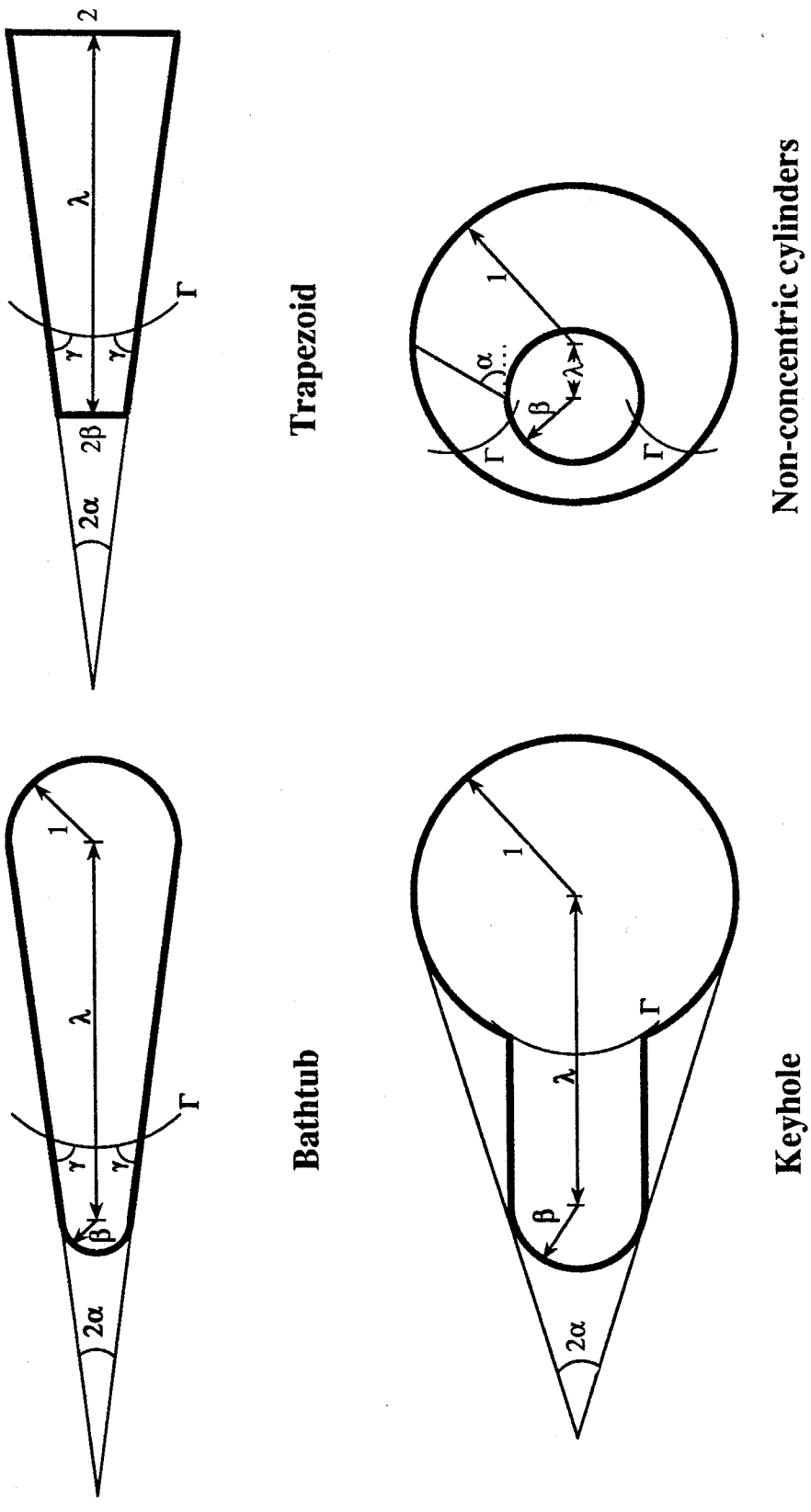

Figure 1 Four container cross sections

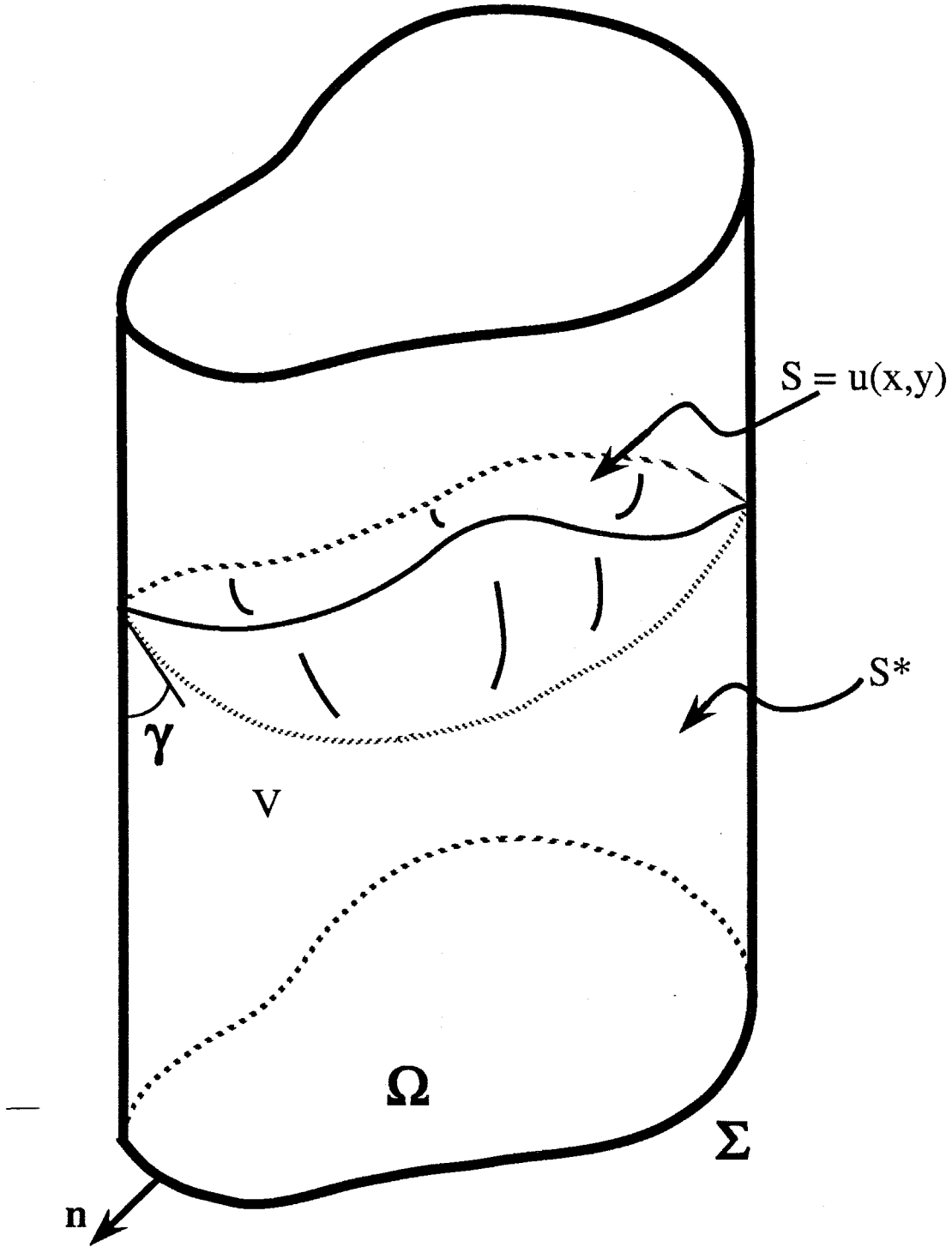

Figure 2 Generic cylinder

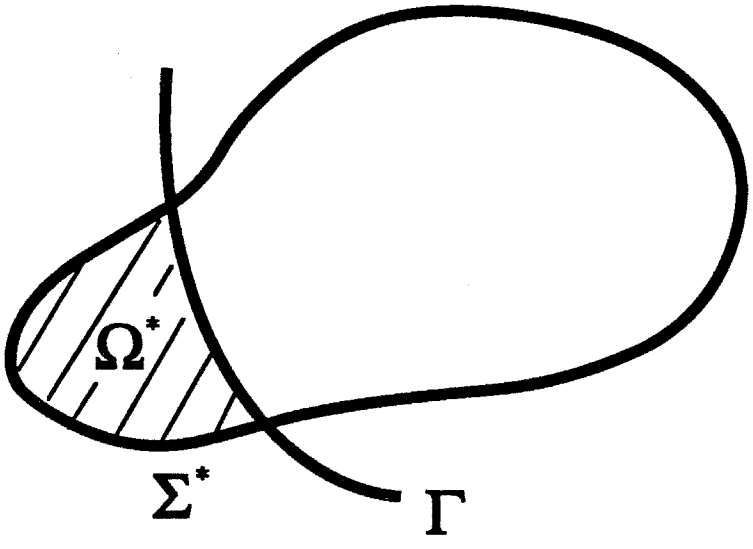

Figure 3 Cross section of generic cylinder

$$\Sigma = 2\left[\,\phi\beta + \frac{(1-\beta)}{\tan\alpha} + \left(\frac{\pi}{2} + \alpha\right)\right]$$

$$\Sigma^* = 2\left[\,\phi\beta + \frac{(T-\beta)}{\tan\alpha}\right]$$

$$\Omega = \phi\beta^2 + \frac{(1-\beta^2)}{\tan\alpha} + \left(\frac{\pi}{2} + \alpha\right)$$

$$\Omega^* = \phi\beta^2 + \frac{(T^2-\beta^2)}{\tan\alpha} - (\theta R_\gamma^2 - T R_\gamma \sin\gamma)$$

$$\theta = \frac{\pi}{2} - \alpha - \gamma \quad ; \quad \phi = \frac{\pi}{2} - \alpha$$

$$\lambda = \frac{(1-\beta)}{\sin\alpha}$$

$$\delta = \frac{(T-\beta)}{\tan\alpha}$$

$$T = \frac{R_\gamma \sin\theta}{\cos\alpha}$$

Figure 4a Φ terms: bathtub

$$\Sigma = 2\left[\,\beta + \frac{(1-\beta)}{\sin\alpha} + 1\,\right]$$

$$\Sigma^* = 2\left[\,\beta + \frac{(R_\gamma \sin\theta - \beta)}{\sin\alpha}\right]$$

$$\Omega = \frac{(1-\beta^2)}{\tan\alpha}$$

$$\Omega^* = \frac{(R_\gamma^2 \sin^2\theta - \beta^2)}{\tan\alpha} - (\theta - \sin\theta\cos\theta)\,R_\gamma^2$$

$$\theta = \frac{\pi}{2} - \alpha - \gamma$$

$$\lambda = \frac{(1-\beta)}{\tan\alpha}$$

$$\delta = \frac{R_\gamma \sin\theta - \beta}{\tan\alpha} - (1 - \cos\theta)\,R_\gamma$$

Figure 4b Φ terms: trapezoid

$$\Sigma = 2\left[\frac{\pi}{2}\beta + h + (\pi - \Theta)\right]$$

$$\Sigma^* = 2\left[\frac{\pi}{2}\beta + h\right]$$

$$\Omega = \frac{\pi}{2}\beta^2 + 2\beta h + (\pi - \Theta) + \beta\cos\Theta$$

$$\Omega^* = \frac{\pi}{2}\beta^2 + 2\beta h - (\theta R_\gamma^2 - \beta R_\gamma \cos\theta)$$

$$\theta = \arcsin\left(\frac{\beta}{R_\gamma}\right)$$

$$\Theta = \arcsin(\beta)$$

$$h = \lambda - \cos\Theta$$

Figure 4c Φ terms: keyhole, h > 0

$$\Sigma = 2\,[\,\phi\,\beta + (\pi - \Theta)]$$

$$\Sigma^* = 2\,\phi\,\beta$$

$$\Omega = \phi\,\beta^2 + (\pi - \Theta) + \lambda\,Y$$

$$\Omega^* = \phi\,\beta^2 - Y\,\beta\cos\,\phi - (\theta\,R_\gamma^2 - Y\,R_\gamma\cos\,\theta)$$

$$\theta = \arcsin\left(\frac{Y}{R_\gamma}\right) \quad ; \quad \phi = \arcsin\left(\frac{Y}{\beta}\right)$$

$$\Theta = \arcsin\,(Y)$$

$$Y = (1 - X^2)^{1/2} \quad ; \quad X = \frac{(1 + \lambda^2 - \beta^2)}{2\lambda}$$

(X,Y) = intersection of two circles: r = β; r = 1

For h > 0 and h < 0

$$\lambda = \frac{(1 - \beta)}{\sin\,\alpha}$$

Figure 4d Φ terms: keyhole, h < 0

$$\Sigma = 2\,[\,\pi\beta + \pi]$$

$$\Sigma^* = 2\,[\,\phi\beta + \Theta]$$

$$\Omega = -\pi\beta^2 + \pi$$

$$\Omega^* = \Theta - (X0)\,Y1 - (\lambda - X0)\,Y2 - \phi\beta^2 - 2\,(\theta R_\gamma^2 - D R_\gamma \cos\theta)$$

$$\theta = \arcsin\left(\frac{D/2}{R_\gamma}\right) \quad ; \quad \phi = \arcsin\left(\frac{Y2}{X2}\right)$$

$$\Theta = \arcsin\left(\frac{Y1}{X1}\right)$$

$$X0 = \frac{-b}{m} \quad ; \quad b = Y1 - m\,X1 \quad ; \quad m = \frac{Y1 - Y2}{X1 - X2}$$

(X1, Y1) = intersection of Γ and outer circle of radius 1

(X2, Y2) = intersection of Γ and inner circle of radius β

$$D = \frac{1}{2}\left((X1 - X2)^2 + (Y1 - Y2)^2\right)^{1/2}$$

$$\lambda = \frac{(1 - \beta)}{\tan\alpha}$$

Figure 4e Φ terms: non-concentric cylinders

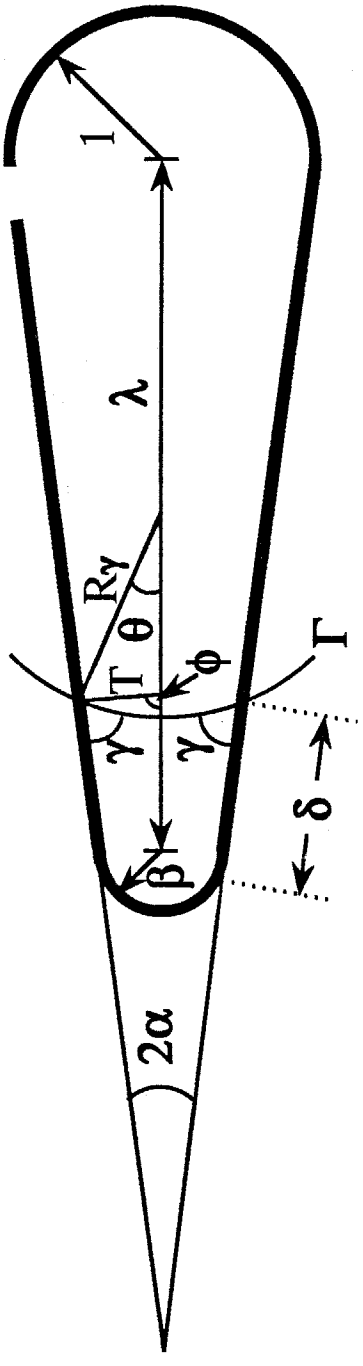

Figure 5 Bathtub

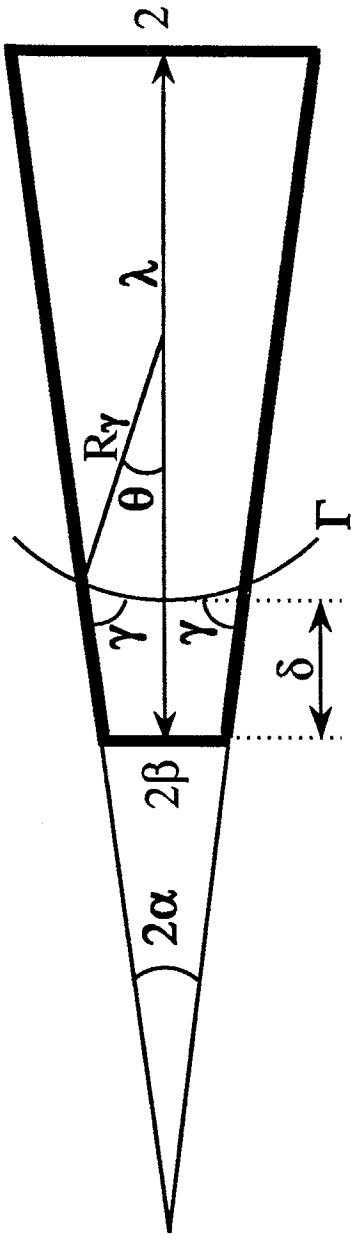

Figure 6 Trapezoid

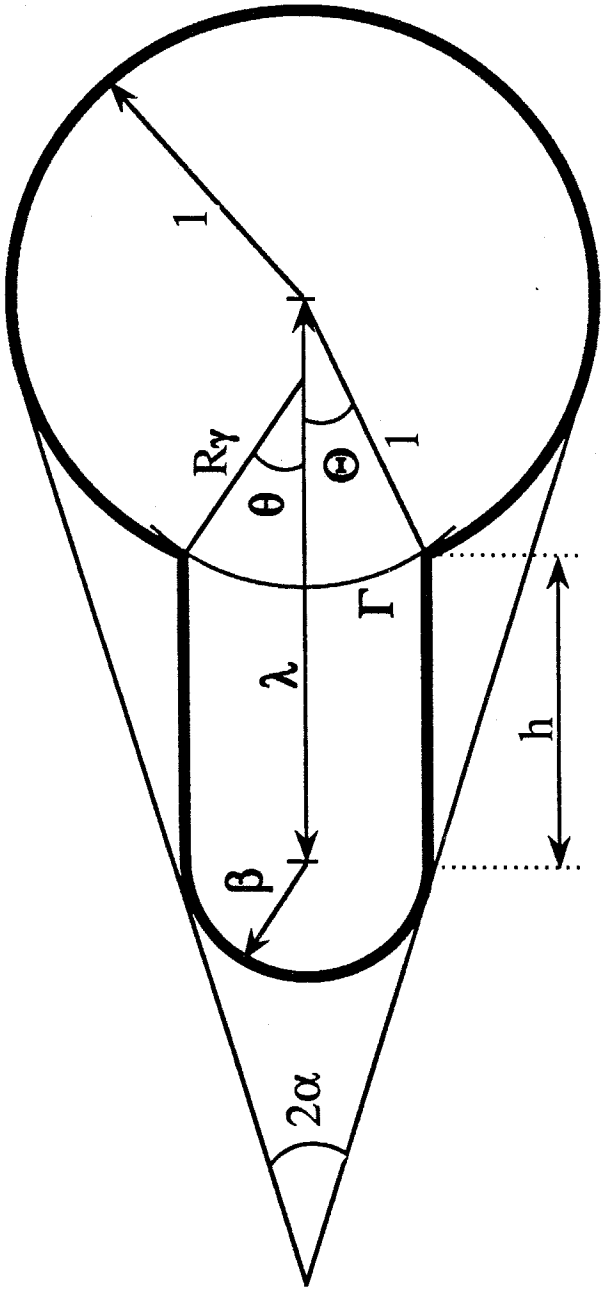

Figure 7a Keyhole, h > 0

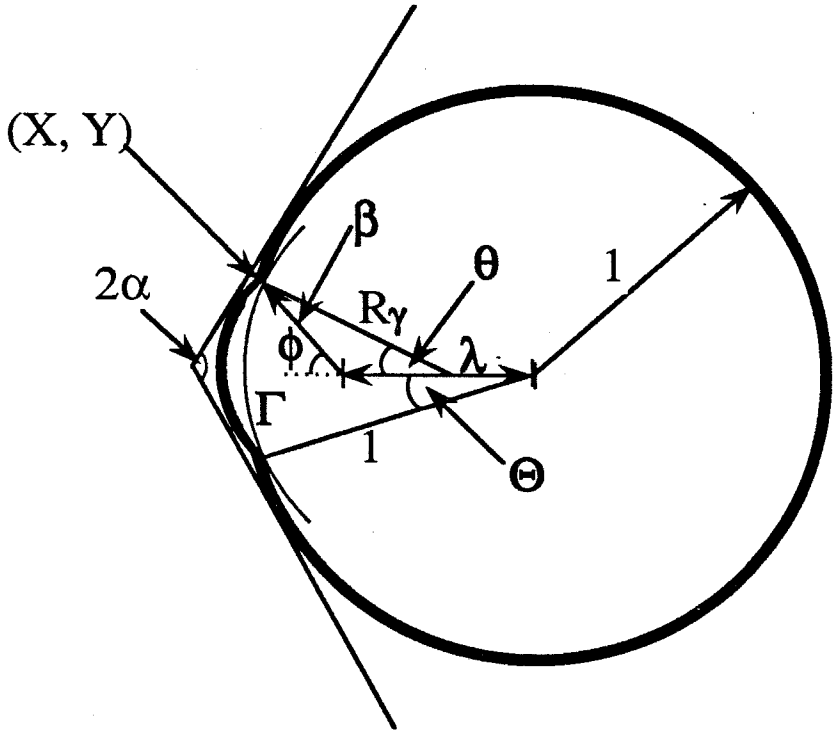

Figure 7b Keyhole, $h < 0$

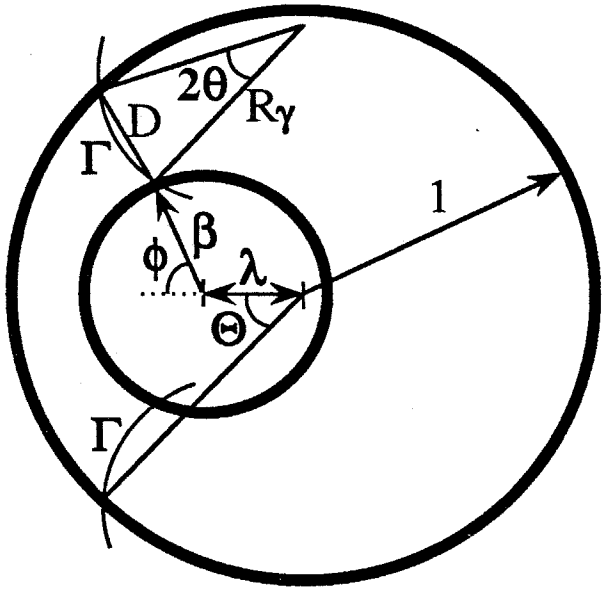

Figure 8a Non-concentric cylinders

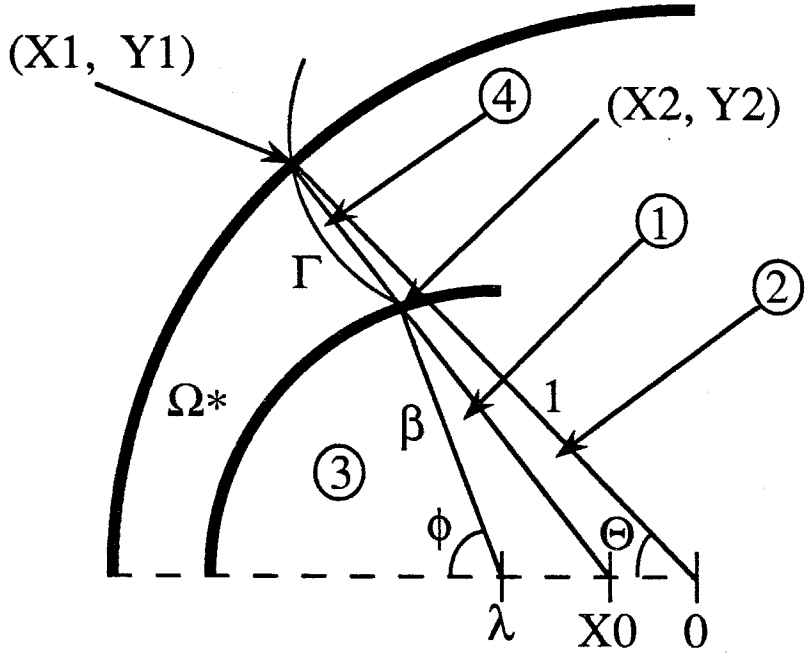

Figure 8b Non-concentric cylinders: detail of Ω*

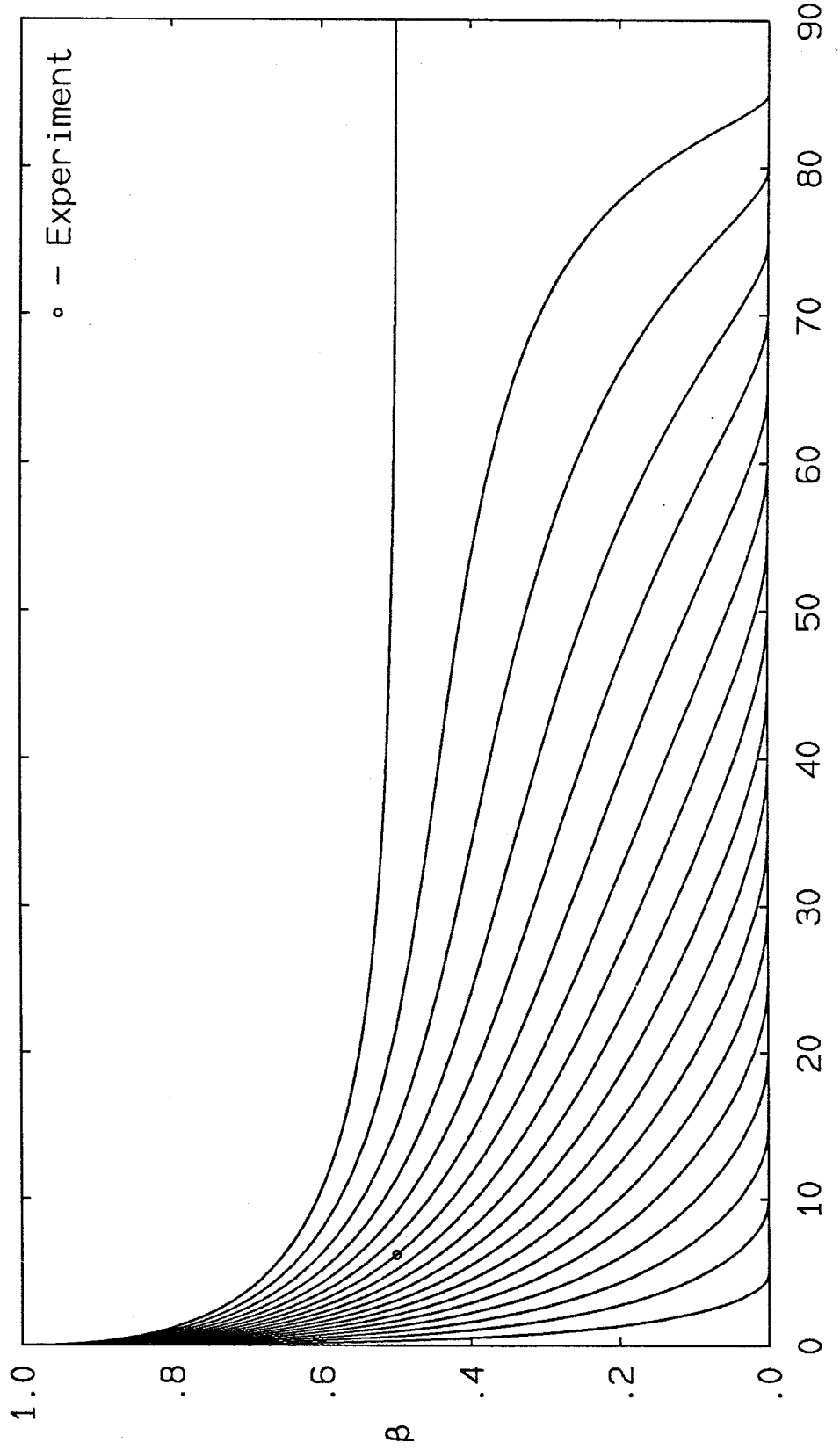

Figure 9a Critical curves: bathtub [γ=0(5)85 degrees]

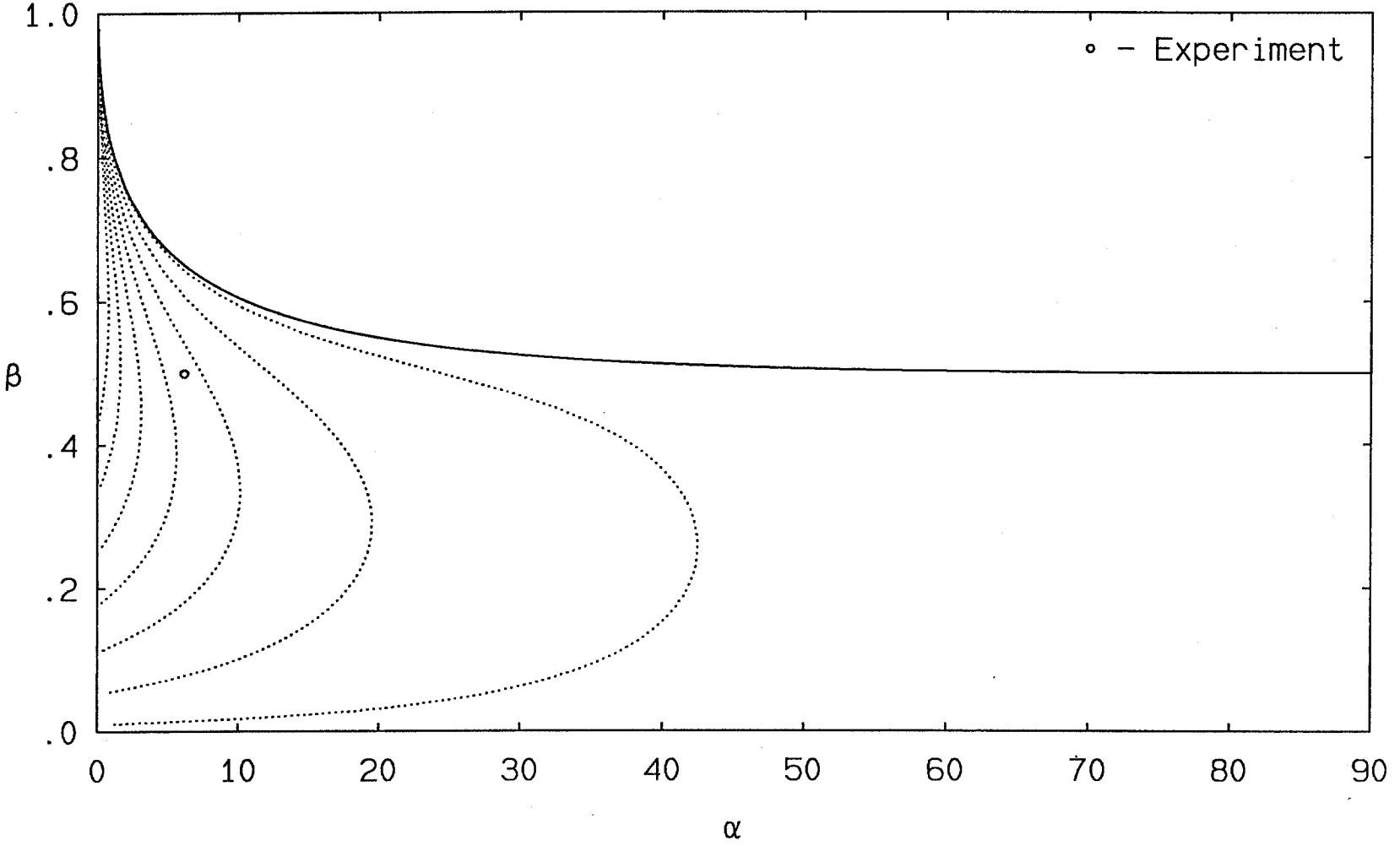

Figure 9b Critical area-ratio curves: bathtub [Acrit=.01,.05(.05).30]

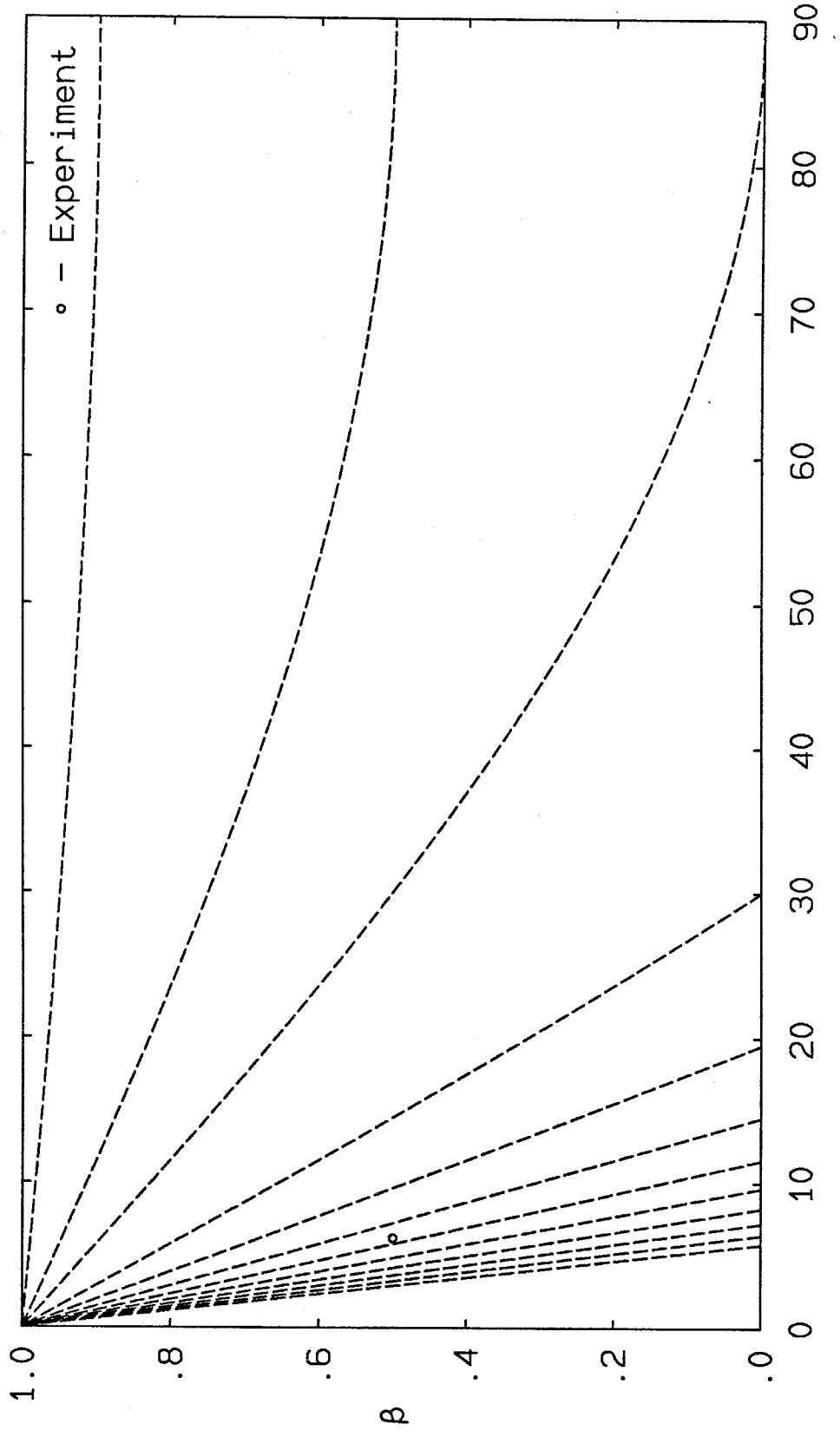

Figure 9c Curves of λ=constant: bathtub [λ=.1,.5,1(1)10]

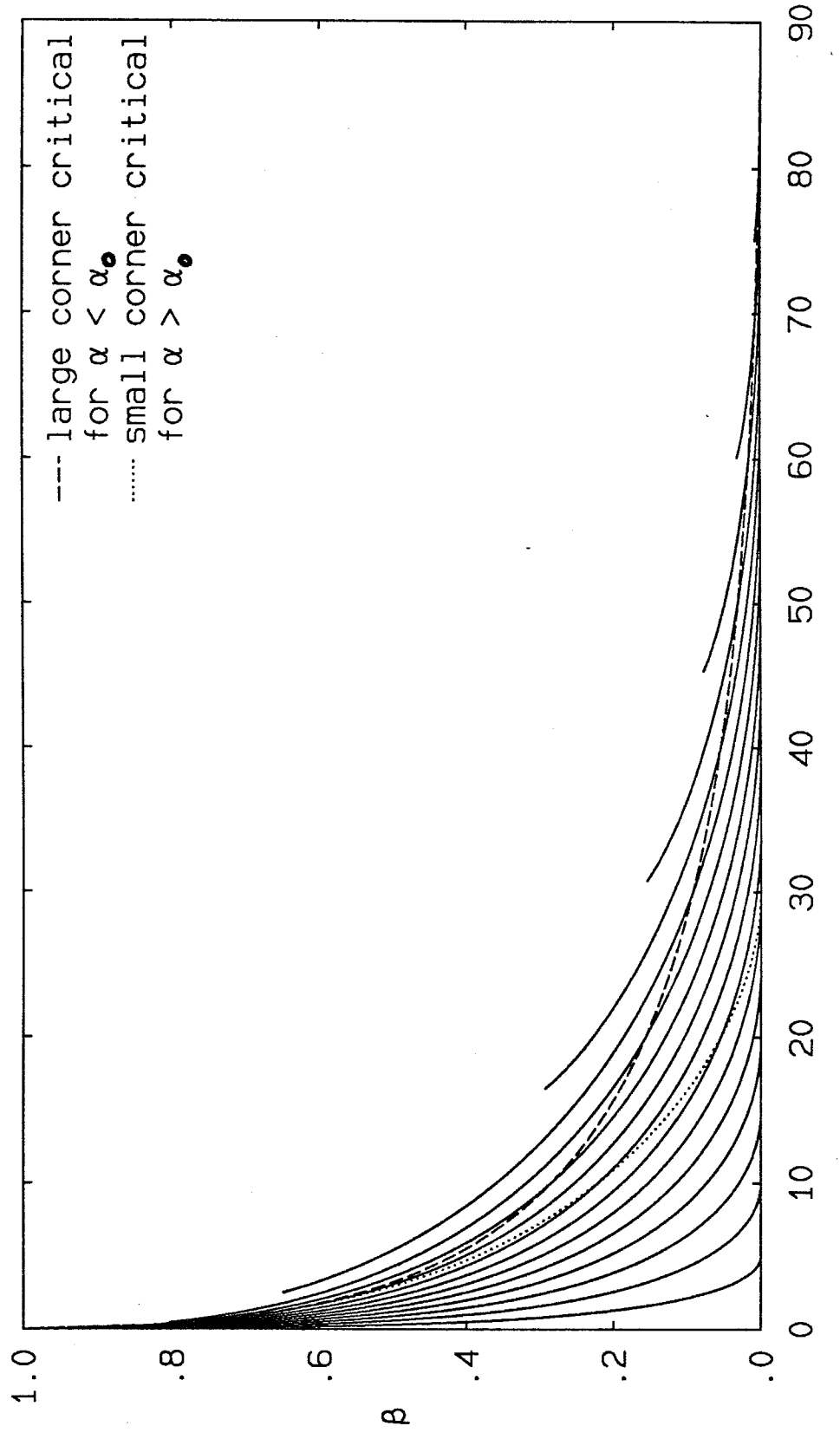

Figure 10a Critical curves: trapzoid [γ=0(5)85 degrees]

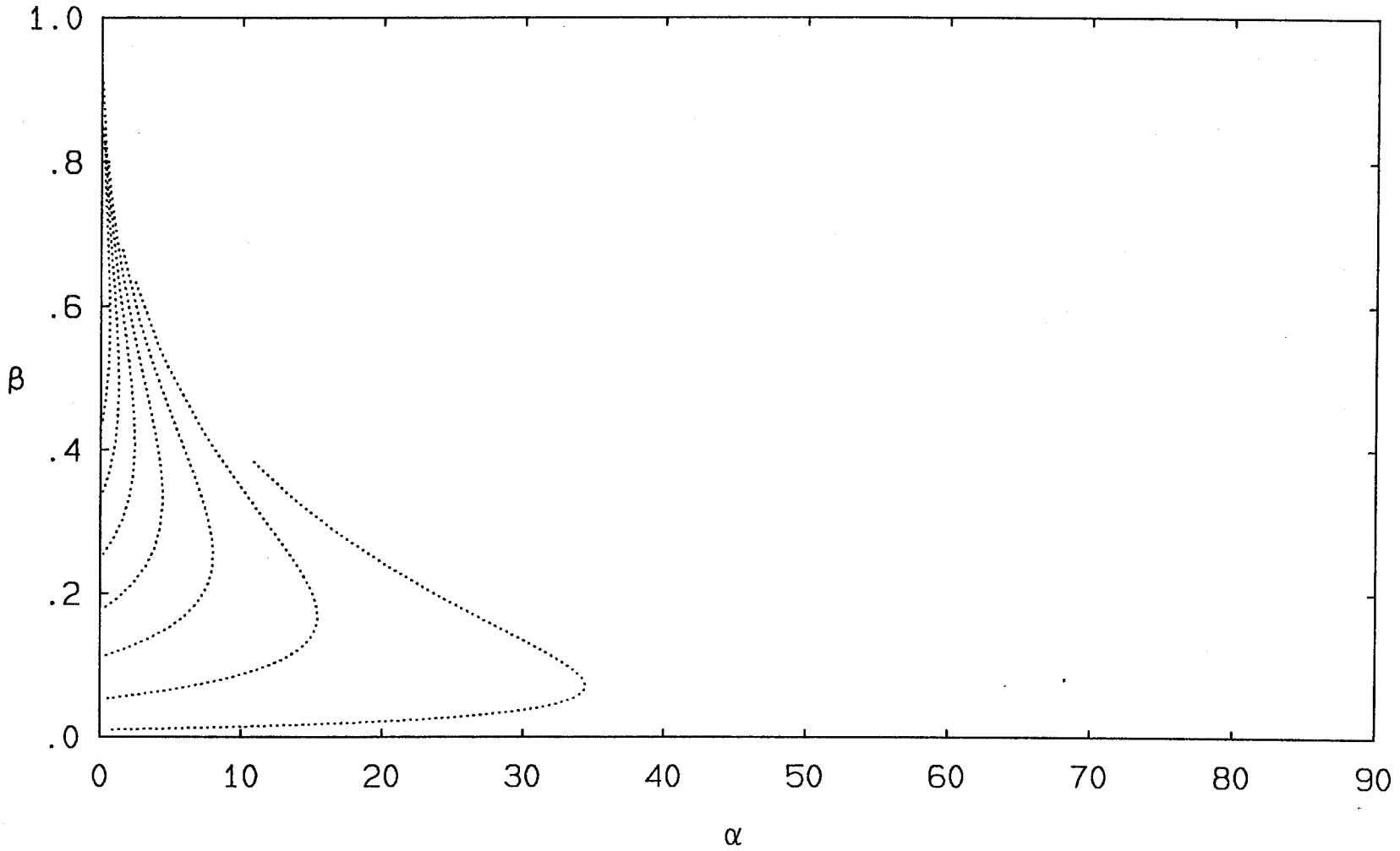

Figure 10b Critical area-ratio curves: trapezoid [Acrit=.01,.05(.05).30]

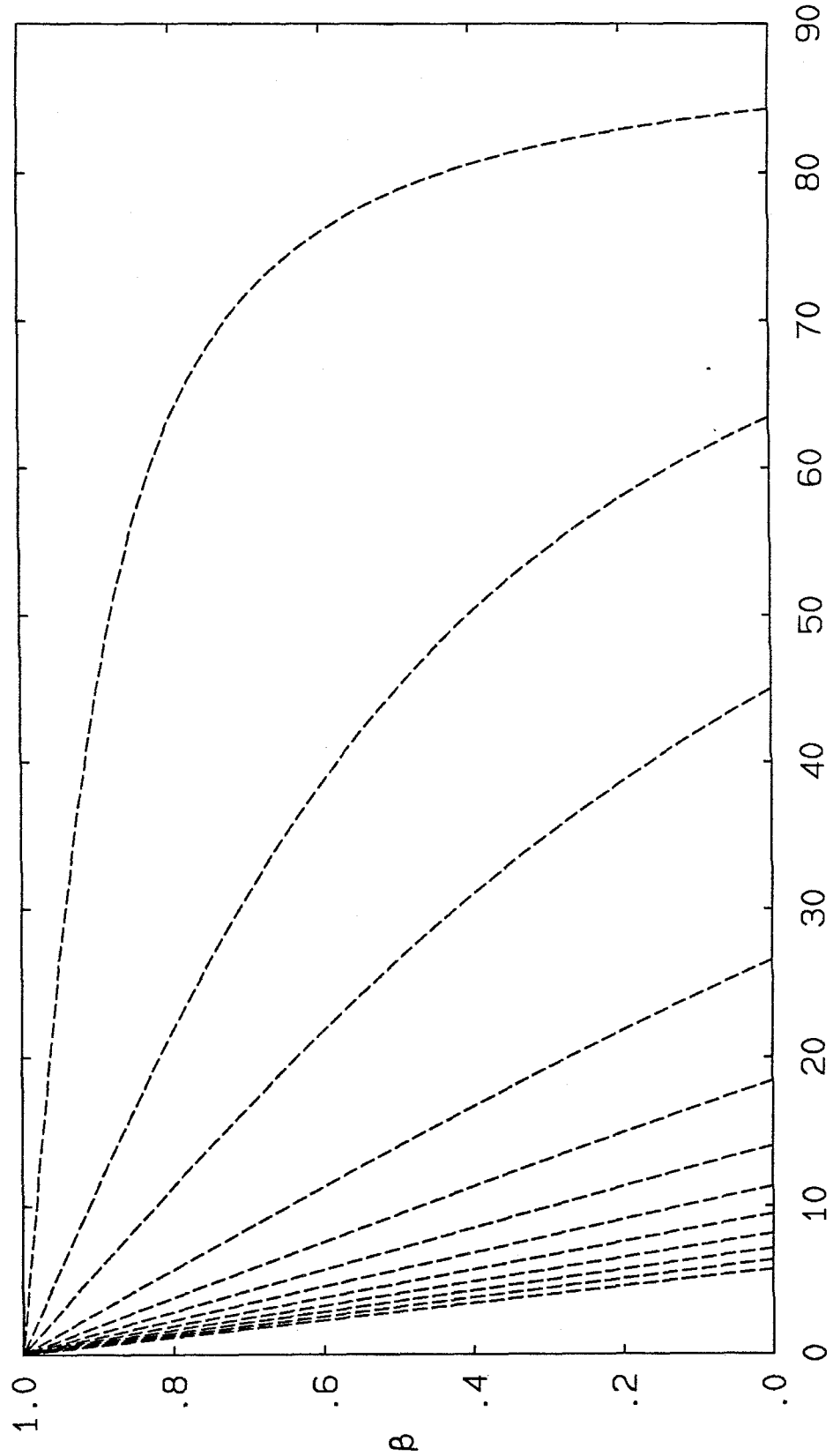

Figure 10c Curves of λ=constant: trapezoid [λ=.1,.5,1(1)10]

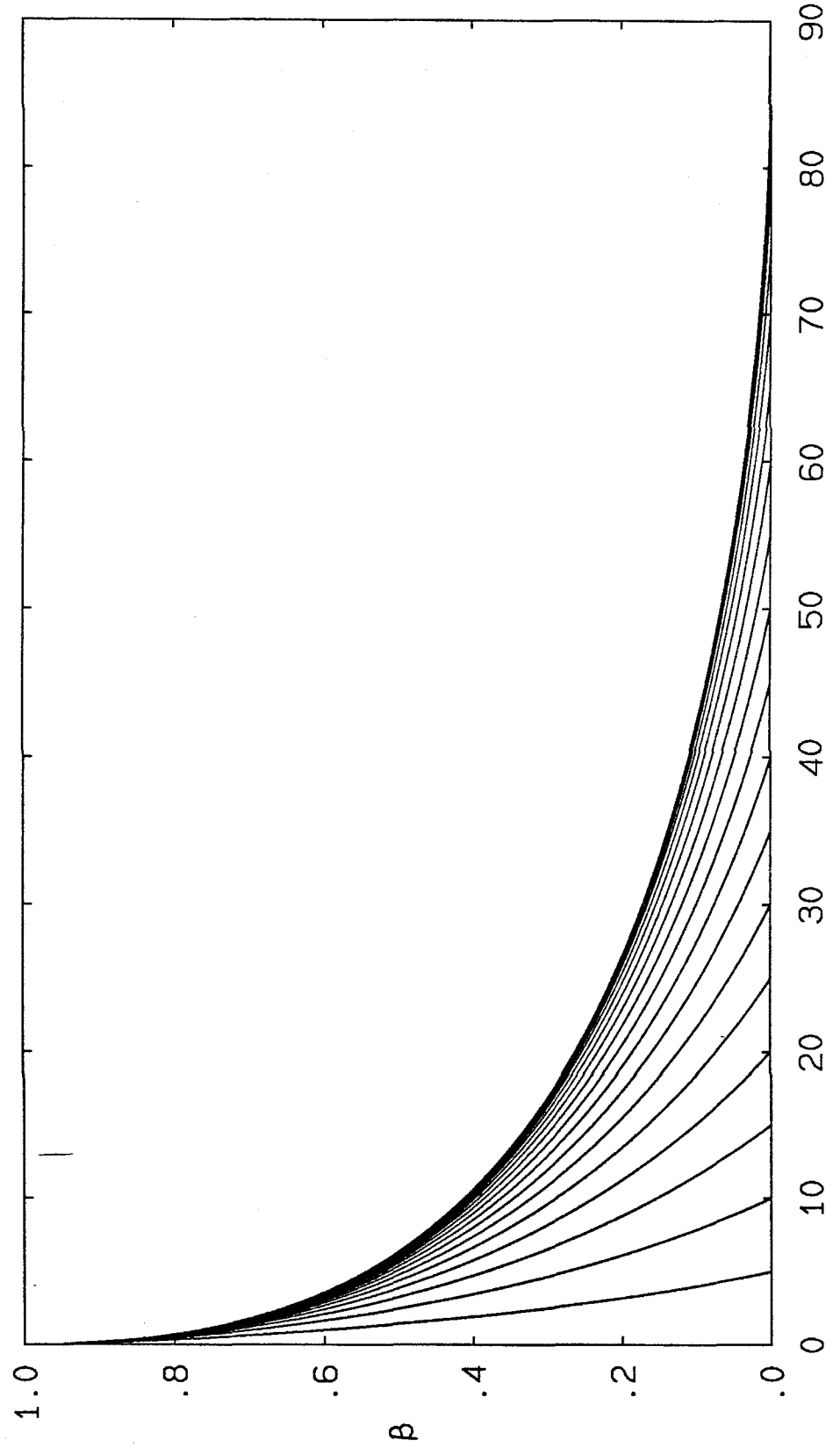

Figure 10d Curves of δ=0: trapzoid [γ=0(5)85 degrees]

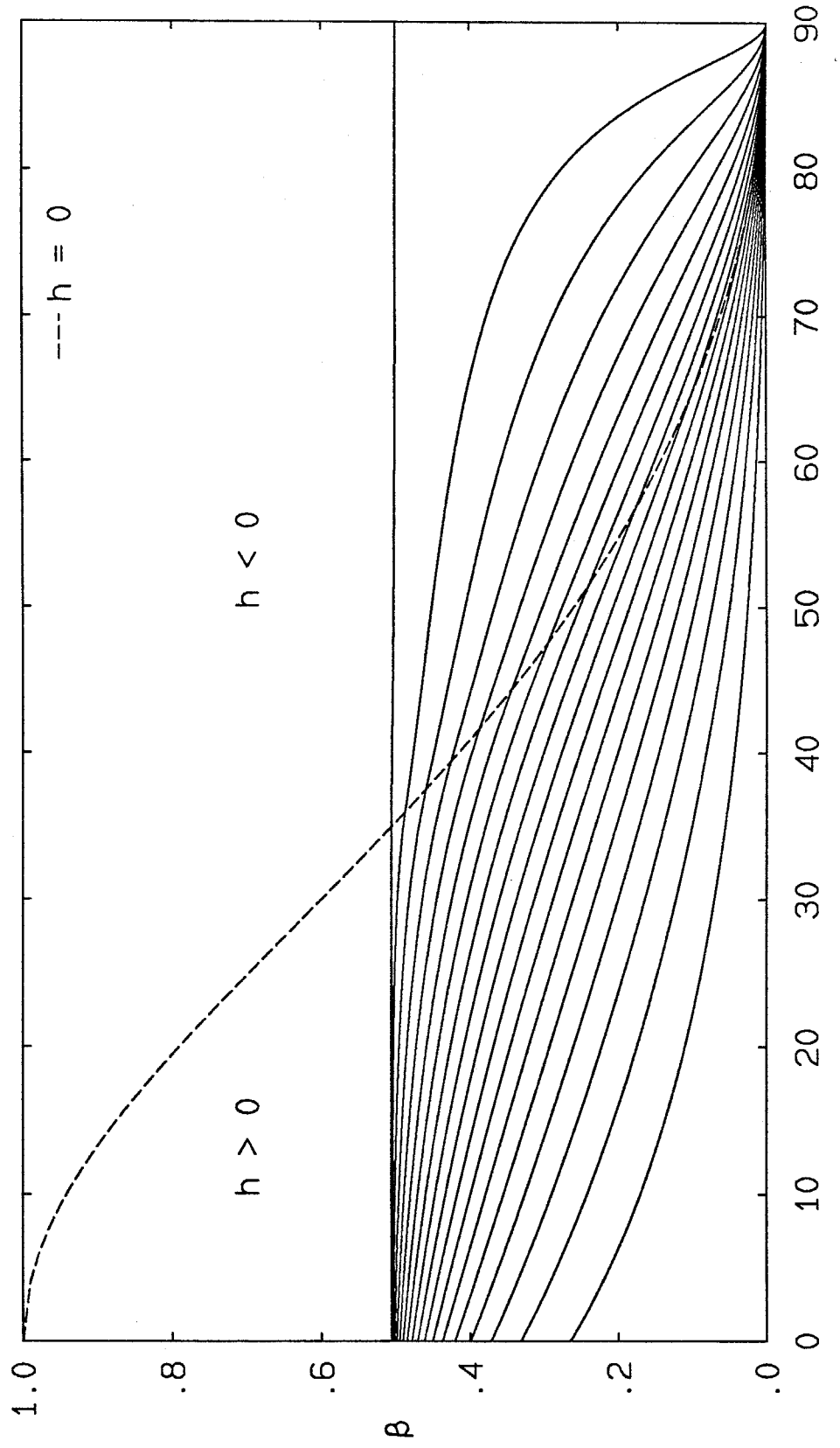

Figure 11a Critical curves: keyhole [γ=0(5)85 degrees]

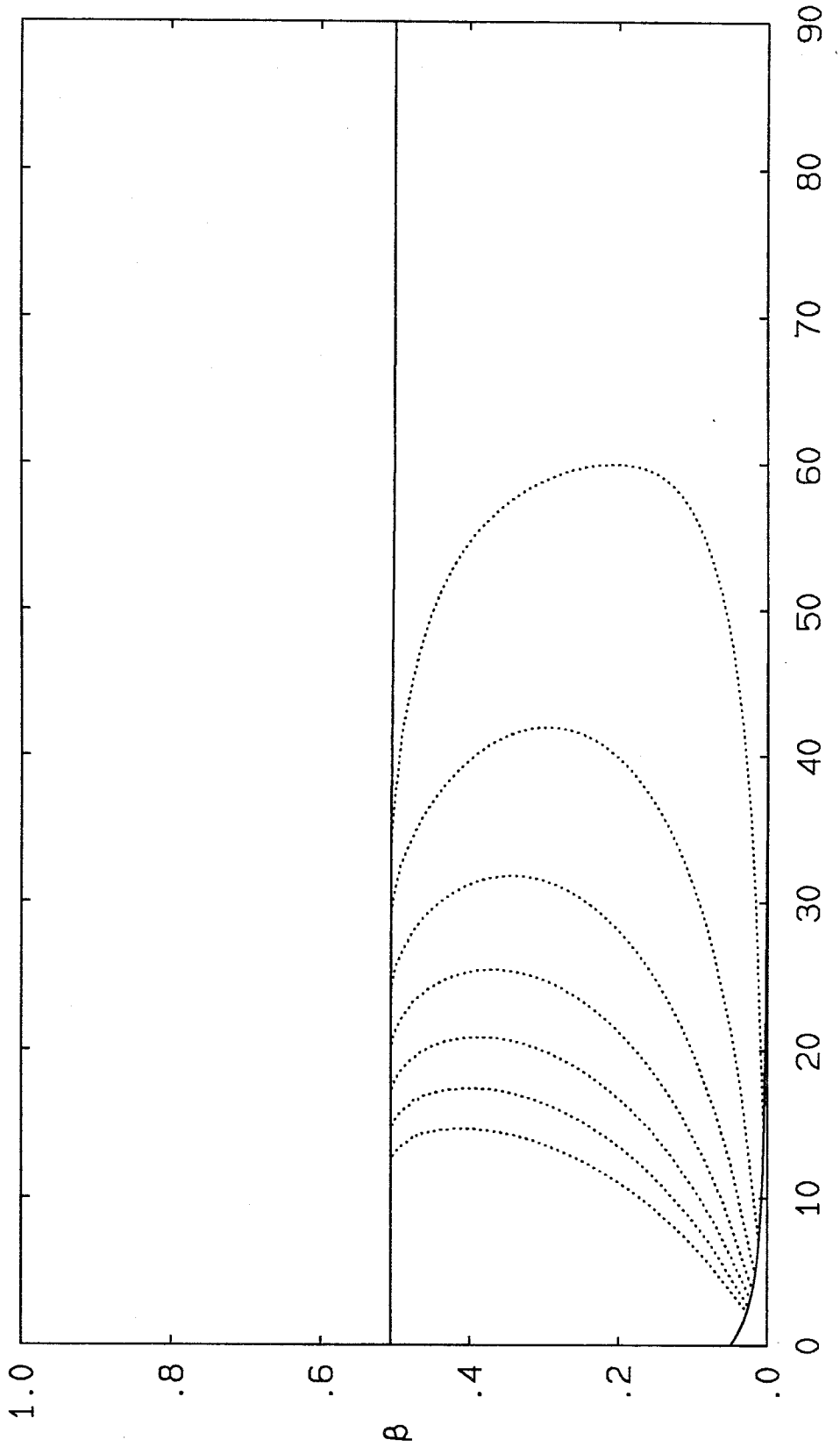

Figure 11b Critical area-ratio curves: keyhole [Acrit=.01,.05(.05).30]

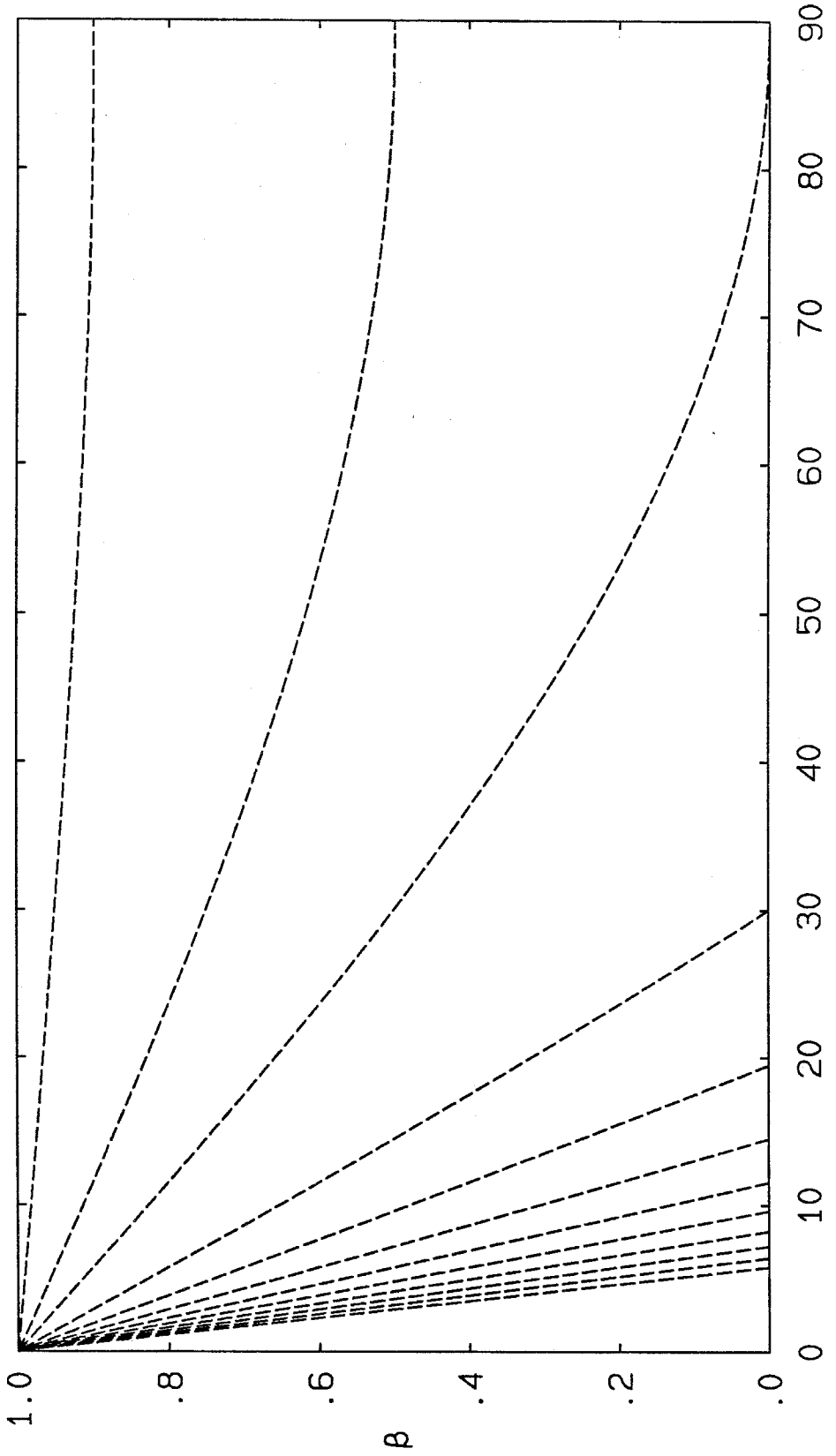

Figure 11c Curves of λ=constant: keyhole [λ=.1,.5,1(1)10]

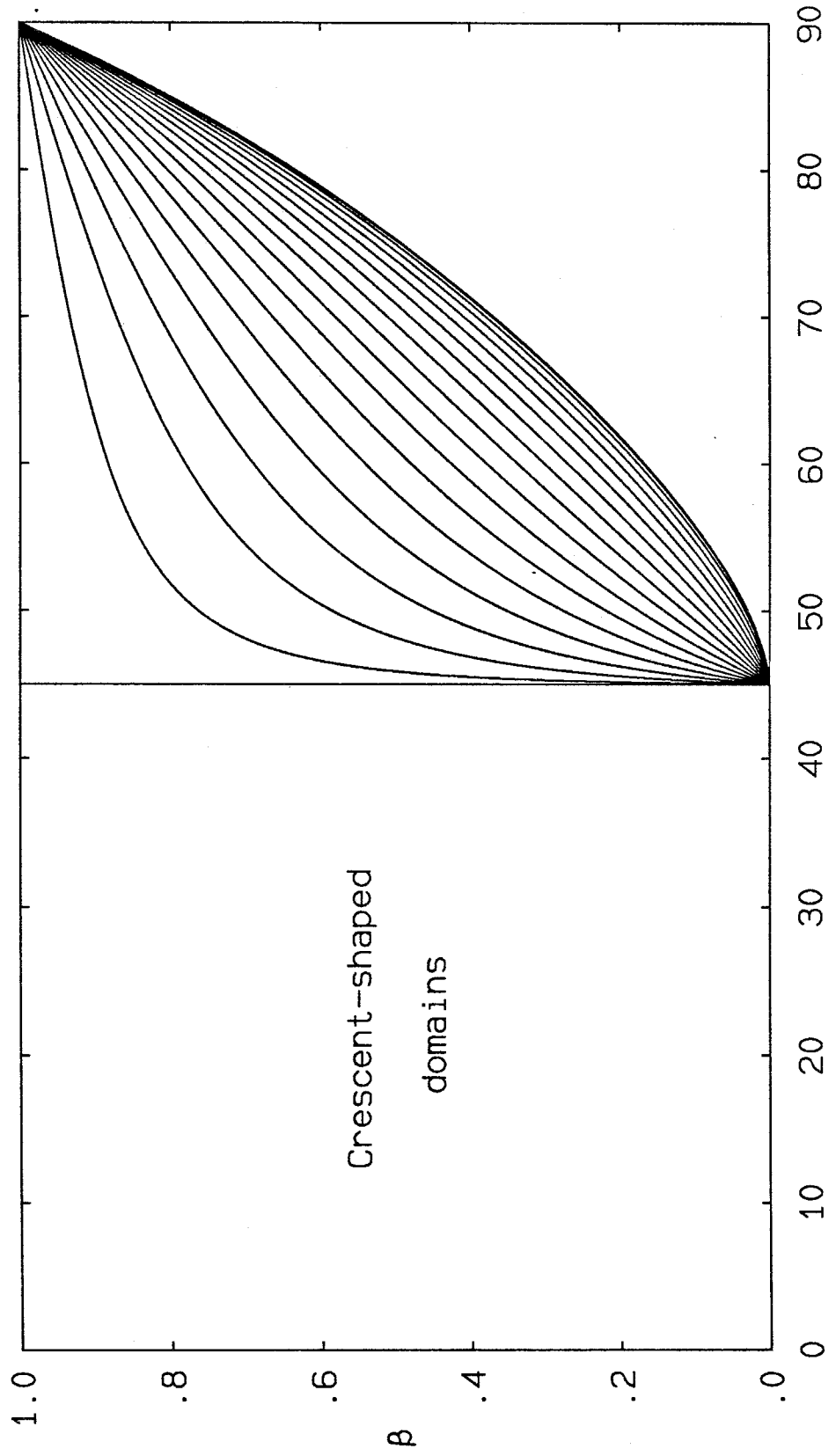

Figure 12a Critical curves: non-concentric cylinders
[γ=1,5(5)85 degrees]

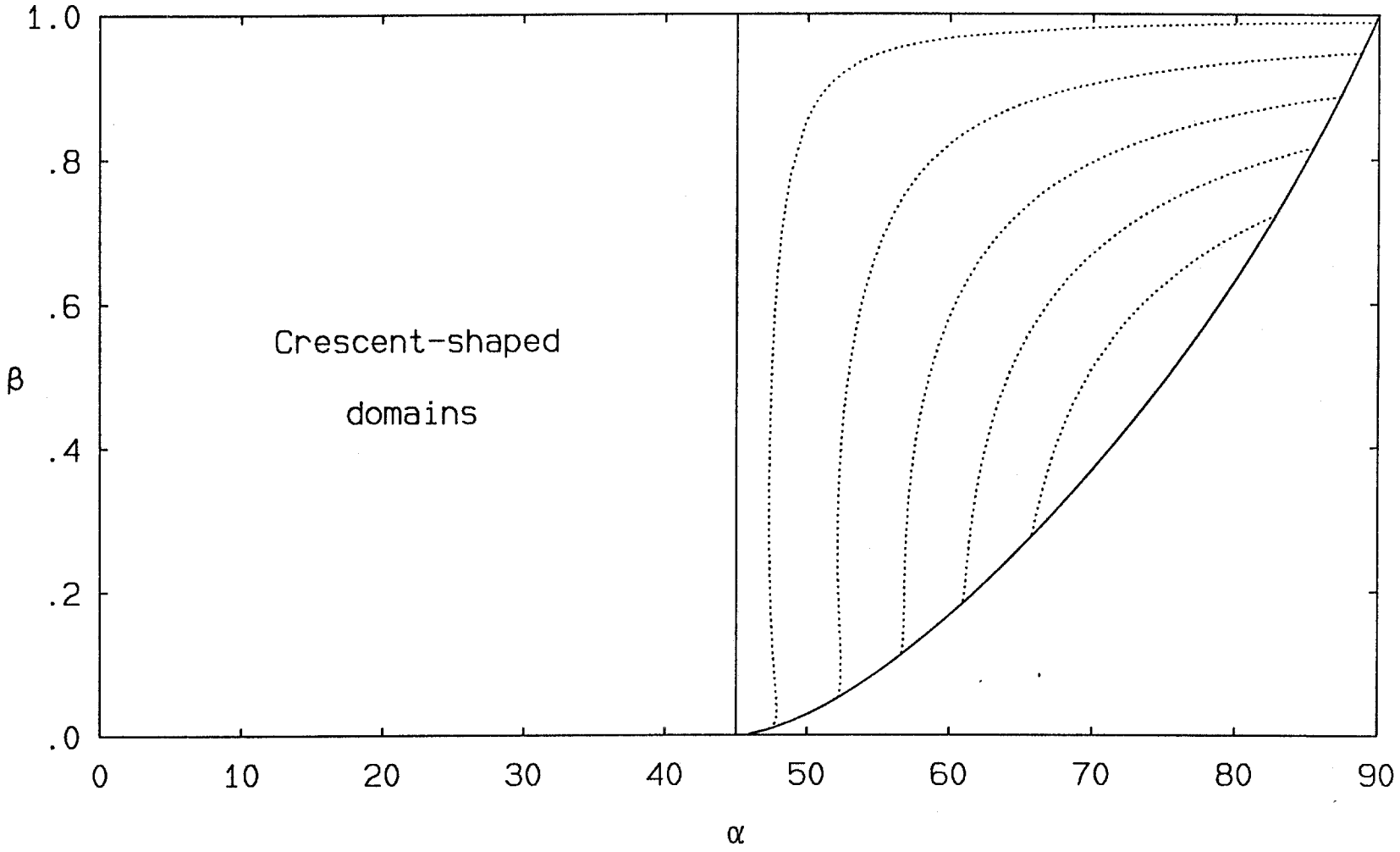

Figure 12b Critical area-ratio curves: non-concentric cylinders
[Acrit=.01,.05(.05).20]

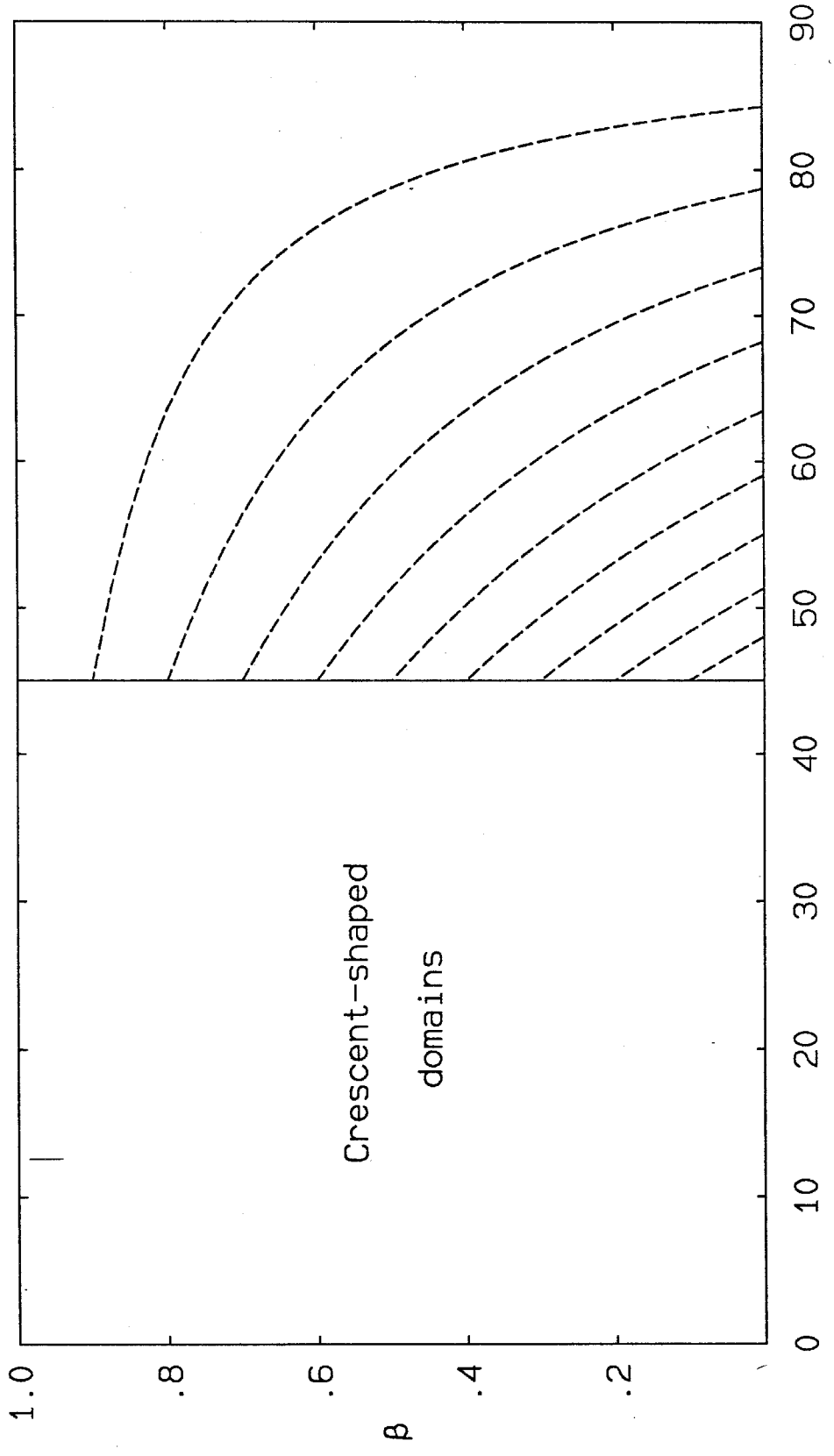

Figure 12c Curves of λ=constant: non-concentric cylinders
[λ=.1(.1).9]]

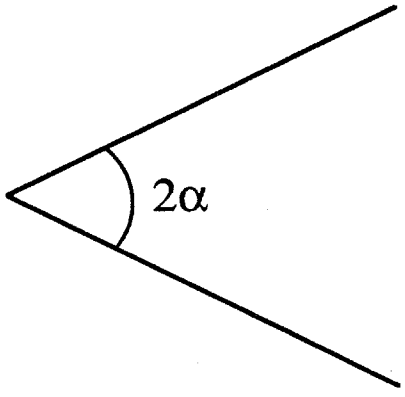

Figure 13 Generic corner

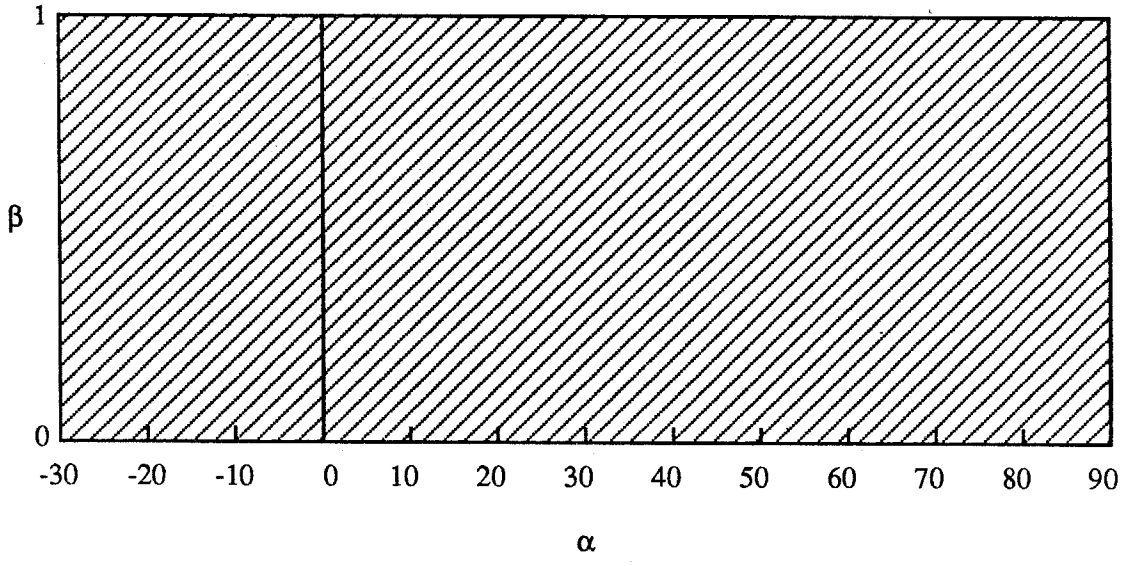

Fig 14a $\gamma = 30$ degrees
(acute corners critical)

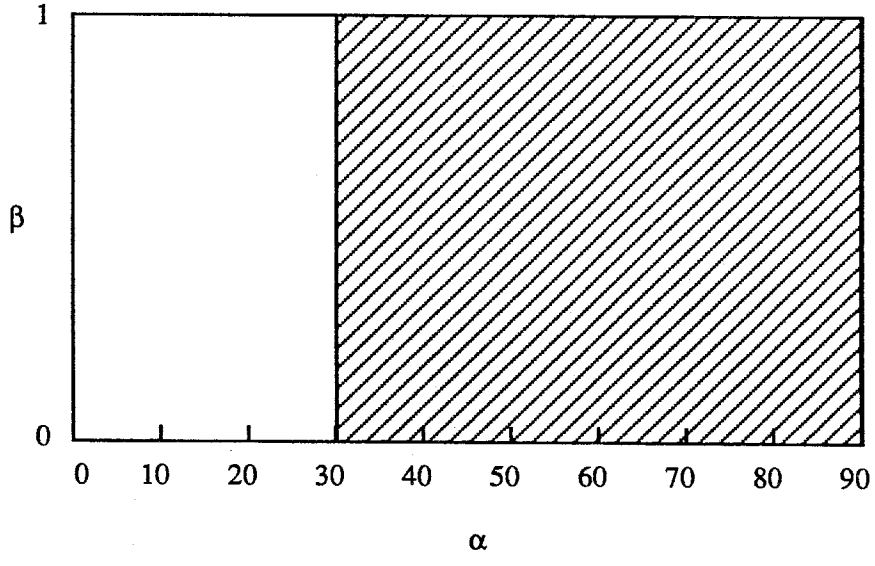

Fig 14b $\gamma = 60$ degrees
(acute corners critical)

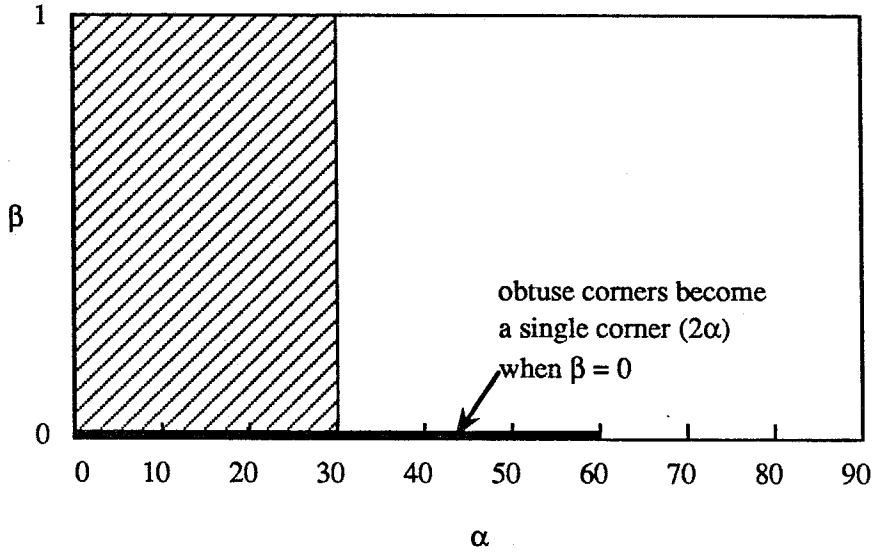

Fig. 14c $\gamma = 30$ degrees
(obtuse corners critical)

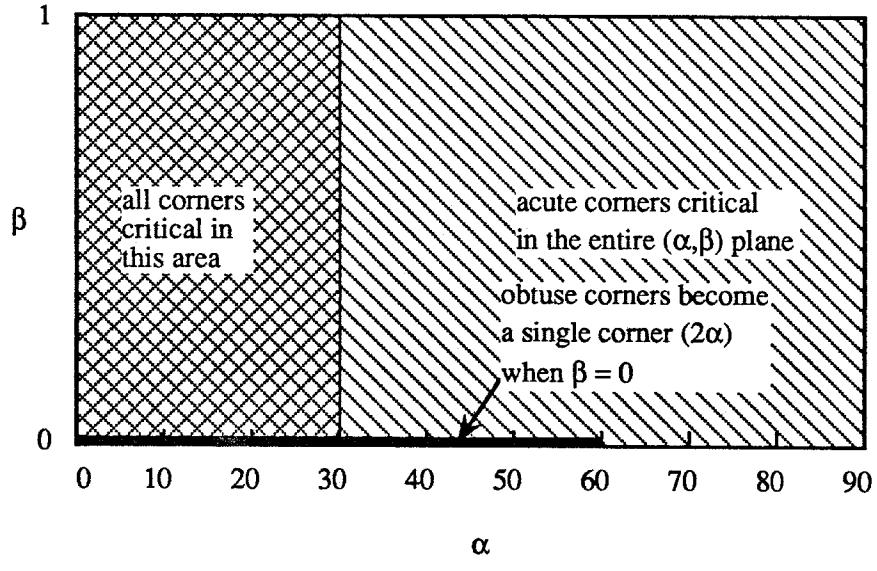

Fig. 14d $\gamma = 30$ degrees
(all corners considered)

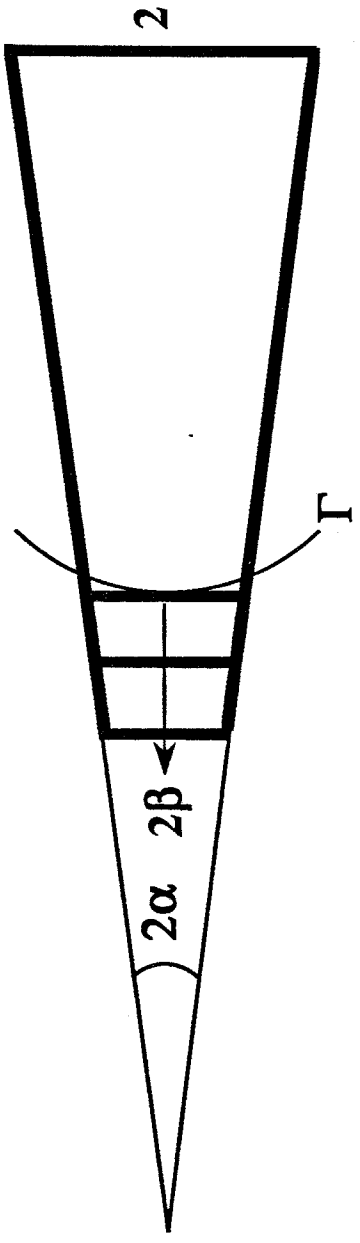

Figure 15 Decreasing β with α fixed: trapezoid

Table 1: Values of β-intercepts for various γ

γ	β
0	0.50647
5	0.50599
10	0.50462
15	0.50241
20	0.49940
25	0.49556
30	0.49089
35	0.48529
40	0.47867
45	0.47085
50	0.46159
55	0.45053
60	0.43715
65	0.42060
70	0.39954
75	0.37150
80	0.33137
85	0.26480
90	0.00000

Chapter V

Dynamic Contact Lines and Angles

G. Smedley and D. Coles
Graduate Aeronautical Laboratory
California Institute of Technology
Mail code: 205-45
Pasadena, CA 91125
U.S.A.

Abstract

The work reported here involves an experimental study of the dynamic contact line, with the intention of making accurate measurements of the contact angle. The contact angle is a critical parameter in the consideration of liquid behavior. A technique based on laser light refraction was developed to measure it. Dynamic contact line experiments were conducted at various velocities, both advancing and receding, using an immiscible liquid pair (nonane/formamide) in contact with glass. An interesting binary behavior of the interface is found that is dependent upon the liquid that is first in contact with the glass plate. Capillary numbers from 4.2×10^{-4} to 8.4×10^{-3} were studied (Contact-line velocities from 0.05 to 1.00 mm/sec).

1 Introduction

The work reported here involves an experimental study of the dynamic contact line, with the intention of making accurate measurements of the contact angle. The literature on this topic reveals an area of research that is plagued by problems of contact angle sensitivity and lack of repeatability (Bikerman 1970, Dussan 1979). The contact angle depends on surface cleanliness, surface roughness, temperature, liquid purity, and other variables, including velocity. The work has involved the design of an instrument for the specific task of measuring the velocity dependence of the contact angle. The apparatus uses refraction of laser light to determine contact angles at the intersection with a transparent solid of the interface between two transparent immiscible liquids.

The technique used is based on the refraction of light at liquid-vapor or liquid-liquid interfaces. In principle, a plate partially immersed in a liquid distorts the interface, which adjusts its shape so as to meet the plate at a prescribed contact angle. If the plate angle is changed, the shape of the surface also changes. At a particular plate angle, called the contact angle, the interface should be horizontal. As light passes through the surface from above, it is refracted. Ray tracing indicates that parallel incident light produces distinctive final light distributions. Fig. 1 depicts three plate angles and three characteristic signatures that the surfaces produce, given that the lower liquid has a higher index of refraction than the upper liquid. If the upper liquid has a higher index, the right and left signatures are interchanged. The dark portion of the signatures lies between the dividing rays that pass on either side of the contact line.

The apparatus, which is described in Sections 2 and 3, employs a motor mounted prism and a lens to produce a uniform parallel scan of laser light. The scan is used to illuminate the interface from above and expose a 1024 element photodiode array below to record the light-intensity signature. The laser scan crosses the array in about 1.4 msec at a repetition rate of 15 Hz. In addition, the apparatus employs a double-acting piston to move the interface at a wide range of speeds, both advancing and receding. The combination of short exposure and reasonably fast repetition rate enables the apparatus to be used to measure dynamic contact angles. The choice of liquids for use in the apparatus is discussed in Section 4. The

experimental procedure is described in Section 5. The data processing, results, and discussion are given in Sections 6 through 8.

2 Experimental Apparatus

The Cell and Rotation Mechanism: The experiments were conducted inside a sealed stainless-steel cell shown in Fig. 2. The inside diameter is 3.000 inches and the inside surface is honed to a 6-8 micro-inch finish. Optical windows, 6 mm thick, on the top and bottom of the cell provide laser-scan passage through the cell. The windows are sealed against internal pressure by spring-loaded teflon face seals and against internal vacuum by back-up rubber O-rings. A glass plate, 50 mm square and 6 mm thick, clamped to a rotatable shaft, provides the solid surface for the study of contact-line and contact-angle phenomena. The shaft passes through the cell from one side to the other with spring-loaded teflon seals and back-up rubber O-rings for sealing. All wetted surfaces are either stainless steel, glass, or teflon.

The angular range of the glass plate is 90°, from perpendicular to parallel with the incoming laser scan. A commercially available 100:1 elliptical-bearing reducer (Harmonic Drive Model HDUS-18-100) provides the means for changing the angle of the glass plate. The output shaft of the reducer is coupled to one end of the shaft supporting the glass plate. A handwheel, a marked dial (100 divisions), and a rotation counter on the input shaft together provide an angular positioning accuracy better than 0.036° for the glass slide. The backlash of the reducer is quoted by the manufacturer to be less than 0.033°.

Double-acting Pistons: The double-acting stainless-steel piston assembly shown in Fig. 3 is employed to displace equal volumes of fluid in order to move the interface vertically inside the cell. The piston bore and the cell bore were honed as one solid tube prior to machining into individual pieces, to ensure that the inside diameters were identical. Once again seals for internal pressure are spring-loaded teflon, and seals for internal vacuum are rubber O-rings.

The piston rod, which is attached to a piston at each end, is itself attached to a precision linear traverse (Aerotech, Inc. Model ATS303M). One revolution of the input shaft to the traverse moves the piston 2 mm with an accuracy of 1 micron/cm, with a total range of 75 mm.

A microstepper motor (Compumotor Corporation Model LE57-83) is used to drive the input shaft. The stepper motor has 25000 steps/rev, with an accuracy of 0.08°. The stepper motor is controlled by a computer over an RS-232 interface to a Compumotor 2100-1 indexer. A check on the movement of the traverse is made by employing a long range (5 inch) Starret dial indicator. Fig. 3 shows its position along with the traverse and motor.

Optical Bench: An optical bench was designed specifically for these experiments. The design employs three shelves for the location of laser, optics, mechanical components, sensors and scanning motor (Fig. 4). The cell and double-acting pistons are located on the second shelf, to accommodate transmitting the laser scan vertically through the cell and sensing the light intensity distribution on the lower side. The laser scan is produced by a prism mounted on the shaft of a hysteresis synchronous motor (Hurst Model HB 900 RPM) located on the upper shelf. The polarized light (λ = 632.8 nm) from a He-Ne laser (Spectra-Physics Model 120) is focused and located on the reflecting surface of the prism using lens 1 and the periscope. A small portion of the total arc of laser light is intercepted by lens 2, which is adjusted to produce a parallel scan. The large prism directs the scan down through the cell to the photodiode array on the lower shelf.

A beam splitter, located just after lens 2, redirects half of the light toward lens 3, where it is focused onto the laser-power monitor. This arrangement enables synchronous measurement of the laser-light intensity that exposes the photodiode array. Adjustment of the intensity of the polarized laser light, to prevent saturation of the photodiode array, is achieved by adjusting the polarization angle of the single polarizer on the top shelf.

Liquid Reservoirs and Plumbing: The liquids are kept in commercially available 500ml HPLC reservoirs (Kontes Article 953980-0502) prior to being transferred into the piston/cell system. These reservoirs facilitate storage under nitrogen. The plumbing used to connect the reservoirs, pistons, and cell is constructed of precision 316 stainless-steel pipe fittings and teflon valves (Fig. 5). A flexible connection between the pistons and cell is provided by including some flexible teflon tubing in the plumbing. Connection to the reservoirs is also through flexible teflon tubing.

3 Instrumentation

Photodiode Array: A photodiode array (EG&G Reticon Model 1024G) is used to detect the light-intensity distribution of the laser scan after passing through the cell. The one-dimensional array has 1024 elements, each 25 micrometers wide. The sensitivity of the array, as rated by the manufacturer, is 2.5 picoamps/microwatt/cm^2. However, the uniformity of response is ±14 percent. The saturation exposure is 1.8 microjoules/cm^2. The array is accompanied by two circuit boards (RC-100B and RC-106) that produce a sample and hold boxcar output. Two inputs, +5 and -14 volts d.c., from a triple-output power supply (Hewlett Packard Model 6236A) were originally used to power the array boards. Noise reduction was achieved by substituting a 5-volt d.c. supply to the array board (RC-106) from three large dry cells in series. This 5-volt supply is used by the board to recharge the photodiode array during each read/recharge cycle. The array requires two signal inputs, a clocking signal and a start pulse. The outputs from the array that are used in this application are the sample-and-hold boxcar signal and the blankout signal. The boxcar signal records the intensity of light on each pixel of the array. The blankout signal is low during the output of the boxcar signal on the video line (Fig. 9). More information about the instrumentation is given in the section that addresses system integration on the next page.

Laser-Power Monitor: The laser-power monitor consists of a phototransistor (Siemens BPX-81) configured according to Fig. 6. For best stability and reduced noise, a 1.5-volt dry cell is used to provide power for the monitor. The signal produced by this monitor is a reference for the temporal variation of the laser power.

The Data-Acquisition System: Contact-line motion and data acquisition are controlled by a laboratory computer system (Data Translation Lab-Datax model DT4236). The system has a DEC LSI-11/23 CPU with 256 kilobytes of RAM and a Winchester hard/floppy disk storage system (Scientific Micro Systems model FWT01177) with 35.6 megabytes of storage available on the hard disk and 1 megabyte of storage available on the floppy. User interface is provided through a DEC VT240 graphics terminal and a Diablo 630/ECS printer. The computer also contains a fast floating point processor (DEC FPF11), a line time clock (DEC KPV11-A), four serial interface ports (DEC DLV11-J), and several data-acquisition boards;

1. 8-channel 12-bit A/D converter (DT3382)
2. 2-channel 12-bit D/A converter (DT3371)
3. Programmable real-time clock (DT2769)
4. 32-line parallel digital I/O (non-DMA) (DT2768)
5. 32-line parallel digital I/O (DMA) (DRV11-B)
6. IEEE-488 GPIB interface (DT2791)

System Integration: It is useful to refer to the block diagram of the system in Fig. 7 and the associated timing diagrams in Fig. 8 and Fig. 9 for the following discussion. The 200 kHz clock pulses, used for the entire experiment, are generated by the programmable real-time clock (DT2769). The start pulses are produced by two phototransistors, mounted inside the box that houses the rotating prism, on the top shelf of the optical bench (Fig. 10). As the laser beam passes across each phototransistor, a TTL pulse is generated.

The motor that creates the laser scan rotates at 900 rpm; therefore, one rotation is completed in approximately 66 msec. During this time, the laser power is measured synchronously with the exposure of the Reticon array, the Reticon array is read, and the data are sent to the disk. Due to slow disk access time, it is necessary to double buffer the output to disk; take one scan and send it to disk while taking the next one.

Two digital outputs, Cntrl 1 and Cntrl 2 from the D/A converter, are used to clear and load the digital long delay. As the beam passes phototransistor 1 (Figs. 7, 10) the computer and the long-delay box are notified by a negative going TTL pulse. Software is used to prepare the A/D converter for the laser-power monitor data on channel 1. Meanwhile, the pulse is synchronized with the clock and used to start the long-delay box, which counts clock pulses to create a delay long enough to allow the laser scan to reach the scan aperture. The laser-power-gate pulse is then switched low to allow the A/D trigger to pass long enough for the A/D converter to record the laser power synchronously with the exposure of the Reticon array. After recording the laser power, software is used to prepare the A/D converter for the Reticon array data on channel 0. The second start pulse, created by phototransistor 2, is synchronized with the clock and sent to the Reticon array. The Reticon simultaneously outputs a low blankout signal and the video data. The blankout signal is used to gate the A/D trigger pulses so that the A/D converter can

record the array output. The A/D converter, which samples once per trigger pulse, takes data at 200kHz only while the array board is sending its video box-car signal. The trigger signal to the A/D board is delayed by approximately one half of a clock period to avoid sampling the switching noise on the box-car signal (Fig. 9). This delay also causes the first pixel to be missed by the A/D converter, however, 1024 values are still recorded. The last recorded value, always near 0, is used as a sychronization indicator. The data acquired from the laser-power monitor and the Reticon array are written to the disk while the next scan is being recorded.

Synchronization of interface motion and data acquisition is achieved by software control. The piston motion is started using the RS-232 interface and data acquisition is initiated after a variable delay loop in the software is completed. This delay is determined by counting the ST2-trigger inputs from phototransistor 1. This delay allows the interface to accelerate to speed and to come into view before data are collected, thus minimizing the number of empty frames that are recorded. The software programmable delay is also useful for the careful timing of delays between recorded scans for generating longer time series.

4 Liquid Pair Decision

The immiscible liquid pair that was used in the apparatus was chosen from Smedley and Coles (1990). Finite time and money would not allow more than a one of the 121 pairs listed in the table to be tested.

To facilitate the study of the interface shape near a moving contact line, the scale of the region of interest should be maximized. The capillary length δ is a suitable choice of length scale;

$$\delta = \left[\frac{\sigma}{\Delta\rho\, g} \right]^{1/2} \tag{1}$$

Consider a contact line in steady-state unwetting motion (Fig. 11), where the length scale δ is a rough measure of the distance from the contact line to the horizontal liquid surface. An arc of radius δ is drawn that encompasses a volume/unit length $\delta^2\gamma$ of liquid. The shear force acting on this volume of liquid is

$$F_\tau = \delta\tau = \delta\mu\frac{U}{\Delta} \tag{2}$$

where Δ is the thickness of the contact region. Assume that the bulk liquid moves at a characteristic velocity U roughly parallel to the solid surface and that $\Delta \approx \delta \sin\gamma$. Therefore,

$$F_\tau \approx \frac{\mu U}{\sin\gamma} \tag{3}$$

The force that produces this motion is the surface-tension force per unit length,

$$F_\sigma = \sigma\cos\gamma \tag{4}$$

In steady-state motion the surface-tension force and the shear force should be balanced, the wetting force is neglected. Thus

$$\sin 2\gamma \approx \frac{\mu}{\sigma} U \quad \text{(the capillary number)} \tag{5}$$

This relationship suggests $\gamma = f\left[\frac{\mu}{\sigma} U\right]$ as measure of the velocity dependence of the contact angle near U = 0. A generic plot of this relationship might look like the one shown in Fig. 12. Provided this non-dimensionalization is the proper one for this problem, the above argument indicates that better resolution of the transition can be obtained by minimizing $\frac{\mu}{\sigma}$ through a careful choice of liquids. If results regarding the behavior at the higher values of $\frac{\mu}{\sigma} U$ are wanted, it may be best to choose a liquid pair with a large $\frac{\mu}{\sigma}$. To recapitulate, liquids that facilitate the study of interface shapes have large capillary length (δ) and small $\frac{\mu}{\sigma}$. To maximize δ, $\frac{\sigma}{\Delta\rho}$ must be maximized. The average viscosity ($\bar{\mu}$) of the liquid pair is used for μ. In addition, a reasonable difference in the index of refraction is required by the diagnostic technique.

Table 1 shows the 15 liquid pairs from Smedley and Coles (1990) having the smallest values of $\frac{\bar{\mu}}{\sigma}$. The pairs are listed in order of increasing $\frac{\bar{\mu}}{\sigma}$. Note that each of the 15 pairs includes formamide, which has the lowest viscosity of the eight hydrophilic liquids listed in Smedley and Coles (1990). Fortunately, formamide is available in very high purity (99$^+$%). The value of δ, the difference in index of refraction, and the available purity of the second liquid if obtained from Aldrich Chemical Company (1989) are also included as important elements of the selection procedure. The largest value of δ found for the liquid pairs listed in Smedley and Coles (1990) was 0.74 cm for 1-bromooctane over formamide, which is ranked twelfth in Table 1. The first two pairs on the list have sizable δ and very high purity. However, the second pair, nonane over formamide, was selected due to the larger difference in the index of refraction for this pair. Despite the fact that this liquid pair has the second lowest value of $\frac{\mu}{\sigma}$ in Table 1, it is still a factor of six larger than the value of $\frac{\mu}{\sigma}$ for water (0.14 x 10^{-3} sec/cm).

5 Experimental Procedure

Cleaning Procedure: Prior to filling the reservoirs or assembling any part of the apparatus, a careful cleaning procedure was followed. It is common experience that contact angles are strongly affected by contamination. For this reason, the following procedure was employed, which is a slight variation of Procedure 'C' as specified by Scientific Specialities Service (1989):

1. Rinse with Freon 113 (1,2,2-trifloro-1,1,2-trichloroethane)
2. Scrub and/or ultrasonic bath with a biodegradable phosphate- free detergent (Chemsolve laboratory glassware cleaner, Malinckrodt)
3. Rinse thoroughly with tap water
4. Rinse with 1:1 nitric acid

5. Rinse with double-distilled deionized water

6. Air dry in an organic-free environment

Prior to assembly, all components were also flushed with high purity nitrogen to eliminate dust particles.

Liquid Transfer to HPLC Reservoirs: Transfer of liquids was achieved as shown in Fig. 13 by inserting one end of flexible tube 2 (carrying nitrogen) and one end of flexible tube 3 into the original bottle of liquid. The other end of tube 3 was located in the HPLC reservoir that was previously flushed with nitrogen using tube 1. By pulling vacuum on tube 4, with tube 1 closed off, the liquid was transferred into the HPLC reservoir through tube 3. When the desired volume of liquid was transferred, vacuum was removed. Nitrogen flow was continued and the vacuum tube was used as a vent. This procedure was used for both liquids. In addition, a small amount ($\approx$ 5 percent) of each liquid was transferred into the reservoir containing the other liquid. The two HPLC reservoirs were then shaken vigorously several times, over several days, to emulsify the liquids and promote mutual saturation. The reservoirs were finally connected to the apparatus through tube 3.

Filling and Emptying Apparatus: Prior to filling, the apparatus was carefully cleaned, flushed with nitrogen, and evacuated through the vacuum connections shown in Fig. 5. The tubing connecting the reservoirs to the apparatus also contained nitrogen. It was therefore necessary to pull vacuum on the reservoirs long enough to eliminate the nitrogen from the tubes. The following procedure was employed:

1. Move piston to minimum B.

2. Evacuate system with 1, 4 closed; 2, 3, 5, 6 open.

3. Bleed nitrogen into system through valve 1 to flush.

4. Connect reservoir that was removed for step 3.

5. Continue evacuating, pull vacuum on reservoirs long enough to eliminate nitrogen from flexible tubes connecting the reservoirs to the apparatus.

6. Close 2, 5.

7. Slowly open 4 to fill lower part of cell, up to the shaft, and small space B with liquid B. If any of the liquid splashes onto the upper window it is removed by heating the window with a blow dryer.

8. Close 4, 6.

9. Slowly open 1 to fill the space A with liquid A.

10. Open 2, to fill the rest of the cell with liquid A.

11. Close 1.

12. Get rid of the air bubble in the cell by first moving the piston to the minimum A position. Tilt the cell to move the bubble near the inlet to the tube leading to piston A. Now, by moving the piston toward minimum B, the bubble is withdrawn from the cell and rises into the purge valve.

13. Open 1 and the purge valve; pressurize reservoir B to push air out of purge valve.

14. Close purge valve, close 1; the system is full.

The following emptying procedure was employed:

1. Move piston to minimum B.

2. Attach low pressure nitrogen to vacuum valves 5 and 6.

3. Close 2, open 1 and 5.

4. Open 2 slowly to allow liquid A to be pushed out of the cell into reservoir 1, then close it.

5. Move piston to minimum A, thus pushing liquid A into reservoir 1 and drawing nitrogen into the apparatus through 5.

6. Open 6 to push liquid A out of the tubes from reservoir 1.

7. Close 1.

8. Close 5, open 4.

9. Move piston to minimum B, thus drawing nitrogen into side A while pushing liquid B and nitrogen into reservoir 2.

10. Open 2, thus pushing liquid B from the cell into reservoir 2.

11. Close 3, open 5 to push liquid B out of the tubes from reservoir 2.

If experiments were to be conducted with one liquid rather than two, the same procedure could be used. However, the low pressure nitrogen would be left attached to valve 1 in step 4 of the filling procedure. In addition, purging of air bubbles from the system would not be necessary.

Cell and Plate Alignment: The cell is aligned with the incoming laser scan to ensure that the scan enters normal to the upper window. This alignment is achieved by stopping the scan motor and tracing the reflection of the beam from the window back to the phototransistor housing. By adjusting the height of the four legs supporting the cell, the reflected beam is made coincident with the incoming beam. This technique achieves normal incidence with an estimated accuracy of ±0.05°. A similar reflection from the liquid-liquid interface is aligned with the incoming beam by shimming the optical bench to tilt the liquid interface in the desired direction, this is the least accurate alignment.

The reflection-alignment procedure is also used to calibrate the angle of the plate inside the cell. In this case, alignment is achieved by changing the plate angle with the handwheel (Fig. 2). The aligned condition is noted on the counter and marked dial and used as the $\theta = 0°$ reference. The estimated accuracy of this alignment technique is very good for the upper window and the glass plate (±0.05°.), however, the alignment of the interface may be off by as much as ±0.2°.

Interface Reference Level: With the plate set at $\theta = 0°$, the interface is raised by manually rotating the compumotor shaft until the interface makes contact with the lower side of the plate. At this point, the compumotor power is turned on and the liquid interface is raised the thickness of the glass plate, taking its volume displacement into account. This final position is noted using the dial indicator pictured in Fig. 3, and defined to be the reference level of the interface.

Plate Measurement Region: A given glass plate may have regions on its surface where the contact angle is different from other portions of the plate surface. Due to the possibility of contact-angle variation over the surface of the plate, all measurements are centered on the same part of the plate. In addition, this position is chosen such that it is visible over a large range of plate angles (Fig. 14).

For a given plate angle, the interface is moved from its reference level (described in the last section) to the starting position on the glass plate. Measurements are made as the interface is moved from the start position to the end position and back at a given velocity. The definition of the reference level makes it possible to locate the starting point on the plate fairly accurately ($\leq$ 1 mm) for most plate angles. Larger errors were found for the smallest plate angles, since a small error in the position of the reference level translates to a large error in the contact-line position in these cases. A greater concern in accurate positioning of the interface is the volume displacement of the glass plate; failure to correct properly for this displacement easily results in positioning errors of the order of half the plate length at small angles.

Distance and Velocity Along Plate: Desired distances and velocities along the plate can only be achieved if the presence of the plate is considered when setting the motor speed and the number of steps. Velocity must be corrected for blockage area at the height of the interface. Distance must be corrected for the amount of liquid volume displaced by the glass plate for the distance of motion desired. These corrections are relatively straightforward, provided the interface makes contact with the front and back surfaces of the glass plate. After the interface passes the bottom corner of the plate, on the shaft end, the blockage area is no longer constant as the interface moves, therefore, for a fixed motor speed, the V_{cl} changes with interface height.

The stepper motor has 25,000 steps per revolution and one revolution moves the double-acting piston a distance of 2 mm. The motor has a restricted range of speeds from 0.001 revs/sec to some torque-limited speed (maximum speed tried was ≈ 0.8 revs/sec) in steps of 0.001 revs/sec. The maximum motor speed is also limited by the fact that the liquid being forced into the cell causes interface disturbances at higher speeds. The velocity of the interface inside the cell, taking into account the area blockage, is

$$V_{pist} = \left[\frac{A_{cell} - A_{glass}}{A_{pist}} \right] V_{int} \tag{6}$$

$$A_{cell} = A_{pist} = \pi r^2_{pist} \tag{7}$$

Where V_{pist} is the velocity of the piston, V_{int} is the vertical velocity of the interface inside the cell, A_{cell} is the cross sectional area of the cell, A_{pist} is the area of the piston, and A_{glass} is the blockage area of the glass at the current interface height. The blockage area is dependent upon a blockage length L_{block} that varies with the plate angle θ, and the width w of the glass plate. L_{block} is the horizontal length of the plate at a given plate angle θ for a given plate thickness T.

$$A_{glass} = L_{block} w = \left[\frac{T}{\sin\theta} \right] w \tag{8}$$

In addition, contact line velocity V_{cl} is related to the vertical velocity of the interface V_{int} by the sine of the plate angle θ.

$$V_{cl} = \frac{V_{int}}{\sin\theta} \tag{9}$$

Therefore, the piston velocity is related to the interface velocity by

$$V_{pist} = V_{cl} \left[\sin\theta - \frac{T w}{\pi r^2_{pist}} \right] \tag{10}$$

The distance that the interface moves inside the cell D_{int} relative to the distance the piston moves D_{pist}, is also dependent upon the presence of the glass plate. This relationship is easily found by multiplying the above expression for the velocity relationships by time.

$$D_{pist} = D_{cl}\left[\sin\theta - \frac{T w}{\pi r^2_{pist}}\right] \tag{11}$$

At small plate angles, the correction for velocity and distance changes when the contact line on the lower side of the plate reaches and passes the bottom corner of the plate on the end that attaches to the shaft. In this case, the correction is essentially the same; however, the blockage length L_{block} is different. As smaller angles are approached, the blockage length goes to infinity according to the given equation. However, the plate is of finite length L, and the maximum possible blockage is the diagonal length of the plate. As the interface approaches the shaft, the blockage length decreases and the speed of the contact line therefore decreases. In these cases, L_{block} was taken as the blockage length at the center of the desired travel. Under these circumstances, the contact-line velocity would be higher than desired when the interface was moving below the midpoint and lower than desired when the interface was moving above the midpoint.

$$L_{block} = \frac{L_{plate}}{\cos\theta} \tag{12}$$

Where L_{plate} is the distance along the plate from the top corner of the plate, near the shaft end, to the center of the desired travel.

Experimental Protocol: The interface was moved and data were collected under programmed control. Manual intervention was required only to adjust the plate angle and enter it into the computer (Fig. 15).

Prior to moving the interface from its reference position to the start position, a 3 second tare was recorded with the plate in the scan. After arriving at the start position, the interface was moved from the starting position to the end position and back at a contact-line velocity of 0.1 mm/sec. This motion was executed so as to define an initial condition on the plate. After this

conditioning stroke, the contact-line velocity was set at the desired value and the receding motion was started. Data were recorded while the interface was in motion. The speed was then changed and the procedure repeated until all the desired contact-line velocities had been recorded for a given plate angle. Upon completing the final velocity, the interface was returned to the reference position. The program then waited for the plate angle to be changed and entered and the procedure was repeated. The above regimen was followed until the desired portion of (plate-angle, velocity) space had been recorded.

The recording of data was performed in several different ways. In earlier experiments, 3 seconds of data, centered on the midpoint of the motion, were recorded at a rate of 15 scans/sec. In other experiments, 2 scans, 1/15 second apart, were recorded at 26 equally spaced intervals of the entire motion. In the latest experiments, single scans were recorded at 52 equally spaced intervals of the entire motion ($\approx$ 1 scan/0.5 mm) in order to generate an extended time history of the contact line motion. In all cases, required delays were implemented by counting motor rotations via the ST2 input to the programmable real-time clock (see *System Integration* in Section 3). Due to the extensive use of software control, these modifications were relatively easy to implement.

6 Processing the Data

Data Storage: The data were stored in binary form in directed-access files, i.e. data were stored and read in blocks of 512 bytes and each block of data has a number associated with it. The first block of each file contains run information for the file, such as date, time, plate angle, interface motion, etc. The remainder of each file contains several scans of data. Each scan consists of a 1 kilobyte record, from the laser-power monitor, of the laser-light intensity that exposed the array, followed by a 2 kilobyte record of the light intensity recorded by the 1024 pixels in the array. Each file is devoted to a single velocity and plate angle, and the files are numbered sequentially in the order that they were taken.

File Handling: All files were stored on the hard disk of the Lab Datax system and copied to 8 inch floppies when the disk became full. Single-sided 8 inch floppies were used to transfer the data files through HYDRA5 to the microVAX cluster (HYDRA0). All data processing was

performed in this environment due to the speed and power available in the cluster, despite the inconvenient data transfer procedure. All data were finally archived to tape storage.

Data Reduction: Fig. 16 shows the light-intensity signature produced by the presence of the optics and the windows of the cell. The array response is not uniform. However, it is within the uniformity specified by the manufacturer (see *Photodiode Array* in Section 3). The RMS deviation Fig 17 computed from an average of 50 scans shows that this response is constant for each pixel to within one percent of the intensity recorded; therefore, a single scan provides a reasonably good record of the light-intensity signature. Note that the light intensity is given in counts from the A/D converter (1 count = 4.8 mV). The dynamic range of the array output is approximately 530 counts. The light-intensity signatures shown have been inverted. The output from the array is actually negative for high light intensity and approximately zero or slightly positive for no light. The inverted view makes the light-intensity signatures easier to interpret, since large numbers represent high light intensity and low numbers represent low light intensity. The base-line intensity is set by adjusting the polarizer on the top shelf of the optical bench (Fig. 4).

A tare level was recorded with the interface at the reference level for each plate angle (Section 5). The tare is the initial picture. An example of tare data is shown in Fig. 18 for a plate angle of approximately 48° and should be compared to the data for the case without a plate in Fig. 16. Note that the plate introduces a few peaks and some optical noise. The deep valley on the right is caused by reflective loss of the light illuminating the end of the plate. Fig. 19 shows a raw light-intensity signature produced by a contact line that is receding at 0.05 mm/sec; note the continued presence of the valley on the right. The raw signature in Fig. 19 is corrected by subtracting the tare in Fig. 18 to produce the result pictured in Fig. 20. The operation of subtraction produces a signature that is corrected for non-uniformity of pixel response and for optical distortions caused by the plate and windows. Note that the valley at the interface has become more noisy in Fig. 20 than it was in the raw trace pictured in Fig. 19. This lack of correction is due to the fact that pixel nonuniformity is greatly reduced at zero light intensity, therefore, the tare (Fig. 18) reintroduces the noise when it is subtracted. It is also important to note that the corrected signature in Fig. 20 is more noisy to the left of the contact

line than to the right of the contact line. The tare was recorded with the interface at the reference position; i.e. formamide in contact with the plate. However, nonane is in contact with the plate to the left of the contact line. Therefore, the correction is not as good to the left of the contact line as it is to the right of the contact line. This fact is of no consequence, since only changes in the part of the signature to the right of the contact line are being considered here (Fig. 1). All signatures shown throughout the rest of this chapter have been subjected to the subtraction correction. In addition to this subtraction correction, many signatures from a given run were shifted and averaged to determine an average profile, on the right side of the contact line, for a particular velocity at a particular plate angle. This procedure of shift-averaging is discussed further in the section: *Try "Sticky" Plate Again* since this processing was only used on the "sticky"-plate data.

7 Discussion of Results

Introduction: During an earlier stage of the experiments, the liquid interface position, during the off state of the apparatus, was not carefully controlled. The signatures that were observed as the contact region traveled along the upper portion of the plate were very different from those that were seen as the contact region traveled along the lower portion of the plate. As the contact region advanced up the plate, initially no lack of light was seen in the signature, however, as the dividing line between the binary states of the surface was crossed, the signature developed first a distinct valley followed by a large peak as shown by the generic light intensity distribution pictured at the right in Fig. 1.

By looking into the cell through the upper window, the contact region on the plate could be observed. During the approach to the dividing line, the contact region was barely visible. However, as the dividing line was met and passed, the contact region became very well defined and thus easily visible. The contact line looked as though the contact angle changed drastically as the dividing line was met and crossed. Before and after crossing this line, the signature remained essentially unchanged as it traveled. Due to the fact that this binary behavior, at least visually, appeared to occur along the full width of the plate, it was assumed that there was some hysteresis effect, perhaps caused by leaving the glass plate partially immersed in the interface at

that level. In an attempt to rid the glass plate of this binary behavior, the interface was moved to the reference point and left for a period of one month. A quick test after this period of time revealed that the binary behavior was essentially unchanged. At this point, new optical quality windows and a thicker glass plate were obtained (the previous plate-glass windows introduced a lot of optical noise). The question before installation, of course, was how the glass plate should be treated prior to installation and during residency in the cell.

In an attempt to understand the effect of pretreatment of the glass plate, a short series of surface treatment tests were conducted.

One spare 2-mm thick glass plate was cleaned according to the procedure outlined at the beginning of Section 5. The plate was then suspended, partially immersed, in an interface between nonane and formamide. After 6 hours in the liquid, the plate was manually moved in and out of the interface while visually observing the behavior of the contact line. Indeed, it was seen to behave in the same binary fashion observed on the plate inside the cell of the apparatus.

Two spare 2-mm thick glass plates were cleaned according to the procedure outlined at the beginning of Section 5. One plate was soaked in nonane and the other was soaked in formamide for a period of 24 hours. When tried in the interface, the formamide-soaked plate was completely "slippery" (smooth contact-line motion) whereas the nonane-soaked plate was completely "sticky" (lack of smooth contact-line motion, a lot of interface deformation). Following this observation, both plates were then suspended, partially immersed, in the interface for 24 hours. A visual check the next day indicated that the binary behavior had set in for the formamide-soaked plate, whereas the nonane-soaked plate remained entirely "sticky".

The hypothesis was that perhaps a thin film of formamide made the plate "slippery". Suspending the plate in the interface caused the film to drain off the portion of the plate located above the interface. The conclusion was to soak the plate in formamide prior to installation into the apparatus and to ensure that the plate was always fully immersed in formamide during the off state of the apparatus. It was felt that this procedure would prevent the occurrence of the binary behavior. It was also expected that the plate could be changed from "slippery" to "sticky" by letting it drain while still inside the cell.

Three types of experiments were conducted with the "slippery" plate. One experiment tested the repeatability of the motion, the second experiment examined changes that occurred throughout (plate angle, velocity) space, and the third experiment examined the higher contact-line velocities. In addition to these experiments, some ray-tracing was done to develop an intuitive feeling for the light-intensity signatures. The results from this work are discussed in the section: *Ray Tracing*.

After completing the first two experiments with the "slippery" plate, an attempt was made to produce a sticky plate by moving the interface to the bottom edge of the plate. The results obtained from these trials are outlined in the section: *Try "Sticky" Plate*. However, the plate did not become "sticky", as expected, except in a very small region. In order to produce a "sticky" plate, the plate had to be removed, cleaned, and soaked in nonane. Results obtained from the "sticky"-plate experiments exhibited the types of light-intensity signatures shown in Fig. 1, and are presented in the section: *Try "Sticky" Plate Again*. Therefore, it was possible to determine the contact angle for various contact-line velocities only on the "sticky" plate.

Repeatability Experiment: The repeatability experiment was conducted after the apparatus was dormant for 12 hours with the liquid interface at the reference position (i.e. plate fully immersed in formamide). The protocol involved moving the interface from the reference position to the start position, then recording data as the interface was moved from the start position to the end position and back at a contact-line speed of 1.0 mm/sec. The interface was moved back to the reference position and the experiment repeated for a total of nine trials at a constant plate angle of 15°. For these experiments, no conditioning stroke was used.

The corrected light-intensity signatures for this experiment are given in Figs. 21-25. Each figure shows nine signatures, each from a different trial. The plots in each figure are read in order from top to bottom and then left to right. The successive figures represent later times in the procession of the advancing contact line across the illuminated portion of the glass plate. The results for the receding portion are not shown, since they are less distinctive and will be seen in the tour of (plate angle, velocity) space that follows. Fig. 21 depicts scan 9 from all nine trials, Fig. 22 depicts scan 19 from all nine trials, and so on to scan 49 in Fig. 25. For this experiment, 2 scans were recorded 1/15 second apart, with a delay of 13/15 seconds between

the pairs of scans. Therefore, a total of 5 seconds has elapsed between scan 9 and scan 19 and thus between each pair of figures.

A general observation is obvious. The nine trials produced light-intensity signatures that are nearly identical at equivalent times. The shape of the moving interface that produced these signatures is essentially repeatable. As the interface advances from right to left there are a few distinguishable features. An intensity maximum leads the intensity minimum. The light intensity changes more abruptly from the maximum to the minimum than from the minimum to the mean level established at the right of each plot. Note that the absence of light is represented by approximately -300 counts for this experiment.

A general consideration required for the understanding of these light-intensity signatures is as follows: if the interface is concave upwards, the light is spread out as it is for a negative lens and if the interface is concave downwards, the light is concentrated as it is for a positive lens. The light intensity signatures seen here indicate that there is a small portion of the interface that is concave downward followed by a larger portion of the interface that is concave upward.

As the interface moves, the signature to the right of the contact region appears to be less noisy than that to the left of the contact region. A tare has been subtracted from the original raw data. That tare was taken with the contact region off the left side of the plot; therefore, optical noise introduced by optical inhomogeneities is better corrected when formamide is in view, than when nonane is in view. In addition, optical noise is better corrected in the flat region of the signature to the right of the contact region, because the curved region introduces a shift in the optical noise that prevents its correction by the subtraction technique. Optical noise on the curved portion of the contact region is worse in Fig. 22 than in Fig. 23 or Fig. 24, since the optical noise on the tare signal is not uniform across the observed area. Fig. 25, which depicts scan 49 from each of the nine trials, does not demonstrate the same degree of repeatability seen in the previous figures. At this point in its travel, the interface interacts with the shaft holding the glass plate, this interaction produces a large dimple in the surface that is seen in six out of the nine trials at scan 49. However, this is an end effect that occurs at the end of the motion and is not the central issue here.

During the repeatability trials the contact line on the back side of the plate passed the lower corner of the plate at the end connected to the shaft. This event, which is not noticeable in the data presented thus far, was easily observed on an oscilloscope that displayed the light intensity signatures in real time. When the contact line passed the corner of the plate, a wave caused deformation of the intensity trace. Passing this point means that the velocity is no longer constant, since the blockage length decreases as the interface moves upwards (see *Distance and Velocity along Plate* in Section 5).

The change in contact-line velocity can be detected from the data by plotting the scan number against the location of the minimum of each corrected light-intensity scan. Fig. 26 depicts these minima for every second scan from the first trial pictured at the upper left of each of Fig. 21-25. Every second scan was used in the mode 1(2)51, since two scans were recorded at each of 26 equal time intervals. Fig. 26 shows that the velocity (pixels/scan), which is the local slope (dx/dy) of this set of points, changes at approximately pixel 350. Note that a steeper line on this plot represents a slower velocity. The dotted line in the figure is the expected slope of the contact-line motion based on the motor speed and the angle of the plate. Scatter in the points is due to optical noise that interferes with the determination of the actual minimum. Regardless of scatter, however, this type of plot offers a means for determining where to observe the interface as well as a means for determining the local velocity of the interface. Fig. 27 depicts sets of tracked minima for each of the nine trials, demonstrating once again the high degree of repeatability. Just as it is possible to track minima, it is also possible to track maxima, as shown in Fig. 28. However, noise interferes more in the case of maxima, since the difference between the maximum and the mean light intensity is smaller than the difference between the minimum and the mean. The change in velocity of the contact region is not as easily seen on the plots of the maxima as it is on the plots of the minima.

Tour of (Plate Angle, Velocity) Space: The experiment involving a tour of (plate angle, velocity) space was conducted to determine any variations in interface shape that might occur as the plate angle and contact-line velocity were changed. Previous test experiments, at larger plate angles, up to 40°, indicated that if a peaked profile were to be seen, such as the one depicted in the diagram on the right in Fig. 1, it should be in the part of parameter space

indicated in Fig. 29. The numbers of each of the following figures that correspond to particular regions in parameter space are inside the circles in Fig. 29. The protocol involved in this experiment is described in Section 5. The recording means used here was the same as for the repeatability experiments just described. Velocities of ± 0.1, 0.2, 0.5, 1.0, 2.0, 5.0 mm/sec were recorded for plate angles of 15°(2°)3°, a total of 84 data files, one for each velocity, and 7 tare data files, one for each plate angle.

Figs. 30-35 depict typical receding signatures, while Figs. 36-41 depict typical advancing signatures. Each plot in each of these figures represents the corrected signature from scan 25 for the receding cases and from scan 41 for the advancing cases. Immediately noticeable is the fact that the receding profiles seen in Figs. 30-35 are very distinct from the advancing profiles seen in Figs. 36-41. Note that absence of light is represented by approximately -225 counts for this experiment.

The advancing profiles are qualitatively similar to those seen in the repeatability experiments with a leading maximum and trailing minimum. Some aspects of these features change with plate angle and advancing speed. As the interface is moved at higher speeds, the maximum is seen to increase in magnitude, and the recovery from the minimum occurs over a smaller spatial scale. This change indicates that the distance along the interface that is affected by the moving contact line decreases with increasing speed. In addition, whatever is causing the maximum, perhaps a leading bump or wave, must be increasing in curvature to focus more light at the maximum intensity point on the array. Another noticeable feature of these profiles is that the minimum is deeper for higher speeds at a given plate angle. The minimum is also deeper for a given speed at larger plate angles.

Note that the signature shown for a plate angle of 7° and velocity of 0.1 mm/sec in Fig. 37 is shifted from the others due to a roundoff error involved in the calculation of the delay between pairs of recorded scans because the motor speed was so low. This error also occurs for all scans taken at a plate angle of 3° in Figs. 38 and 41. Otherwise, despite their recorded position, these signatures are essentially unchanged as they cross the illuminated region, as seen earlier with the repeatability data in Figs. 21-25. This same error made itself apparent in the -0.1 mm/sec signature for 7° in Fig. 34 and at 3° in Figs. 32 and 35.

The receding profiles seen in Figs. 30-35, although less distinctive than the advancing ones in Figs. 36-41, still have characteristics that change with speed and plate angle in a manner very similar to the advancing ones. The minima are larger at lower speeds, opposite to the advancing case, and at larger angles, just as in the advancing case. In fact, at smaller angles and higher speeds, the signatures seem independent of speed (Fig. 34 for 7° and 5°). In all receding cases, the fall from average light intensity to the minimum appears to occur over the same spatial scale as the rise from the minimum back up to the average. This fall and rise were different in the advancing cases. In addition, there are no detectable maxima in the receding cases.

Plots of tracked minima for various plate angles and advancing speeds are shown in Figs 42-45. Note that all of the plots tend to have similar slope, despite widely varying speeds. This similarity in slope is testimony to the accuracy of delay between pairs of scans, such that a complete record of the moving interface is obtained. To determine the time between plotted points, add 2 to the value of DELTA (given below each plot) to get the number of scans between recorded ones and divide by 15 scans/sec to get the time. Note, that calculated delays yield even samples across the array at larger angles in Figs. 42 and 44. Fig. 43 depicts plots that demonstrate absence of minima for early times. This anomaly is due to a offset in space caused by an error in the known position of the interface at the start reference level. Despite this positioning error, a sizable number of the scans recorded the interface. Similar positioning error is seen for all speeds at a given angle. However, the middle figure in the left column of Fig. 43 is distinctly different from the others in the same row, due to the error in the calculation of the delay between scans discussed above for 7° at 0.1 mm/sec.

The plots of minima yield information regarding the passage of the interface beyond the lower corner at the end of the plate attached to the shaft. In the repeatability experiments, which were conducted at a plate angle of 15°, the velocity change was seen to occur somewhere near pixel 350. As the angle is decreased, it is expected that this break point should move to the right. Indeed, at 13° this point appears to be near pixel 500, at 9° it is near pixel 750, and at 5° it is probably off the right side of the array.

Try "Sticky" Plate: After obtaining the previous data and not finding the expected light intensity profiles (Fig. 1), the plate was left hanging for 24 hours with the interface at the bottom edge of the plate. The hope was to produce a "sticky" plate that would then yield different light-intensity signatures from those seen with the "slippery" plate.

The only evidence of "sticky"-plate behavior was found at the left-most extent of the illuminated region of the plate. A time series of the results for a plate angle of 5° and a speed of 0.1 mm/sec is shown in Figs. 46-47. Once again, plots are read from top to bottom, left to right in order of increasing time. Approximately 11 seconds elapsed between the plots shown. Notice that the contact region advances in the expected way in the plots shown in Fig. 46. However, the behavior changes dramatically in the plots shown in Fig. 47. A distinct valley forms, indicating a distinct lack of light, then in a short moment between scans 43 and 45, the contact region pops back into a near normal shape. As this was observed on the oscilloscope, the return to a near-normal state occurred on a time scale on the order of 1/15 second. This behavior was seen to occur in this region for all speeds and angles tested that day, except however, at larger angles where it moved out of the field of view. The example shown for 5° was chosen since it presents the best view of this region of the plate. A slow speed was chosen so that the transition could be more carefully observed. Aside from this anomaly, no other effect was seen as a result of the overnight drainage.

Higher Speeds: No other part of the plate appeared to be affected by the hanging of the plate, therefore, some runs were made at high speeds on the "slippery" part to see if any further change in signature occurred. This set of experiments was conducted at 5° because slower motor speeds are required for a given contact-line speed if the angle is smaller and the amount of liquid that needs to be moved to produce the 25-mm motion of the contact line is also smaller at small angles. A summary of the results is shown in Fig. 48. Note that the scans have been chosen such that the contact region is in nearly the same place for all speeds. Plots of increasing speed are presented from top to bottom and then left to right. Plots of signatures obtained from speeds of 0.1, 0.2, 0.5, 1.0, 2.0, 5.0, 10.0, 20.0, and 25.0 mm/sec are presented. Note, once again, that as the speed is increased, the valley gets deeper, but fails to reach the no-light level of plots seen in Fig. 47. In addition, the leading maximum, seen before, increases

in size up to 5.0 mm/sec but seems to remain relatively unchanged at the three highest speeds. A very well defined broad maximum is seen on the trailing portion of the valley. This trailing maximum was not as visible at the highest speeds shown in Figs. 39-41, but a second look now makes it more evident. This is evidence that the curvature of the surface has changed sign in this region, as is discussed further in *Ray Tracing* below.

The plate was left hanging vertical with the interface at the bottom edge of the plate for a period of 5 days. Perhaps more time was required for the formamide to drain off the plate. A set of runs was done at a plate angle of 15° and revealed that the contact-line behavior was essentially the same as it had been for the 24 hour case discussed earlier. Apparently the reversible nature of the plate surface, discussed in the introduction to section 7, would not occur for the plate inside the cell.

Ray Tracing: In order to develop a better understanding of the light intensity signatures that were observed experimentally, a ray tracing program was written to compute trajectories of light rays passing through the cell. For the calculations, handbook values were used for the indices of refraction of nonane, formamide, and optical glass. The interface on the lower side of the plate was assumed to be out of the light path (a very good assumption for small plate angles). The glass window at the bottom of the cell was included, since a large amount of refraction occurs at the glass-air interface where the largest change in the index of refraction is found. The program was designed to compute refraction for arbitrary interface shapes provided they are defined by an equation that is single valued. Distances from the plate to the window and from the window to the sensing element were not scaled, but chosen to be reasonable.

Fig. 49 depicts a light-ray pattern produced by a logarithmic interface. The interface is concave downward and produces a concentration of light at the bottom edge of the plot. A discontinuity in the slope at the contact line produces a diverging set of rays and an unlighted region. The light intensity in these ray-tracing diagrams is roughly proportional to the inverse of the spacing of adjacent rays. If this inverse were plotted, the light intensity distribution for this case would look much like that seen in the right diagram of Fig. 1.

A flat interface is shown in Fig. 50 and demonstrates a diverging set of rays at the contact line. Elsewhere, the intensity of light is uniform, just as depicted in the center diagram of Fig. 1. Fig. 51 shows the light intensity pattern produced by an interface that is concave upwards, in this case a decaying exponential with the slope at the glass surface chosen to represent an angle of 10°. Once again, the discontinuity in the slope produces a valley. Less noticeable is the fact that the rays to the right of the valley actually diverge slightly and become uniformly spaced near the right extent of the light scan. This behavior represents a long climb out of the minimum intensity at the valley before uniform intensity is reached. This result is similar to that seen in the left diagram of Fig. 1.

Note that in the three cases outlined above and depicted in Figs. 49-51, a discontinuity of slope exists where the interface meets the surface of the glass plate. In each case, this discontinuity produced a diverging set of rays and an unlighted region. If no discontinuity in slope occurs, i.e. the interface is tangent with the glass plate, the void no longer occurs. Fig. 52 shows an interface that generates a light distribution with a slight valley that has a slow recovery back to uniform light intensity. In all the observations of moving contact regions on the "slippery" plate, no lack of light was found. This lack of a distinct valley indicates that no discontinuity of slope was produced at the contact region, or that a very small and therefore undetectable discontinuity was produced. If no discontinuity exists, the contact angle must be 0° or very close to 0°.

Observed signatures for larger advancing velocities on the "slippery" plate have a trailing maximum that suggests the presence of negative curvature in the corresponding region of the interface. A possible shape consisting of a parabola that meets the glass plate at 0° and a smoothly connected logarithm produces the light intensity profile pictured in Fig. 53 that resembles slightly that seen in the experiments.

As yet unresolved is the meaning of the leading maximum for advancing cases. For the presence of this maximum, an area of negative curvature must exist that precedes the contact region. Perhaps a thin film of formamide is resident on the plate. This film would remain undetected as long as the surface of the film remained parallel to the glass plate. However, if the film were to bulge upward, forming a surface that is concave downward, a concentration of

light would be found on the detector. Perhaps a small wave is being pushed out ahead of the contact region as it moves, and it becomes larger as the interface moves at higher speeds. Similarly, the slow decrease in light intensity on the trailing side of the intensity minimum in the receding signatures is also not explained by the ray tracing.

Try "Sticky" Plate Again: The plate was removed, cleaned according to the cleaning procedure and soaked in nonane for a period of 12 hours. The plate was then installed in the apparatus and the interface was always left below the plate. After about 20 hours of soaking in nonane, a set of runs was made at 1.0 mm/sec for plate angles of 40°(5°)15°; 45°(5°)60°; 40° to see if "sticky"-plate behavior would be seen. Indeed, the plate was found to be sticky, and profiles like the ones shown in Fig. 1 were seen. The flattest intensity signature appeared to be at a plate angle of about 18° for this contact-line velocity. Two days later a more refined set of experiments was conducted that included plate angles of 25°(2°)11° and speeds of ±0.05, 0.1, 0.2, 0.5, and 1.0 mm/sec. However, the intensity signatures seen during this experiment were not the same as they had been 2 days earlier. The signatures suggested that the receding contact angle was much larger. The experiment was continued from 27°(2°)35°, 40°(5°)50°, for the same speeds. These signatures suggested that the receding angle was larger than 40°. The next day, another set of experiments for angles of 38°(2°)56° confirmed the results of the previous day. Apparently the condition of the plate surface had stabilized. Six days later, after adjusting the apparatus for larger angles, a set of experiments was conducted for plate angles of 66°(2°)38° and the same 5 speeds. These data demonstrated qualitatively similar behavior to those obtained 6 days earlier; therefore, these data are described below.

Light-intensity signatures for these cases are shown in the standard form in Figs. 54-74. Fig. 54 indicates the samples recorded in (velocity, plate angle) space; the numbers inside the circles are the numbers of the corresponding figures that follow. Therefore, each figure of Fig. 55-74 depicts a block out of the parameter space. For this presentation, scan 34 was selected, since it was the first scan within which the receding interface becomes visible at the left edge of the signature for the largest plate angle, see top signatures Fig. 55 and Fig. 60. Note, that a very distinct valley is present in the signature, indication of a discontinuity at the contact line that produces a pair of diverging rays. Advancing signatures have a very strong peak seen in

Figs. 65-74; whereas receding signatures seen in Figs. 55-64 do not. Note that absence of light is represented by approximately -125 counts for this experiment.

There are some notable features of the light-intensity signatures pictured in Figs. 55-74. At large plate angles, the end of the glass plate is very close to the left extent of the light-intensity signature. This presence is easily seen in Fig. 55 and Fig. 60 as a flat region approximately 200 pixels long, bordered on each side by upward and downward pointing spikes. The spikes are indicators of poorly corrected window presence due to curvature of the interface in that region. This is especially notable for the advancing cases in Fig. 65 and Fig. 70. As the plate is moved to smaller angles, follow through Figs. 55-59 or Figs. 60-64, its presence becomes less notable. Another effect that causes distortion of the corrected light-intensity signature is waves on the liquid interface. These waves are caused by interference from the jet of liquid entering the cell as the liquid interface is moved at high speeds at large angles (see Fig. 55 for V_{cl} = -1.0 mm/sec at a plate angle of 64°). Despite the problems inherent with distorted interfaces caused by these effects, they are easily recognizable and therefore easily avoided or noted.

Note that the width of the no-light region is smaller in the receding cases seen in Figs. 57-59 and Figs. 61-64 than in the advancing cases seen in Figs. 67-69 and Figs. 72-74. The no-light region for the receding cases is approximately 200 pixels wide whereas it is approximately 300 pixels wide for the advancing cases. This difference in width indicates that there is a greater discontinuity in slope at the contact line for the advancing cases.

A closer look at the receding signatures in a given column of parameter space indicates how the signature changes as the plate angle is varied. A sample of receding signatures for a contact-line velocity of -0.05 mm/sec and plate angles from 54° to 38° is shown in Fig 75. The vertical scale of these signatures has been magnified from 600 counts to 300 counts to better illustrate the change in shape of the signature. The upper left plot in Fig. 75 is for a plate angle of 54°. Note that the part of the signature to the right of the valley is concave downward, indicating that it is produced from an interface that is concave upward in this region (see Fig 1). The lower right plot is for a plate angle of 38°. Note that part of the signature to the right of the valley is concave upward, indicating that the interface is concave downward in this region, see Fig. 1.

The range of angles shown in Fig. 75 demonstrates the change in concavity of the interface as the plate angle is changed for a given speed. Judging from the signatures shown, one might guess that the contact angle for this speed is about 45° based on the fact that the signatures indicate that a flat signature should be found for this angle. However, there is some change in the signature as the interface moves across the plate that is not evident in a single scan. In some areas of the plate, the interface was seen to stick momentarily, thus changing the signature, while in other areas the interface moves very smoothly, with little change in the signature. Sticky regions of the plate were avoided by locating the right edge of the no-light region of the signature and tracking its progress. In order to locate the right edge, each signature was searched until a threshold of -20 was crossed. The pixel locations were plotted against the scan number as shown in Fig. 76. The upper plot is representative of the receding cases, and the lower plot is representative of the advancing cases. The dotted line in each plot is the expected slope computed using the motor speed and plate angle for each case. The slope of the dotted line agrees quite well for the later scans in the advancing case, whereas the receding interface is moving slower than expected. This discrepancy in slope is relatively small, but unresolved, it may be an optical effect. A line drawn through the points was used to indicated regions of constant velocity. Points that were not on the line indicated regions of non-constant velocity. For each velocity, at each plate angle, up to three sets of scans were chosen that lay on a line. The upper plot in Fig. 77 shows all the suitable scans from a plate angle of 48° and velocity of -0.05 mm/sec that were shifted and averaged. The lower plot shows the same for an advancing velocity of +0.05 mm/sec. In addition, each plot in Fig. 77 also shows an envelope of the minimum value and the maximum value at a given pixel to give some idea of the variation in the shape of the signature as the contact line moves across the plate. In some cases, a few scans were thrown out if they were located at the beginning or end of a set of scans and were significantly different from the average scan. In other cases, at the larger plate angles, many of the later receding scans and earlier advancing scans were thrown out due to interference caused by the presence of the shadow from the end of the glass plate. This culling procedure was performed by plotting the average, the minimum, and the maximum values at a given pixel on a single plot as shown in Fig. 77, and by plotting the individual scans that were at the beginning or end of a set of scans selected from Fig. 76. The remaining sets of

scans were shifted and averaged. Each of the shifted and averaged scans was visually checked on the terminal and was manually cut using cross hairs to remove the tail end of the averaged record. The trace in the upper plot of Fig. 77 was cut at pixel 351 and the trace in the lower plot was cut at pixel 553. The cutting of the record further removed interference from the shadow of the end of the plate. The remaining data were fitted by a decaying exponential using a nonlinear-least-squares subroutine from Numerical Recipes (1986) that was modified, to be more robust, by Phillip Tokumaru. The first 9 points of each averaged signature were ignored to eliminate interference from a small peak on the profile on the right side of the valley that is visible in Fig. 75. In addition, the origin of the exponential was shifted to x=10, the location of the first point. The multiplier of the exponential was plotted against plate angle for each receding velocity in Figs 78 to 82, to determine the zero crossing that indicates a flat signature. The equation of the least-squares fit to the data is given in the legend of each figure. The zero crossing for each velocity represents the contact angle for that velocity. It is interesting to note that the slope of the fitted line is apparently independent of the velocity, since the data overlap when plotted together in Fig. 83.

The above procedure was also employed to determine the contact angles for the advancing cases. The motion in these cases was much more stable, therefore, not as much culling of the signatures had to be done, aside from omitting scans at the larger angles that suffered from glass-plate interference. However, in the advancing cases, the light-intensity signature contained a peak at all angles and velocities measured since the maximum angle attainable by the apparatus was 66°. Therefore, it was necessary to extrapolate to find a zero crossing for the multiplier of the exponential fit to the advancing light-intensity signatures. Plots of the multipliers are given in Figs. 84 to 88. A quadratic fit was found to be appropriate for these data. The quadratic coefficients are given in the legend for x^0, x^1, and x^2. Once again, when all the velocities are plotted together, in Fig. 89, they overlap just as they did in the receding case. The extrapolated zero crossings were determined by solving for the largest root of the quadratic fit for each velocity. It is important to note that this is a distant extrapolation and is therefore not claimed to be very accurate, however, the result is a consistent one and therefore worth mentioning.

The end result of the data processing is the plot of contact angle vs. velocity given in Fig. 90. It is found that the contact angle depends only on the sign of the velocity and not on its magnitude for the range of velocities studied. The dashed line in the figure represents the maximum limit of the plate angle. The receding contact angle is approximately 50° whereas the advancing angle is approximately 78°. The capillary numbers varied from: $\frac{\mu}{\sigma}V = 4.2 \times 10^{-4}$ to 8.4×10^{-3}.

8 Conclusions and Recommendations

The results obtained for the "slippery" plate indicate a difference in the interface shape depending upon whether the interface is advancing or receding. Intuition and ray tracing indicate that the contact region must be concave upward in both cases. In addition, the radius of curvature of the interface in the advancing case must be smaller than it is for the receding case, since the advancing signature recovers from the minimum more quickly than the receding one. The minimum is deeper in the advancing case, indicating a faster change of slope near the glass plate than for the receding case. Results for the "sticky" plate indicate a behavior that is very different from that seen on the "slippery" one. There is a great difference between the advancing and receding velocities. Experiments conducted with the "sticky" plate yielded the change in light-intensity signatures that was expected from Fig. 1. Decaying-exponential curve fits to shift-averaged signatures yielded the dependence of the contact angle on the velocity. For receding velocities ranging from 0.05 mm/sec to 1.00 mm/sec, the contact angle was found to be independent of the speed with a value of 50°. For the advancing velocities, the contact angle was also independent of the speed with an extrapolated value of 78°. The contact angle depends only on the sign of the velocity for the velocities studied.

Recommendations: It would be useful to try different liquid pairs to check for a dependence of the contact-angle behavior on $\frac{\mu}{\sigma}$, and to find out whether the binary surface behavior that was observed with nonane/formamide is a general result or not. A thin plate is better used for work at small angles, since the interface on the lower surface goes beyond the bottom corner at the shaft-end of the plate at a later time. The thick plate, which yields a greater physical

separation between the contact line on the front and the back of the plate, is better suited for larger angles because it eliminates the problem of light interference from the contact line on the lower side of the plate.

A longer plate would facilitate experiments at smaller plate angles. In the current arrangement, at the smaller plate angles ($\theta < 10°$), the velocity of the interface decreased as the interface advanced up the plate. This change in velocity was caused by the fact that the interface was unable to make contact with both the front side and the back side of the plate at any interface height. Therefore, when the interface was on the front side of the plate, it was also above the lower corner of the plate at the shaft-end. As a result, as the interface moved, the blockage area changed and therefore the velocity of the interface changed. A longer plate would enable the experimenter to move the interface at a constant velocity near the end of the plate opposite the shaft. A longer plate would also enable the end of the plate to remain in the field of view at larger angles. In addition to the longer plate, a longer scan would also help to enlarge the usable angle range of the apparatus. It is important to note that the portion of the laser scan that extends beyond the ends of the Reticon array should be masked at the scan aperture. There is also a large reflection from one corner of the end of the plate opposite the shaft that can be removed by masking that portion of the scan at the large prism with a thin strip of tape.

Changing of test plates located inside the cell is a difficult task that could be simplified slightly if the cell were designed such that each lid is secured to the cell separately. In the current design, the two lids are held in place by four long pieces of rod, threaded on the ends, that pass from top to bottom through both lids. Removal of one lid requires the other lid to be removed also.

Another observation amounting to hindsight is that it is not necessary to have the inside diameter of the piston equal to the inside diameter of the cell when trying to determine the velocity of the contact line. The important aspect of these dimensions is that they be accurately known. The current setup has a minimum contact-line speed of about 0.002 mm/sec if the glass plate is vertical. This minimum speed increases with decreasing plate angles. However, the apparatus would yield lower speeds if a second double-acting piston, smaller in diameter, were

added in parallel with the large one. The large piston would be used for rough positioning of the interface and the small piston would be used to pump smaller amounts of liquid enabling slower speeds to be achieved.

References

"Aldrich Catalog Handbook of Fine Chemicals (1989-90)", Aldrich Chemical Co., Milwaukee, Wisconsin, 1989.

Bikerman, J. J. (1970) *Physical Surfaces*, Academic Press, New York.

Dussan, E. B. (1979) On the spreading of liquids on solid surfaces: Static and dynamic contact lines. In: *Annual Reviews of Fluid Mechanics* **11**, 371-400.

"Numerical Recipes The Art of Scientific Computing", Cambridge University Press, New York, NY, 1986.

Smedley, G. and Coles, D. Some transparent immiscible liquid pairs. J. of Colloid and Interface Science (To appear 1990).

Scientific Specialties Service Inc. Randallstown, MD 21133. Pre-Cleaned Bottle Book, 1988, p.16.

Table 1. Liquid pairs with small $\frac{\bar{\mu}}{\sigma}$

Liquid pair $\left[\frac{\text{liquid 1}}{\text{liquid 2}}\right]$	$\frac{\bar{\mu}}{\sigma} \times 10^3$ $\left[\frac{\text{sec}}{\text{cm}}\right]$	δ (cm)	Δ i.r. (i.r.$_2$ – i.r.$_1$)	Purity (Aldrich)
formamide / 1–bromobutane	0.54	0.55	-0.007	99$^+$%
nonane / formamide	0.84	0.26	+0.042	99$^+$%
1–chlorohexane / formamide	1.09	0.29	+0.027	99%
isopropyl benzene / formamide	1.20	0.27	-0.045	99%
dihexyl ether / formamide	1.32	0.24	+0.027	---
formamide / bromocyclohexane	1.42	0.33	+0.049	95%
ethyl caprylate / formamide	2.11	0.22	+0.029	99$^+$%
butyl benzoate / formamide	2.16	0.32	-0.049	99%
2,6–dimethyl – 4 –heptanone / formamide	2.22	0.18	+0.034	90%
butyl butyrate / formamide	2.27	0.20	+0.039	98%
butyl acrylate / formamide	2.40	0.20	+0.028	99$^+$%
1–bromooctane / formamide	2.44	0.74	-0.005	99%
1–decene / formamide	2.80	0.15	+0.025	94%
methyl caprylate / formamide	2.92	0.20	+0.030	99%
methyl benzoate / formamide	3.11	0.47	-0.069	99%

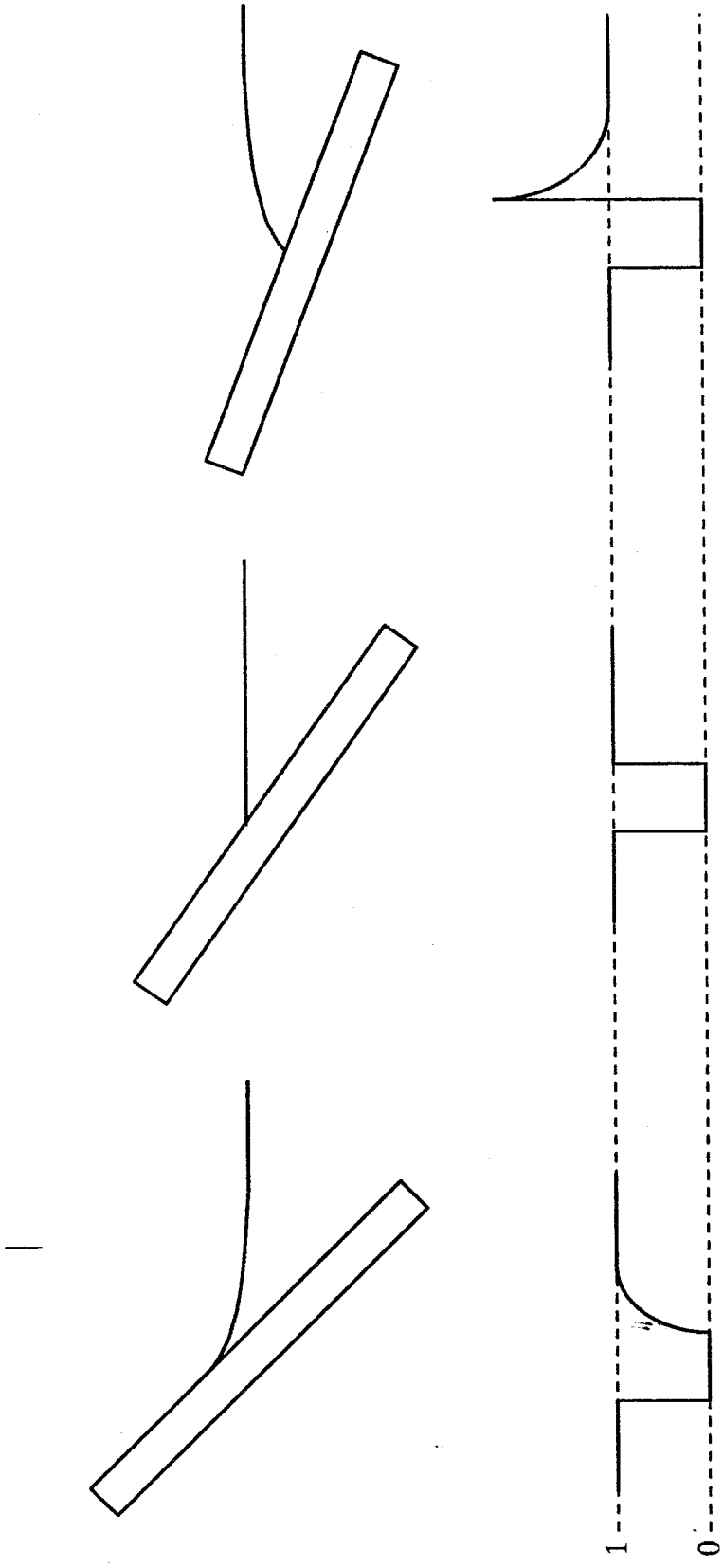

Fig. 1 Generic light intensity distributions

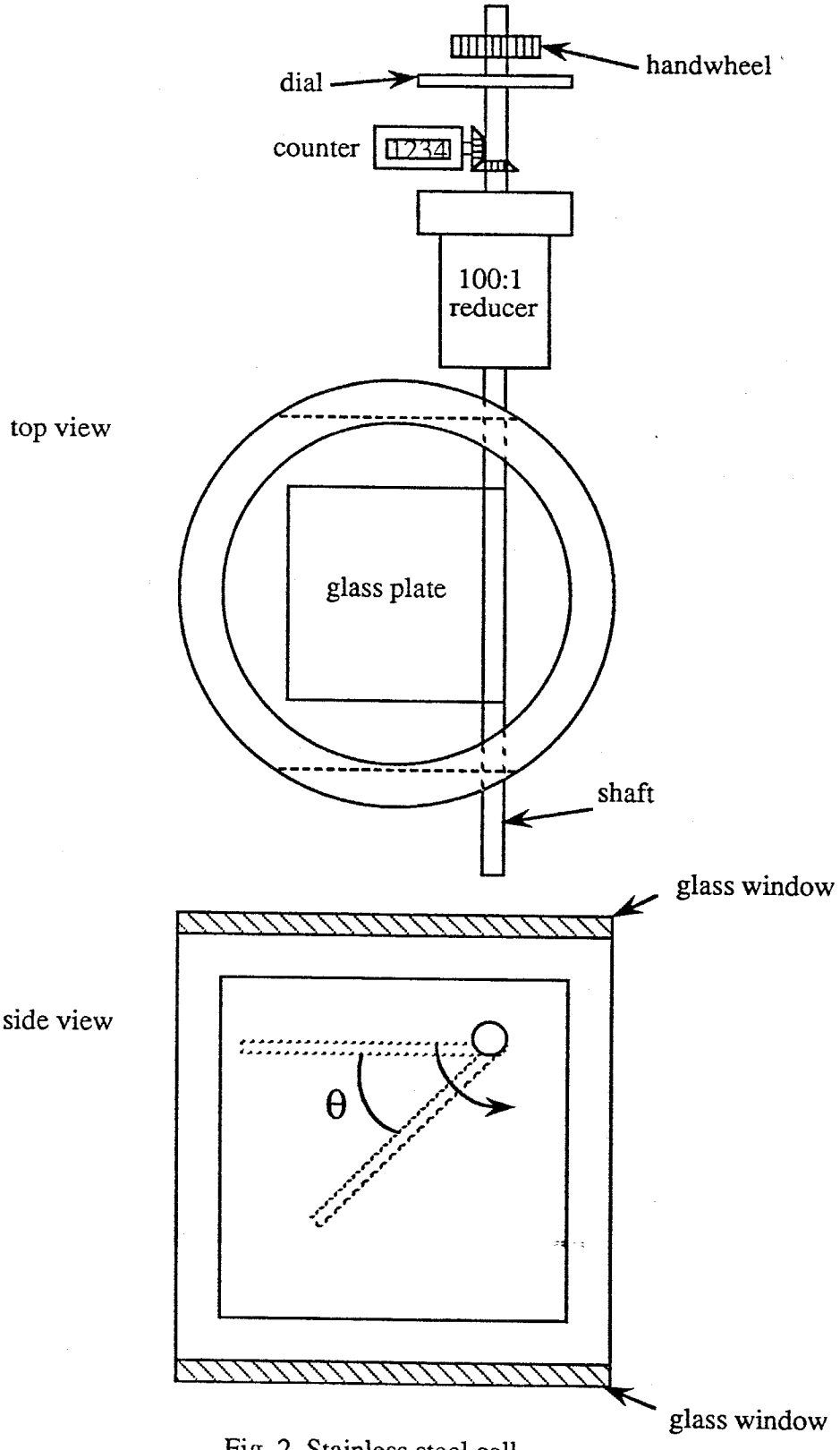

Fig. 2 Stainless steel cell

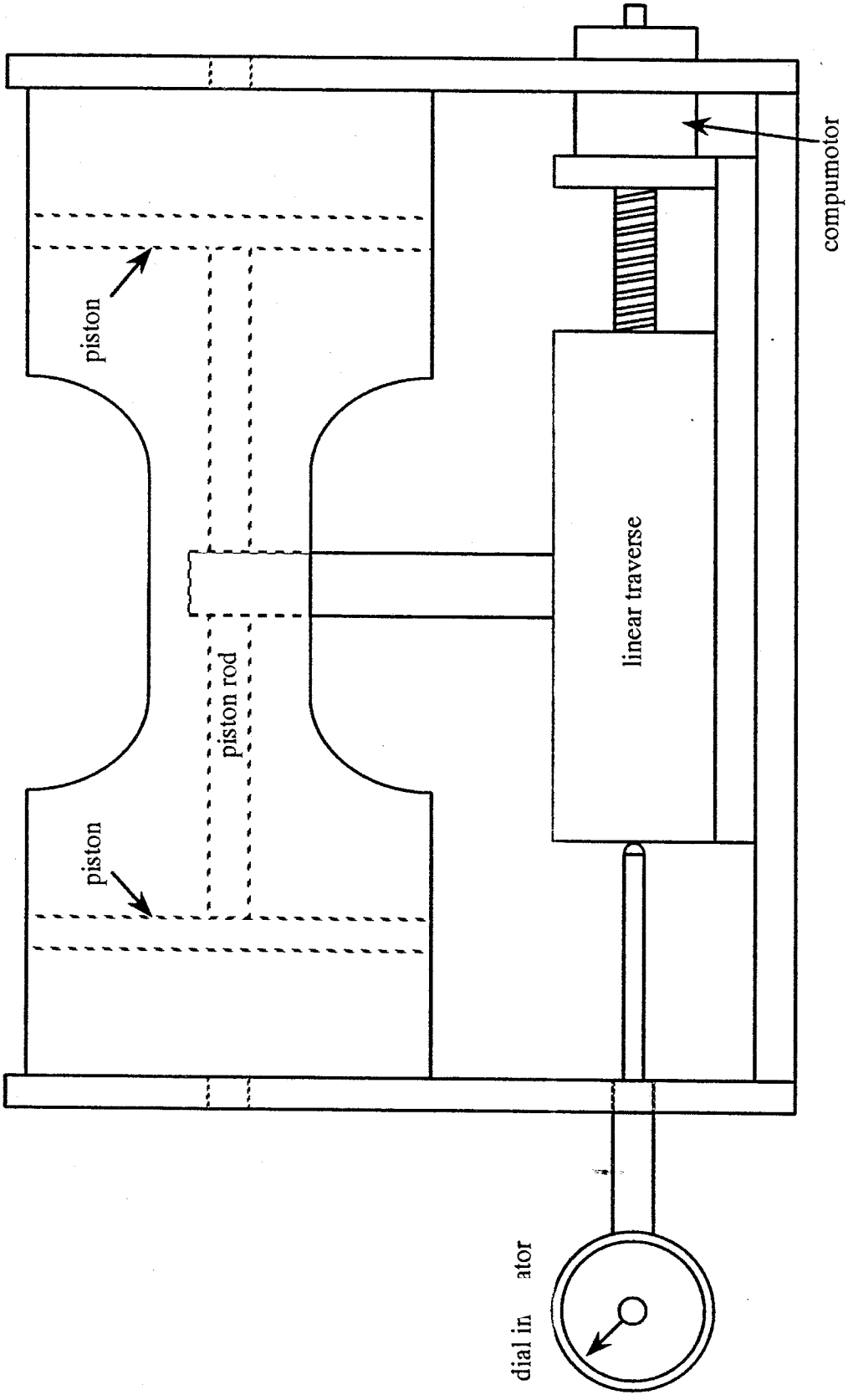

Fig. 3 Piston assembly

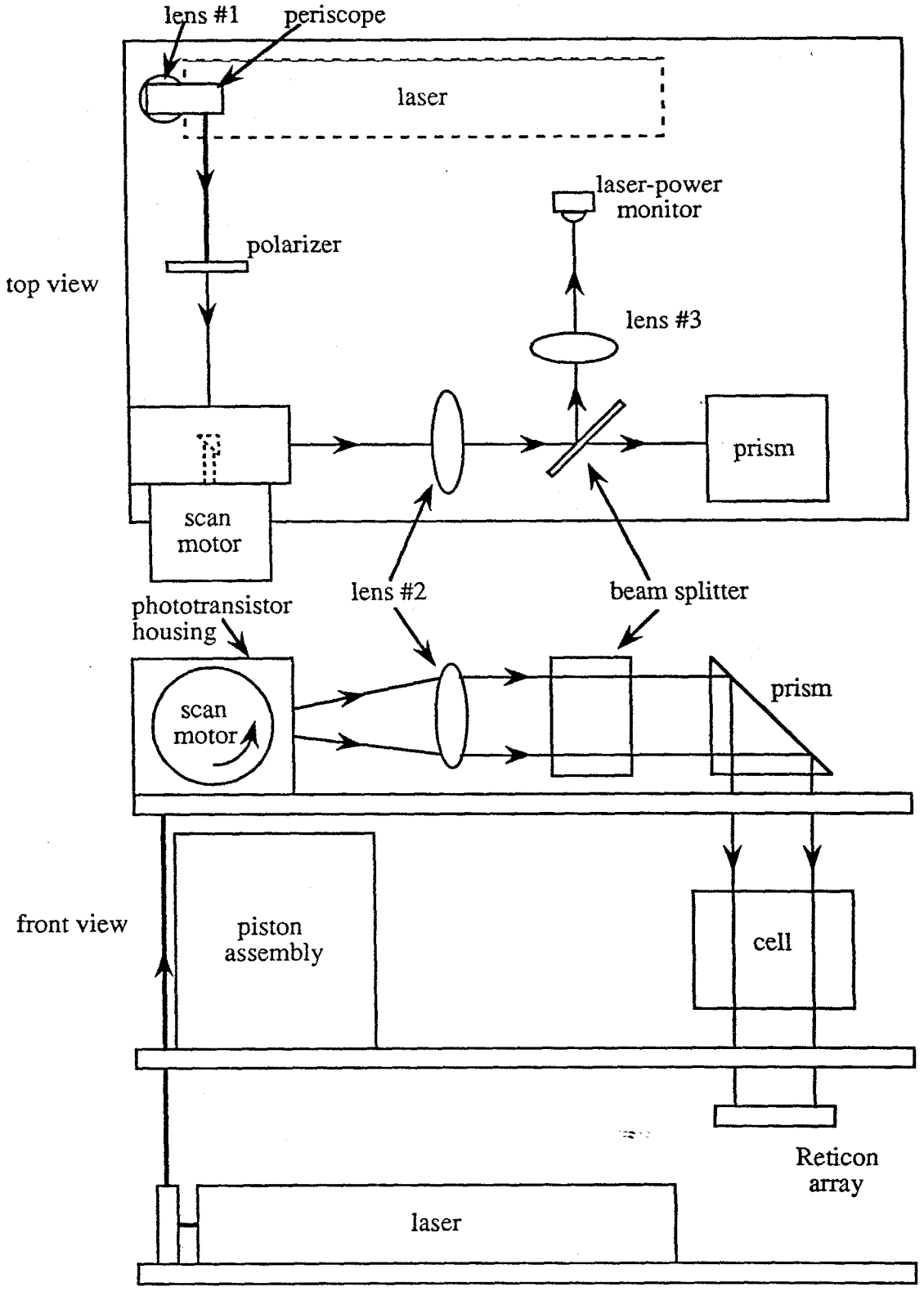

Fig. 4 Optical bench

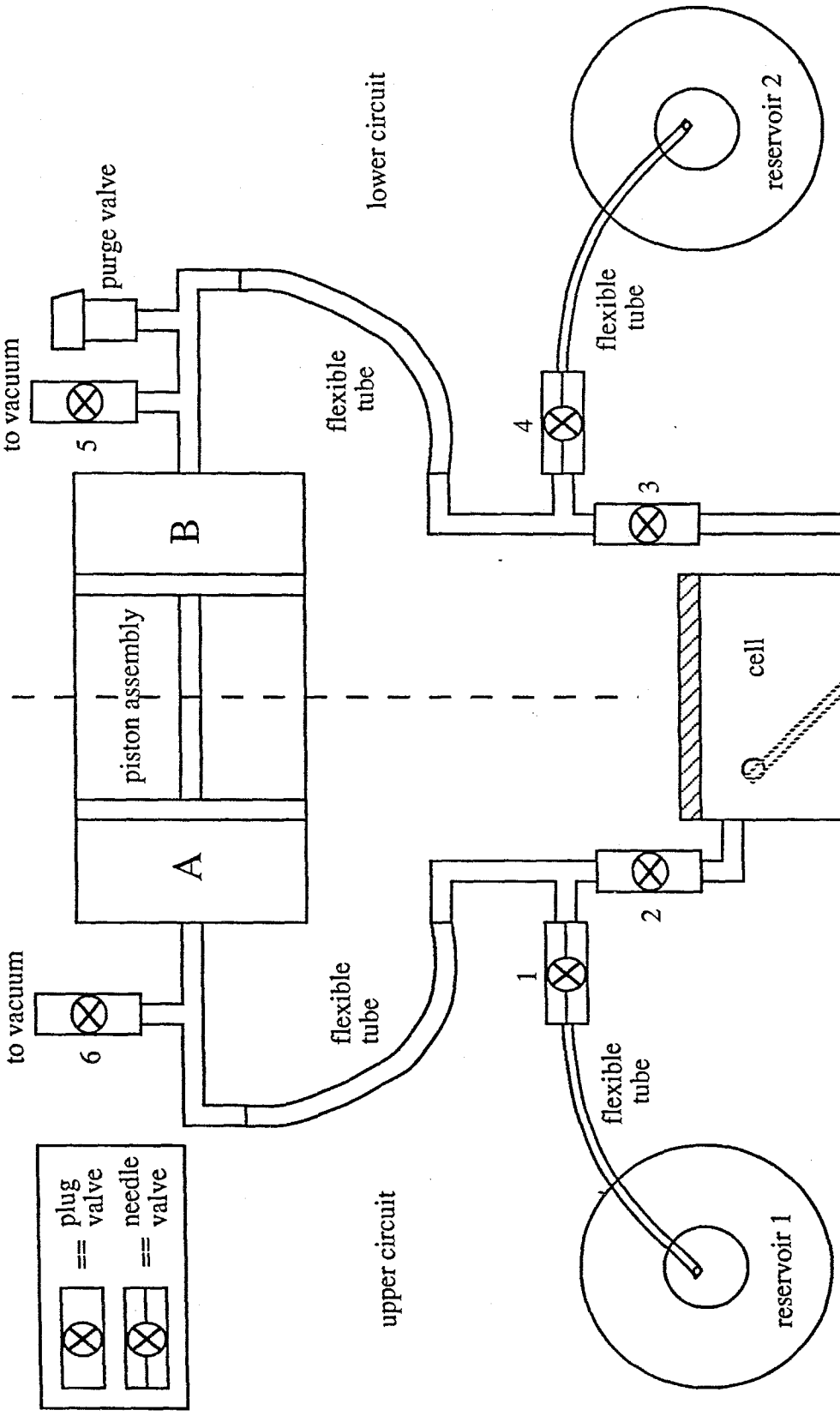

Fig. 5 Plumbing connections

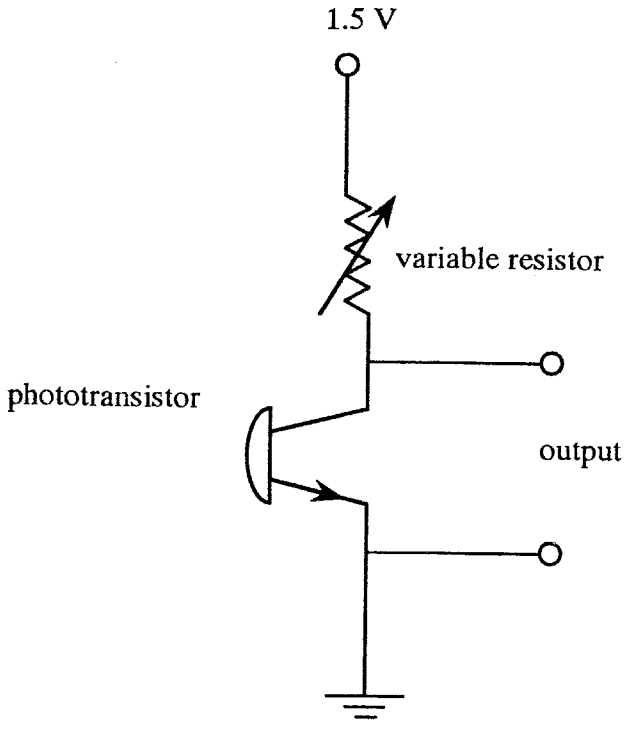

Fig. 6 Laser-power monitor circuit

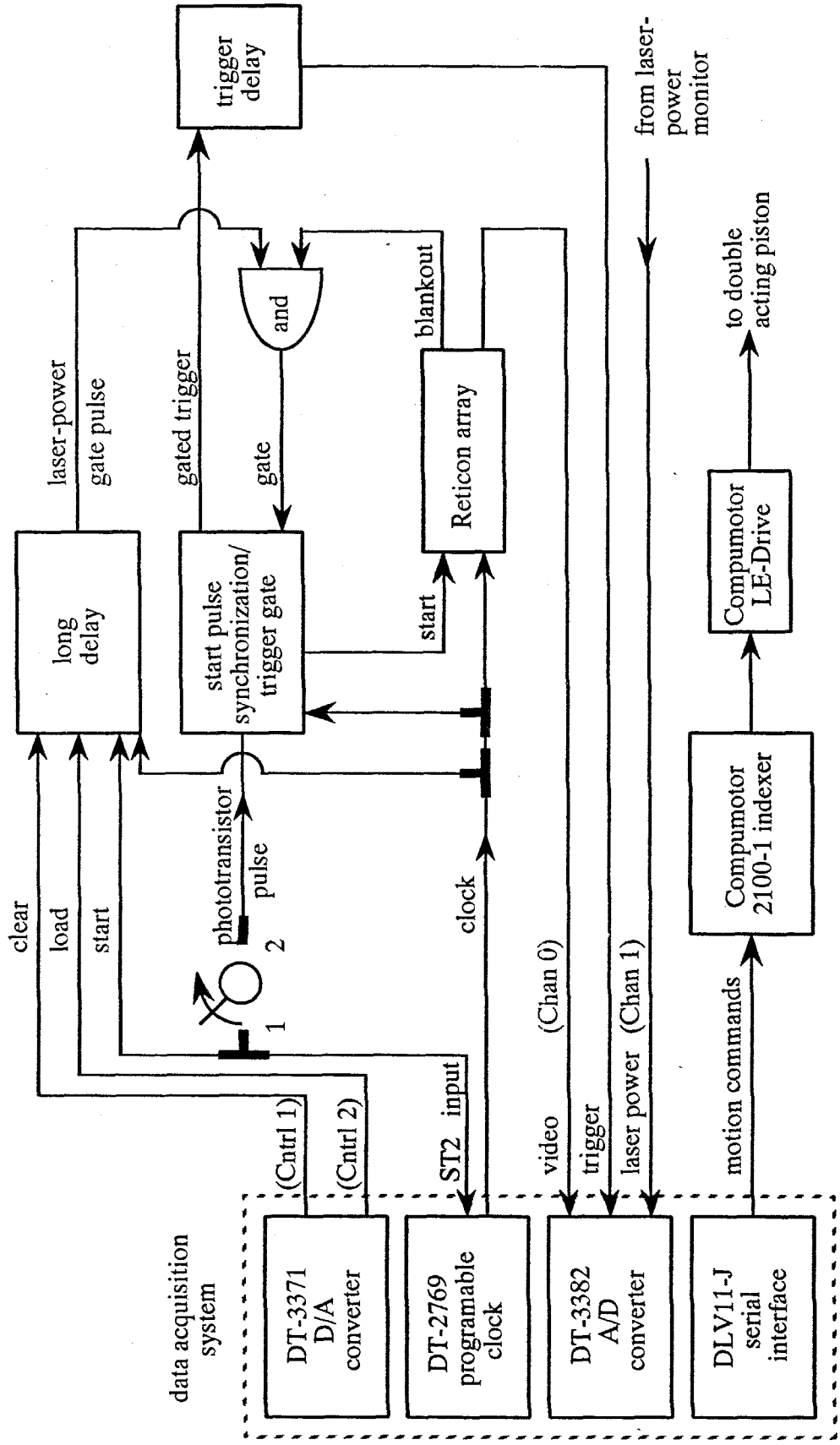

Fig. 7 Block diagram of device interconnection

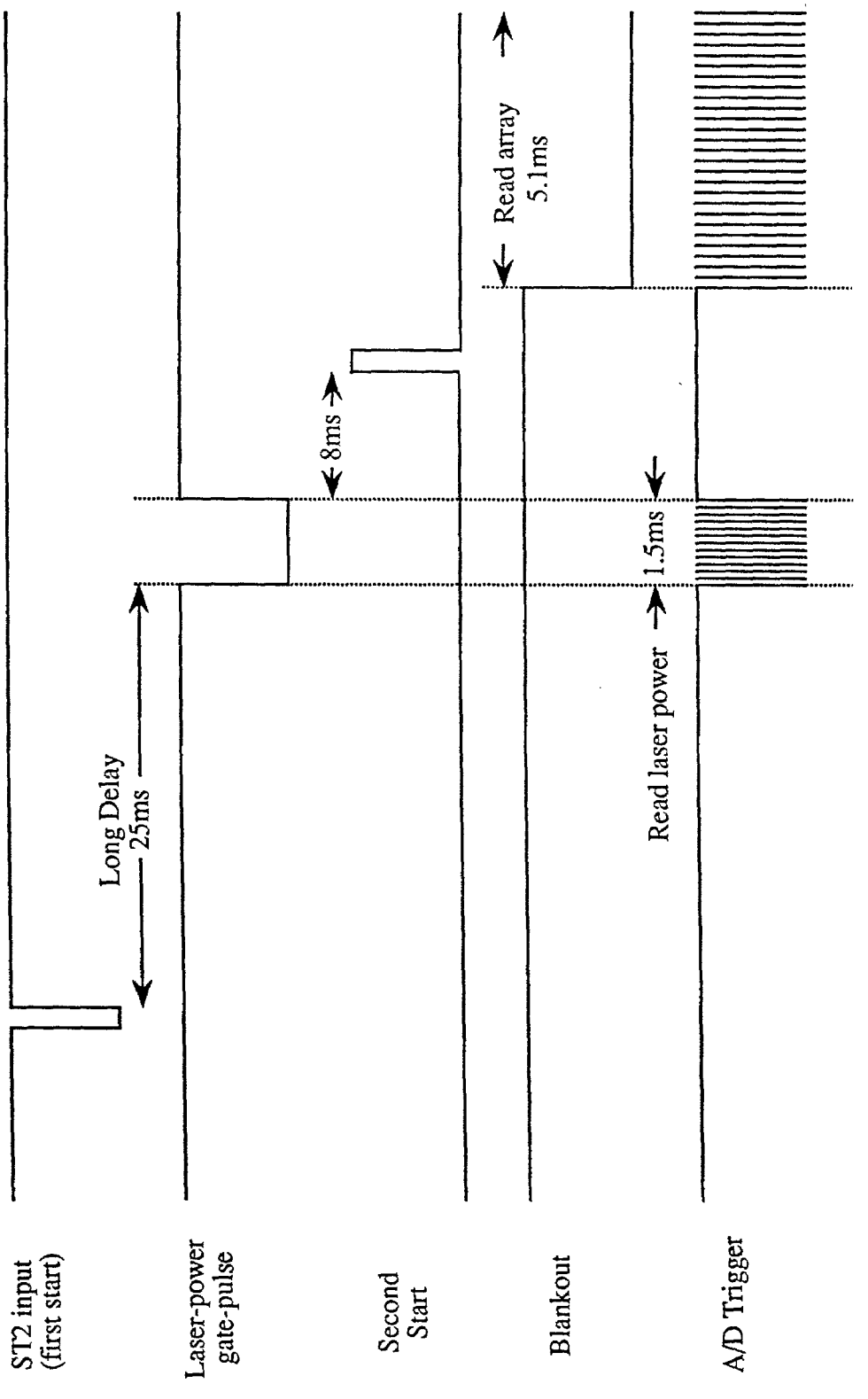

Fig. 8 Timing diagram for data acquisition

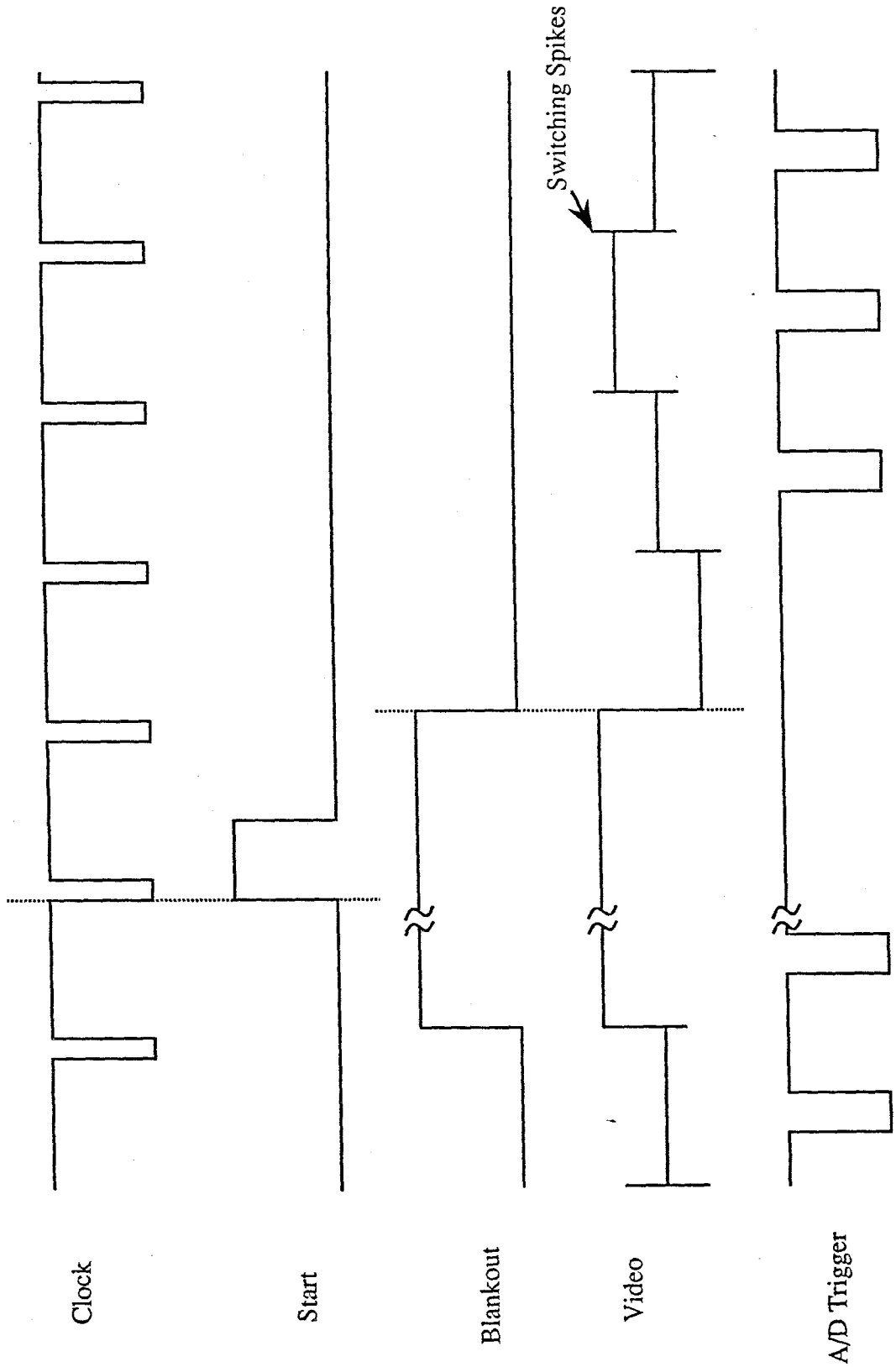

Fig. 9 Detail of Timing diagram for data acquisition

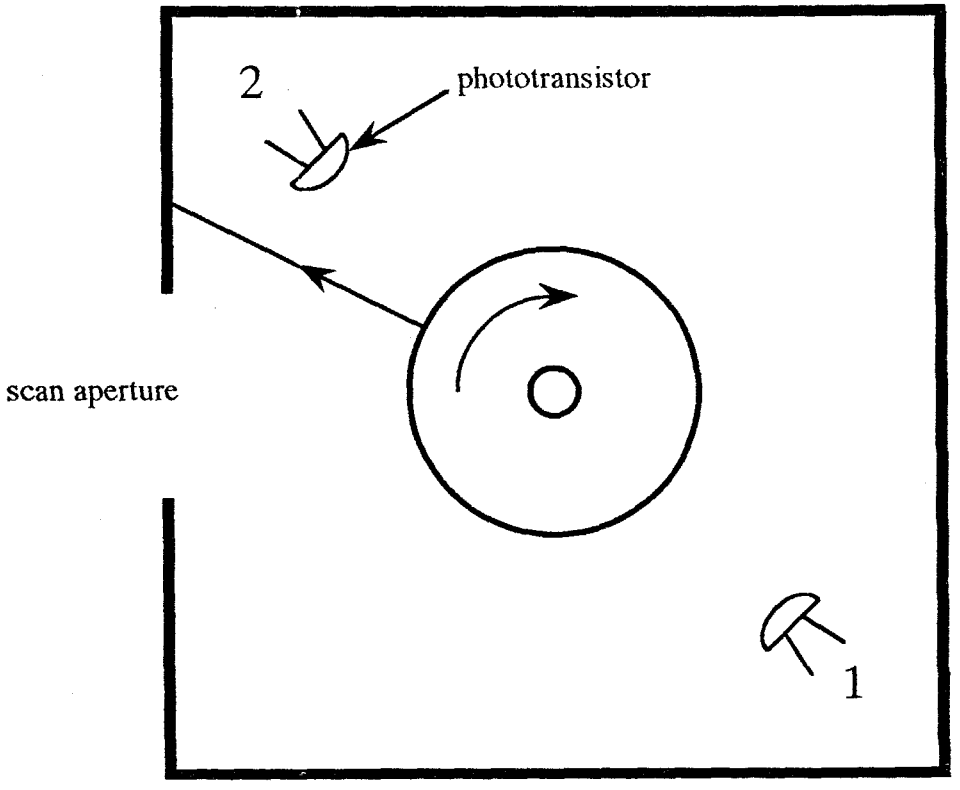

Fig. 10 Detail of phototransistor position

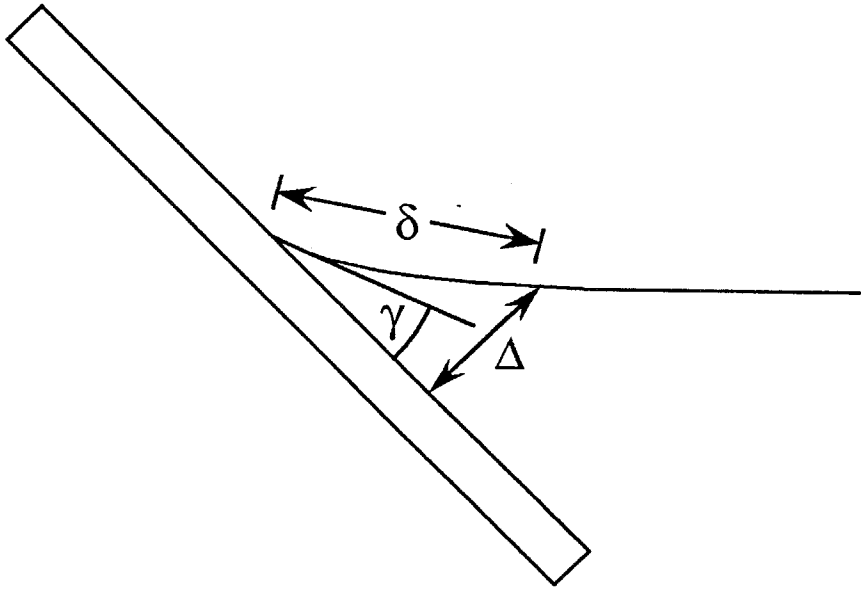

Fig 11 Contact line unwetting

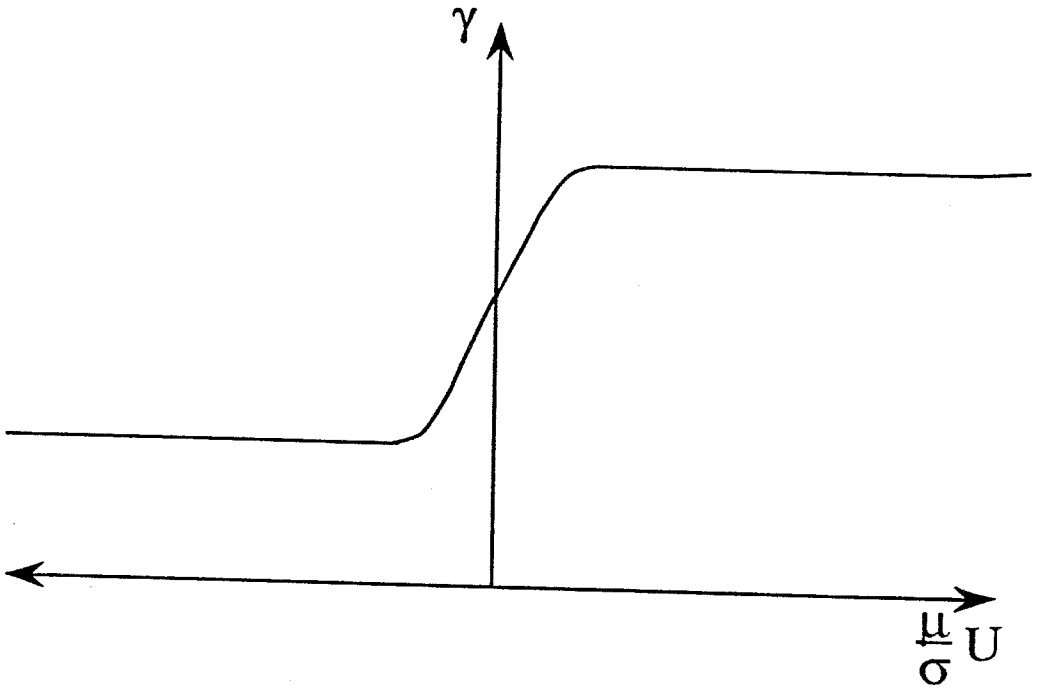

Fig. 12 Generic plot of contact angle vs. velocity

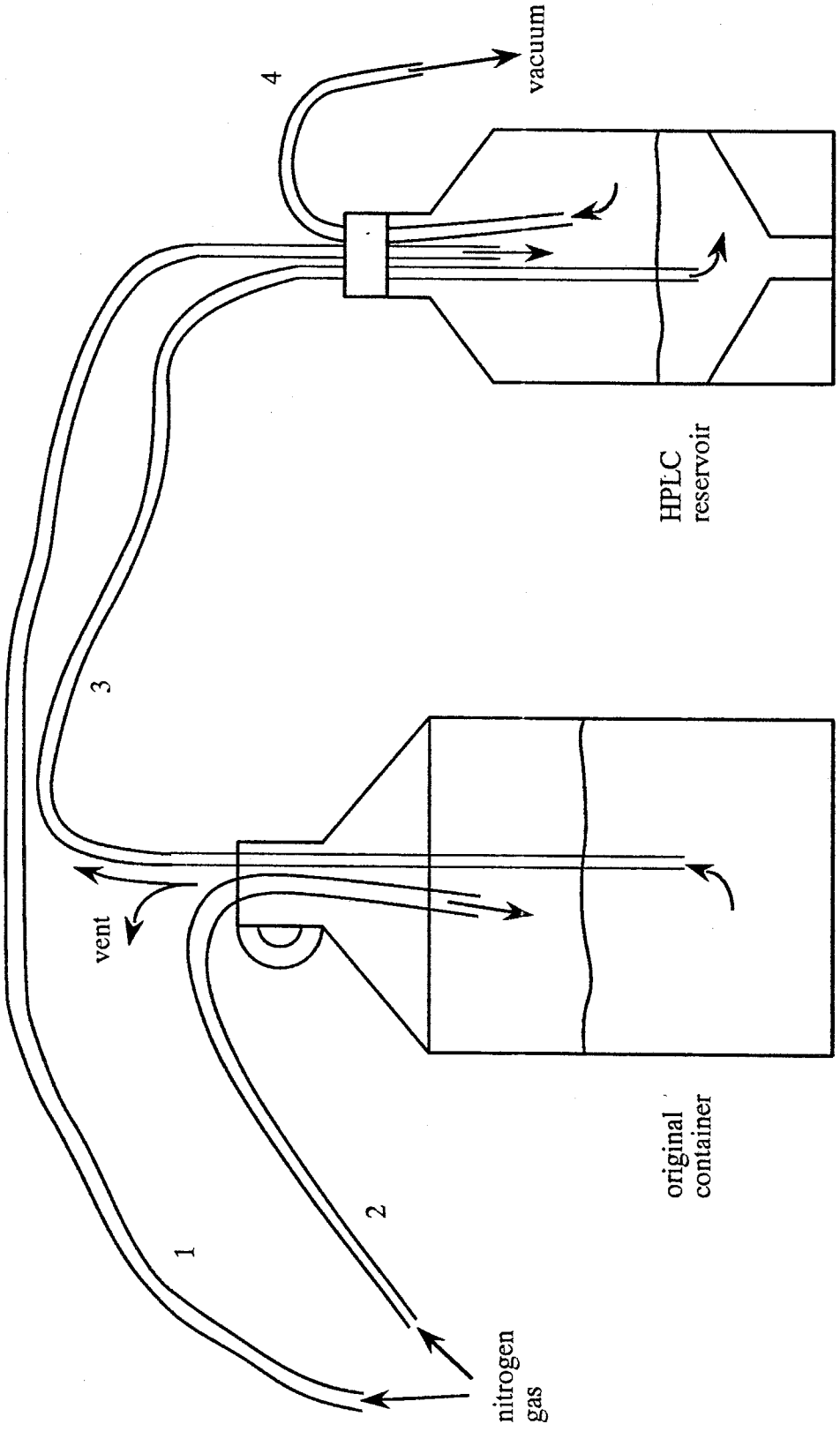

Fig. 13 Liquid transfer from original container to HPLC reservoir

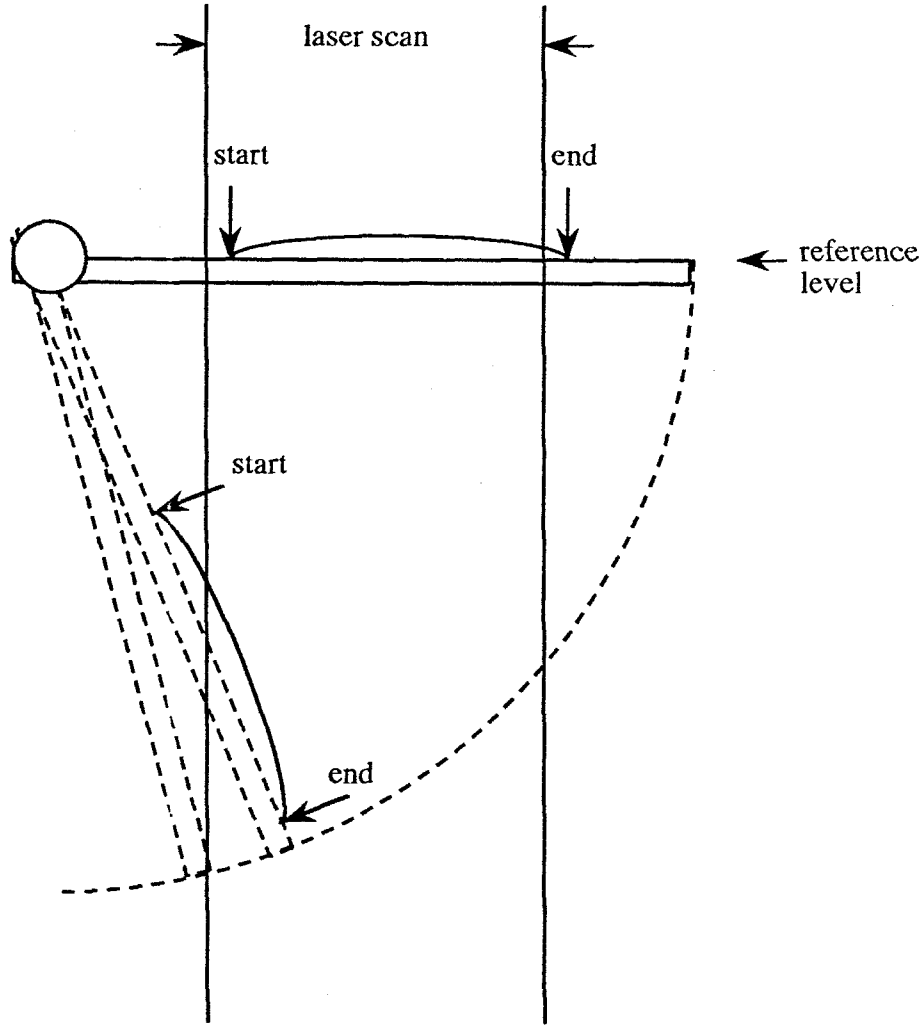

Figure 14 Measurement region on plate

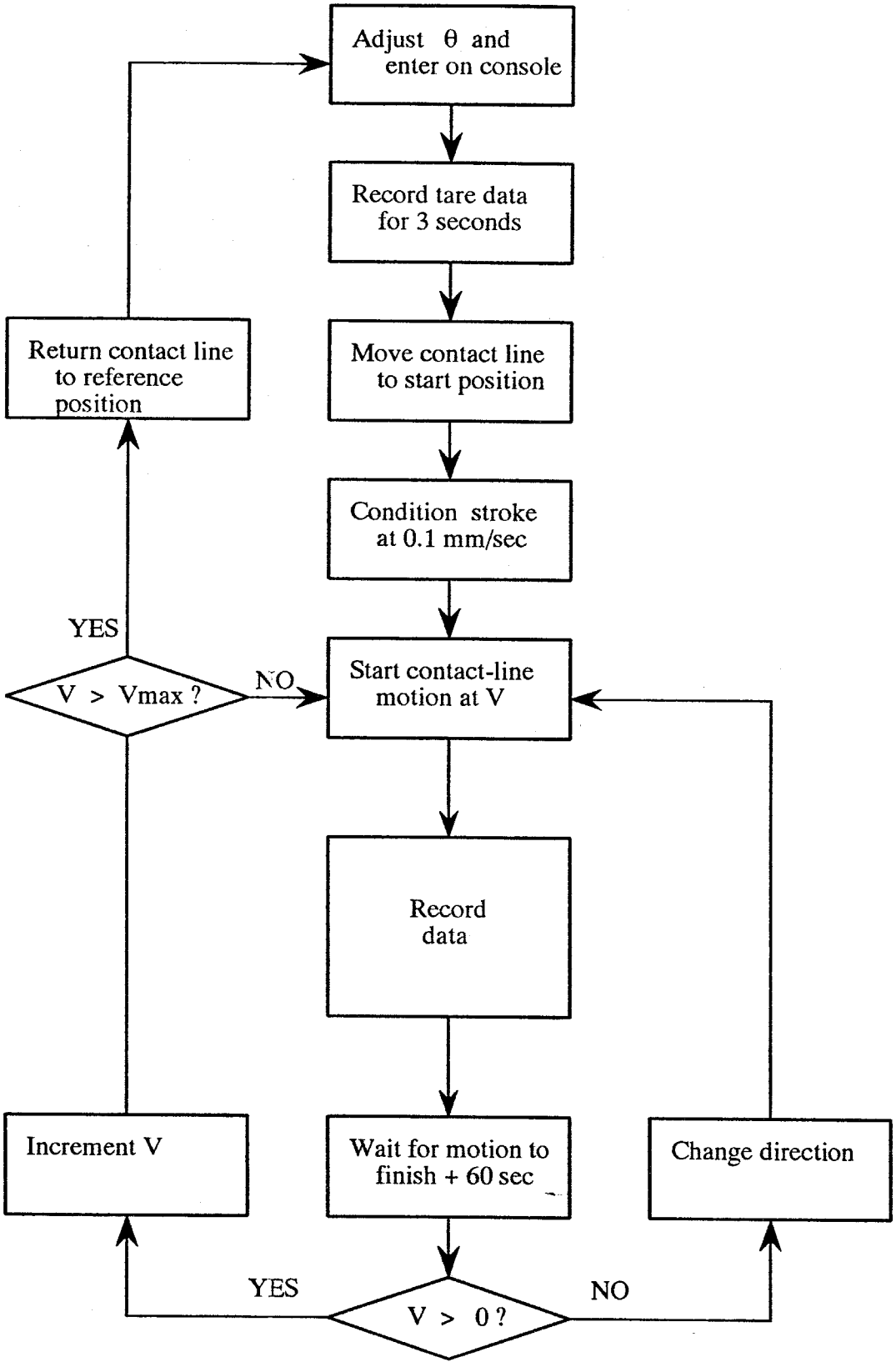

Fig. 15 Data acquisition flow chart

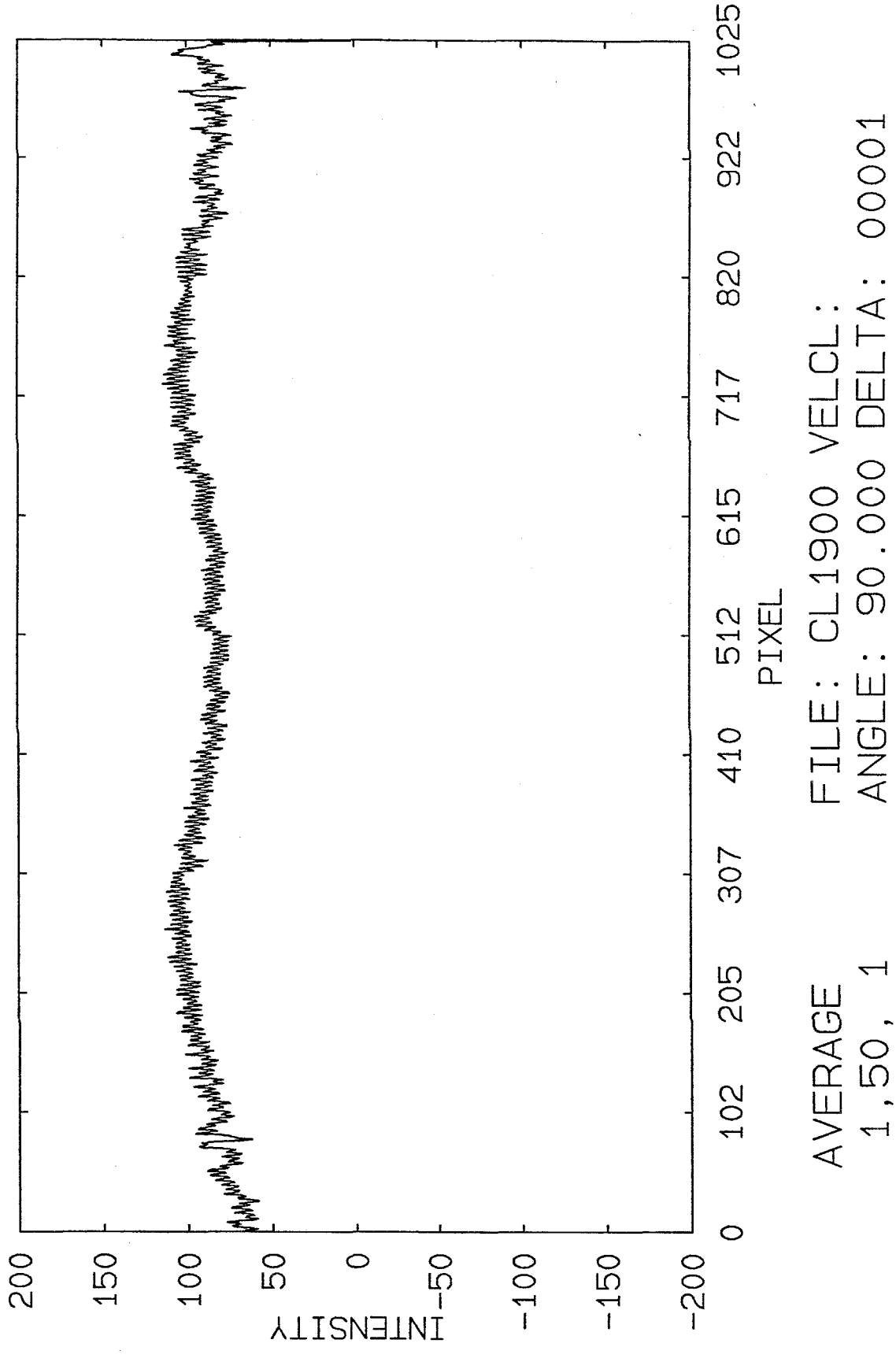
AVERAGE
1,50, 1
FILE: CL1900 VELCL:
ANGLE: 90.000 DELTA: 00001
INTENSITY
PIXEL
200
150
100
50
0
-50
-100
-150
-200
0
102
205
307
410
512
615
717
820
922
1025

Figure 16

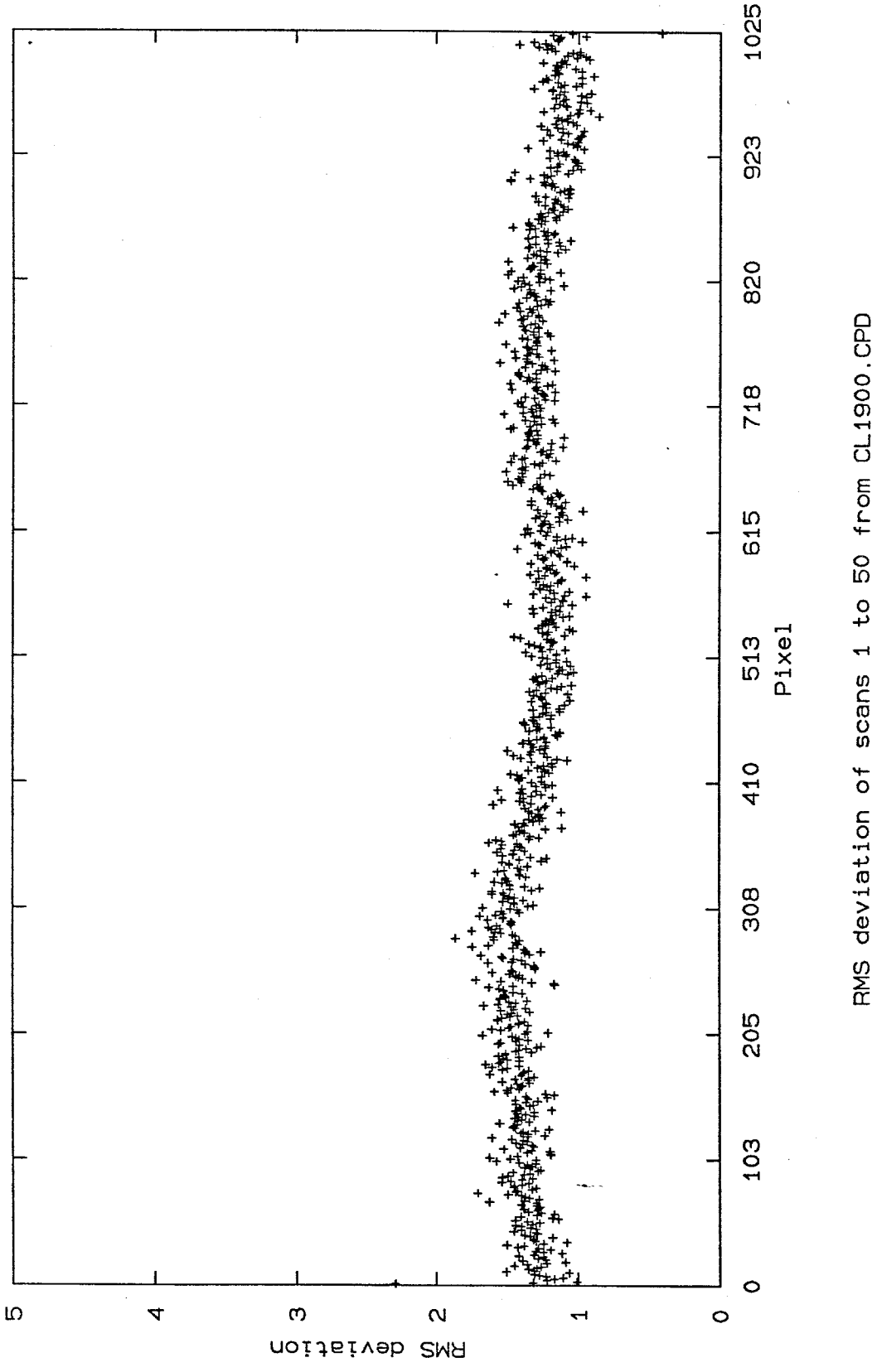
RMS deviation of scans 1 to 50 from CL1900.CPD
RMS deviation
Pixel
0
1
2
3
4
5
0
103
205
308
410
513
615
718
820
923
1025

Figure 17

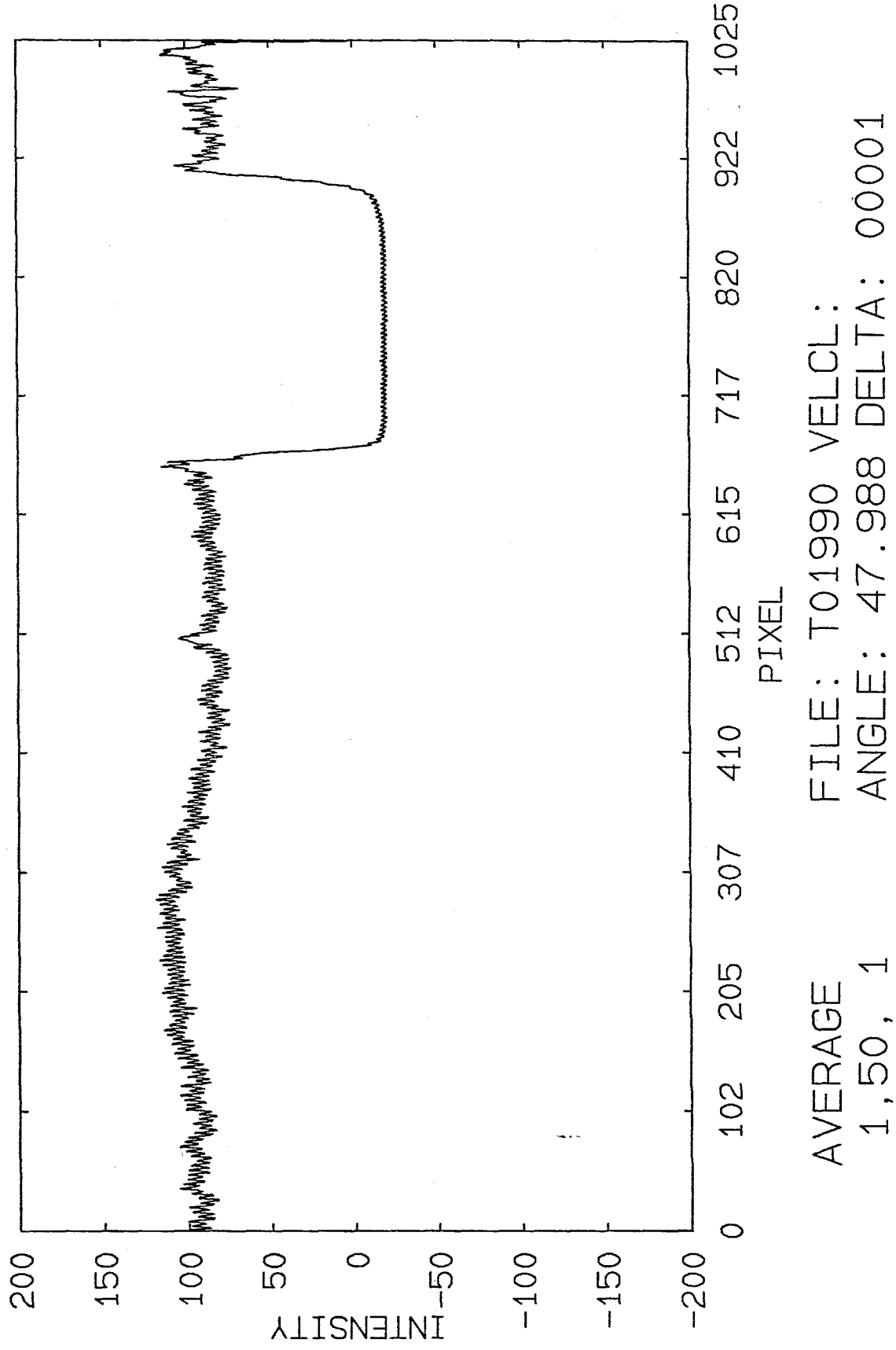
200
150
100
50
0
-50
-100
-150
-200
INTENSITY
0
102
205
307
410
512
615
717
820
922
1025
PIXEL
AVERAGE
1,50, 1
FILE: T01990 VELCL:
ANGLE: 47.988 DELTA: 00001

Figure 18

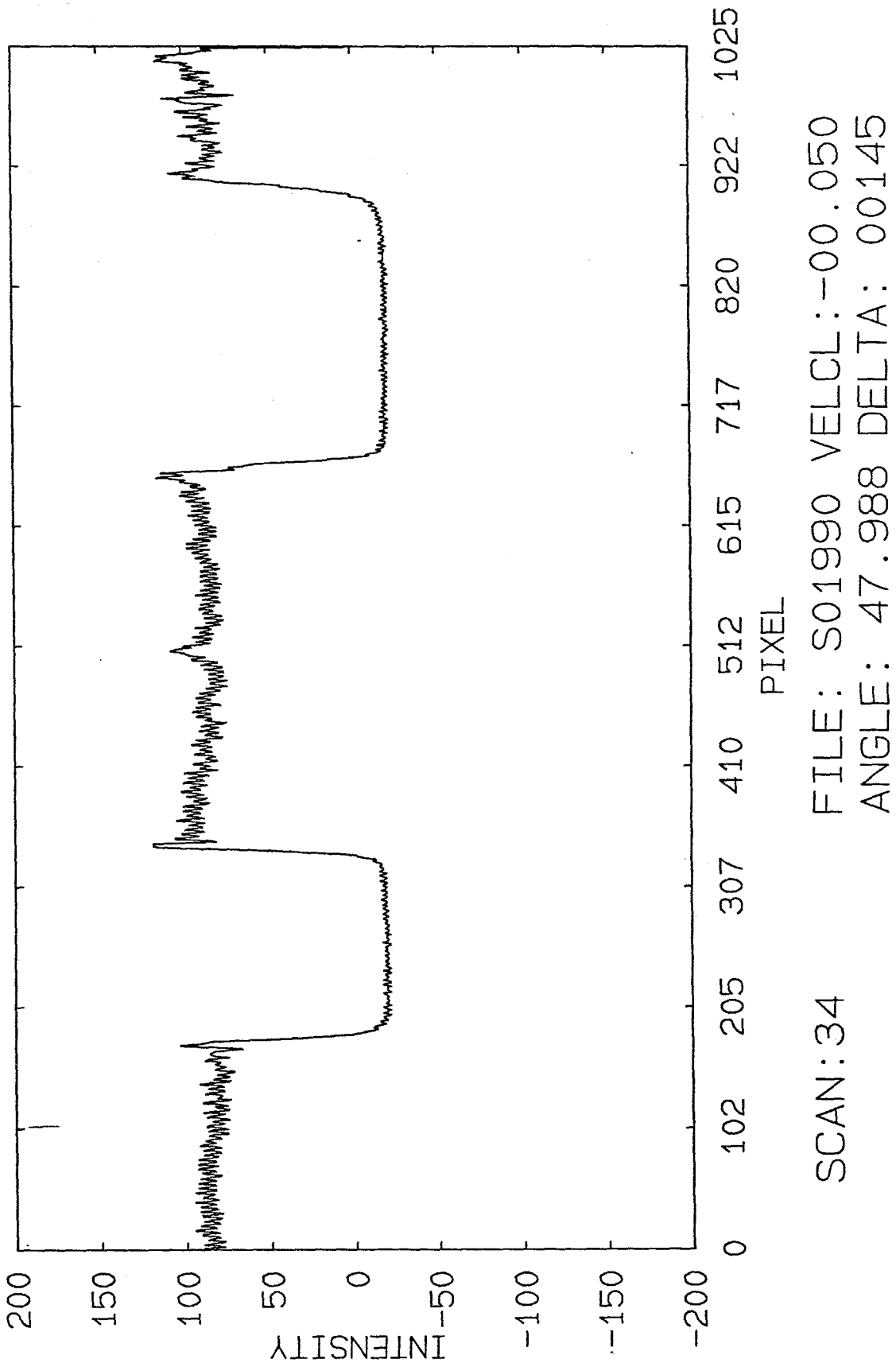
200
150
100
50
0
-50
-100
-150
-200
INTENSITY
0
102
205
307
410
512
615
717
820
922
1025
PIXEL
SCAN:34
FILE: S01990 VELCL:-00.050
ANGLE: 47.988 DELTA: 00145

Figure 19

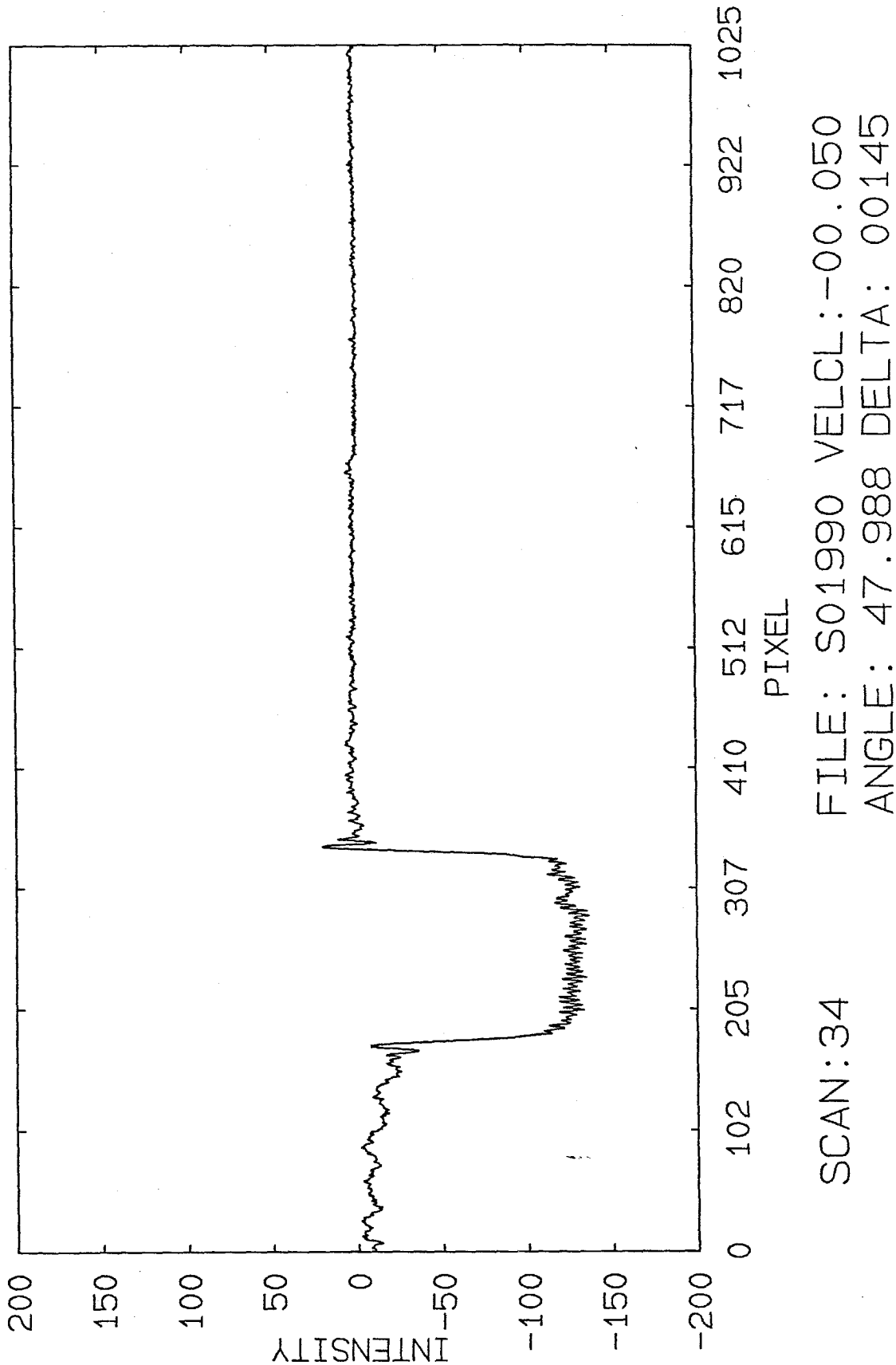
INTENSITY
200
150
100
50
0
-50
-100
-150
-200
0
102
205
307
410
512
615
717
820
922
1025
PIXEL
SCAN:34
FILE: S01990 VELCL:-00.050
ANGLE: 47.988 DELTA: 00145

Figure 20

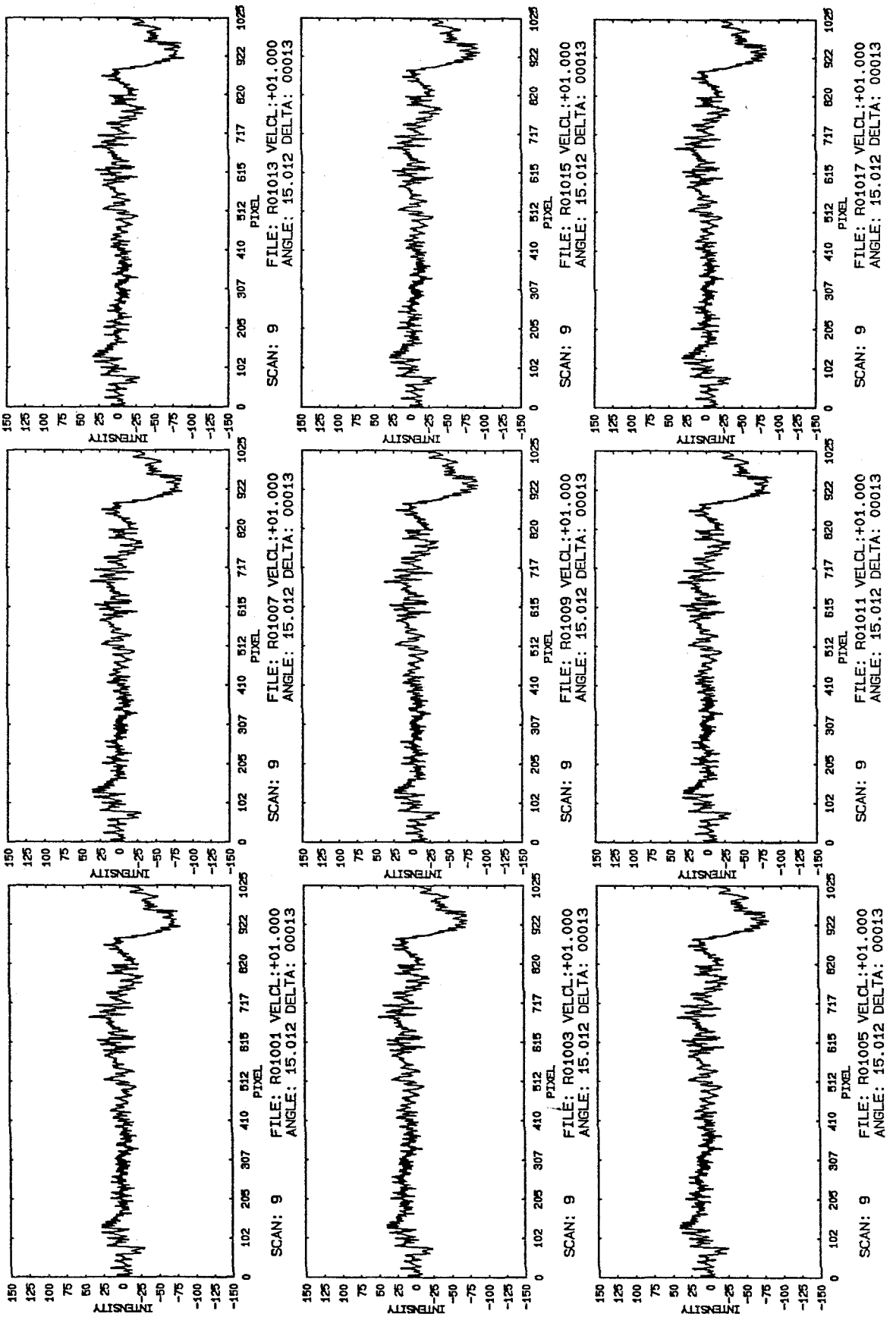
INTENSITY
PIXEL
SCAN: 9
FILE: R01001 VELCL:+01.000
ANGLE: 15.012 DELTA: 00013
FILE: R01003 VELCL:+01.000
ANGLE: 15.012 DELTA: 00013
FILE: R01005 VELCL:+01.000
ANGLE: 15.012 DELTA: 00013
FILE: R01007 VELCL:+01.000
ANGLE: 15.012 DELTA: 00013
FILE: R01009 VELCL:+01.000
ANGLE: 15.012 DELTA: 00013
FILE: R01011 VELCL:+01.000
ANGLE: 15.012 DELTA: 00013
FILE: R01013 VELCL:+01.000
ANGLE: 15.012 DELTA: 00013
FILE: R01015 VELCL:+01.000
ANGLE: 15.012 DELTA: 00013
FILE: R01017 VELCL:+01.000
ANGLE: 15.012 DELTA: 00013

Figure 21

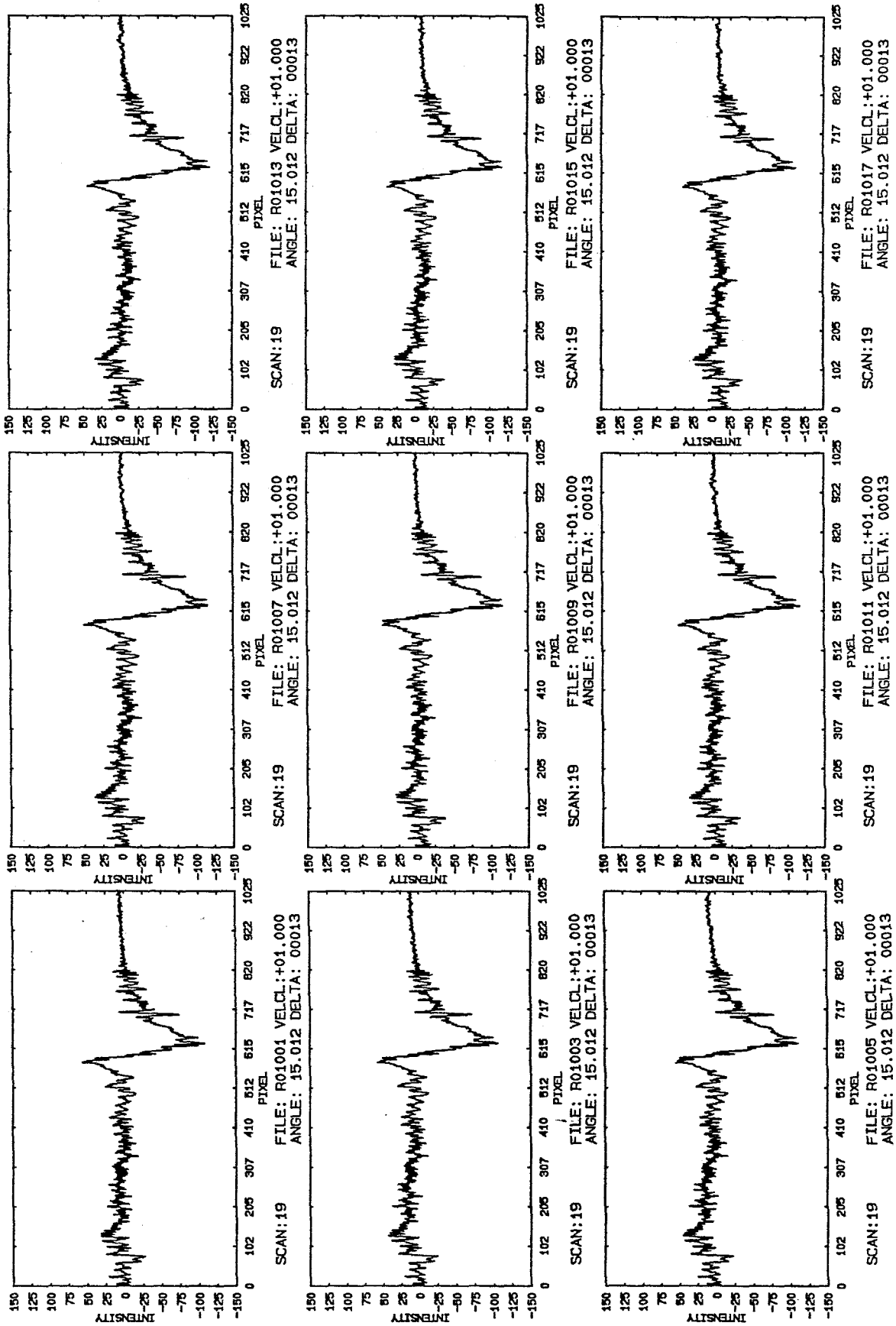
INTENSITY
PIXEL
SCAN:19
FILE: R01001 VELCL:+01.000
ANGLE: 15.012 DELTA: 00013
FILE: R01003 VELCL:+01.000
ANGLE: 15.012 DELTA: 00013
FILE: R01005 VELCL:+01.000
ANGLE: 15.012 DELTA: 00013
FILE: R01007 VELCL:+01.000
ANGLE: 15.012 DELTA: 00013
FILE: R01009 VELCL:+01.000
ANGLE: 15.012 DELTA: 00013
FILE: R01011 VELCL:+01.000
ANGLE: 15.012 DELTA: 00013
FILE: R01013 VELCL:+01.000
ANGLE: 15.012 DELTA: 00013
FILE: R01015 VELCL:+01.000
ANGLE: 15.012 DELTA: 00013
FILE: R01017 VELCL:+01.000
ANGLE: 15.012 DELTA: 00013

Figure 22

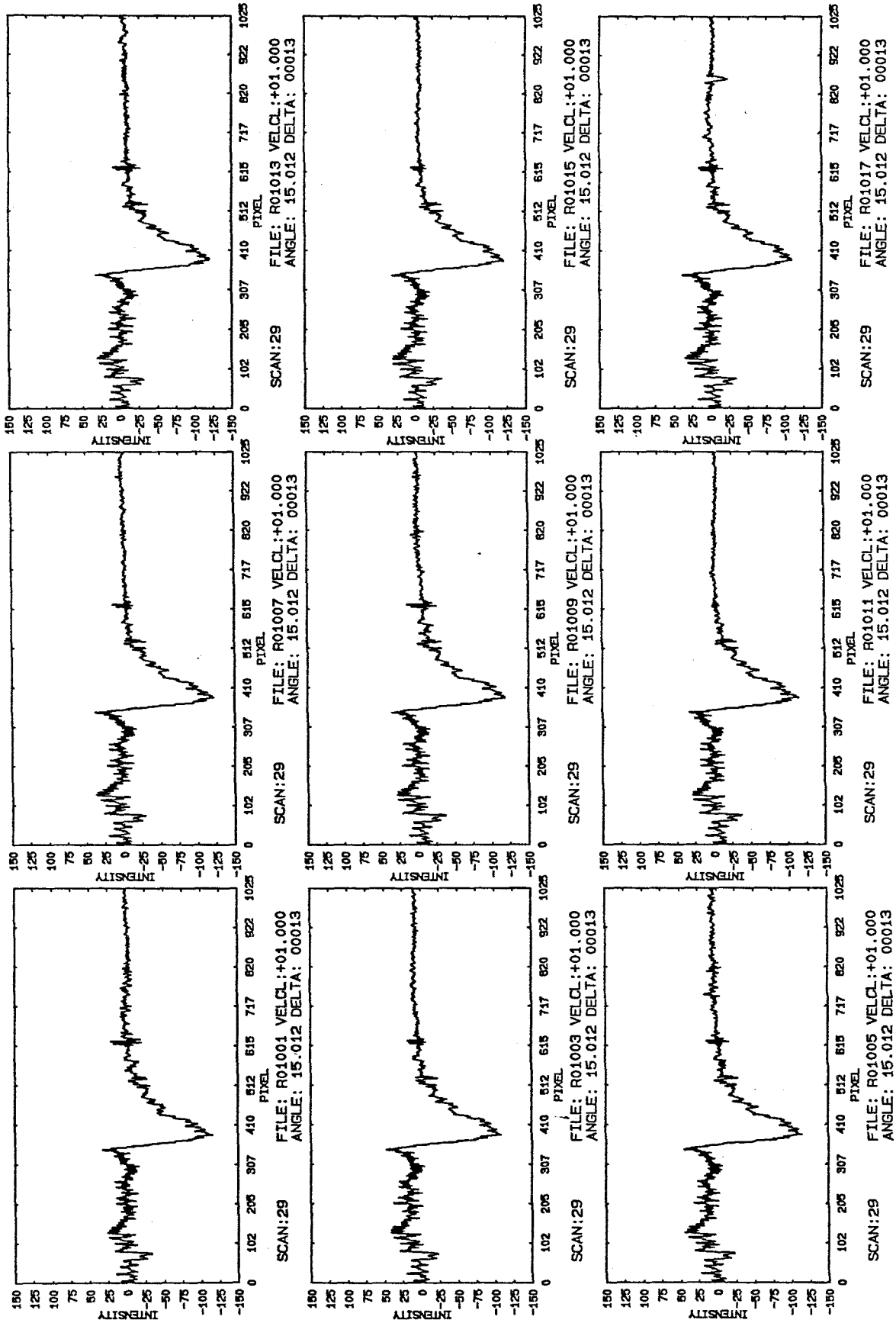
INTENSITY
PIXEL
SCAN:29
FILE: R01001 VELCL:+01.000
ANGLE: 15.012 DELTA: 00013
FILE: R01003 VELCL:+01.000
ANGLE: 15.012 DELTA: 00013
FILE: R01005 VELCL:+01.000
ANGLE: 15.012 DELTA: 00013
FILE: R01007 VELCL:+01.000
ANGLE: 15.012 DELTA: 00013
FILE: R01009 VELCL:+01.000
ANGLE: 15.012 DELTA: 00013
FILE: R01011 VELCL:+01.000
ANGLE: 15.012 DELTA: 00013
FILE: R01013 VELCL:+01.000
ANGLE: 15.012 DELTA: 00013
FILE: R01015 VELCL:+01.000
ANGLE: 15.012 DELTA: 00013
FILE: R01017 VELCL:+01.000
ANGLE: 15.012 DELTA: 00013

Figure 23

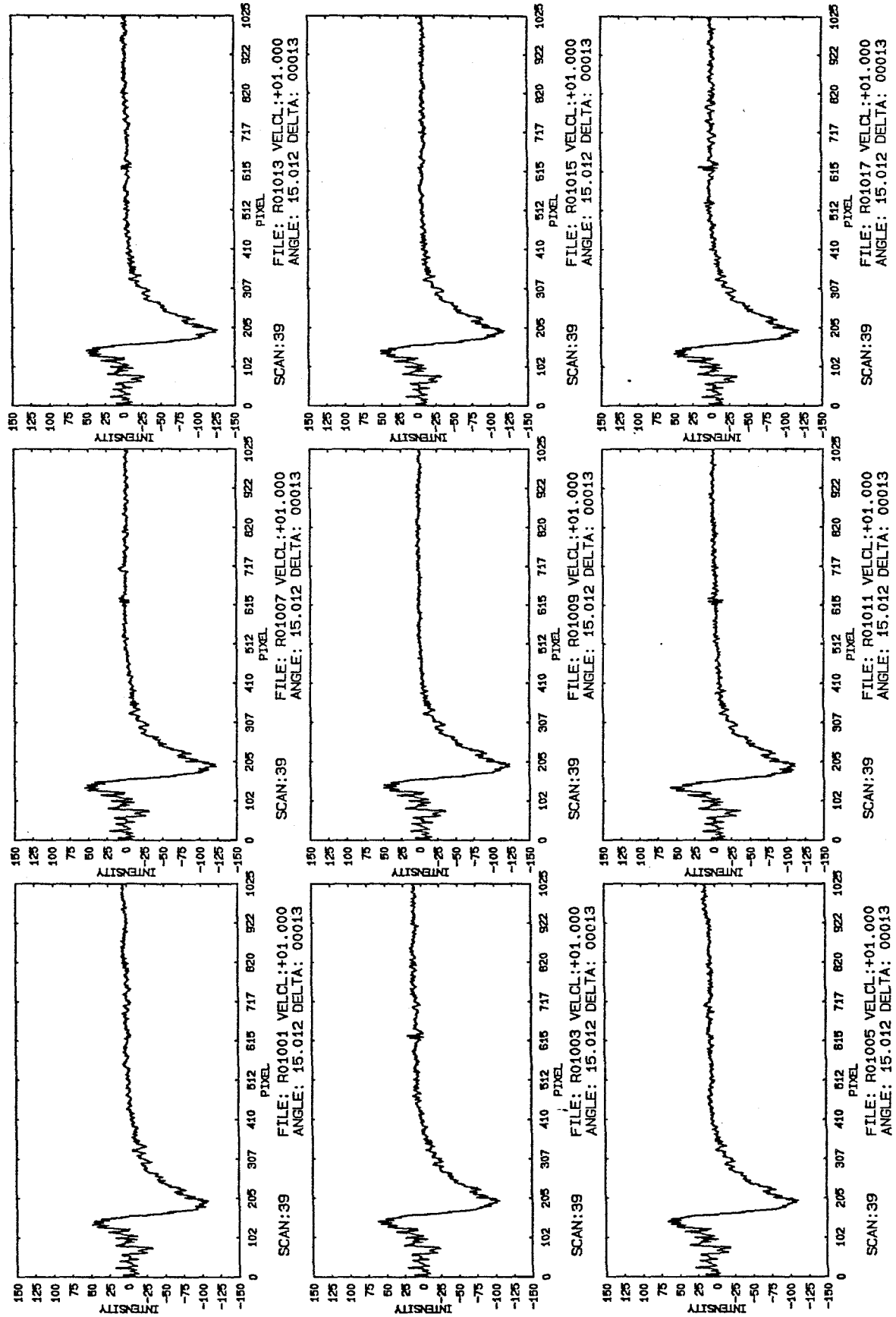
INTENSITY
PIXEL
SCAN:39
FILE: R01001 VELCL:+01.000
ANGLE: 15.012 DELTA: 00013
FILE: R01003 VELCL:+01.000
FILE: R01005 VELCL:+01.000
FILE: R01007 VELCL:+01.000
FILE: R01009 VELCL:+01.000
FILE: R01011 VELCL:+01.000
FILE: R01013 VELCL:+01.000
FILE: R01015 VELCL:+01.000
FILE: R01017 VELCL:+01.000

Figure 24

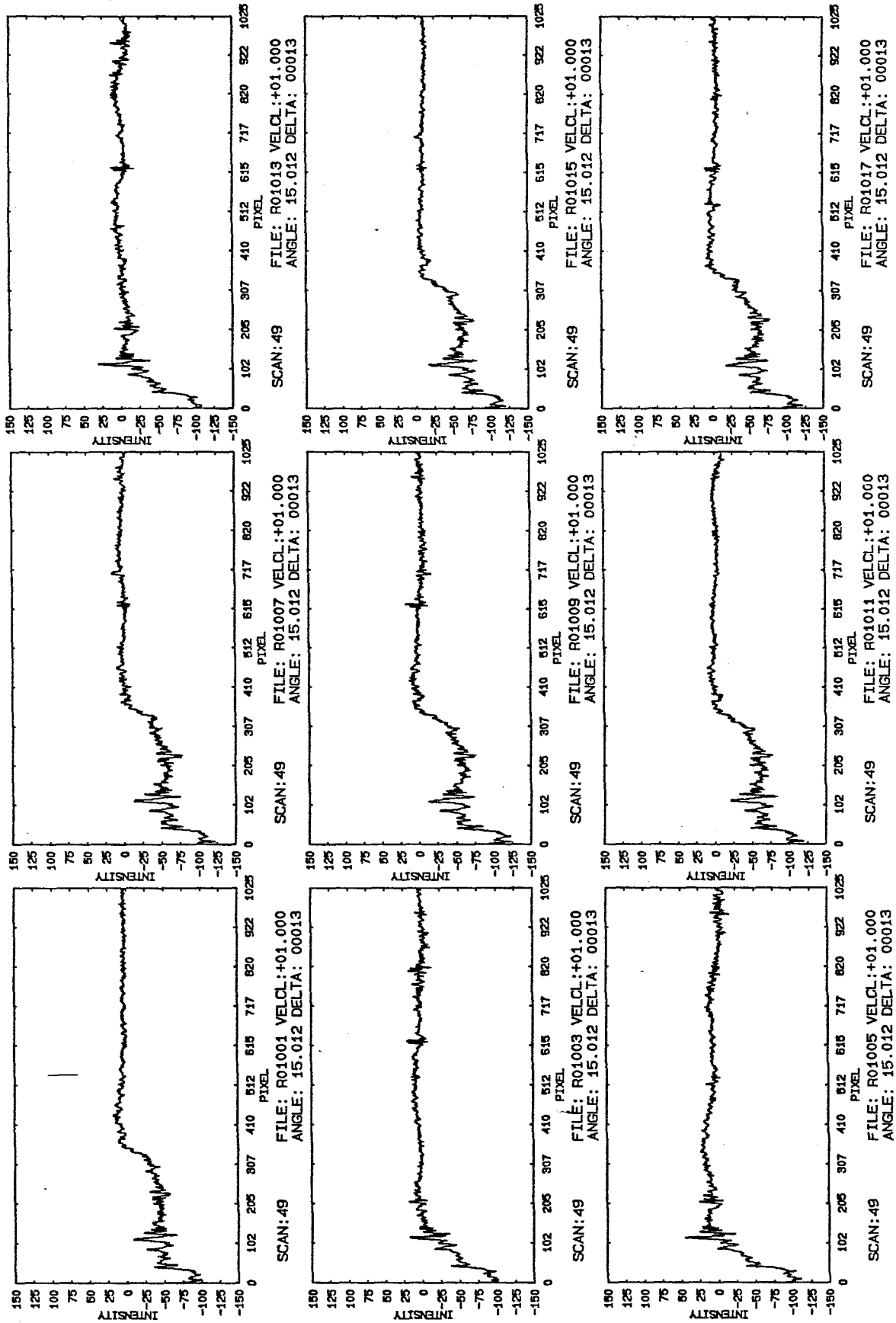
INTENSITY
PIXEL
SCAN:49
FILE: R01001 VELCL:+01.000
ANGLE: 15.012 DELTA: 00013
FILE: R01003 VELCL:+01.000
ANGLE: 15.012 DELTA: 00013
FILE: R01005 VELCL:+01.000
ANGLE: 15.012 DELTA: 00013
FILE: R01007 VELCL:+01.000
ANGLE: 15.012 DELTA: 00013
FILE: R01009 VELCL:+01.000
ANGLE: 15.012 DELTA: 00013
FILE: R01011 VELCL:+01.000
ANGLE: 15.012 DELTA: 00013
FILE: R01013 VELCL:+01.000
ANGLE: 15.012 DELTA: 00013
FILE: R01015 VELCL:+01.000
ANGLE: 15.012 DELTA: 00013
FILE: R01017 VELCL:+01.000
ANGLE: 15.012 DELTA: 00013

Figure 25

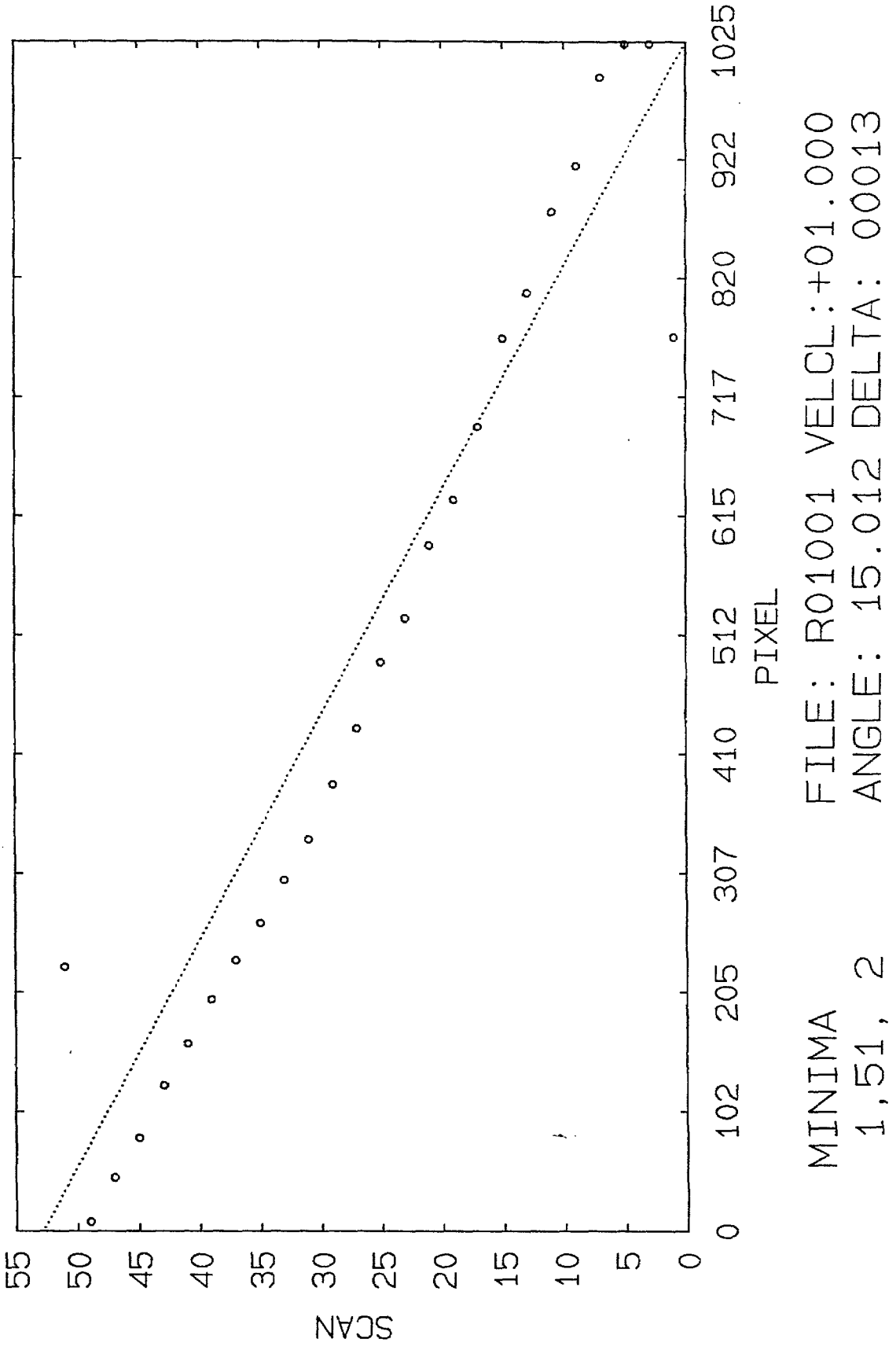
FILE: R01001 VELCL:+01.000
ANGLE: 15.012 DELTA: 00013
MINIMA
1,51, 2
SCAN
55
50
45
40
35
30
25
20
15
10
5
0
0
102
205
307
410
512
615
717
820
922
1025
PIXEL

Figure 26

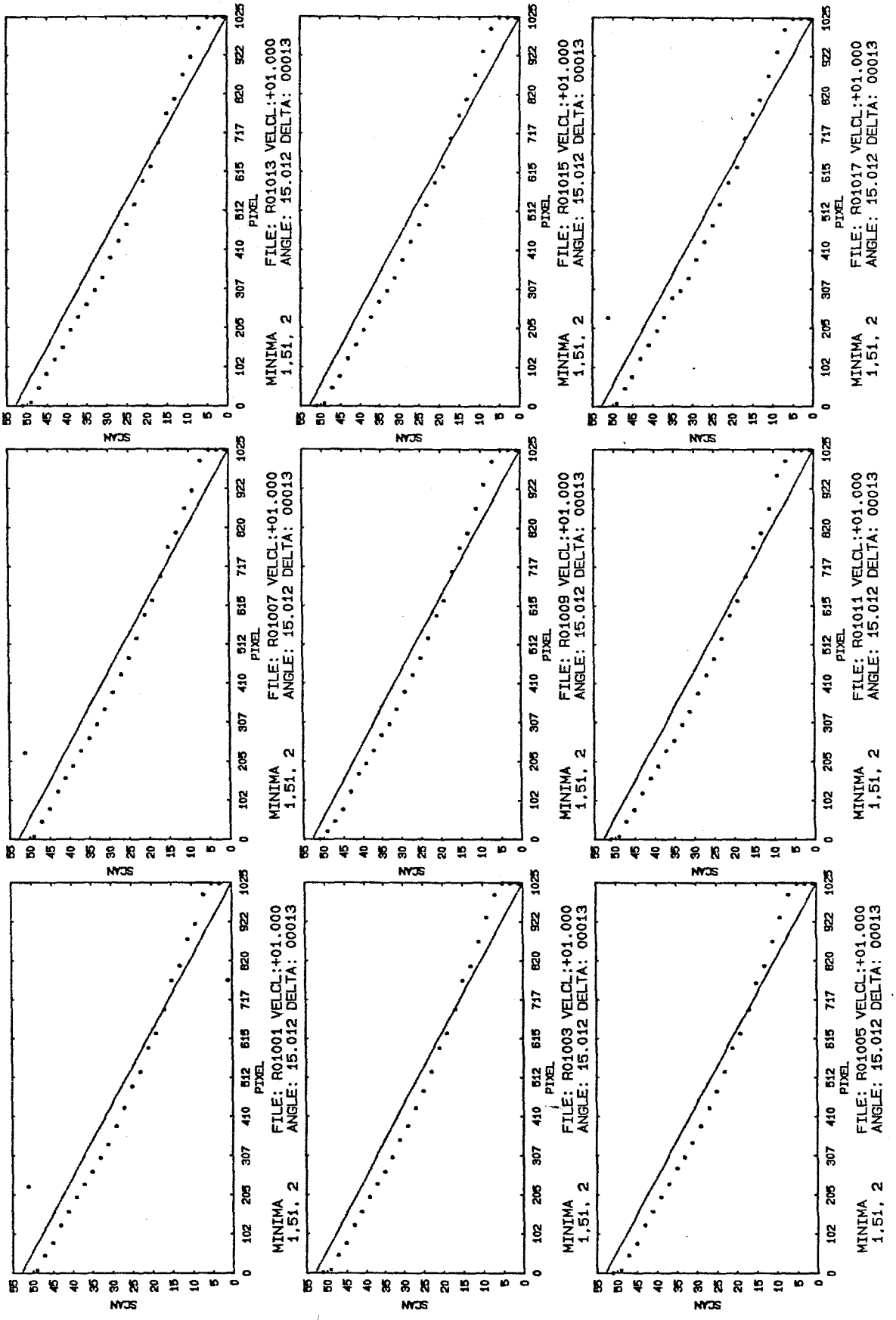
SCAN
PIXEL
MINIMA
1,51, 2
FILE: R01001 VELCL:+01.000
ANGLE: 15.012 DELTA: 00013
FILE: R01003 VELCL:+01.000
ANGLE: 15.012 DELTA: 00013
FILE: R01005 VELCL:+01.000
ANGLE: 15.012 DELTA: 00013
FILE: R01007 VELCL:+01.000
ANGLE: 15.012 DELTA: 00013
FILE: R01009 VELCL:+01.000
ANGLE: 15.012 DELTA: 00013
FILE: R01011 VELCL:+01.000
ANGLE: 15.012 DELTA: 00013
FILE: R01013 VELCL:+01.000
ANGLE: 15.012 DELTA: 00013
FILE: R01015 VELCL:+01.000
ANGLE: 15.012 DELTA: 00013
FILE: R01017 VELCL:+01.000
ANGLE: 15.012 DELTA: 00013

Figure 27

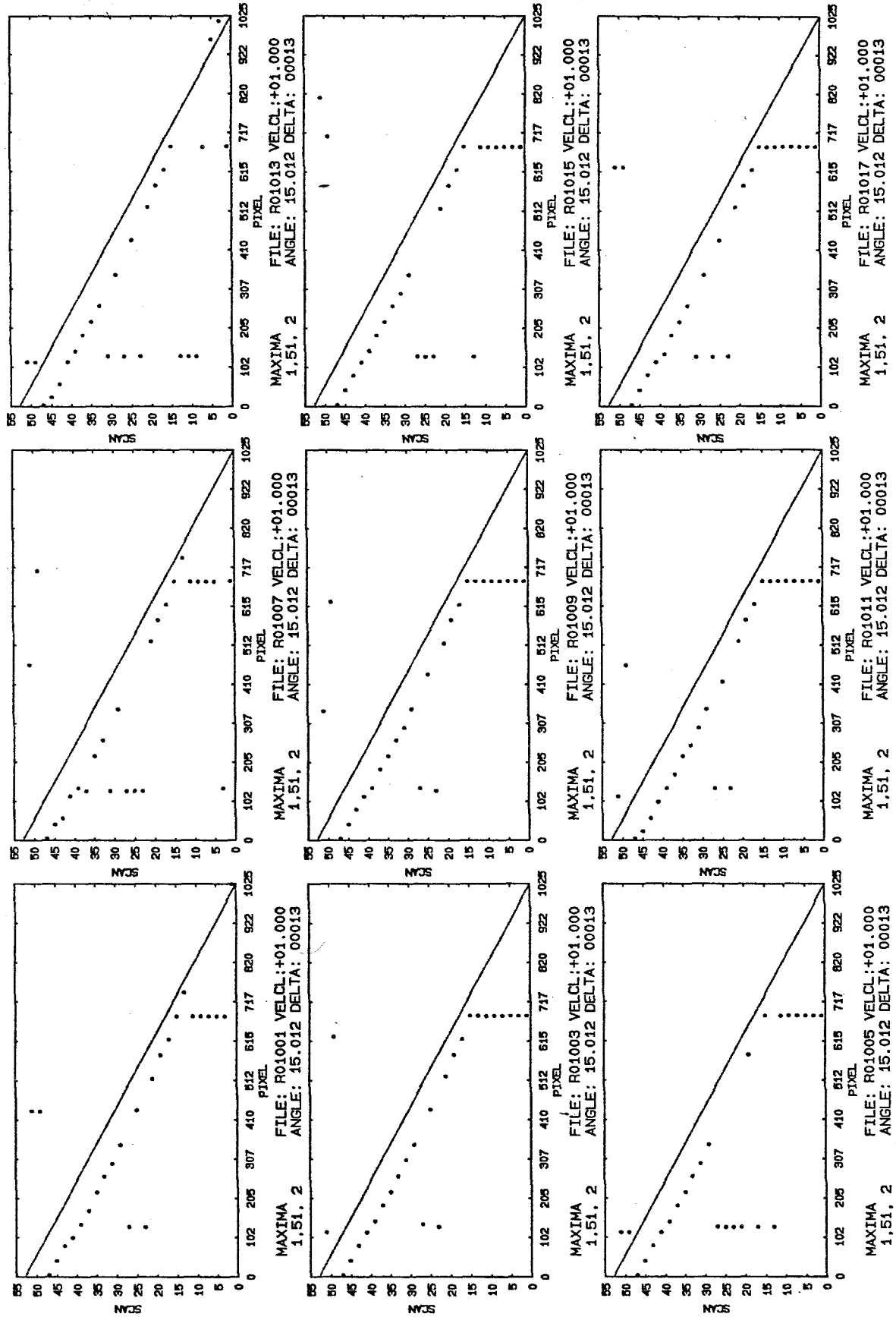
FILE: R01001 VELCL:+01.000
ANGLE: 15.012 DELTA: 00013
MAXIMA
1,51, 2
FILE: R01003 VELCL:+01.000
ANGLE: 15.012 DELTA: 00013
MAXIMA
1,51, 2
FILE: R01005 VELCL:+01.000
ANGLE: 15.012 DELTA: 00013
MAXIMA
1,51, 2
FILE: R01007 VELCL:+01.000
ANGLE: 15.012 DELTA: 00013
MAXIMA
1,51, 2
FILE: R01009 VELCL:+01.000
ANGLE: 15.012 DELTA: 00013
MAXIMA
1,51, 2
FILE: R01011 VELCL:+01.000
ANGLE: 15.012 DELTA: 00013
MAXIMA
1,51, 2
FILE: R01013 VELCL:+01.000
ANGLE: 15.012 DELTA: 00013
MAXIMA
1,51, 2
FILE: R01015 VELCL:+01.000
ANGLE: 15.012 DELTA: 00013
MAXIMA
1,51, 2
FILE: R01017 VELCL:+01.000
ANGLE: 15.012 DELTA: 00013
SCAN
PIXEL

Figure 28

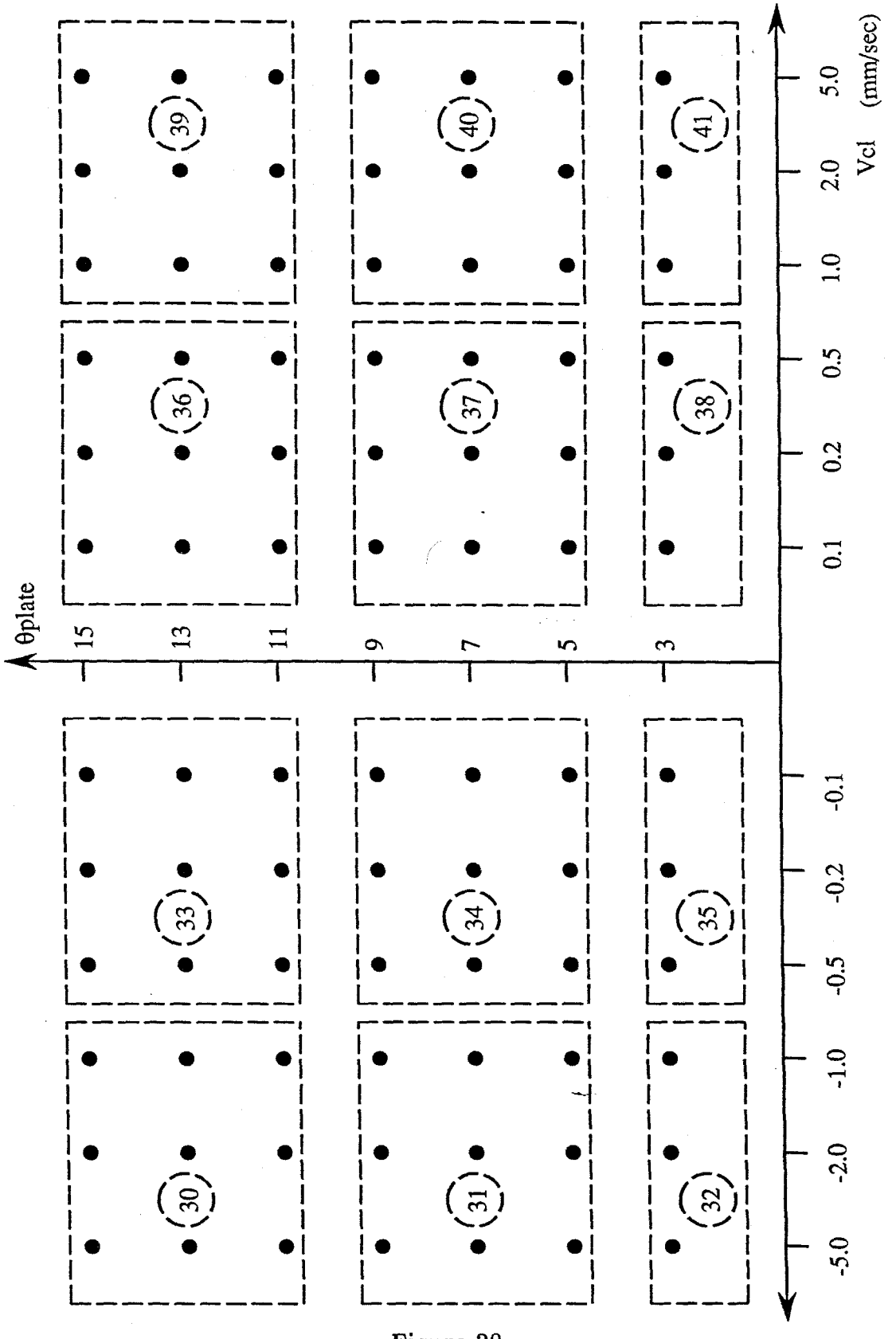

(Plate-angle, Velocity) space for "slippery"-plate experiments

Figure 29

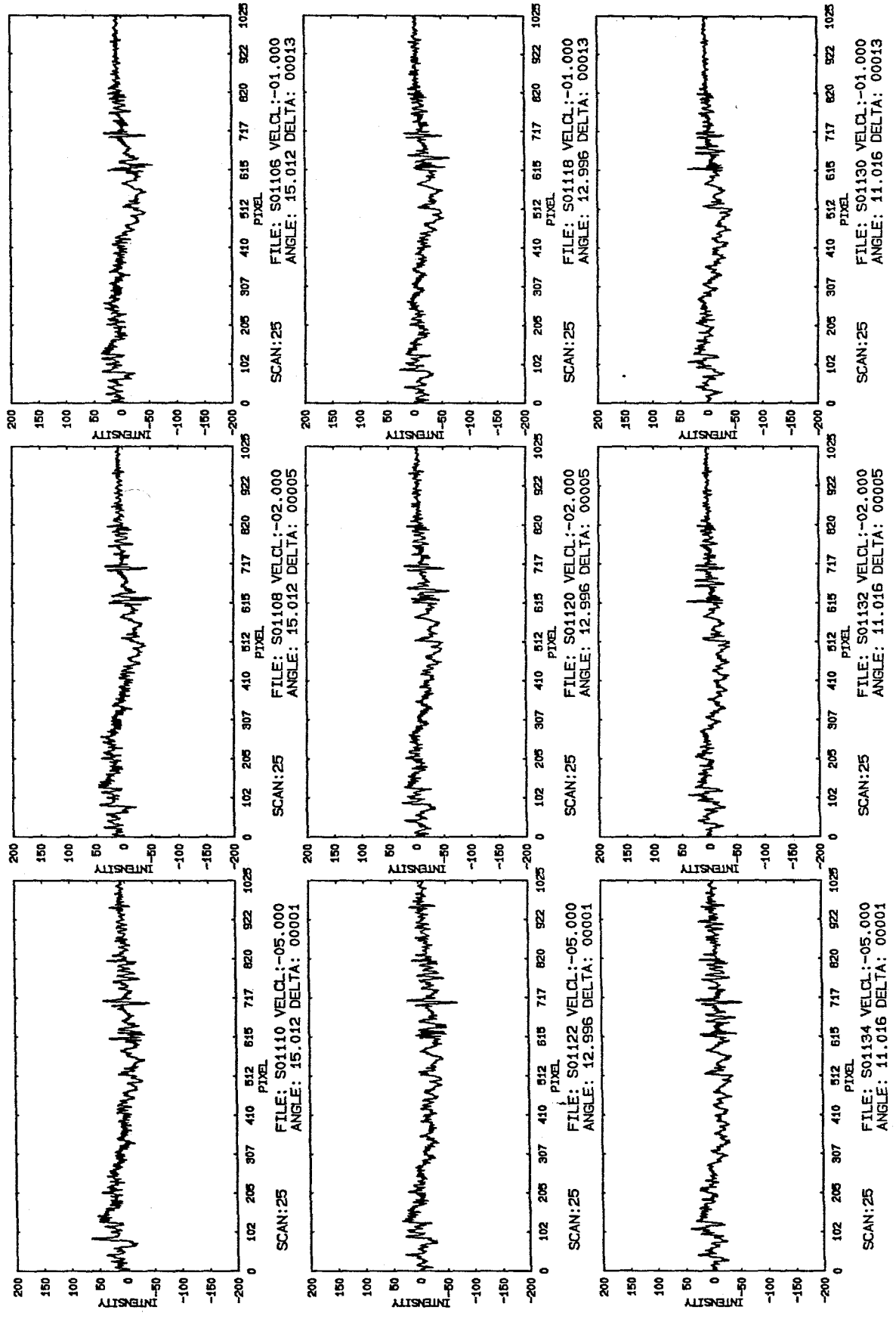
INTENSITY
PIXEL
SCAN:25
FILE: S01105 VELCL:-01.000
ANGLE: 15.012 DELTA: 00013
FILE: S01108 VELCL:-02.000
ANGLE: 15.012 DELTA: 00005
FILE: S01110 VELCL:-05.000
ANGLE: 15.012 DELTA: 00001
FILE: S01118 VELCL:-01.000
ANGLE: 12.996 DELTA: 00013
FILE: S01120 VELCL:-02.000
ANGLE: 12.996 DELTA: 00005
FILE: S01122 VELCL:-05.000
ANGLE: 12.996 DELTA: 00001
FILE: S01130 VELCL:-01.000
ANGLE: 11.016 DELTA: 00013
FILE: S01132 VELCL:-02.000
ANGLE: 11.016 DELTA: 00005
FILE: S01134 VELCL:-05.000
ANGLE: 11.016 DELTA: 00001

Figure 30

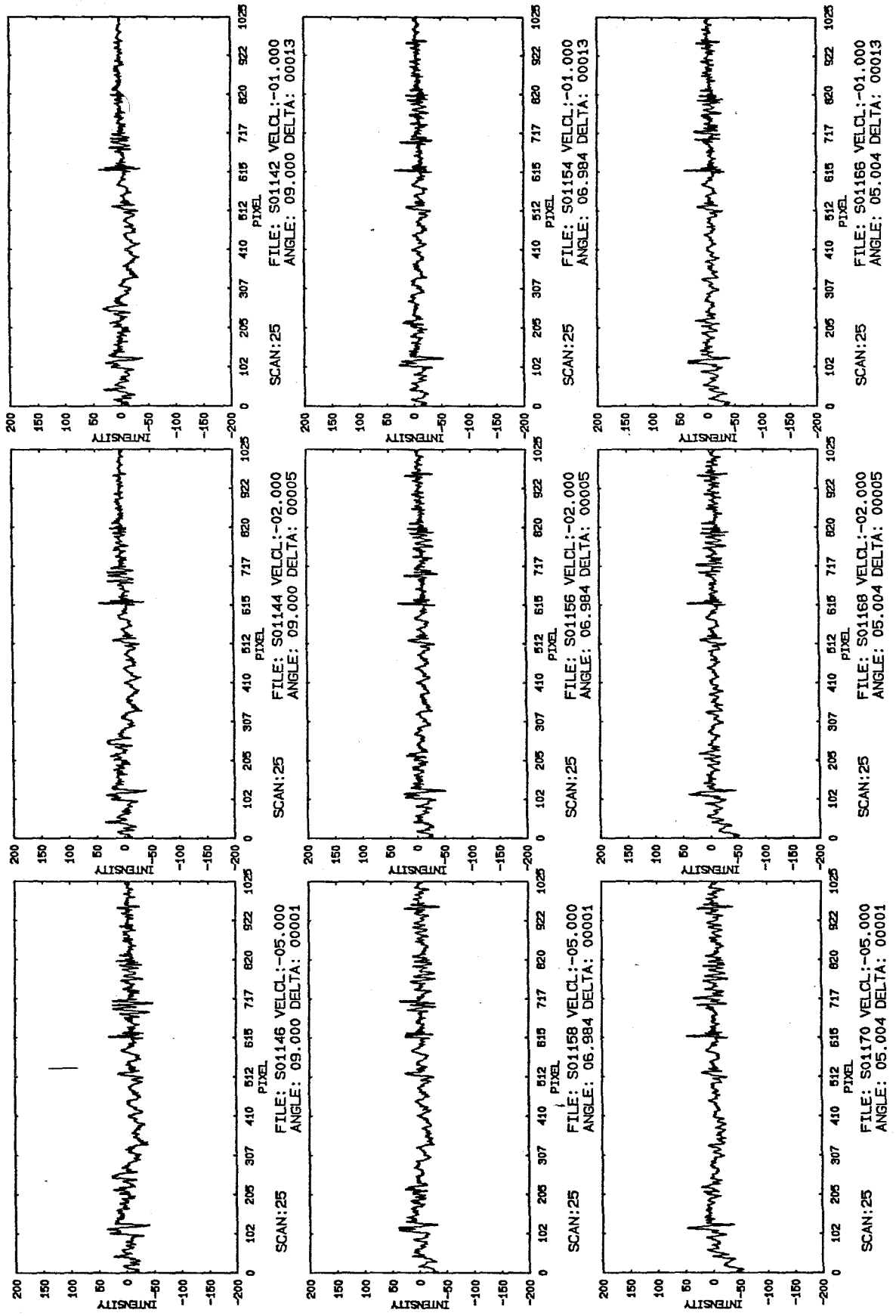
INTENSITY
PIXEL
SCAN:25
FILE: S01142 VELCL:-01.000
ANGLE: 09.000 DELTA: 00013
FILE: S01144 VELCL:-02.000
ANGLE: 09.000 DELTA: 00005
FILE: S01146 VELCL:-05.000
ANGLE: 09.000 DELTA: 00001
FILE: S01154 VELCL:-01.000
ANGLE: 06.984 DELTA: 00013
FILE: S01156 VELCL:-02.000
ANGLE: 06.984 DELTA: 00005
FILE: S01158 VELCL:-05.000
ANGLE: 06.984 DELTA: 00001
FILE: S01166 VELCL:-01.000
ANGLE: 05.004 DELTA: 00013
FILE: S01168 VELCL:-02.000
ANGLE: 05.004 DELTA: 00005
FILE: S01170 VELCL:-05.000
ANGLE: 05.004 DELTA: 00001

Figure 31

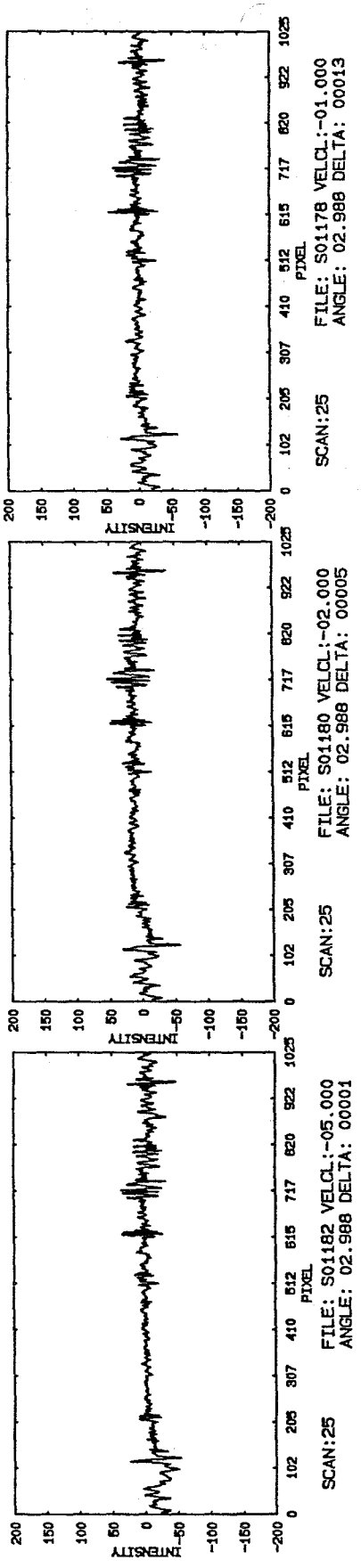
INTENSITY
PIXEL
SCAN:25
FILE: S01182 VELCL:-05.000
ANGLE: 02.988 DELTA: 00001
SCAN:25
FILE: S01180 VELCL:-02.000
ANGLE: 02.988 DELTA: 00005
SCAN:25
FILE: S01178 VELCL:-01.000
ANGLE: 02.988 DELTA: 00013

Figure 32

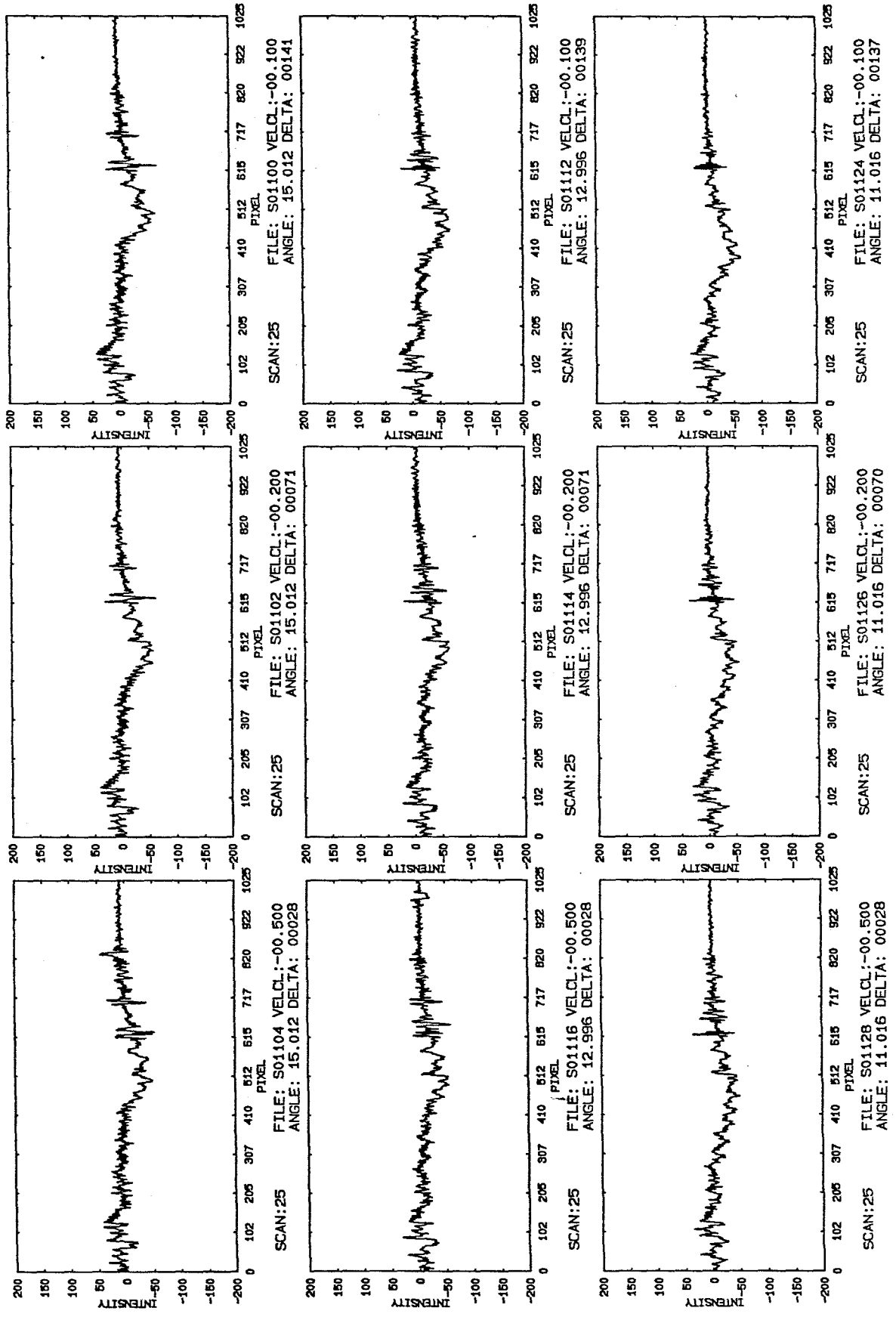
INTENSITY
PIXEL
SCAN:25
FILE: S01100 VELCL:-00.100
ANGLE: 15.012 DELTA: 00141
FILE: S01102 VELCL:-00.200
ANGLE: 15.012 DELTA: 00071
FILE: S01104 VELCL:-00.500
ANGLE: 15.012 DELTA: 00028
FILE: S01112 VELCL:-00.100
ANGLE: 12.996 DELTA: 00139
FILE: S01114 VELCL:-00.200
ANGLE: 12.996 DELTA: 00071
FILE: S01116 VELCL:-00.500
ANGLE: 12.996 DELTA: 00028
FILE: S01124 VELCL:-00.100
ANGLE: 11.016 DELTA: 00137
FILE: S01126 VELCL:-00.200
ANGLE: 11.016 DELTA: 00070
FILE: S01128 VELCL:-00.500
ANGLE: 11.016 DELTA: 00028

Figure 33

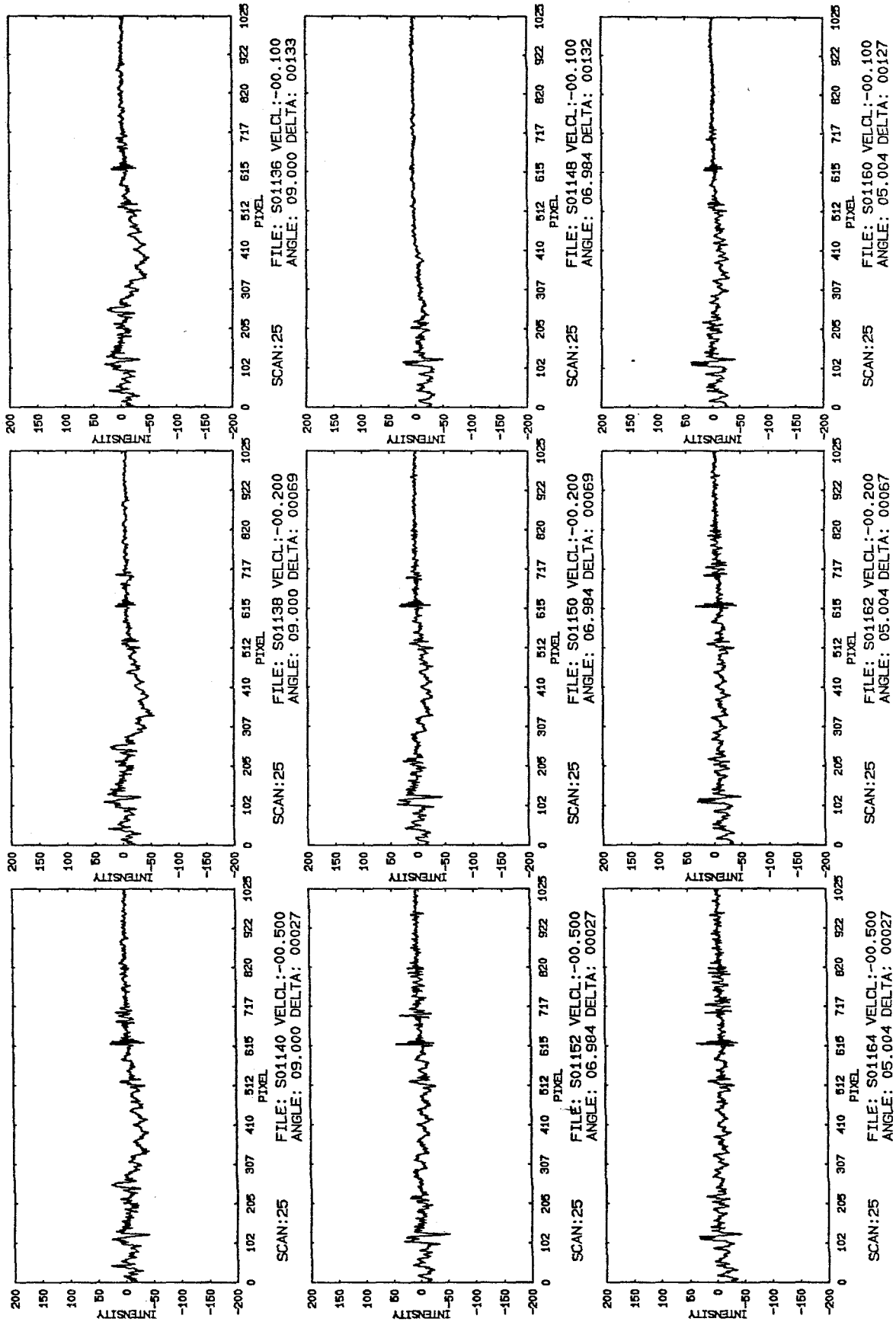
INTENSITY
PIXEL
SCAN:25
FILE: S01136 VELCL:-00.100
ANGLE: 09.000 DELTA: 00133
FILE: S01138 VELCL:-00.200
ANGLE: 09.000 DELTA: 00069
FILE: S01140 VELCL:-00.500
ANGLE: 09.000 DELTA: 00027
FILE: S01148 VELCL:-00.100
ANGLE: 06.984 DELTA: 00132
FILE: S01150 VELCL:-00.200
ANGLE: 06.984 DELTA: 00069
FILE: S01152 VELCL:-00.500
ANGLE: 06.984 DELTA: 00027
FILE: S01160 VELCL:-00.100
ANGLE: 05.004 DELTA: 00127
FILE: S01162 VELCL:-00.200
ANGLE: 05.004 DELTA: 00067
FILE: S01164 VELCL:-00.500
ANGLE: 05.004 DELTA: 00027

Figure 34

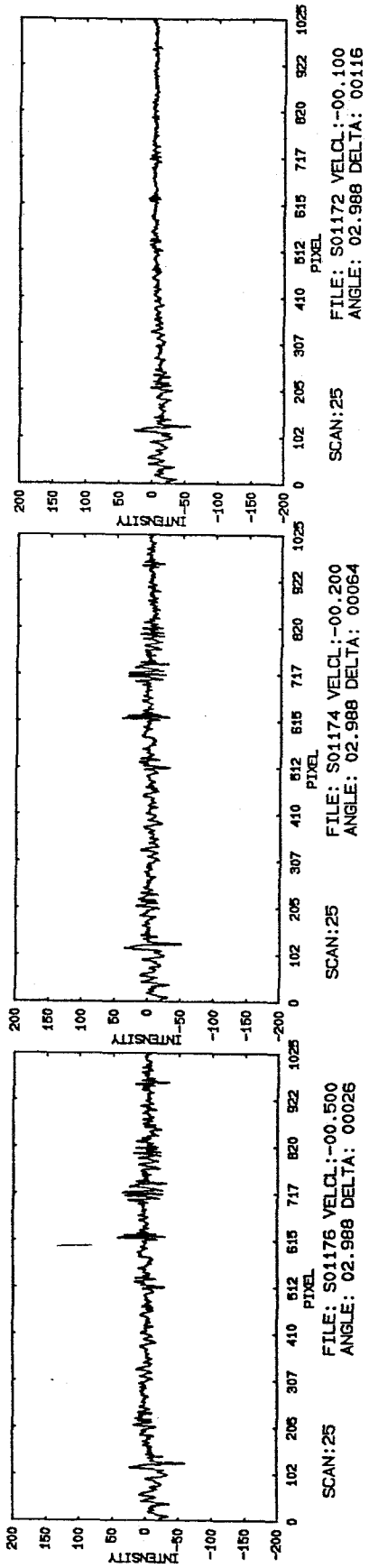
INTENSITY
PIXEL
SCAN:25
FILE: S01176 VELCL:-00.500
ANGLE: 02.988 DELTA: 00026
SCAN:25
FILE: S01174 VELCL:-00.200
ANGLE: 02.988 DELTA: 00064
SCAN:25
FILE: S01172 VELCL:-00.100
ANGLE: 02.988 DELTA: 00116

Figure 35

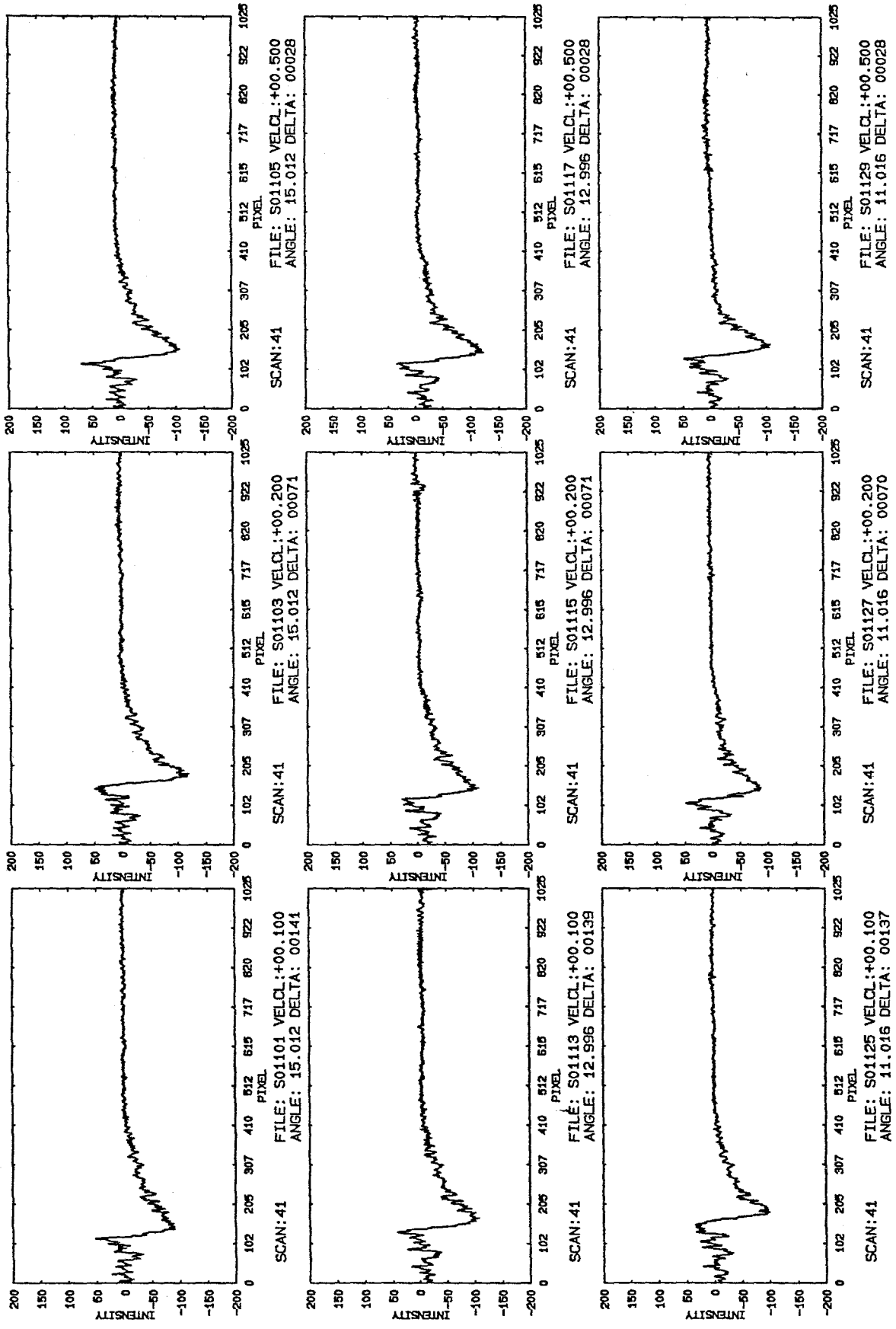
INTENSITY
PIXEL
SCAN:41
FILE: S01101 VELCL:+00.100
ANGLE: 15.012 DELTA: 00141
FILE: S01103 VELCL:+00.200
ANGLE: 15.012 DELTA: 00071
FILE: S01105 VELCL:+00.500
ANGLE: 15.012 DELTA: 00028
FILE: S01113 VELCL:+00.100
ANGLE: 12.996 DELTA: 00139
FILE: S01115 VELCL:+00.200
ANGLE: 12.996 DELTA: 00071
FILE: S01117 VELCL:+00.500
ANGLE: 12.996 DELTA: 00028
FILE: S01125 VELCL:+00.100
ANGLE: 11.016 DELTA: 00137
FILE: S01127 VELCL:+00.200
ANGLE: 11.016 DELTA: 00070
FILE: S01129 VELCL:+00.500
ANGLE: 11.016 DELTA: 00028

Figure 36

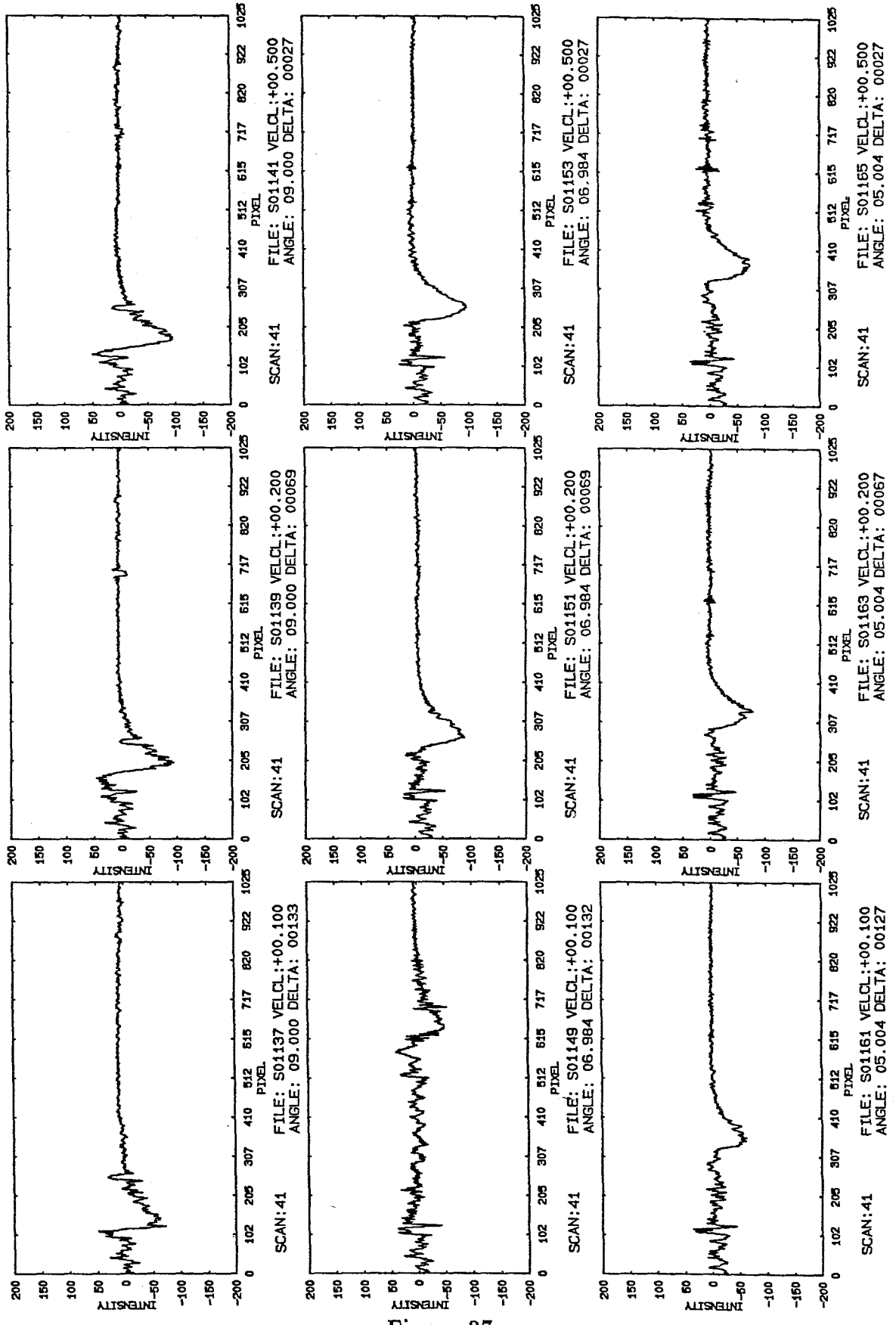
INTENSITY
PIXEL
SCAN:41
FILE: S01137 VELCL:+00.100
ANGLE: 09.000 DELTA: 00133
FILE: S01139 VELCL:+00.200
ANGLE: 09.000 DELTA: 00069
FILE: S01141 VELCL:+00.500
ANGLE: 09.000 DELTA: 00027
FILE: S01149 VELCL:+00.100
ANGLE: 06.984 DELTA: 00132
FILE: S01151 VELCL:+00.200
ANGLE: 06.984 DELTA: 00069
FILE: S01153 VELCL:+00.500
ANGLE: 06.984 DELTA: 00027
FILE: S01161 VELCL:+00.100
ANGLE: 05.004 DELTA: 00127
FILE: S01163 VELCL:+00.200
ANGLE: 05.004 DELTA: 00067
FILE: S01165 VELCL:+00.500
ANGLE: 05.004 DELTA: 00027

Figure 37

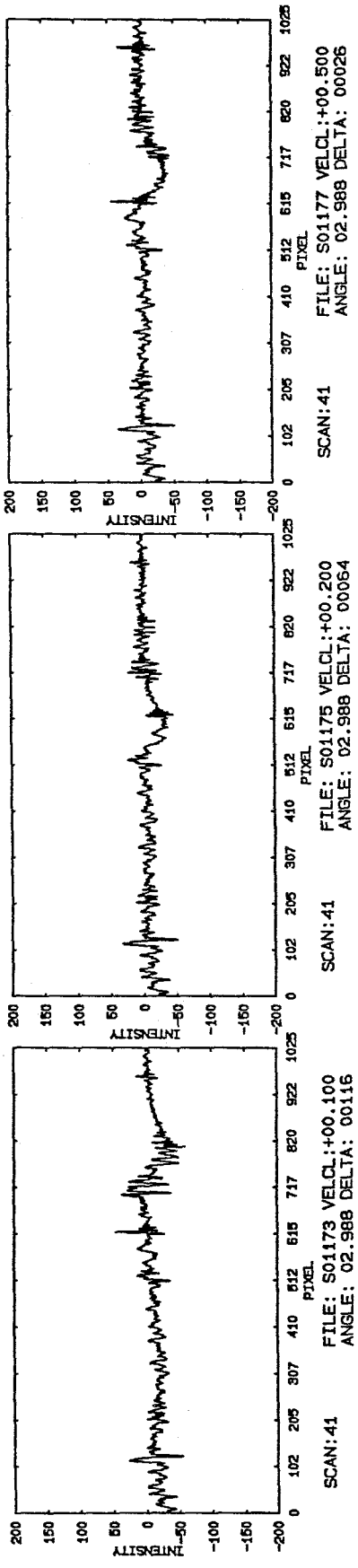
INTENSITY
PIXEL
SCAN:41
FILE: S01173 VELCL:+00.100
ANGLE: 02.988 DELTA: 00116
FILE: S01175 VELCL:+00.200
ANGLE: 02.988 DELTA: 00064
FILE: S01177 VELCL:+00.500
ANGLE: 02.988 DELTA: 00026

Figure 38

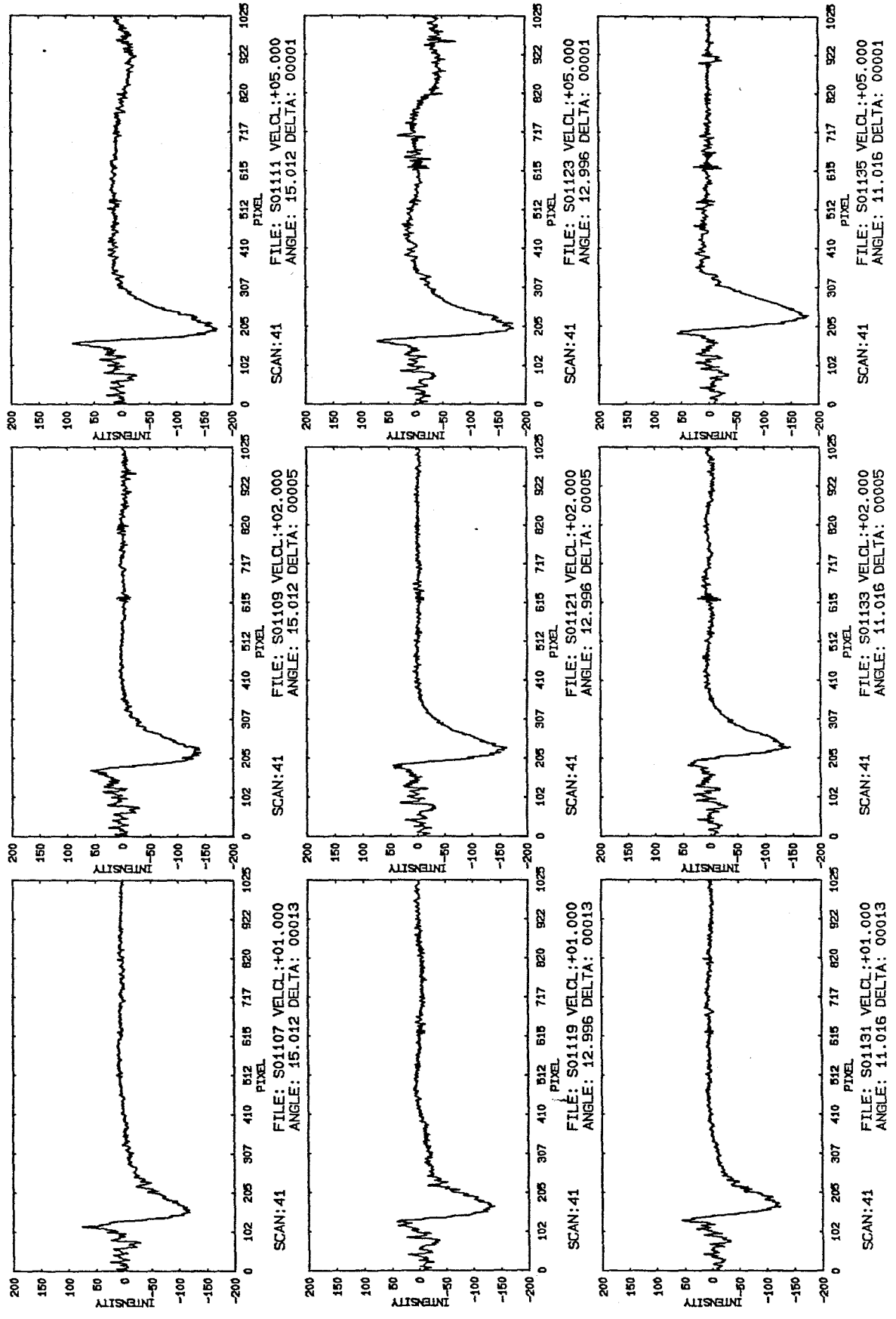
INTENSITY
PIXEL
SCAN:41
FILE: S01107 VELCL:+01.000
ANGLE: 15.012 DELTA: 00013
FILE: S01109 VELCL:+02.000
ANGLE: 15.012 DELTA: 00005
FILE: S01111 VELCL:+05.000
ANGLE: 15.012 DELTA: 00001
FILE: S01119 VELCL:+01.000
ANGLE: 12.996 DELTA: 00013
FILE: S01121 VELCL:+02.000
ANGLE: 12.996 DELTA: 00005
FILE: S01123 VELCL:+05.000
ANGLE: 12.996 DELTA: 00001
FILE: S01131 VELCL:+01.000
ANGLE: 11.016 DELTA: 00013
FILE: S01133 VELCL:+02.000
ANGLE: 11.016 DELTA: 00005
FILE: S01135 VELCL:+05.000
ANGLE: 11.016 DELTA: 00001

Figure 39

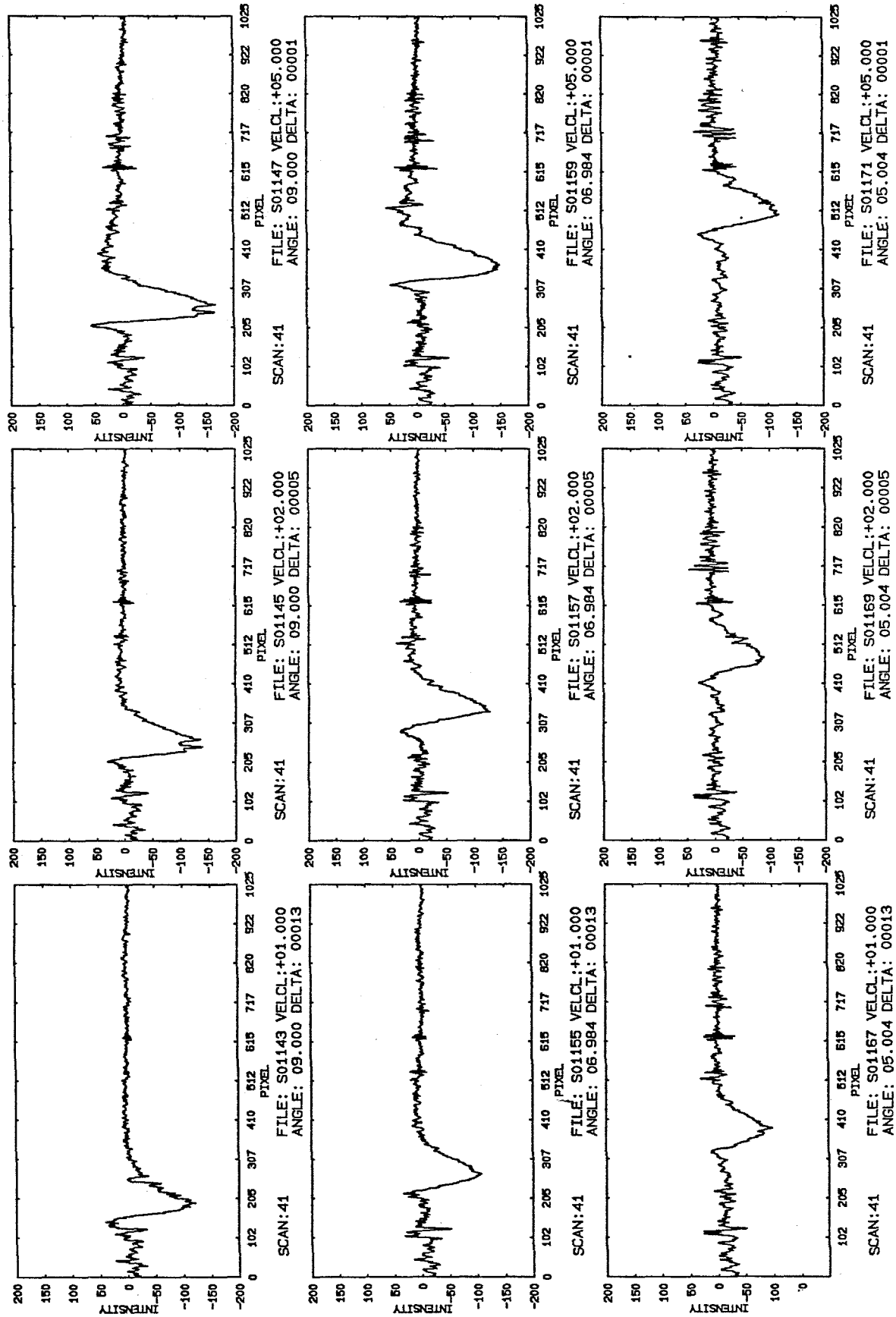
INTENSITY
PIXEL
SCAN:41
FILE: S01143 VELCL:+01.000
ANGLE: 09.000 DELTA: 00013
FILE: S01145 VELCL:+02.000
ANGLE: 09.000 DELTA: 00005
FILE: S01147 VELCL:+05.000
ANGLE: 09.000 DELTA: 00001
FILE: S01155 VELCL:+01.000
ANGLE: 06.984 DELTA: 00013
FILE: S01157 VELCL:+02.000
ANGLE: 06.984 DELTA: 00005
FILE: S01159 VELCL:+05.000
ANGLE: 06.984 DELTA: 00001
FILE: S01167 VELCL:+01.000
ANGLE: 05.004 DELTA: 00013
FILE: S01169 VELCL:+02.000
ANGLE: 05.004 DELTA: 00005
FILE: S01171 VELCL:+05.000
ANGLE: 05.004 DELTA: 00001

Figure 40

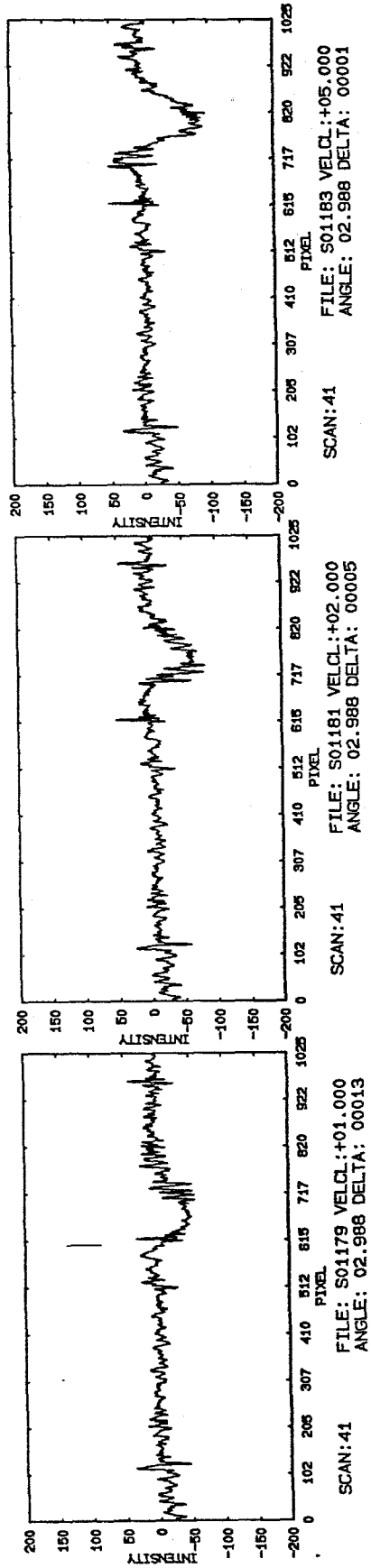
INTENSITY
PIXEL
SCAN:41
FILE: S01179 VELCL:+01.000
ANGLE: 02.988 DELTA: 00013
FILE: S01181 VELCL:+02.000
ANGLE: 02.988 DELTA: 00005
FILE: S01183 VELCL:+05.000
ANGLE: 02.988 DELTA: 00001

Figure 41

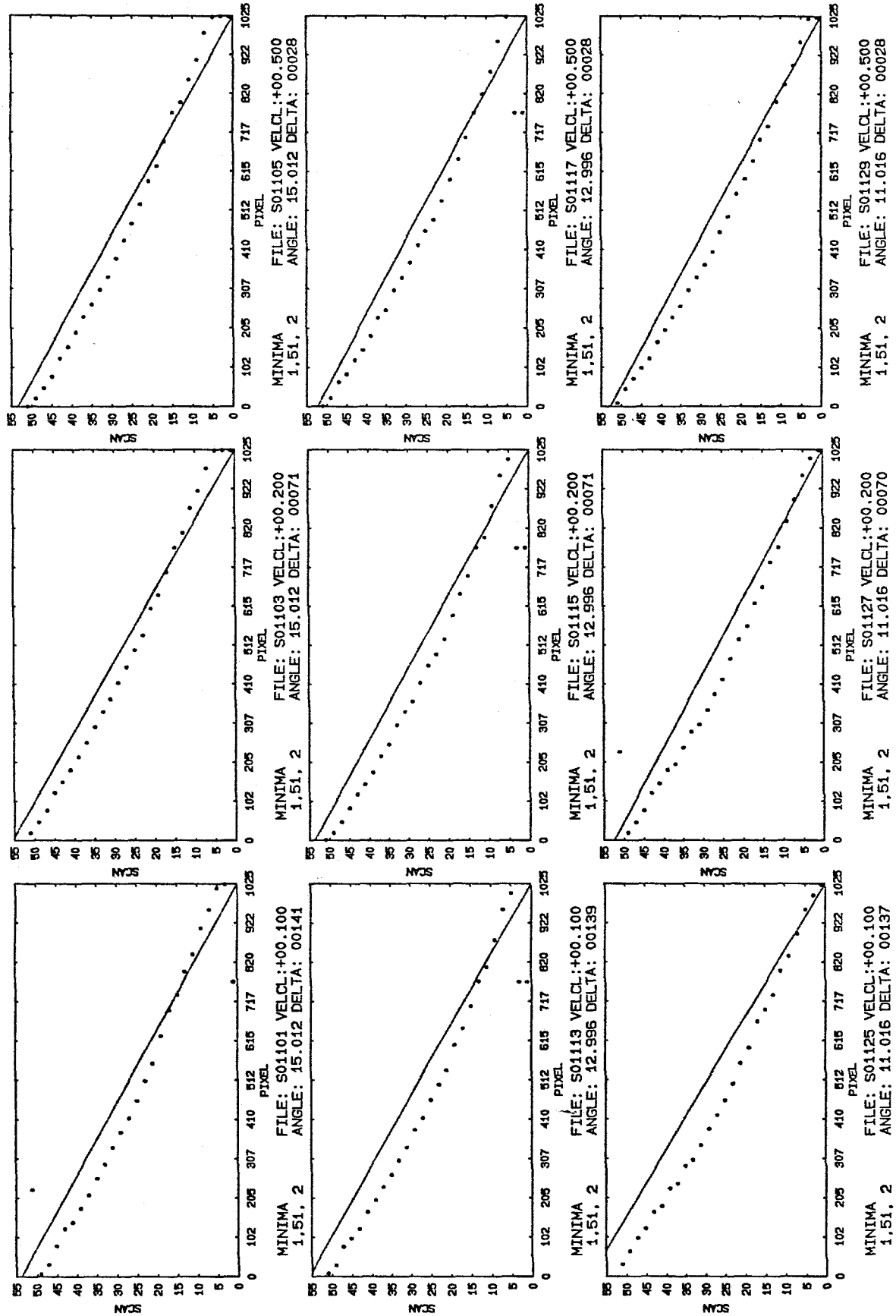
SCAN
PIXEL
MINIMA
1,51, 2
FILE: S01101 VELCL:+00.100
ANGLE: 15.012 DELTA: 00141
FILE: S01103 VELCL:+00.200
ANGLE: 15.012 DELTA: 00071
FILE: S01105 VELCL:+00.500
ANGLE: 15.012 DELTA: 00028
FILE: S01113 VELCL:+00.100
ANGLE: 12.996 DELTA: 00139
FILE: S01115 VELCL:+00.200
ANGLE: 12.996 DELTA: 00071
FILE: S01117 VELCL:+00.500
ANGLE: 12.996 DELTA: 00028
FILE: S01125 VELCL:+00.100
ANGLE: 11.016 DELTA: 00137
FILE: S01127 VELCL:+00.200
ANGLE: 11.016 DELTA: 00070
FILE: S01129 VELCL:+00.500
ANGLE: 11.016 DELTA: 00028

Figure 42

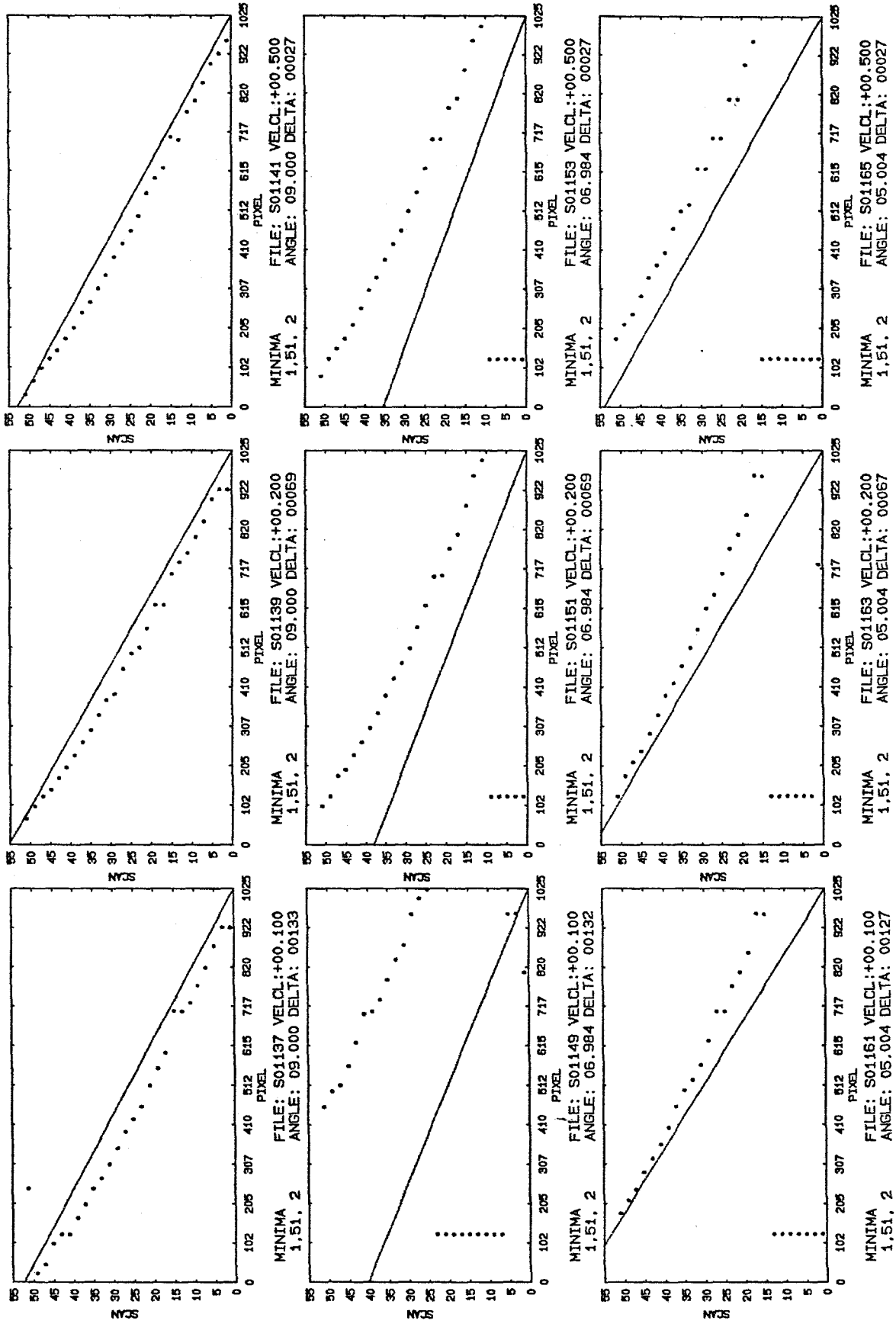
FILE: S01137 VELCL:+00.100
ANGLE: 09.000 DELTA: 00133
MINIMA
1,51, 2
FILE: S01139 VELCL:+00.200
ANGLE: 09.000 DELTA: 00069
MINIMA
1,51, 2
FILE: S01141 VELCL:+00.500
ANGLE: 09.000 DELTA: 00027
MINIMA
1,51, 2
FILE: S01149 VELCL:+00.100
ANGLE: 06.984 DELTA: 00132
MINIMA
1,51, 2
FILE: S01151 VELCL:+00.200
ANGLE: 06.984 DELTA: 00069
MINIMA
1,51, 2
FILE: S01153 VELCL:+00.500
ANGLE: 06.984 DELTA: 00027
MINIMA
1,51, 2
FILE: S01161 VELCL:+00.100
ANGLE: 05.004 DELTA: 00127
MINIMA
1,51, 2
FILE: S01163 VELCL:+00.200
ANGLE: 05.004 DELTA: 00067
MINIMA
1,51, 2
FILE: S01165 VELCL:+00.500
ANGLE: 05.004 DELTA: 00027
MINIMA
1,51, 2
SCAN
PIXEL

Figure 43

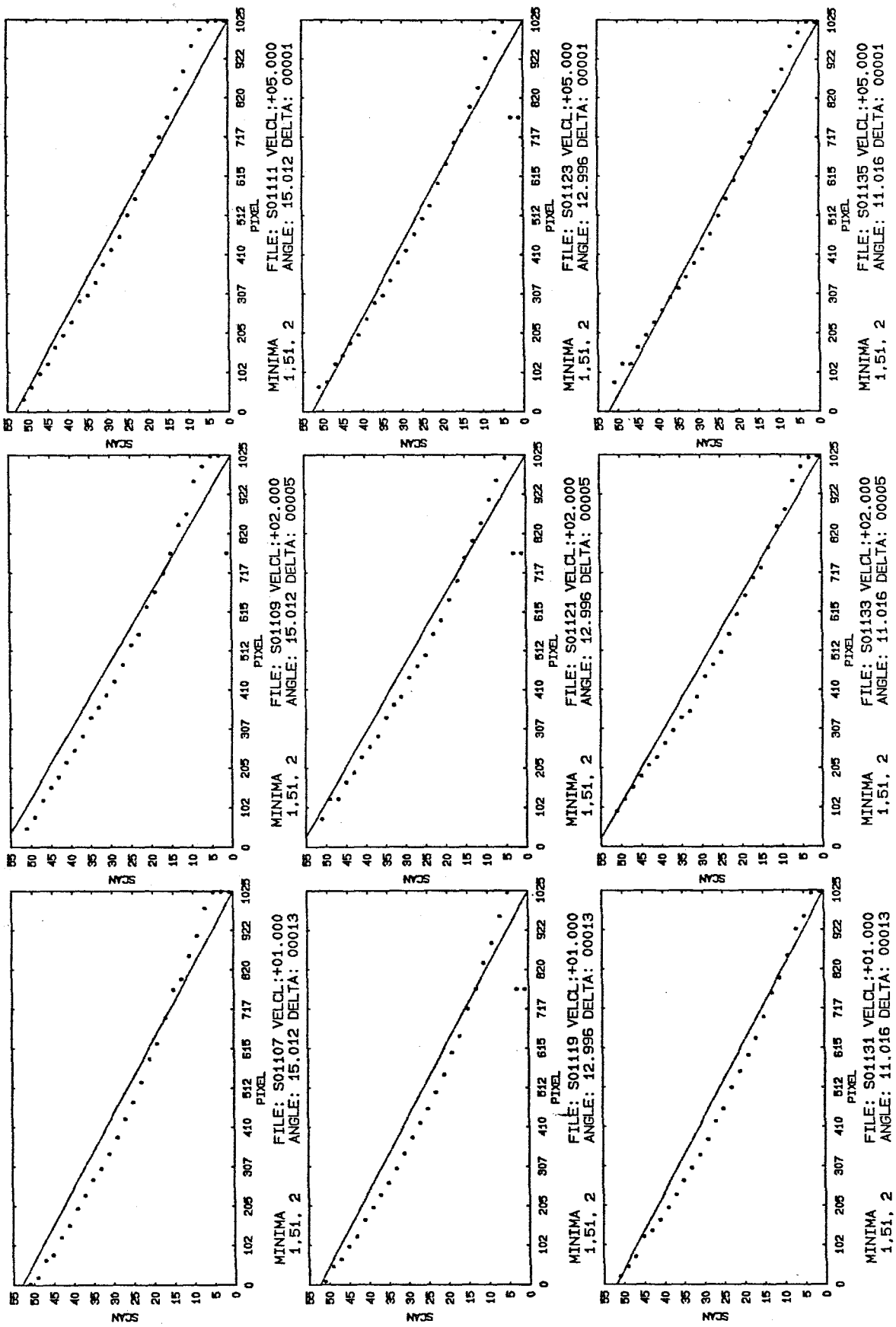
SCAN
PIXEL
MINIMA
1,51, 2
FILE: S01107 VELCL:+01.000
ANGLE: 15.012 DELTA: 00013
FILE: S01109 VELCL:+02.000
ANGLE: 15.012 DELTA: 00005
FILE: S01111 VELCL:+05.000
ANGLE: 15.012 DELTA: 00001
FILE: S01119 VELCL:+01.000
ANGLE: 12.996 DELTA: 00013
FILE: S01121 VELCL:+02.000
ANGLE: 12.996 DELTA: 00005
FILE: S01123 VELCL:+05.000
ANGLE: 12.996 DELTA: 00001
FILE: S01131 VELCL:+01.000
ANGLE: 11.016 DELTA: 00013
FILE: S01133 VELCL:+02.000
ANGLE: 11.016 DELTA: 00005
FILE: S01135 VELCL:+05.000
ANGLE: 11.016 DELTA: 00001

Figure 44

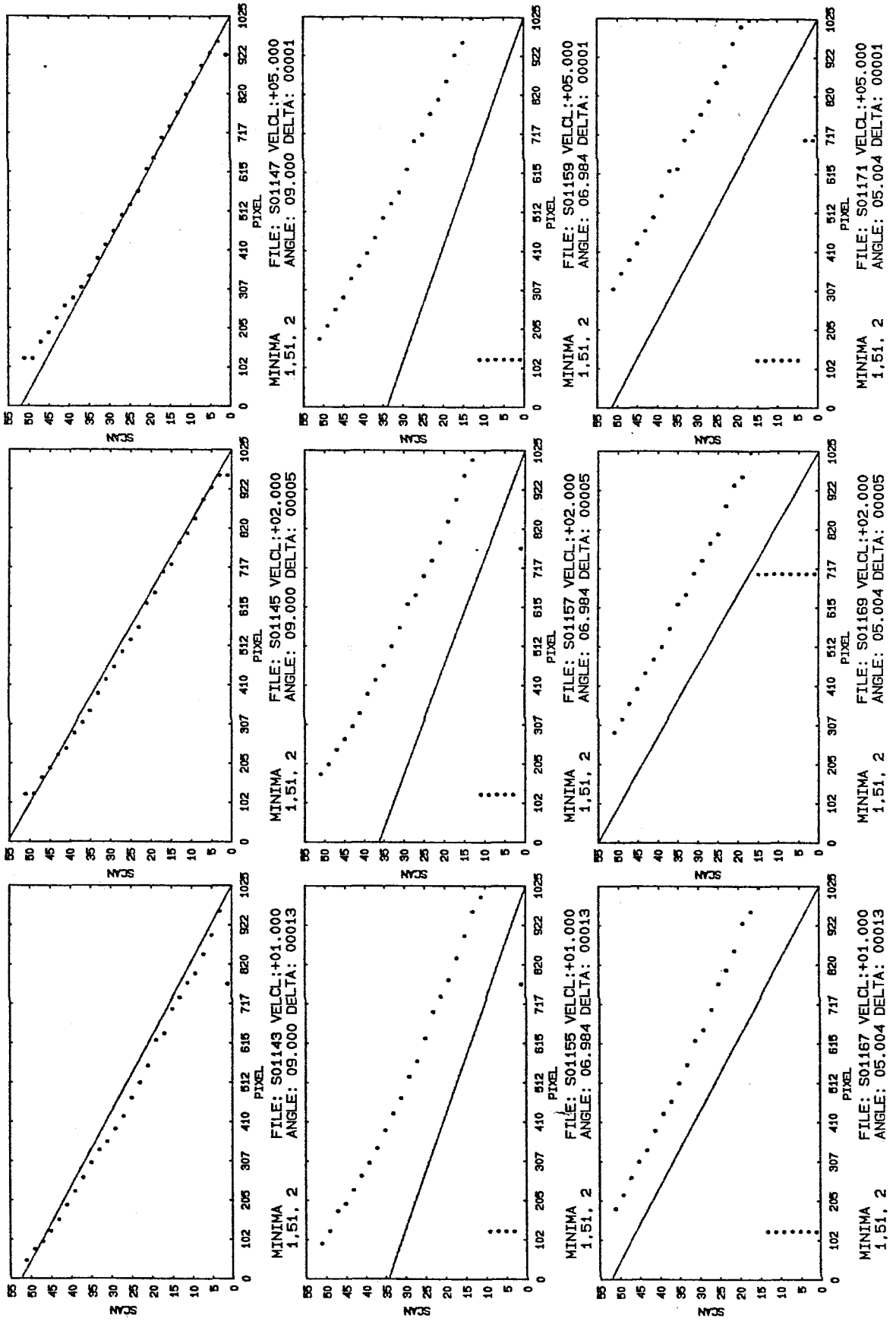
SCAN
PIXEL
MINIMA
1,51, 2
FILE: S01143 VELCL:+01.000
ANGLE: 09.000 DELTA: 00013
FILE: S01145 VELCL:+02.000
ANGLE: 09.000 DELTA: 00005
FILE: S01147 VELCL:+05.000
ANGLE: 09.000 DELTA: 00001
FILE: S01155 VELCL:+01.000
ANGLE: 06.984 DELTA: 00013
FILE: S01157 VELCL:+02.000
ANGLE: 06.984 DELTA: 00005
FILE: S01159 VELCL:+05.000
ANGLE: 06.984 DELTA: 00001
FILE: S01167 VELCL:+01.000
ANGLE: 05.004 DELTA: 00013
FILE: S01169 VELCL:+02.000
ANGLE: 05.004 DELTA: 00005
FILE: S01171 VELCL:+05.000
ANGLE: 05.004 DELTA: 00001

Figure 45

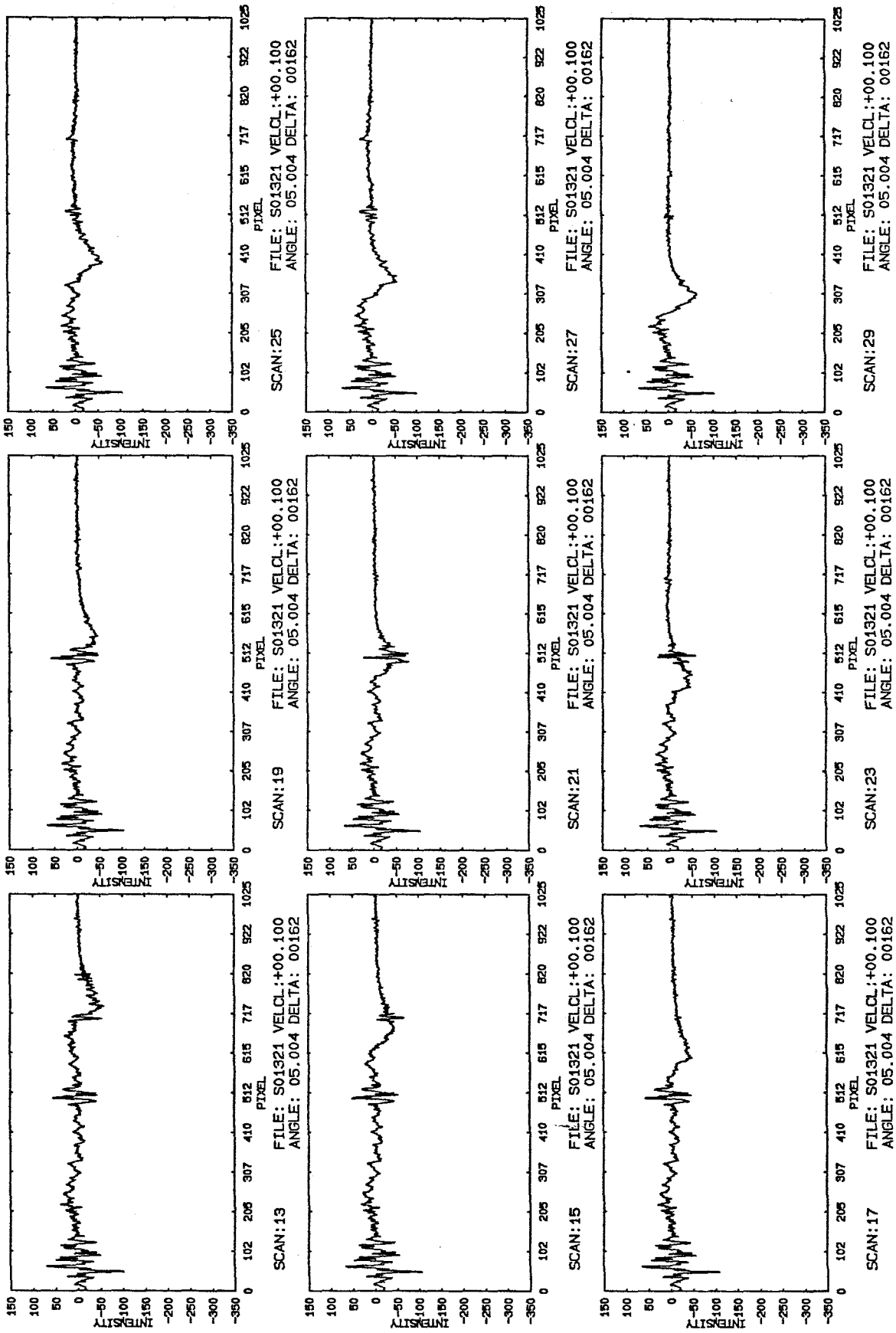
SCAN:13
FILE: S01321 VELCL:+00.100
ANGLE: 05.004 DELTA: 00162
SCAN:15
FILE: S01321 VELCL:+00.100
ANGLE: 05.004 DELTA: 00162
SCAN:17
FILE: S01321 VELCL:+00.100
ANGLE: 05.004 DELTA: 00162
SCAN:19
FILE: S01321 VELCL:+00.100
ANGLE: 05.004 DELTA: 00162
SCAN:21
FILE: S01321 VELCL:+00.100
ANGLE: 05.004 DELTA: 00162
SCAN:23
FILE: S01321 VELCL:+00.100
ANGLE: 05.004 DELTA: 00162
SCAN:25
FILE: S01321 VELCL:+00.100
ANGLE: 05.004 DELTA: 00162
SCAN:27
FILE: S01321 VELCL:+00.100
ANGLE: 05.004 DELTA: 00162
SCAN:29
FILE: S01321 VELCL:+00.100
ANGLE: 05.004 DELTA: 00162
INTENSITY
PIXEL

Figure 46

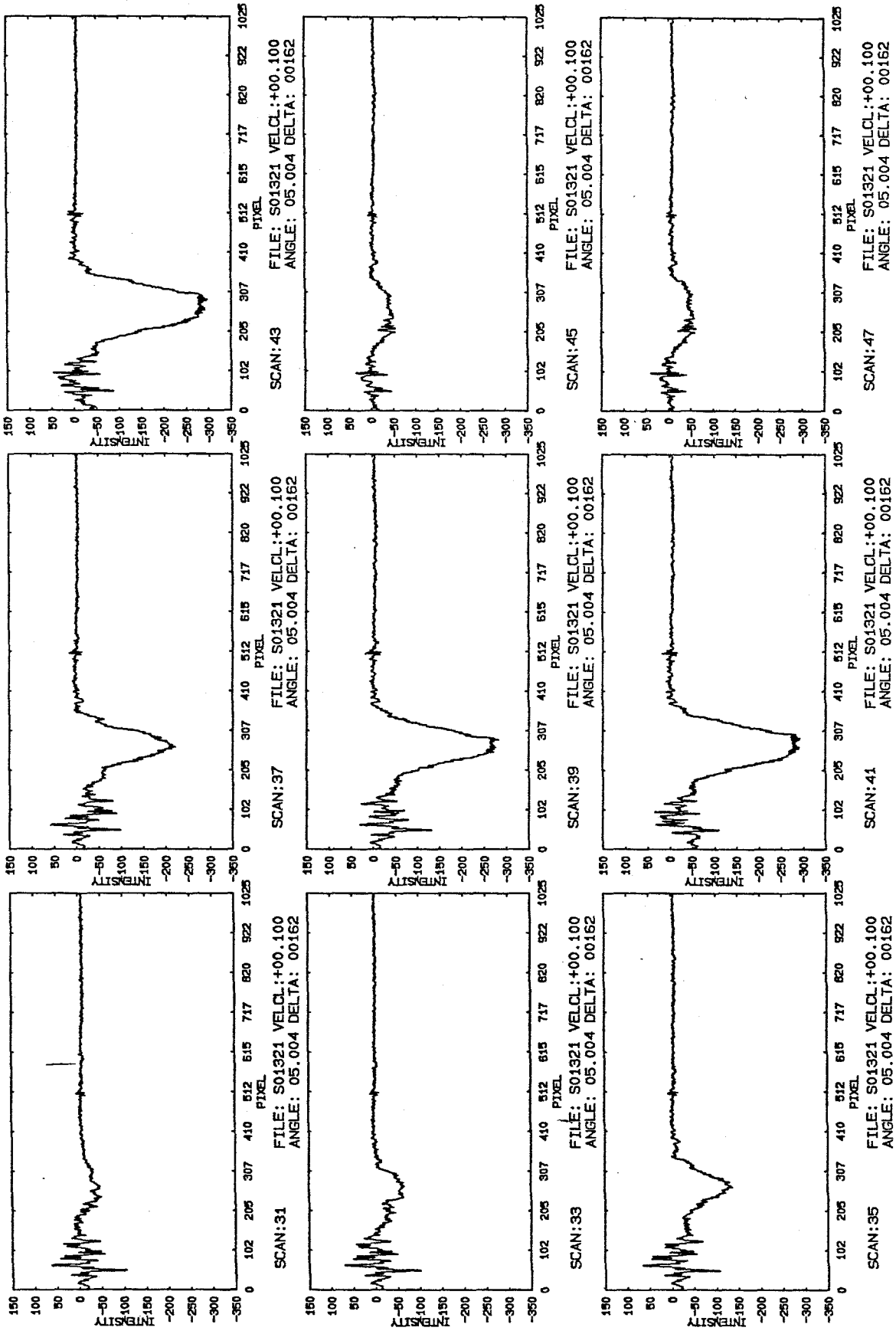
INTENSITY
PIXEL
SCAN:31
FILE: S01321 VELCL:+00.100
ANGLE: 05.004 DELTA: 00162
SCAN:33
FILE: S01321 VELCL:+00.100
ANGLE: 05.004 DELTA: 00162
SCAN:35
FILE: S01321 VELCL:+00.100
ANGLE: 05.004 DELTA: 00162
SCAN:37
FILE: S01321 VELCL:+00.100
ANGLE: 05.004 DELTA: 00162
SCAN:39
FILE: S01321 VELCL:+00.100
ANGLE: 05.004 DELTA: 00162
SCAN:41
FILE: S01321 VELCL:+00.100
ANGLE: 05.004 DELTA: 00162
SCAN:43
FILE: S01321 VELCL:+00.100
ANGLE: 05.004 DELTA: 00162
SCAN:45
FILE: S01321 VELCL:+00.100
ANGLE: 05.004 DELTA: 00162
SCAN:47
FILE: S01321 VELCL:+00.100
ANGLE: 05.004 DELTA: 00162

Figure 47

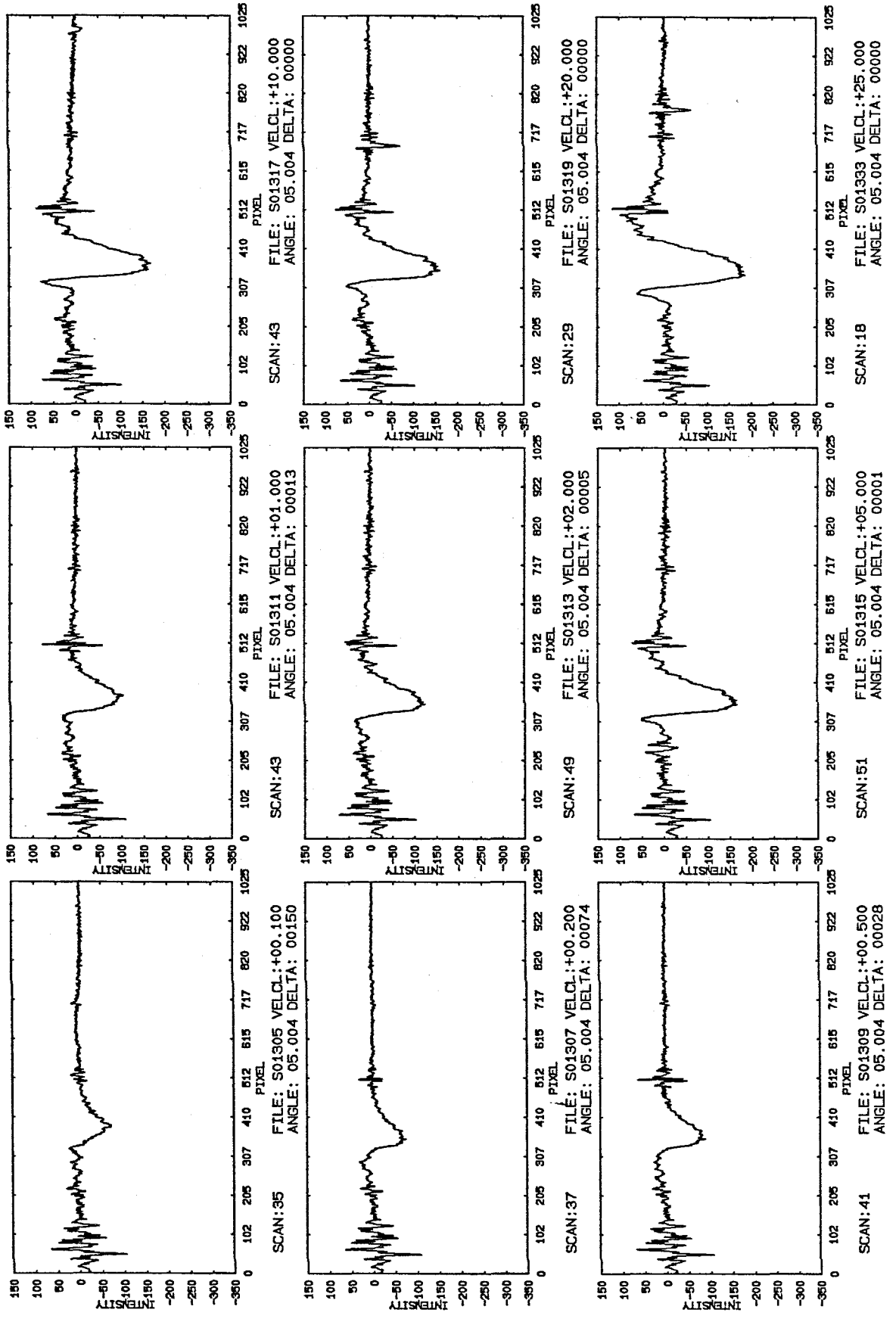
INTENSITY
PIXEL
SCAN:35
FILE: S01305 VELCL:+00.100
ANGLE: 05.004 DELTA: 00150
SCAN:37
FILE: S01307 VELCL:+00.200
ANGLE: 05.004 DELTA: 00074
SCAN:41
FILE: S01309 VELCL:+00.500
ANGLE: 05.004 DELTA: 00028
SCAN:43
FILE: S01311 VELCL:+01.000
ANGLE: 05.004 DELTA: 00013
SCAN:49
FILE: S01313 VELCL:+02.000
ANGLE: 05.004 DELTA: 00005
SCAN:51
FILE: S01315 VELCL:+05.000
ANGLE: 05.004 DELTA: 00001
SCAN:43
FILE: S01317 VELCL:+10.000
ANGLE: 05.004 DELTA: 00000
SCAN:29
FILE: S01319 VELCL:+20.000
ANGLE: 05.004 DELTA: 00000
SCAN:18
FILE: S01333 VELCL:+25.000
ANGLE: 05.004 DELTA: 00000

Figure 48

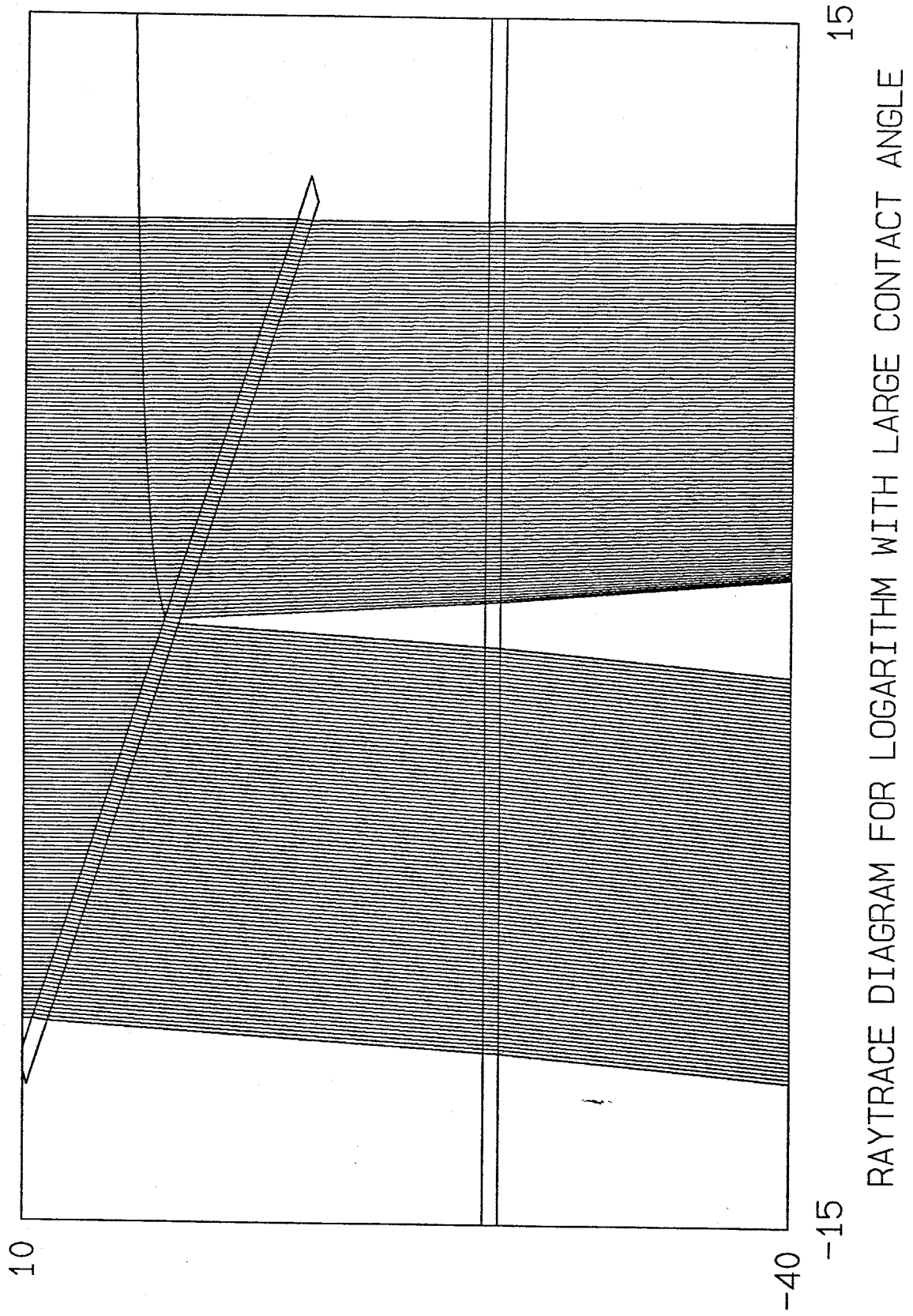
RAYTRACE DIAGRAM FOR LOGARITHM WITH LARGE CONTACT ANGLE
15
-15
10
-40

Figure 49

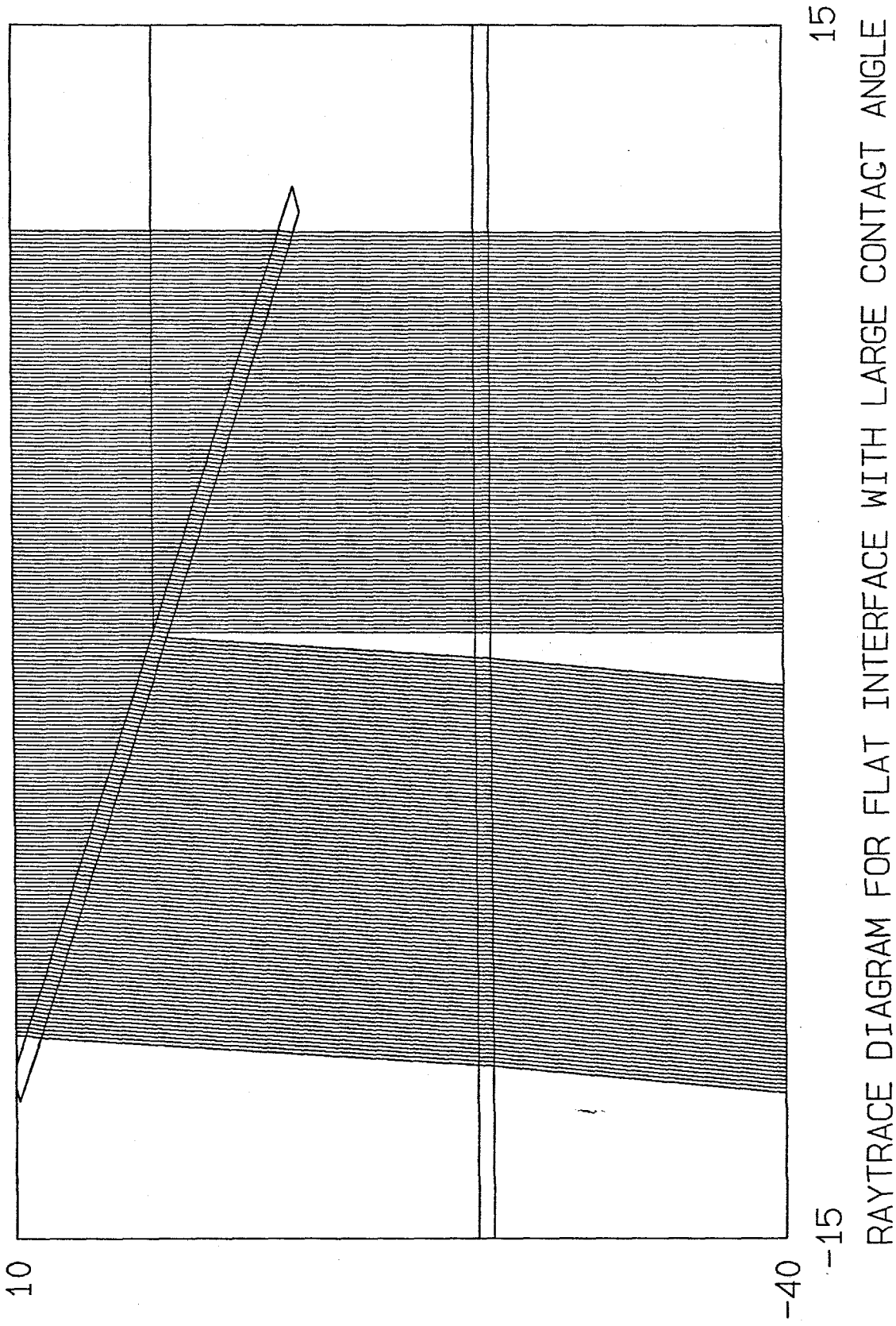
RAYTRACE DIAGRAM FOR FLAT INTERFACE WITH LARGE CONTACT ANGLE
15
-15
10
-40

Figure 50

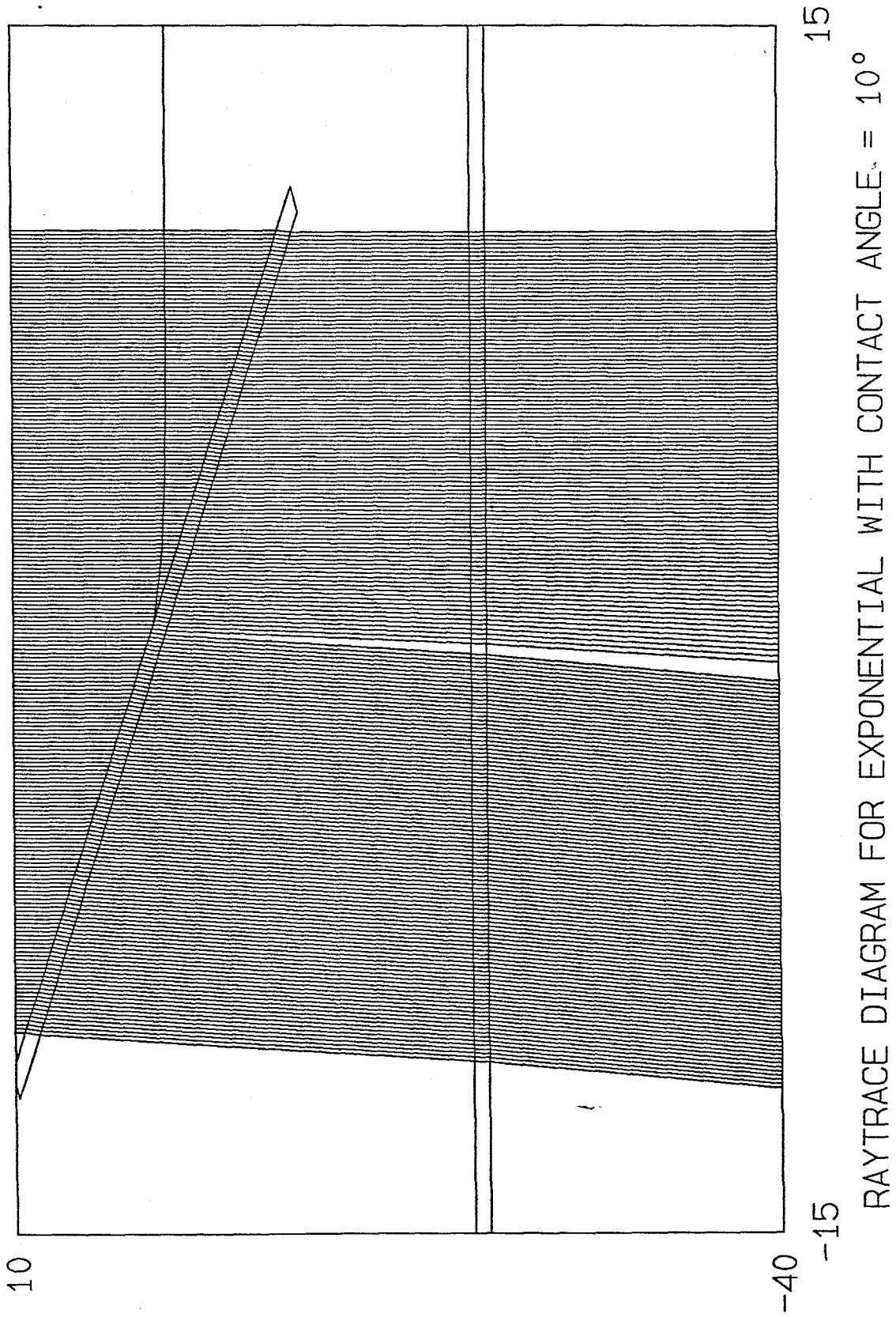
RAYTRACE DIAGRAM FOR EXPONENTIAL WITH CONTACT ANGLE = 10°
15
-15
10
-40

Figure 51

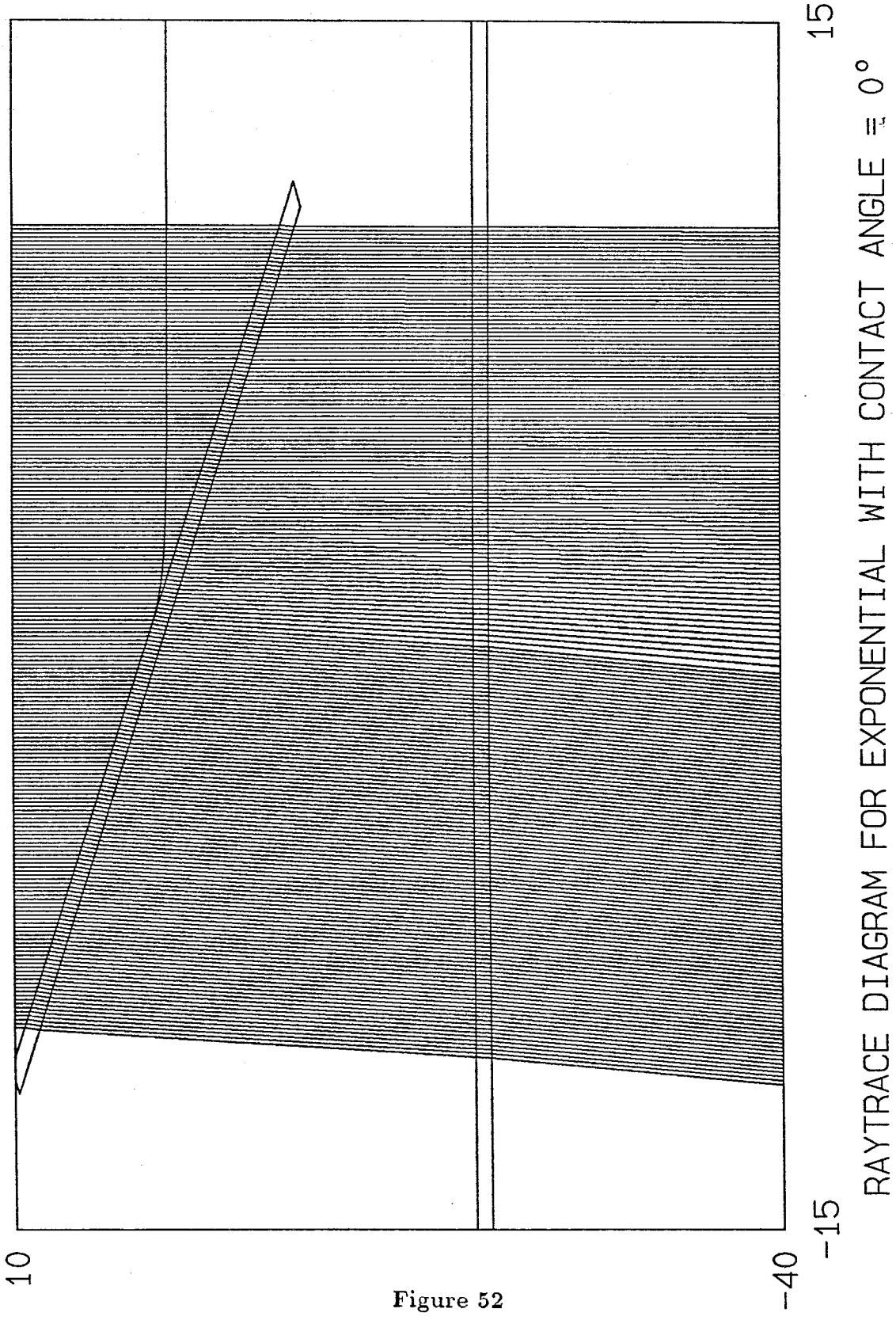
RAYTRACE DIAGRAM FOR EXPONENTIAL WITH CONTACT ANGLE = 0°
15
-15
10
-40

Figure 52

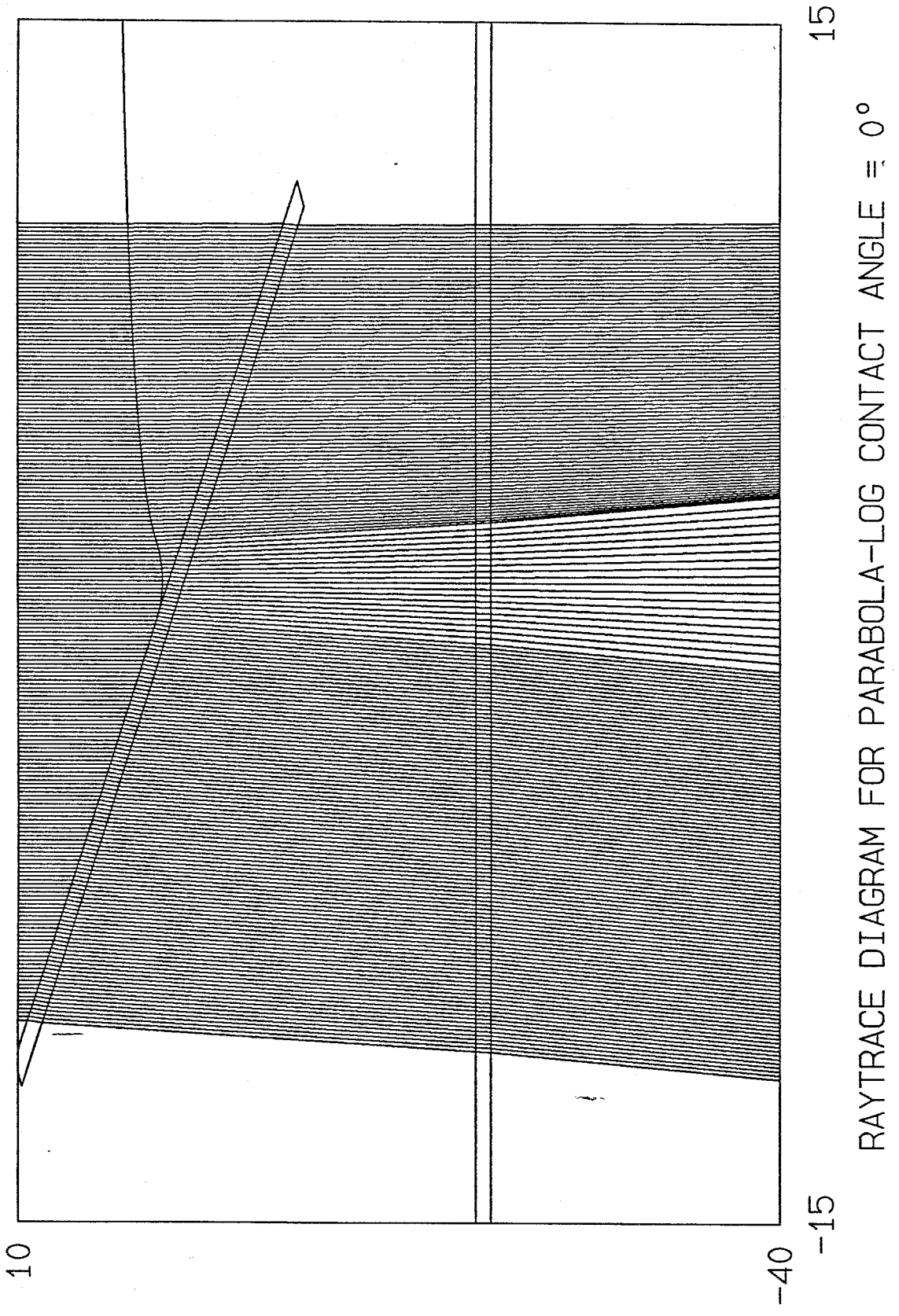
RAYTRACE DIAGRAM FOR PARABOLA-LOG CONTACT ANGLE = 0°
15
-15
10
-40

Figure 53

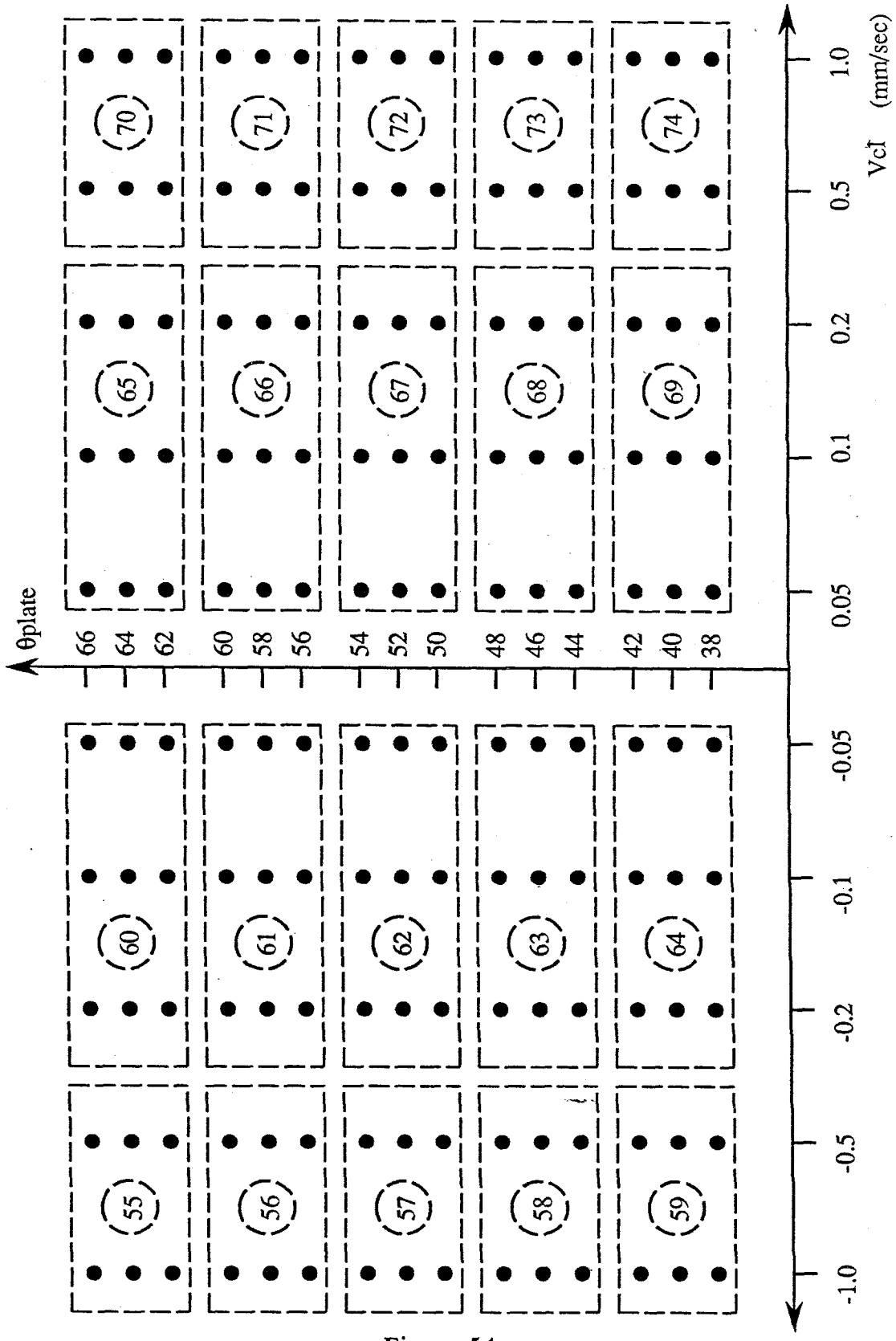

Figure 54

(Plate-angle, Velocity) space for "sticky"-plate experiments

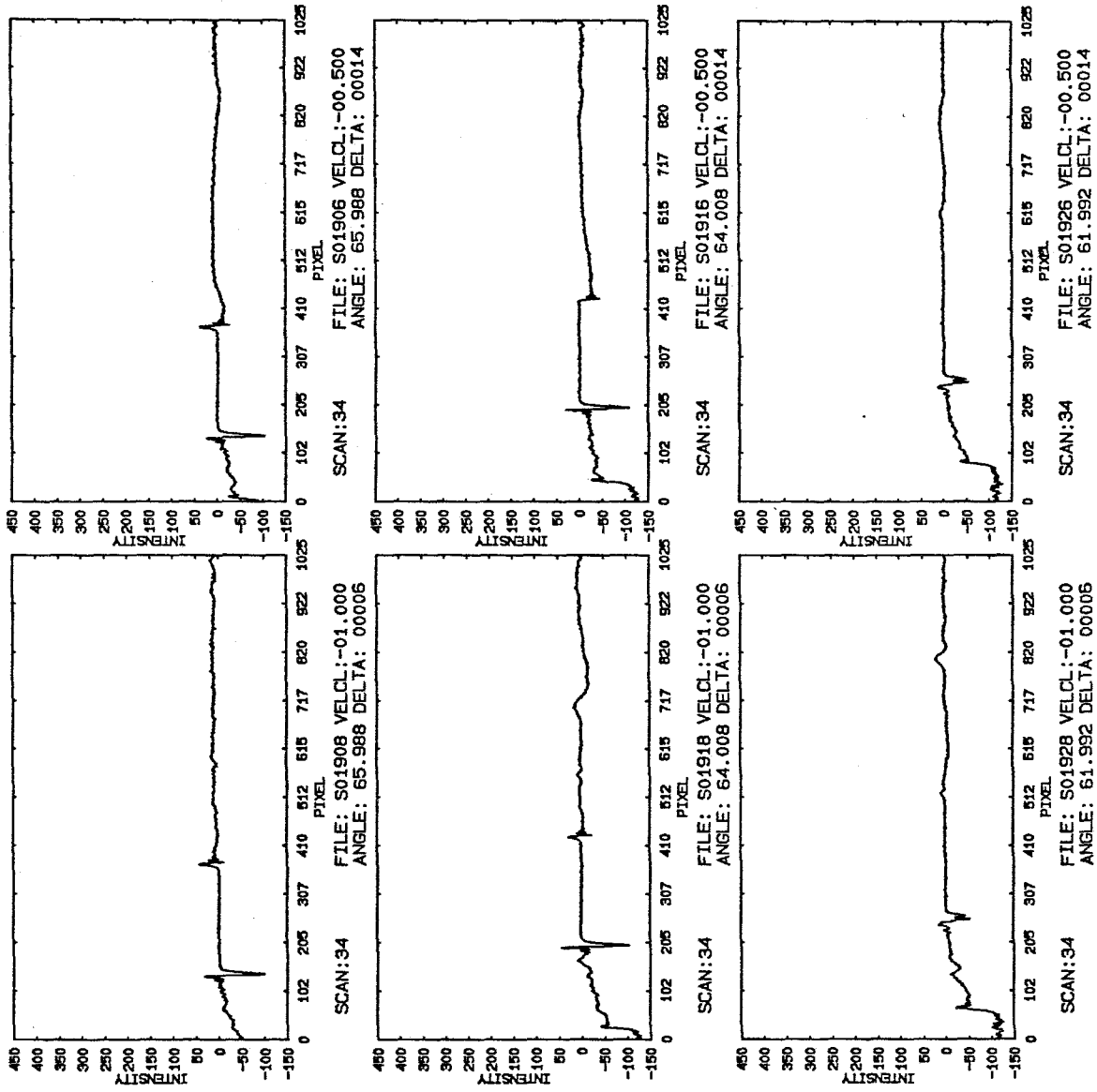
SCAN:34
FILE: S01906 VELCL:-00.500
ANGLE: 65.988 DELTA: 00014
SCAN:34
FILE: S01916 VELCL:-00.500
ANGLE: 64.008 DELTA: 00014
SCAN:34
FILE: S01926 VELCL:-00.500
ANGLE: 61.992 DELTA: 00014
SCAN:34
FILE: S01908 VELCL:-01.000
ANGLE: 65.988 DELTA: 00006
SCAN:34
FILE: S01918 VELCL:-01.000
ANGLE: 64.008 DELTA: 00006
SCAN:34
FILE: S01928 VELCL:-01.000
ANGLE: 61.992 DELTA: 00006
INTENSITY
PIXEL

Figure 55

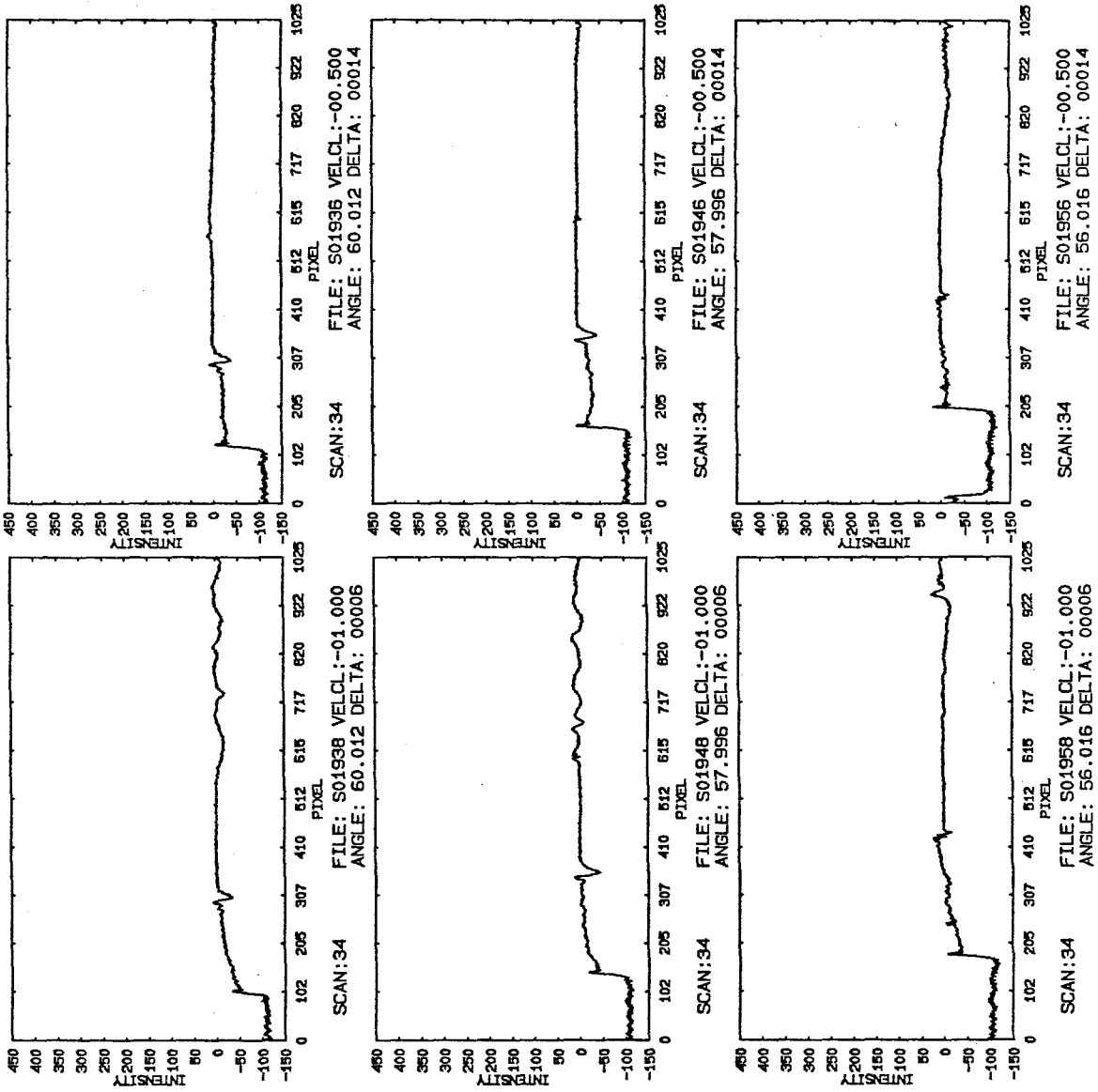
SCAN:34
FILE: S01936 VELCL:-00.500
ANGLE: 60.012 DELTA: 00014
SCAN:34
FILE: S01946 VELCL:-00.500
ANGLE: 57.996 DELTA: 00014
SCAN:34
FILE: S01956 VELCL:-00.500
ANGLE: 56.016 DELTA: 00014
SCAN:34
FILE: S01938 VELCL:-01.000
ANGLE: 60.012 DELTA: 00006
SCAN:34
FILE: S01948 VELCL:-01.000
ANGLE: 57.996 DELTA: 00006
SCAN:34
FILE: S01958 VELCL:-01.000
ANGLE: 56.016 DELTA: 00006
INTENSITY
PIXEL

Figure 56

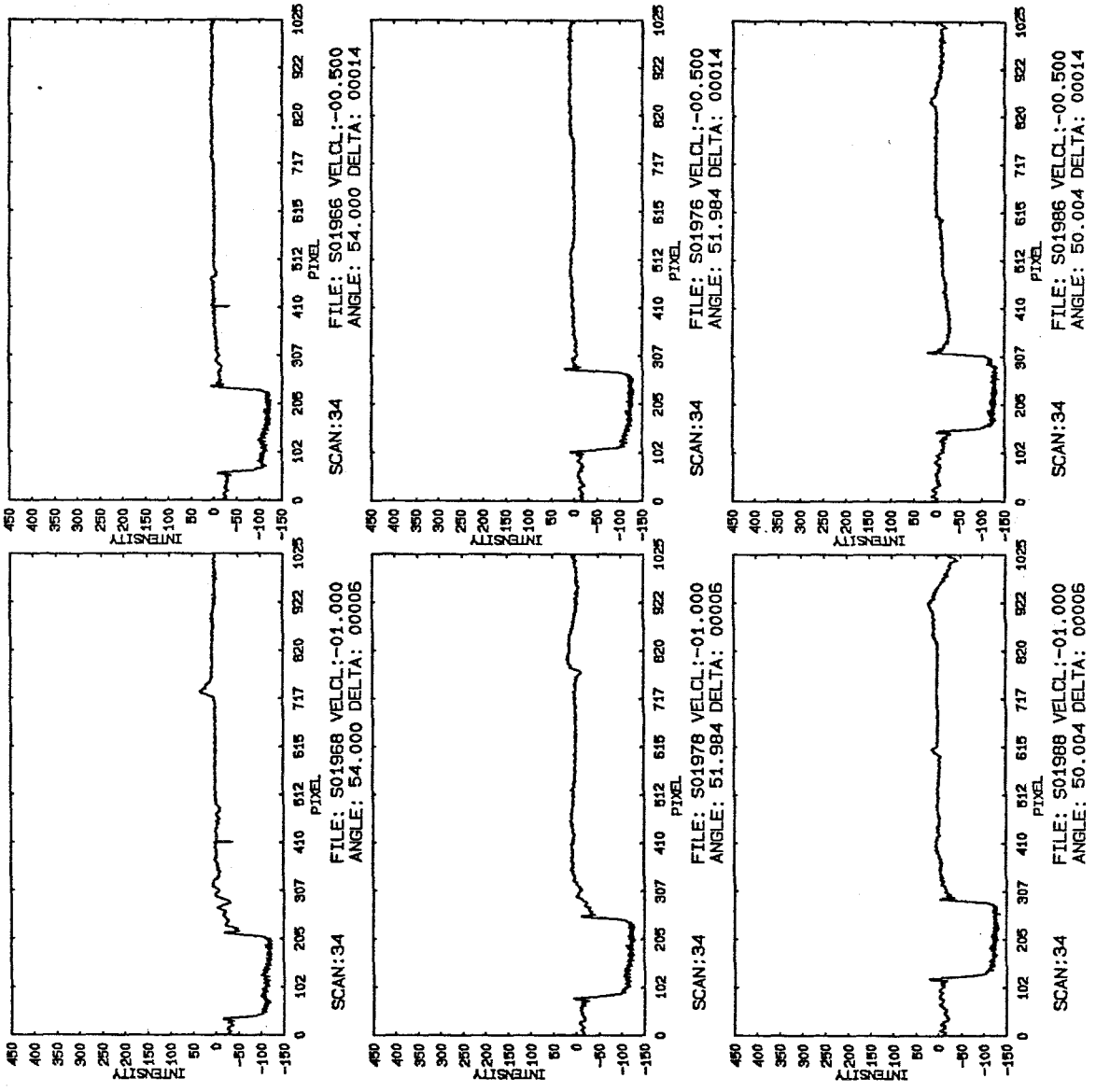
INTENSITY
PIXEL
SCAN:34
FILE: S01966 VELCL:-00.500
ANGLE: 54.000 DELTA: 00014
FILE: S01968 VELCL:-01.000
ANGLE: 54.000 DELTA: 00006
FILE: S01976 VELCL:-00.500
ANGLE: 51.984 DELTA: 00014
FILE: S01978 VELCL:-01.000
ANGLE: 51.984 DELTA: 00006
FILE: S01986 VELCL:-00.500
ANGLE: 50.004 DELTA: 00014
FILE: S01988 VELCL:-01.000
ANGLE: 50.004 DELTA: 00006

Figure 57

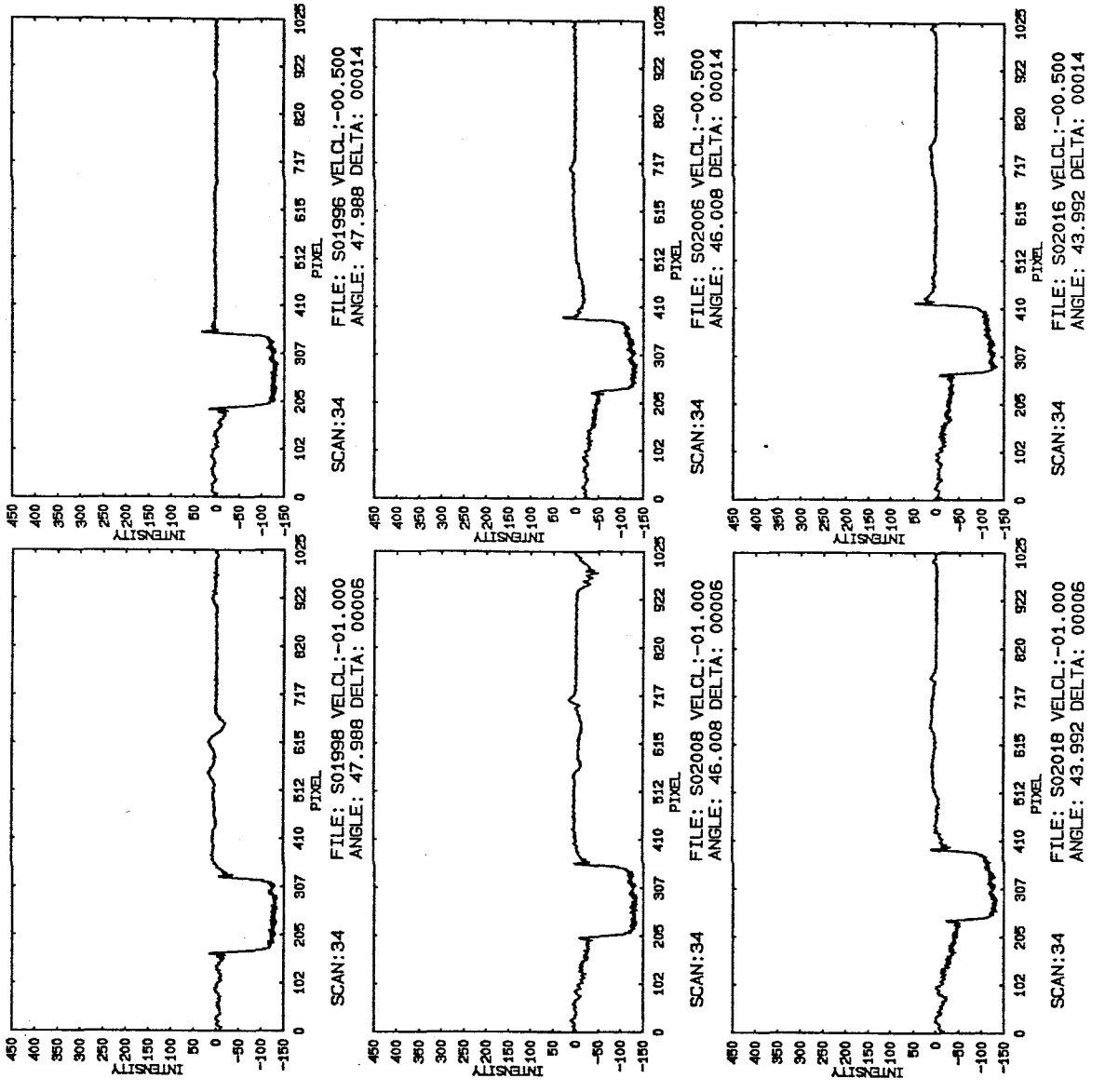
SCAN:34
FILE: S01998 VELCL:-01.000
ANGLE: 47.988 DELTA: 00006
SCAN:34
FILE: S01996 VELCL:-00.500
ANGLE: 47.988 DELTA: 00014
SCAN:34
FILE: S02008 VELCL:-01.000
ANGLE: 46.008 DELTA: 00006
SCAN:34
FILE: S02006 VELCL:-00.500
ANGLE: 46.008 DELTA: 00014
SCAN:34
FILE: S02018 VELCL:-01.000
ANGLE: 43.992 DELTA: 00006
SCAN:34
FILE: S02016 VELCL:-00.500
ANGLE: 43.992 DELTA: 00014
INTENSITY
PIXEL

Figure 58

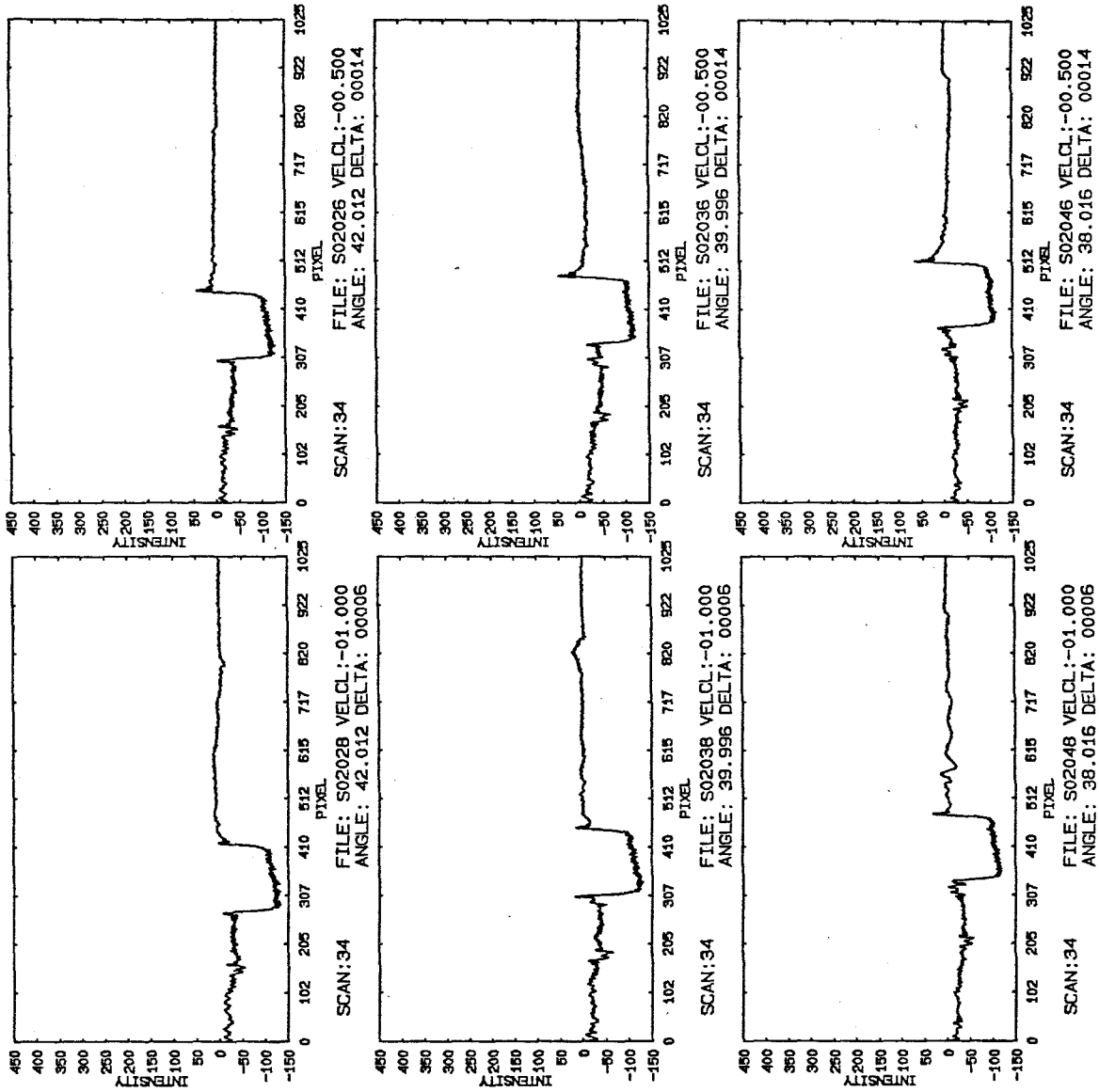
INTENSITY
PIXEL
SCAN:34
FILE: S02026 VELCL:-00.500
ANGLE: 42.012 DELTA: 00014
FILE: S02028 VELCL:-01.000
ANGLE: 42.012 DELTA: 00006
FILE: S02036 VELCL:-00.500
ANGLE: 39.996 DELTA: 00014
FILE: S02038 VELCL:-01.000
ANGLE: 39.996 DELTA: 00006
FILE: S02046 VELCL:-00.500
ANGLE: 38.016 DELTA: 00014
FILE: S02048 VELCL:-01.000
ANGLE: 38.016 DELTA: 00006

Figure 59

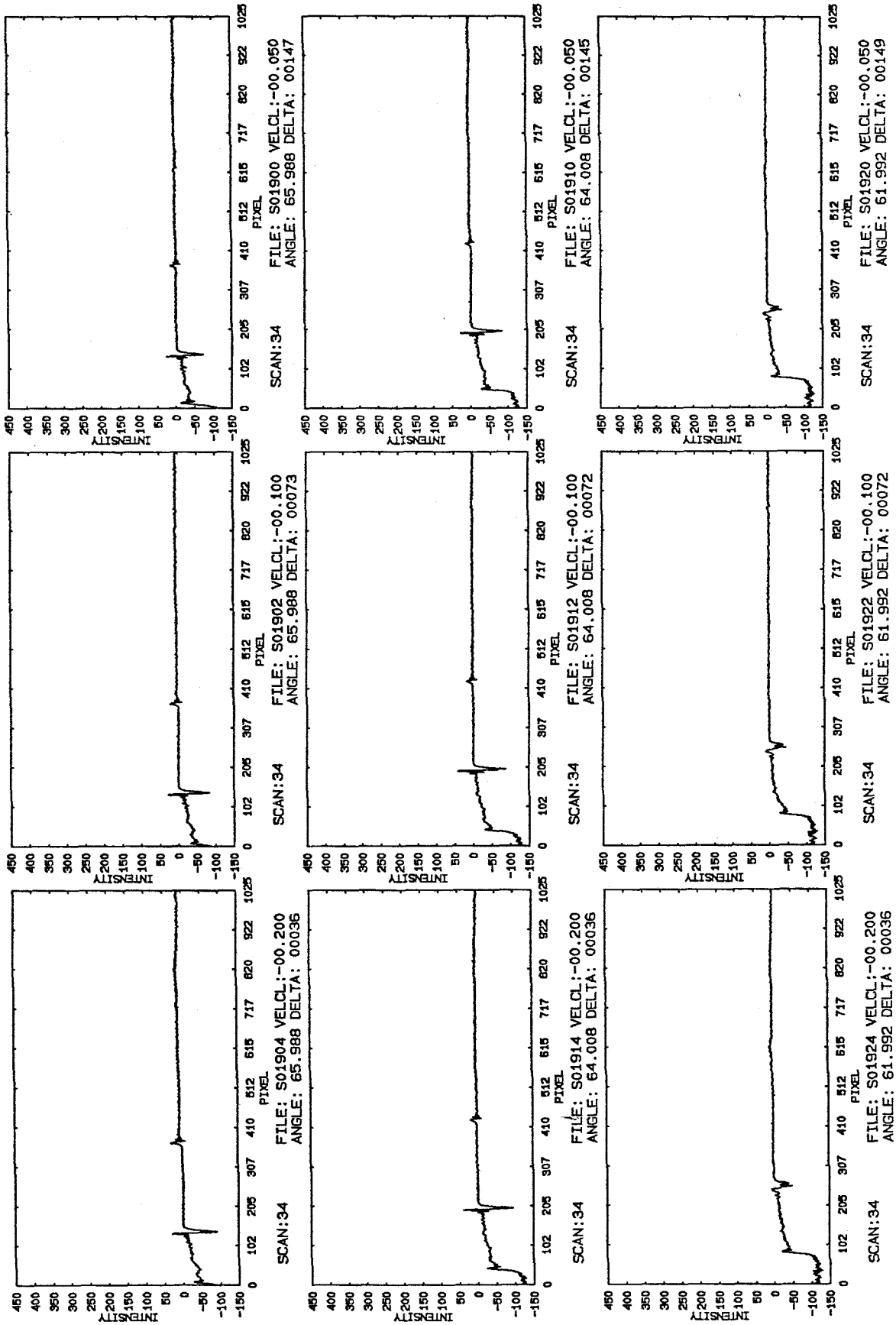
INTENSITY
PIXEL
SCAN:34
FILE: S01900 VELCL:-00.050
ANGLE: 65.988 DELTA: 00147
FILE: S01902 VELCL:-00.100
ANGLE: 65.988 DELTA: 00073
FILE: S01904 VELCL:-00.200
ANGLE: 65.988 DELTA: 00036
FILE: S01910 VELCL:-00.050
ANGLE: 64.008 DELTA: 00145
FILE: S01912 VELCL:-00.100
ANGLE: 64.008 DELTA: 00072
FILE: S01914 VELCL:-00.200
ANGLE: 64.008 DELTA: 00036
FILE: S01920 VELCL:-00.050
ANGLE: 61.992 DELTA: 00149
FILE: S01922 VELCL:-00.100
ANGLE: 61.992 DELTA: 00072
FILE: S01924 VELCL:-00.200
ANGLE: 61.992 DELTA: 00036

Figure 60

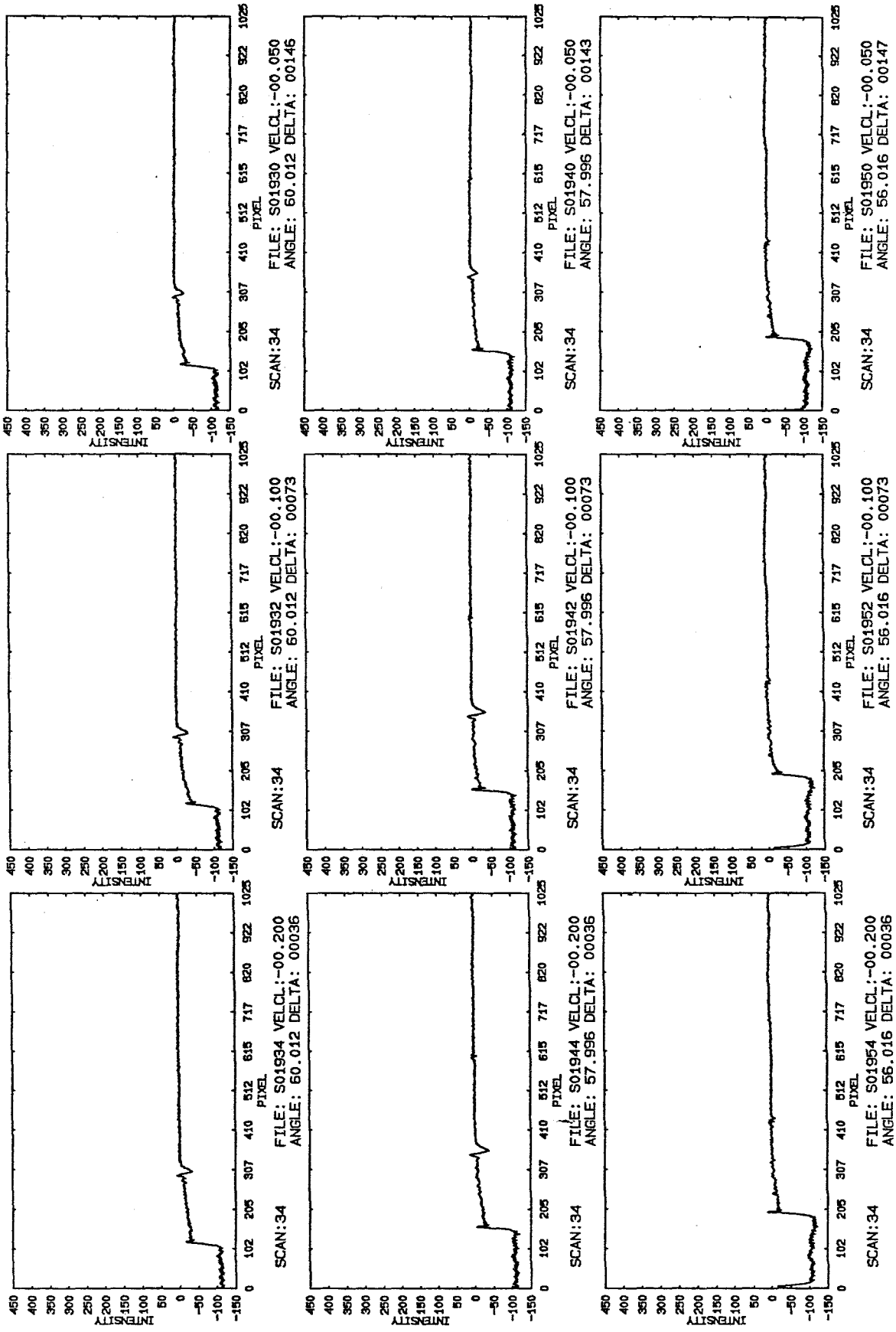
INTENSITY
PIXEL
SCAN:34
FILE: S01930 VELCL:-00.050
ANGLE: 60.012 DELTA: 00146
FILE: S01932 VELCL:-00.100
ANGLE: 60.012 DELTA: 00073
FILE: S01934 VELCL:-00.200
ANGLE: 60.012 DELTA: 00036
FILE: S01940 VELCL:-00.050
ANGLE: 57.996 DELTA: 00143
FILE: S01942 VELCL:-00.100
ANGLE: 57.996 DELTA: 00073
FILE: S01944 VELCL:-00.200
ANGLE: 57.996 DELTA: 00036
FILE: S01950 VELCL:-00.050
ANGLE: 56.016 DELTA: 00147
FILE: S01952 VELCL:-00.100
ANGLE: 56.016 DELTA: 00073
FILE: S01954 VELCL:-00.200
ANGLE: 56.016 DELTA: 00036

Figure 61

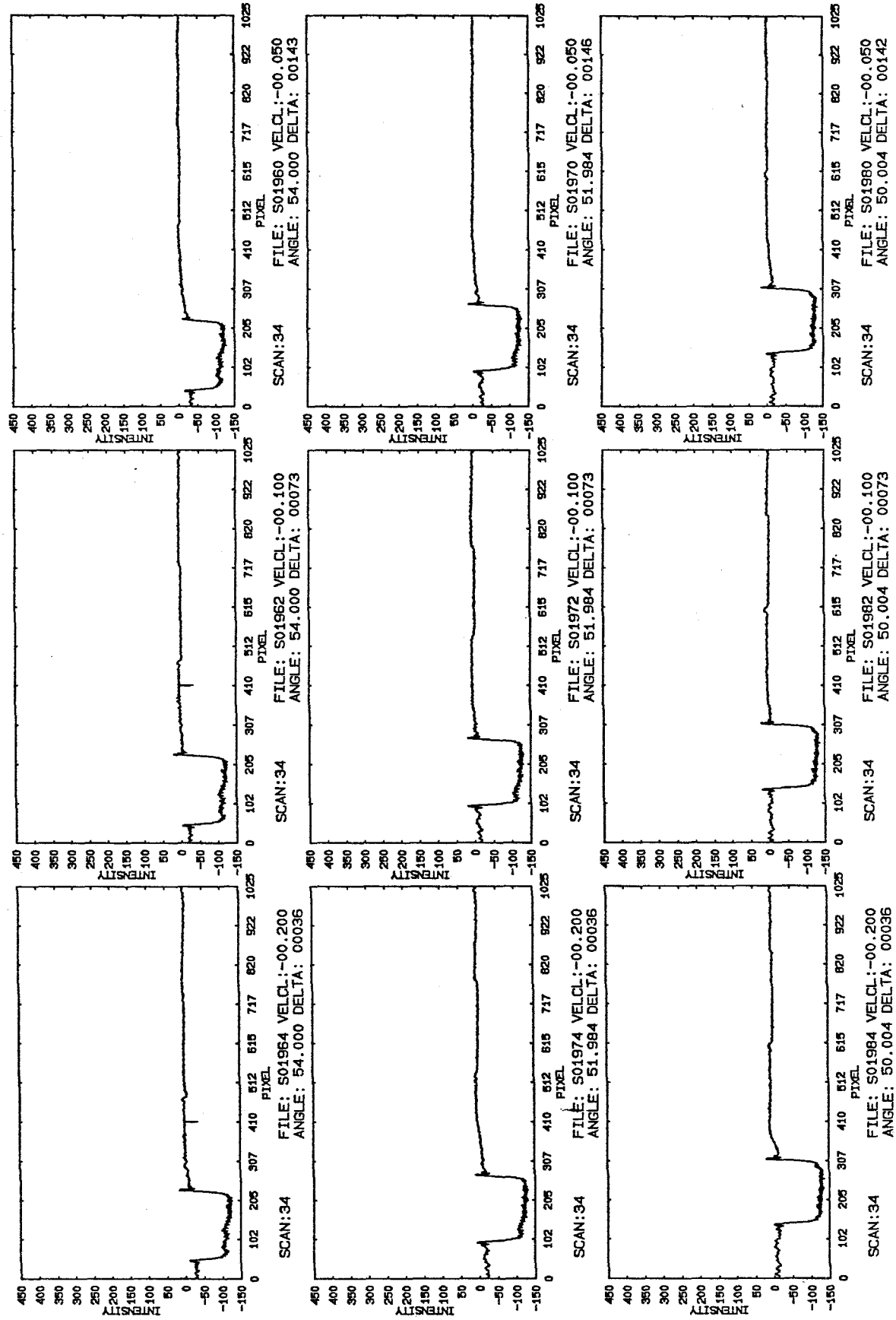
INTENSITY
PIXEL
SCAN:34
FILE: S01964 VELCL:-00.200
ANGLE: 54.000 DELTA: 00036
FILE: S01962 VELCL:-00.100
ANGLE: 54.000 DELTA: 00073
FILE: S01960 VELCL:-00.050
ANGLE: 54.000 DELTA: 00143
FILE: S01974 VELCL:-00.200
ANGLE: 51.984 DELTA: 00036
FILE: S01972 VELCL:-00.100
ANGLE: 51.984 DELTA: 00073
FILE: S01970 VELCL:-00.050
ANGLE: 51.984 DELTA: 00146
FILE: S01984 VELCL:-00.200
ANGLE: 50.004 DELTA: 00036
FILE: S01982 VELCL:-00.100
ANGLE: 50.004 DELTA: 00073
FILE: S01980 VELCL:-00.050
ANGLE: 50.004 DELTA: 00142

Figure 62

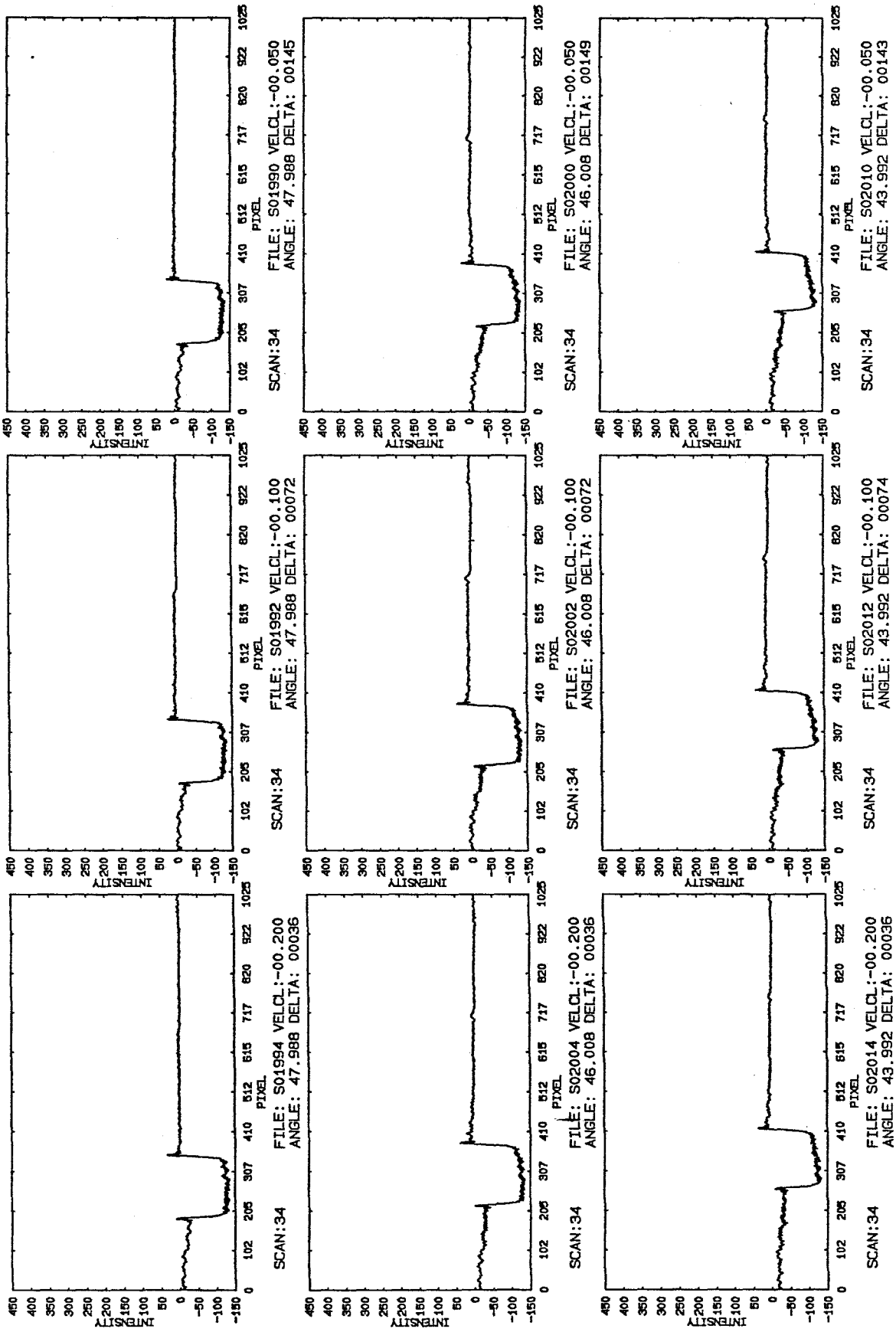
INTENSITY
PIXEL
SCAN:34
FILE: S01990 VELCL:-00.050
ANGLE: 47.988 DELTA: 00145
FILE: S01992 VELCL:-00.100
ANGLE: 47.988 DELTA: 00072
FILE: S01994 VELCL:-00.200
ANGLE: 47.988 DELTA: 00036
FILE: S02000 VELCL:-00.050
ANGLE: 46.008 DELTA: 00149
FILE: S02002 VELCL:-00.100
ANGLE: 46.008 DELTA: 00072
FILE: S02004 VELCL:-00.200
ANGLE: 46.008 DELTA: 00036
FILE: S02010 VELCL:-00.050
ANGLE: 43.992 DELTA: 00143
FILE: S02012 VELCL:-00.100
ANGLE: 43.992 DELTA: 00074
FILE: S02014 VELCL:-00.200
ANGLE: 43.992 DELTA: 00036

Figure 63

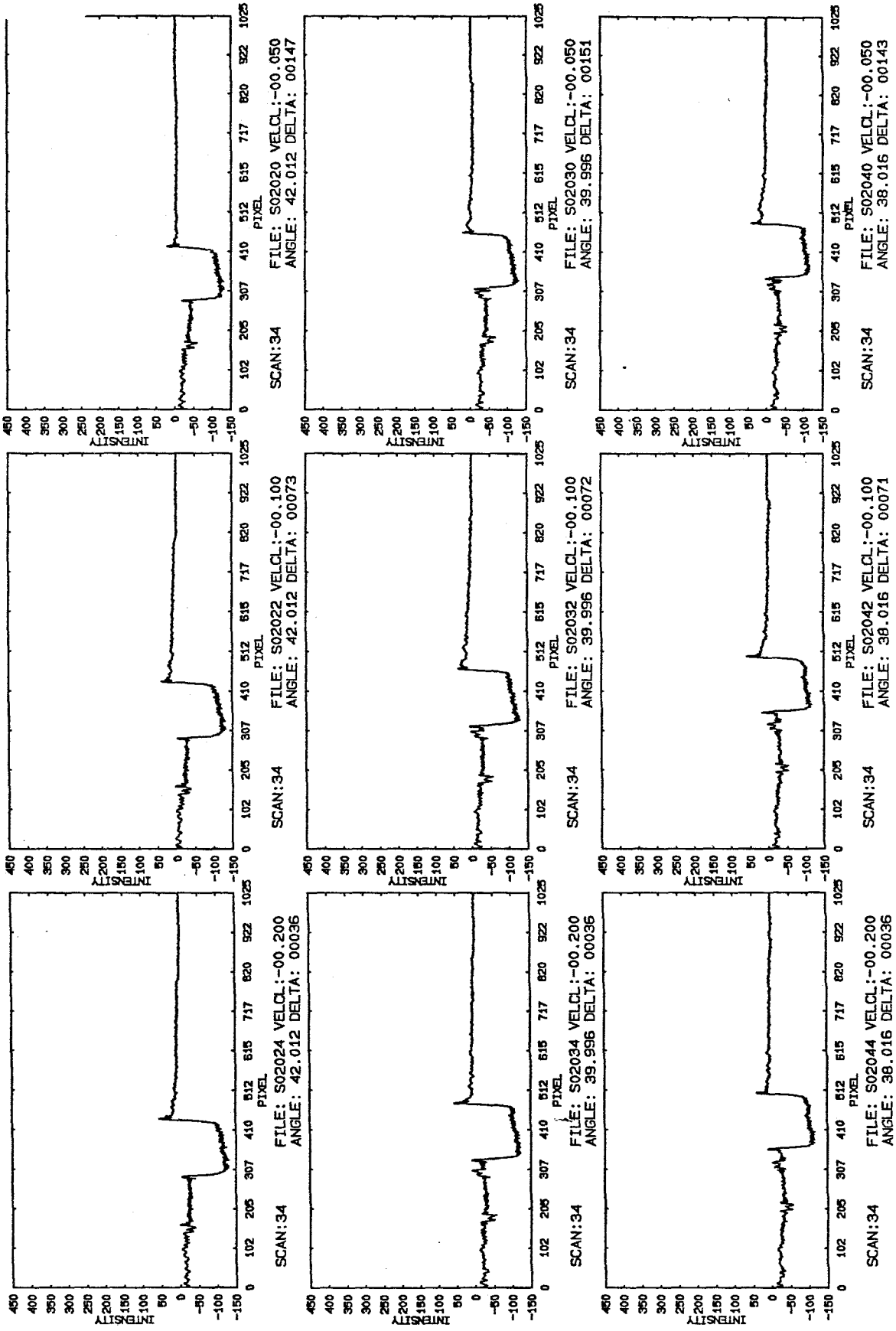
INTENSITY
PIXEL
SCAN:34
FILE: S02020 VELCL:-00.050
ANGLE: 42.012 DELTA: 00147
FILE: S02022 VELCL:-00.100
ANGLE: 42.012 DELTA: 00073
FILE: S02024 VELCL:-00.200
ANGLE: 42.012 DELTA: 00036
FILE: S02030 VELCL:-00.050
ANGLE: 39.996 DELTA: 00151
FILE: S02032 VELCL:-00.100
ANGLE: 39.996 DELTA: 00072
FILE: S02034 VELCL:-00.200
ANGLE: 39.996 DELTA: 00036
FILE: S02040 VELCL:-00.050
ANGLE: 38.016 DELTA: 00143
FILE: S02042 VELCL:-00.100
ANGLE: 38.016 DELTA: 00071
FILE: S02044 VELCL:-00.200
ANGLE: 38.016 DELTA: 00036

Figure 64

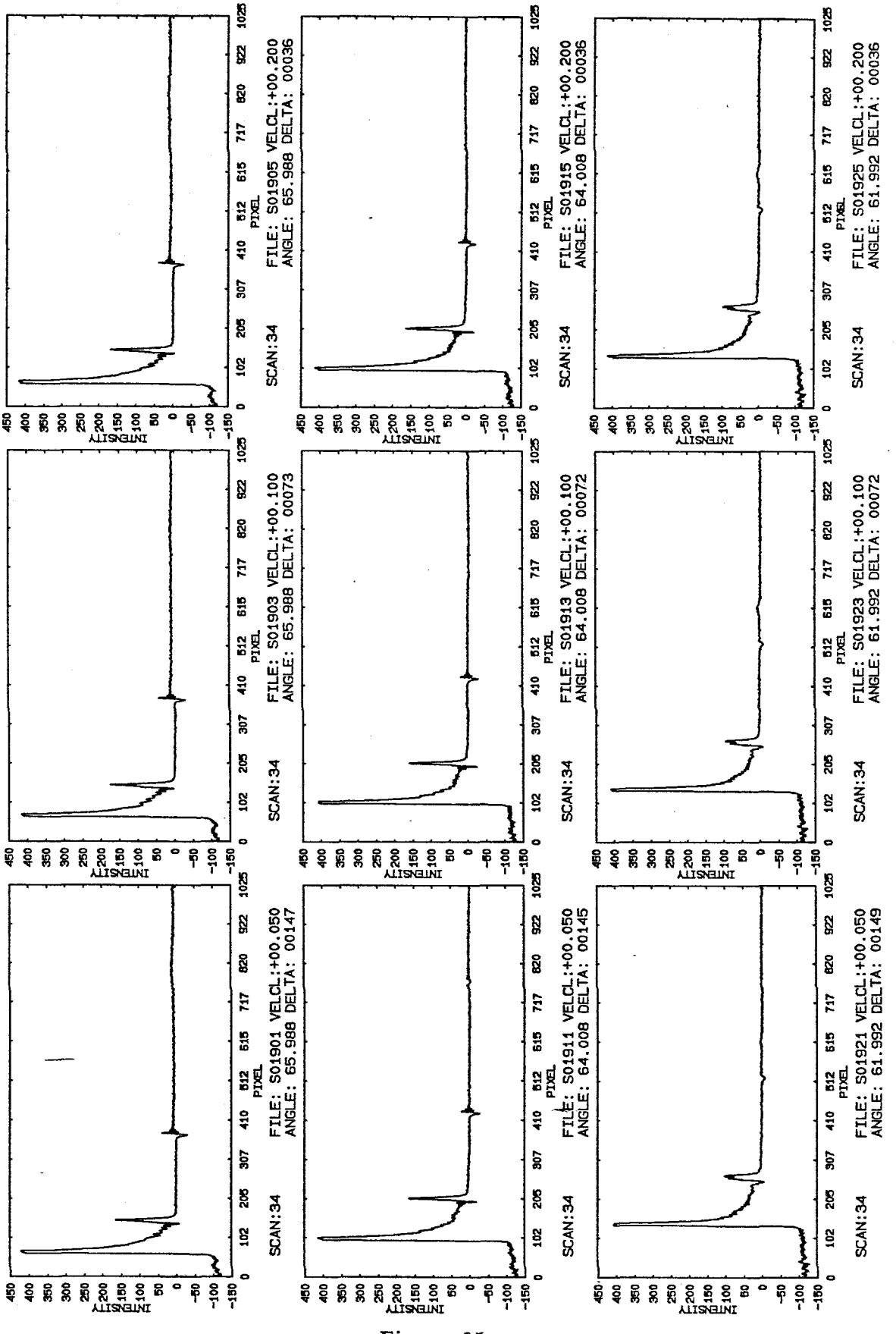
INTENSITY
PIXEL
SCAN:34
FILE: S01901 VELCL:+00.050
ANGLE: 65.988 DELTA: 00147
FILE: S01903 VELCL:+00.100
ANGLE: 65.988 DELTA: 00073
FILE: S01905 VELCL:+00.200
ANGLE: 65.988 DELTA: 00036
FILE: S01911 VELCL:+00.050
ANGLE: 64.008 DELTA: 00145
FILE: S01913 VELCL:+00.100
ANGLE: 64.008 DELTA: 00072
FILE: S01915 VELCL:+00.200
ANGLE: 64.008 DELTA: 00036
FILE: S01921 VELCL:+00.050
ANGLE: 61.992 DELTA: 00149
FILE: S01923 VELCL:+00.100
ANGLE: 61.992 DELTA: 00072
FILE: S01925 VELCL:+00.200
ANGLE: 61.992 DELTA: 00036

Figure 65

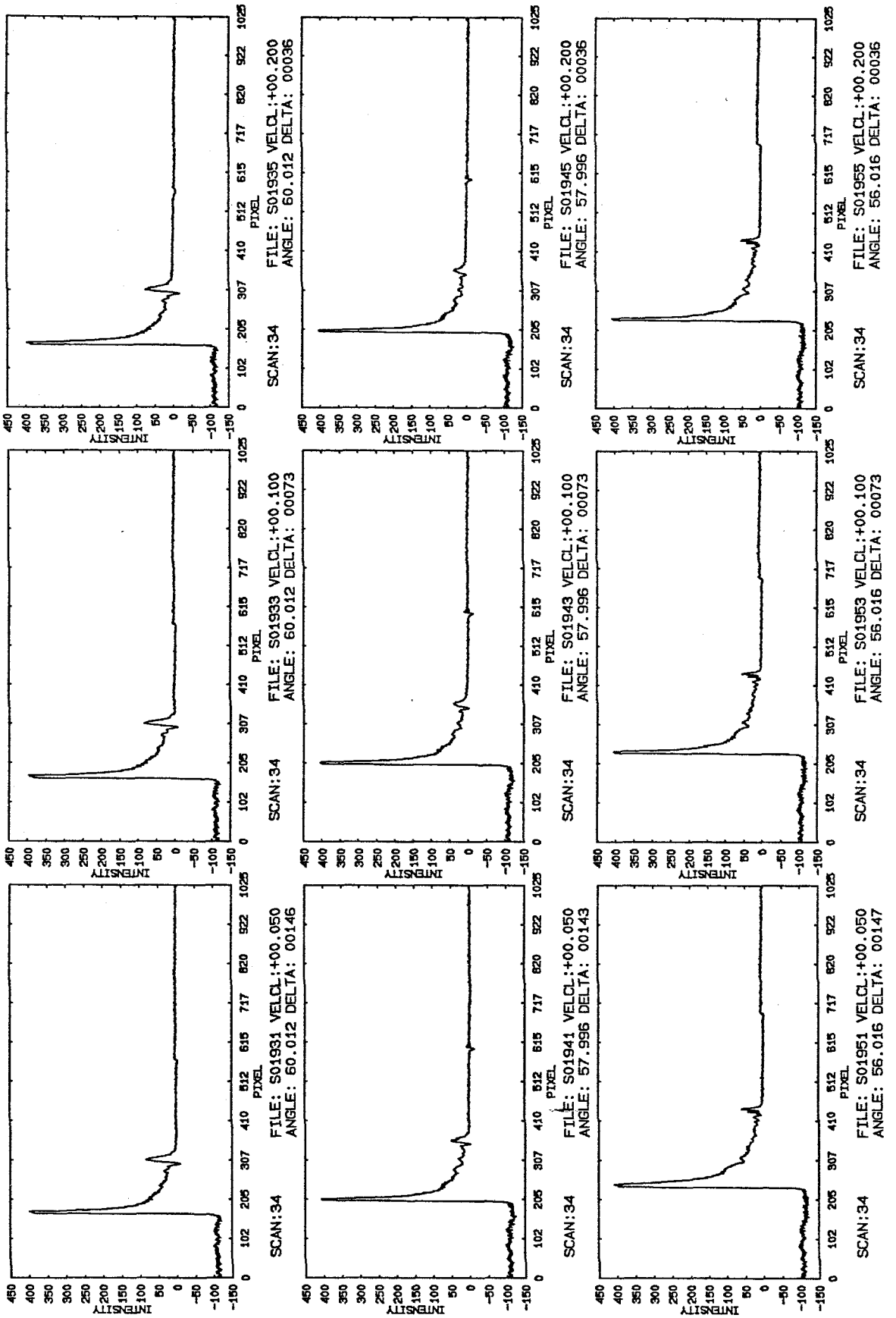
INTENSITY
PIXEL
SCAN:34
FILE: S01931 VELCL:+00.050
ANGLE: 60.012 DELTA: 00146
FILE: S01933 VELCL:+00.100
ANGLE: 60.012 DELTA: 00073
FILE: S01935 VELCL:+00.200
ANGLE: 60.012 DELTA: 00036
FILE: S01941 VELCL:+00.050
ANGLE: 57.996 DELTA: 00143
FILE: S01943 VELCL:+00.100
ANGLE: 57.996 DELTA: 00073
FILE: S01945 VELCL:+00.200
ANGLE: 57.996 DELTA: 00036
FILE: S01951 VELCL:+00.050
ANGLE: 56.016 DELTA: 00147
FILE: S01953 VELCL:+00.100
ANGLE: 56.016 DELTA: 00073
FILE: S01955 VELCL:+00.200
ANGLE: 56.016 DELTA: 00036

Figure 66

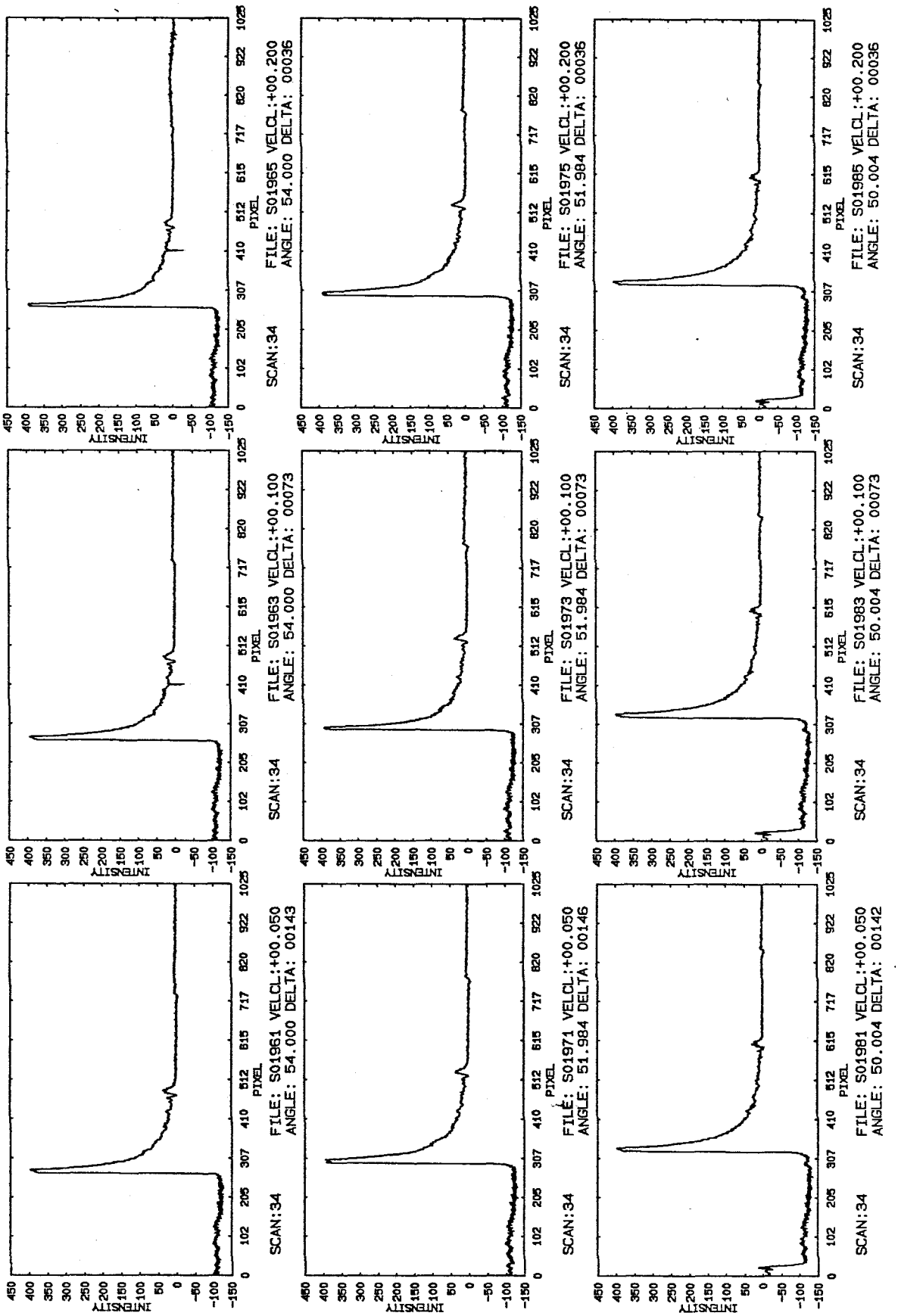
INTENSITY
PIXEL
SCAN:34
FILE: S01961 VELCL:+00.050
ANGLE: 54.000 DELTA: 00143
FILE: S01963 VELCL:+00.100
ANGLE: 54.000 DELTA: 00073
FILE: S01965 VELCL:+00.200
ANGLE: 54.000 DELTA: 00036
FILE: S01971 VELCL:+00.050
ANGLE: 51.984 DELTA: 00146
FILE: S01973 VELCL:+00.100
ANGLE: 51.984 DELTA: 00073
FILE: S01975 VELCL:+00.200
ANGLE: 51.984 DELTA: 00036
FILE: S01981 VELCL:+00.050
ANGLE: 50.004 DELTA: 00142
FILE: S01983 VELCL:+00.100
ANGLE: 50.004 DELTA: 00073
FILE: S01985 VELCL:+00.200
ANGLE: 50.004 DELTA: 00036

Figure 67

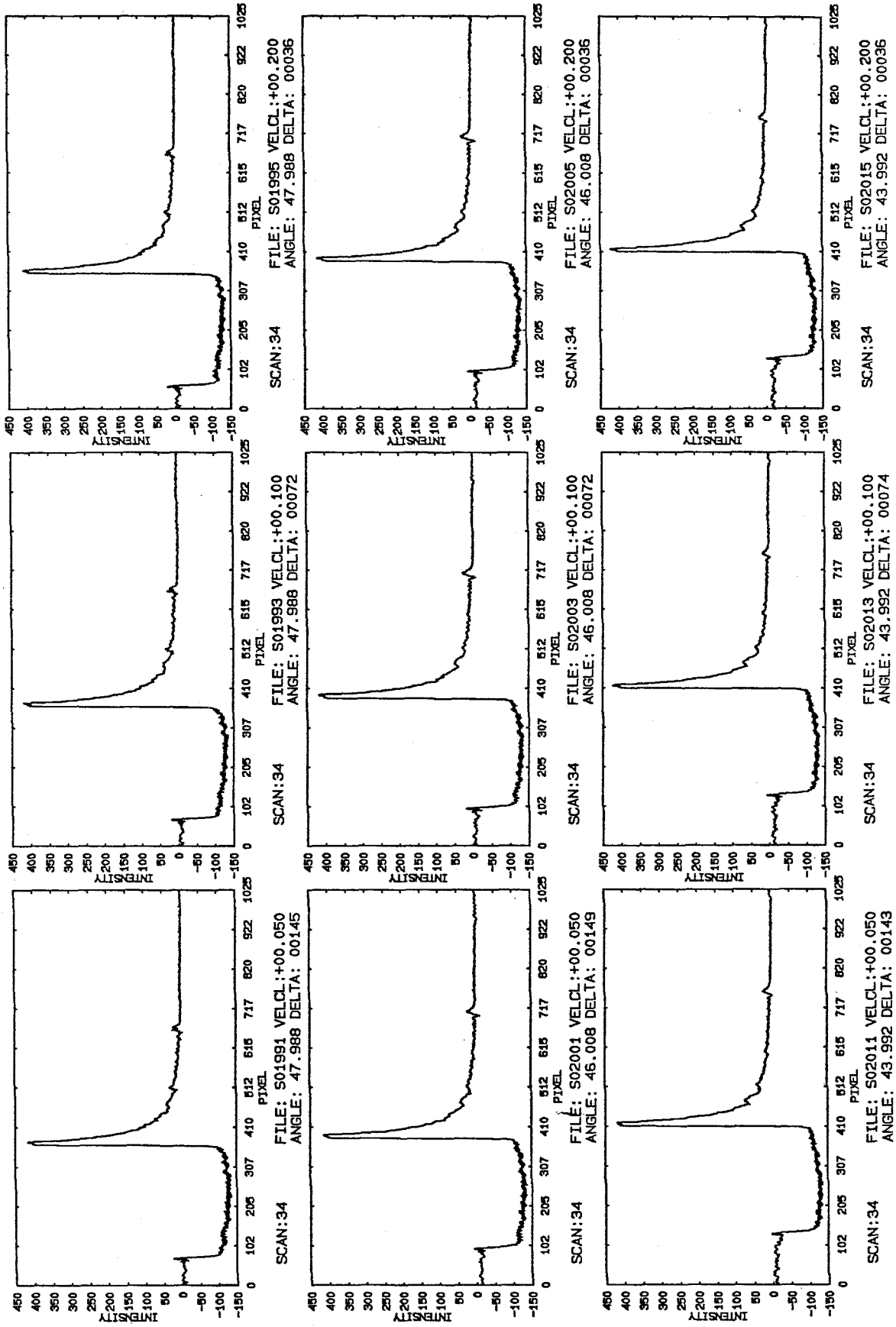
INTENSITY
PIXEL
SCAN:34
FILE: S01995 VELCL:+00.200
ANGLE: 47.988 DELTA: 00036
FILE: S01993 VELCL:+00.100
ANGLE: 47.988 DELTA: 00072
FILE: S01991 VELCL:+00.050
ANGLE: 47.988 DELTA: 00145
FILE: S02005 VELCL:+00.200
ANGLE: 46.008 DELTA: 00036
FILE: S02003 VELCL:+00.100
ANGLE: 46.008 DELTA: 00072
FILE: S02001 VELCL:+00.050
ANGLE: 46.008 DELTA: 00149
FILE: S02015 VELCL:+00.200
ANGLE: 43.992 DELTA: 00036
FILE: S02013 VELCL:+00.100
ANGLE: 43.992 DELTA: 00074
FILE: S02011 VELCL:+00.050
ANGLE: 43.992 DELTA: 00143

Figure 68

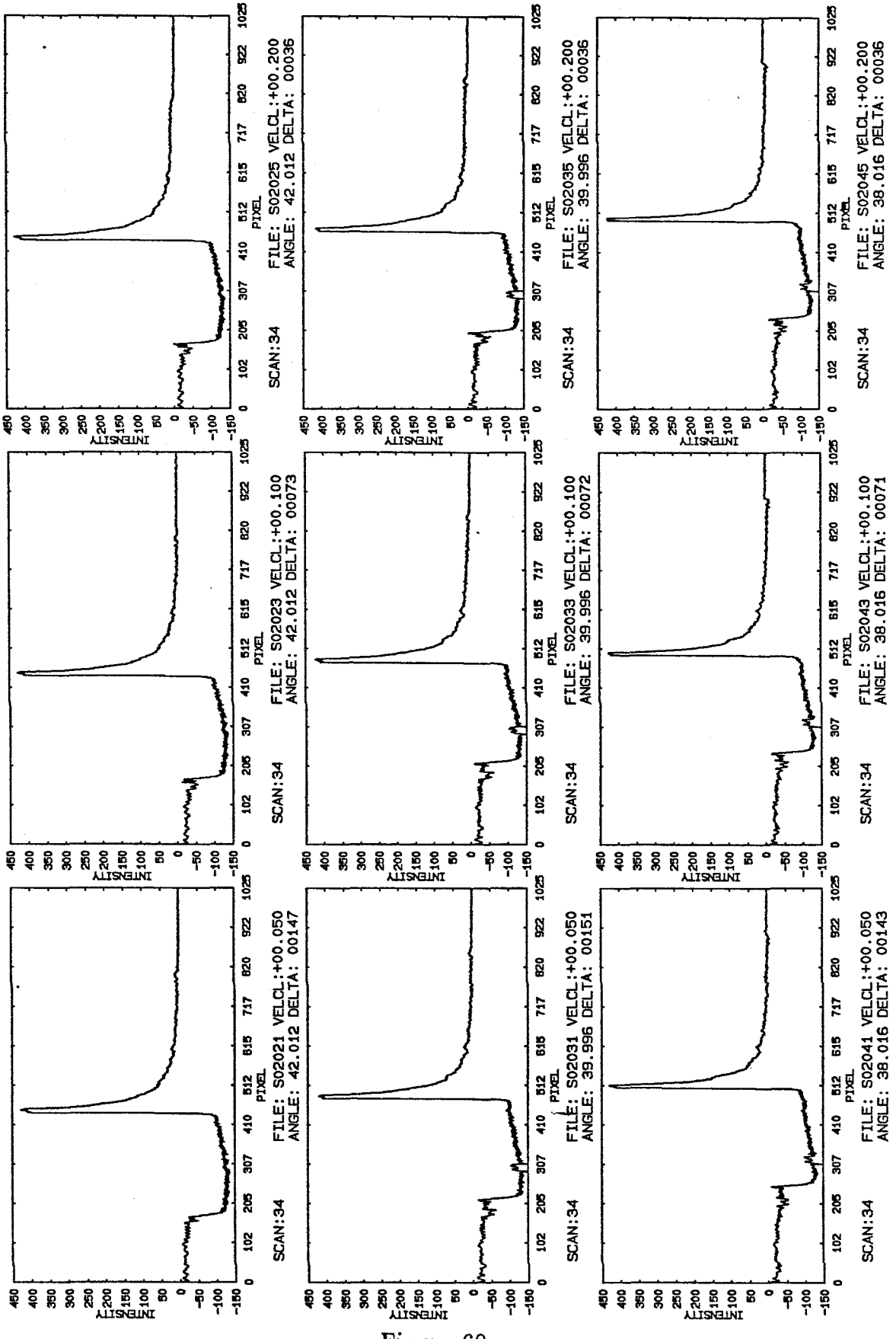
INTENSITY
PIXEL
SCAN:34
FILE: S02021 VELCL:+00.050
ANGLE: 42.012 DELTA: 00147
FILE: S02031 VELCL:+00.050
ANGLE: 39.996 DELTA: 00151
FILE: S02041 VELCL:+00.050
ANGLE: 38.016 DELTA: 00143
FILE: S02023 VELCL:+00.100
ANGLE: 42.012 DELTA: 00073
FILE: S02033 VELCL:+00.100
ANGLE: 39.996 DELTA: 00072
FILE: S02043 VELCL:+00.100
ANGLE: 38.016 DELTA: 00071
FILE: S02025 VELCL:+00.200
ANGLE: 42.012 DELTA: 00036
FILE: S02035 VELCL:+00.200
ANGLE: 39.996 DELTA: 00036
FILE: S02045 VELCL:+00.200
ANGLE: 38.016 DELTA: 00036

Figure 69

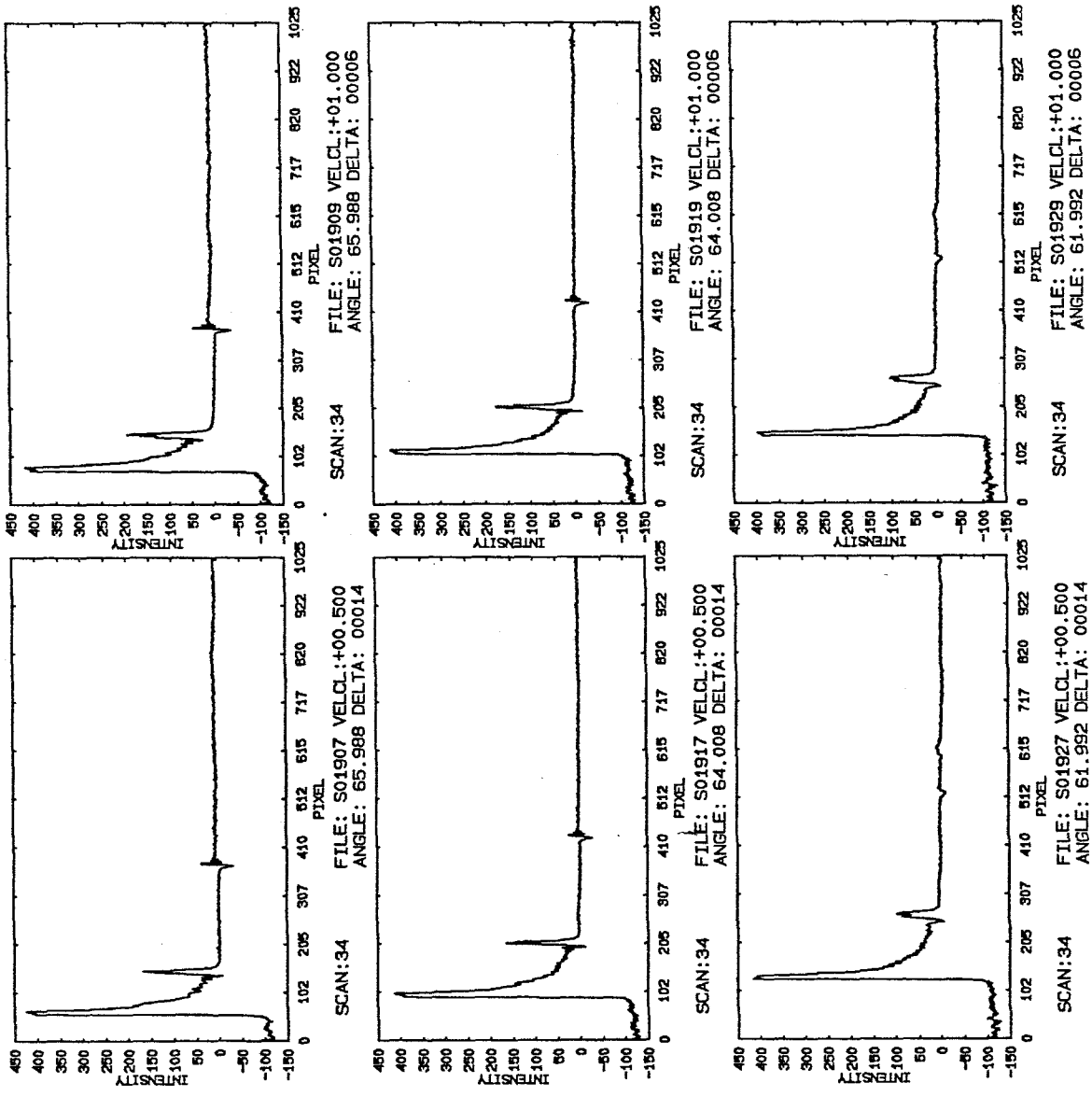
INTENSITY
PIXEL
SCAN:34
FILE: S01907 VELCL:+00.500
ANGLE: 65.988 DELTA: 00014
FILE: S01909 VELCL:+01.000
ANGLE: 65.988 DELTA: 00006
FILE: S01917 VELCL:+00.500
ANGLE: 64.008 DELTA: 00014
FILE: S01919 VELCL:+01.000
ANGLE: 64.008 DELTA: 00006
FILE: S01927 VELCL:+00.500
ANGLE: 61.992 DELTA: 00014
FILE: S01929 VELCL:+01.000
ANGLE: 61.992 DELTA: 00006

Figure 70

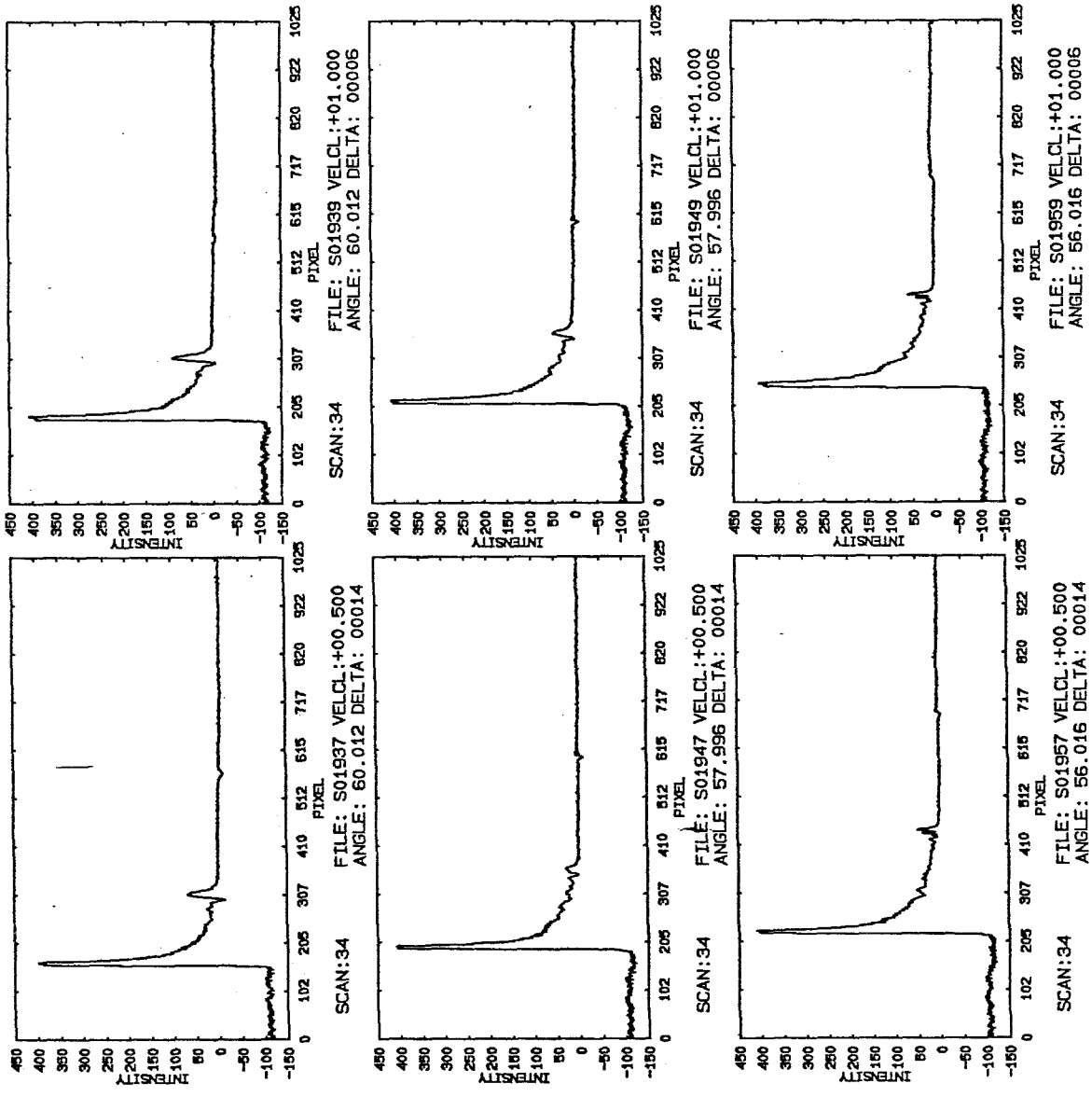
INTENSITY
PIXEL
SCAN:34
FILE: S01937 VELCL:+00.500
ANGLE: 60.012 DELTA: 00014
FILE: S01939 VELCL:+01.000
ANGLE: 60.012 DELTA: 00006
FILE: S01947 VELCL:+00.500
ANGLE: 57.996 DELTA: 00014
FILE: S01949 VELCL:+01.000
ANGLE: 57.996 DELTA: 00006
FILE: S01957 VELCL:+00.500
ANGLE: 56.016 DELTA: 00014
FILE: S01959 VELCL:+01.000
ANGLE: 56.016 DELTA: 00006

Figure 71

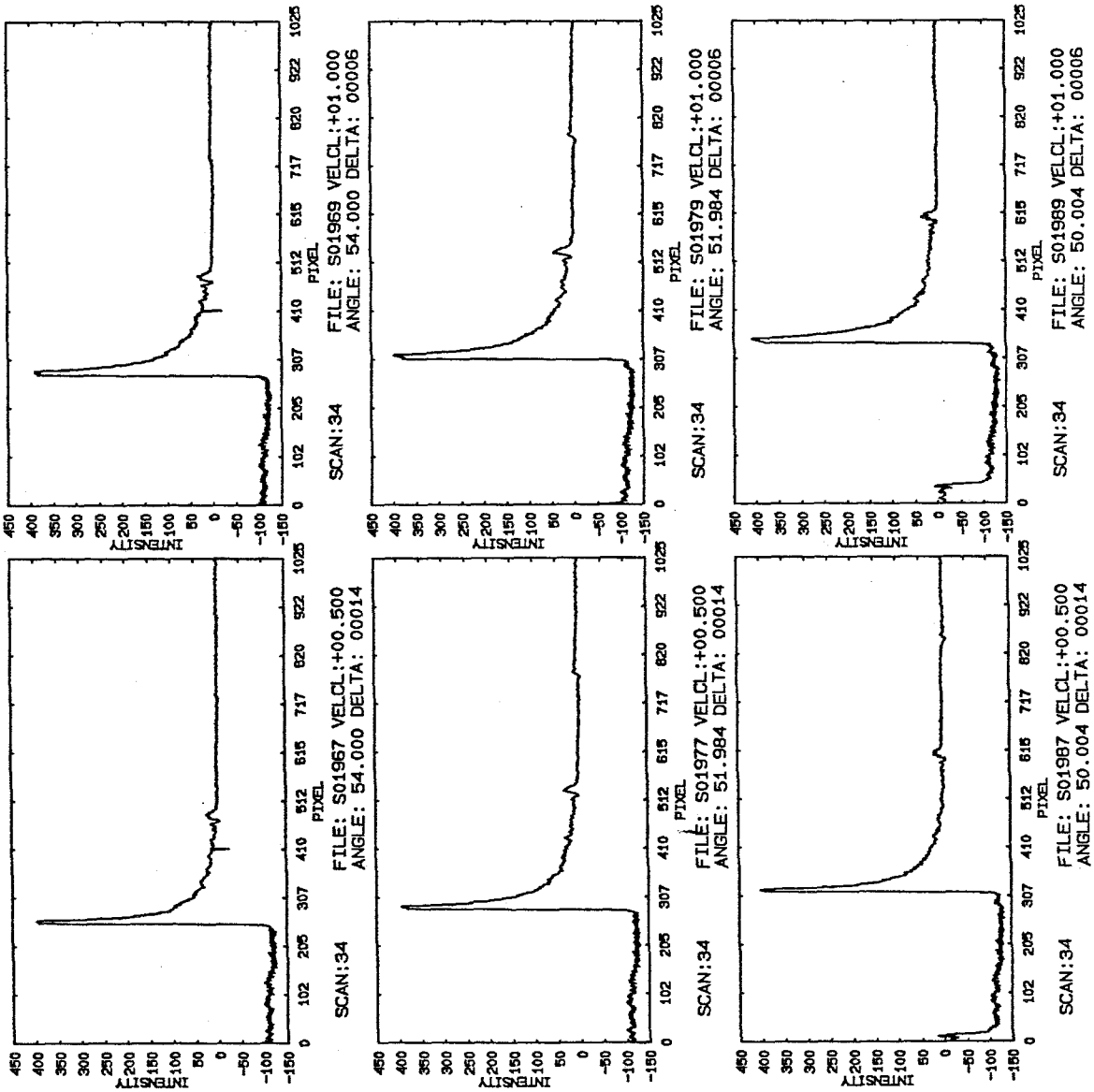
INTENSITY
PIXEL
SCAN:34
FILE: S01967 VELCL:+00.500
ANGLE: 54.000 DELTA: 00014
FILE: S01969 VELCL:+01.000
ANGLE: 54.000 DELTA: 00006
FILE: S01977 VELCL:+00.500
ANGLE: 51.984 DELTA: 00014
FILE: S01979 VELCL:+01.000
ANGLE: 51.984 DELTA: 00006
FILE: S01987 VELCL:+00.500
ANGLE: 50.004 DELTA: 00014
FILE: S01989 VELCL:+01.000
ANGLE: 50.004 DELTA: 00006

Figure 72

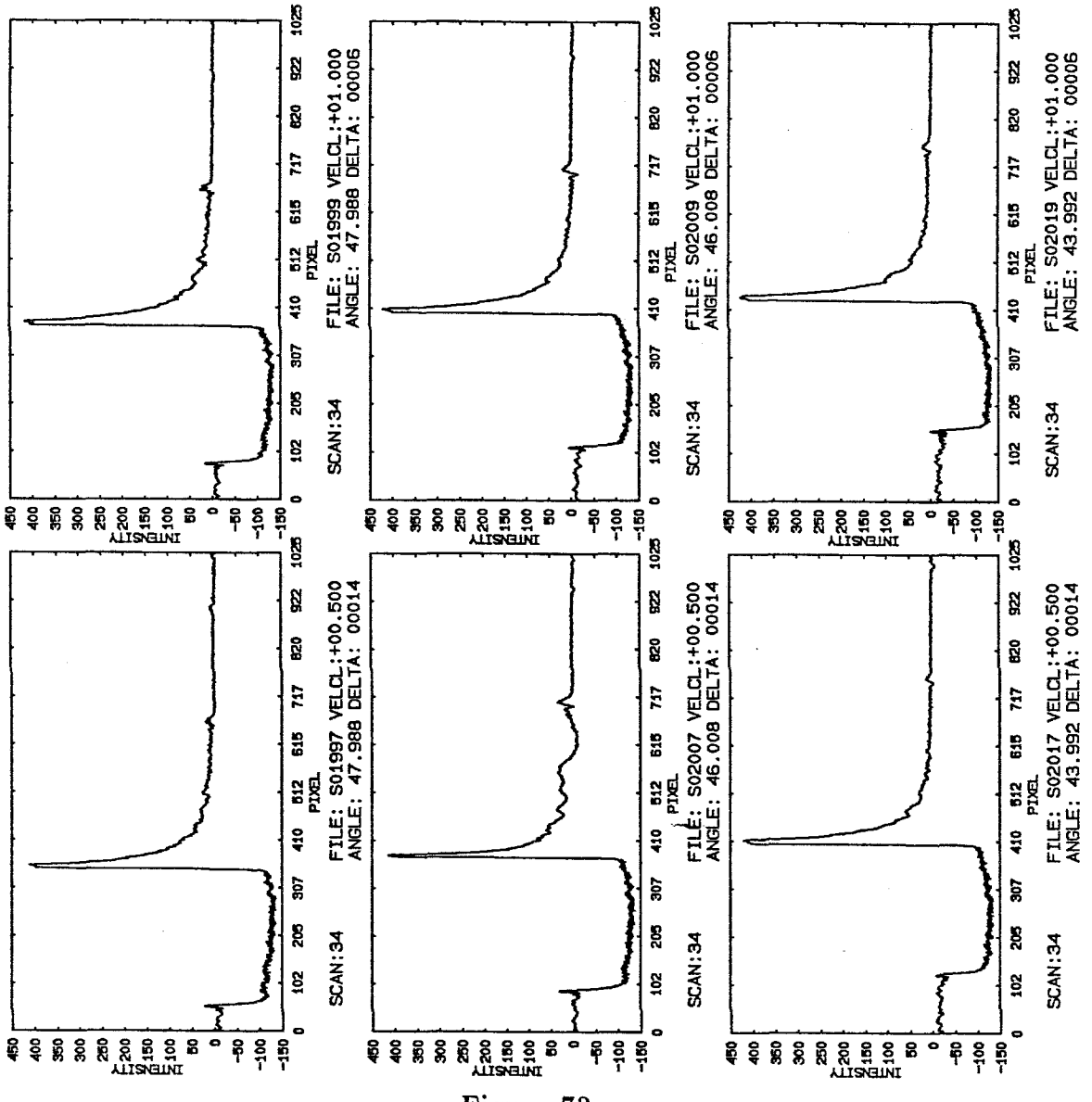
INTENSITY
PIXEL
SCAN:34
FILE: S01997 VELCL:+00.500
ANGLE: 47.988 DELTA: 00014
FILE: S01999 VELCL:+01.000
ANGLE: 47.988 DELTA: 00006
FILE: S02007 VELCL:+00.500
ANGLE: 46.008 DELTA: 00014
FILE: S02009 VELCL:+01.000
ANGLE: 46.008 DELTA: 00006
FILE: S02017 VELCL:+00.500
ANGLE: 43.992 DELTA: 00014
FILE: S02019 VELCL:+01.000
ANGLE: 43.992 DELTA: 00006

Figure 73

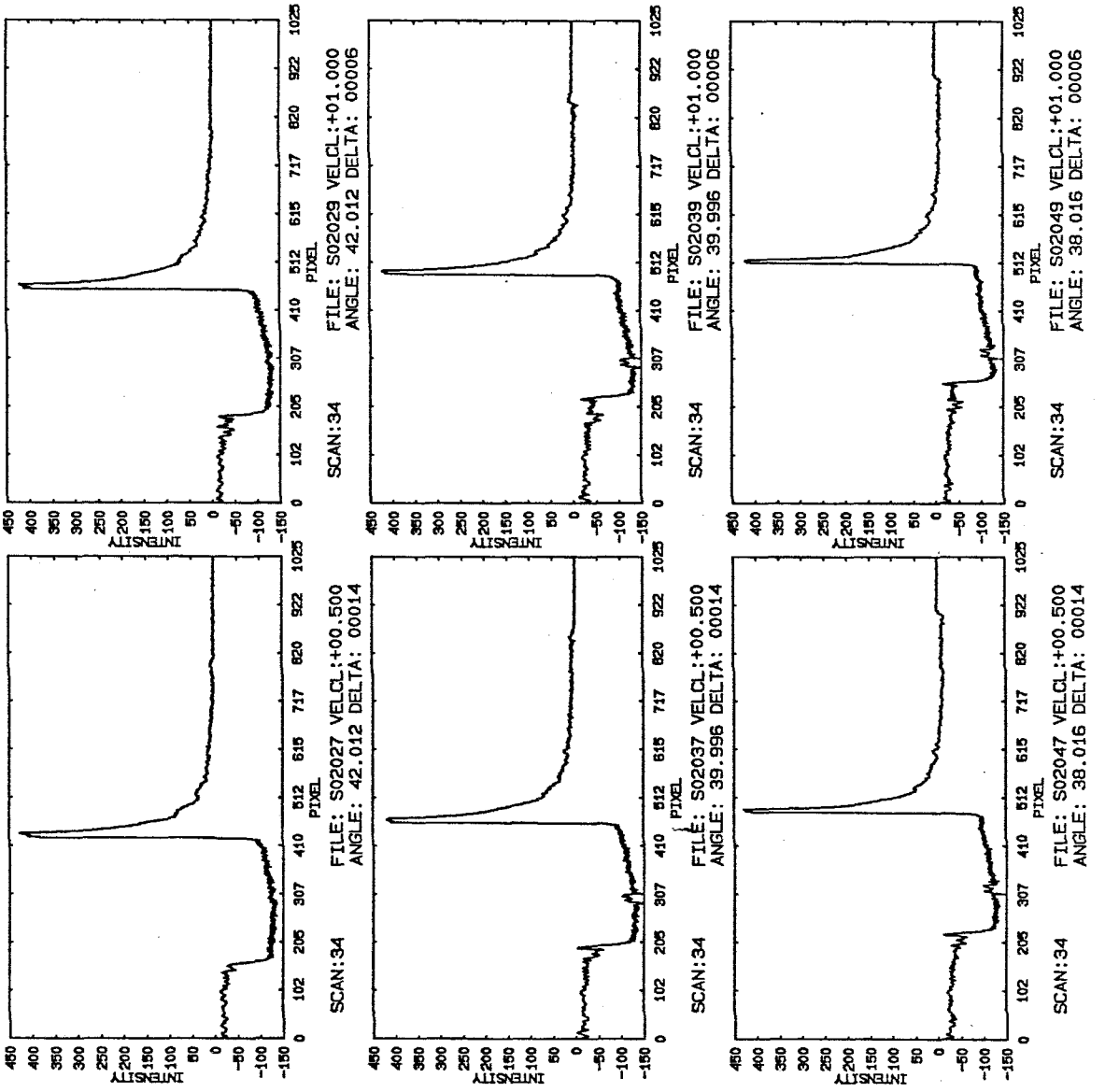
INTENSITY
PIXEL
SCAN:34
FILE: S02027 VELCL:+00.500
ANGLE: 42.012 DELTA: 00014
FILE: S02029 VELCL:+01.000
ANGLE: 42.012 DELTA: 00006
FILE: S02037 VELCL:+00.500
ANGLE: 39.996 DELTA: 00014
FILE: S02039 VELCL:+01.000
ANGLE: 39.996 DELTA: 00006
FILE: S02047 VELCL:+00.500
ANGLE: 38.016 DELTA: 00014
FILE: S02049 VELCL:+01.000
ANGLE: 38.016 DELTA: 00006

Figure 74

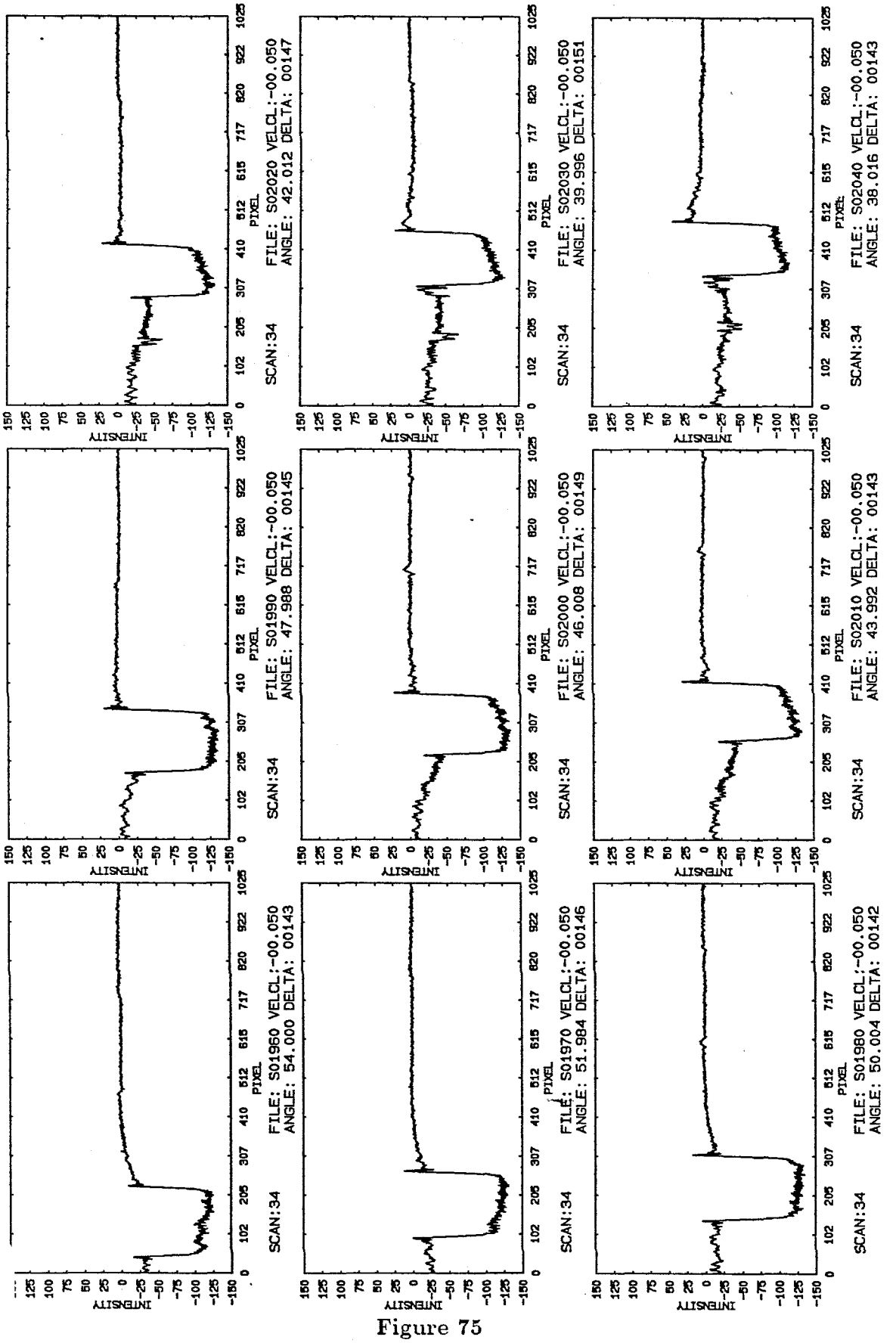
INTENSITY
PIXEL
SCAN:34
FILE: S01960 VELCL:-00.050
ANGLE: 54.000 DELTA: 00143
FILE: S01970 VELCL:-00.050
ANGLE: 51.984 DELTA: 00146
FILE: S01980 VELCL:-00.050
ANGLE: 50.004 DELTA: 00142
FILE: S01990 VELCL:-00.050
ANGLE: 47.988 DELTA: 00145
FILE: S02000 VELCL:-00.050
ANGLE: 46.008 DELTA: 00149
FILE: S02010 VELCL:-00.050
ANGLE: 43.992 DELTA: 00143
FILE: S02020 VELCL:-00.050
ANGLE: 42.012 DELTA: 00147
FILE: S02030 VELCL:-00.050
ANGLE: 39.996 DELTA: 00151
FILE: S02040 VELCL:-00.050
ANGLE: 38.016 DELTA: 00143

Figure 75

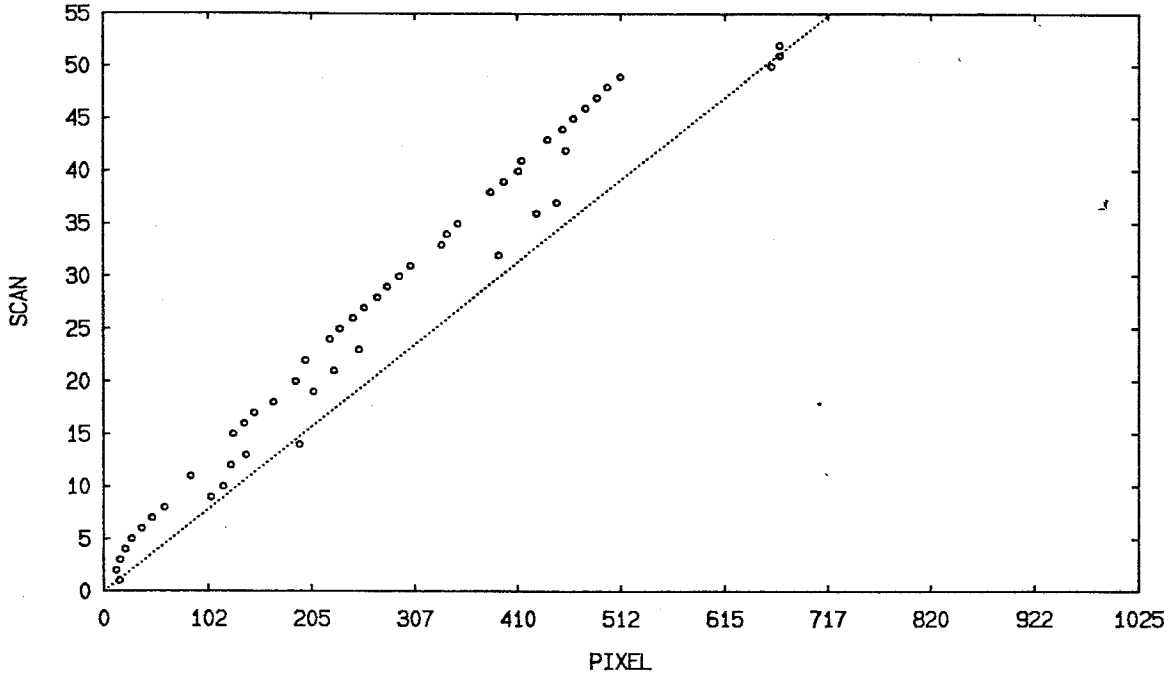

RISE 01-MAR-90 14:44:11 UPR: NONANE LWR: FRMIDE PLATE:29.900
1,52, 1 MOTOR: V00.017 A010.000 D00211633 H- DELAY:00000
FILE: S01990 VELCL:-00.050 ANGLE: 47.988 DELTA: 00145 NUMDEL: 00052

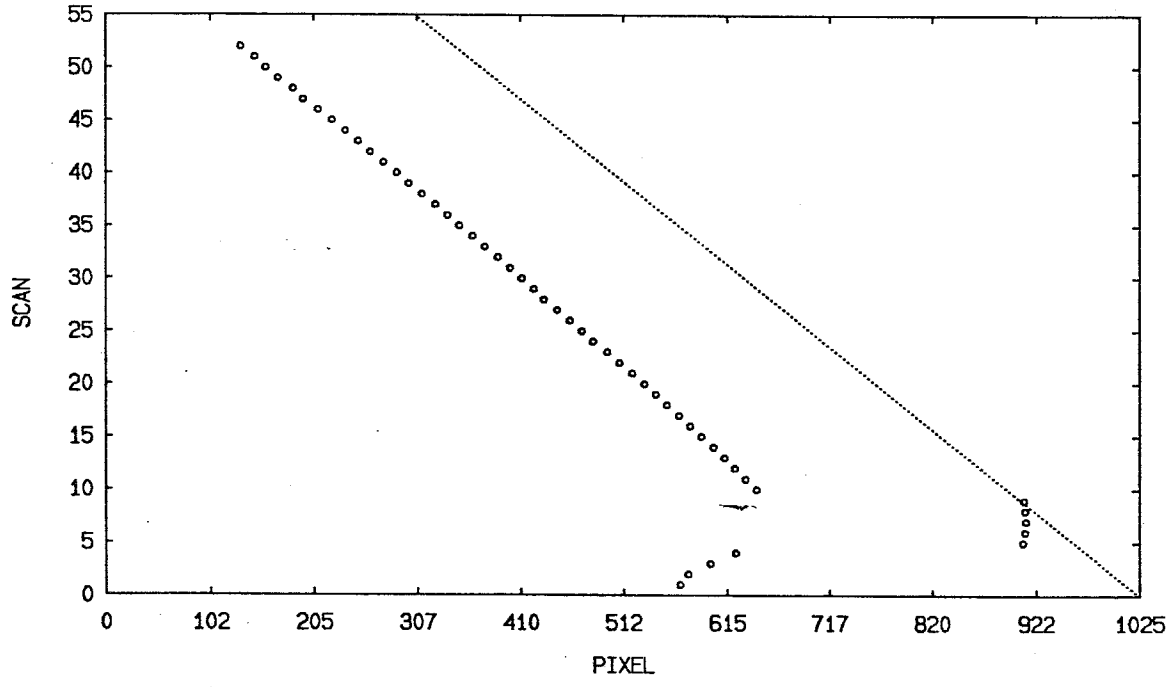

RISE 01-MAR-90 14:44:13 UPR: NONANE LWR: FRMIDE PLATE:29.900
1,52, 1 MOTOR: V00.017 A010.000 D00211633 H+ DELAY:00000
FILE: S01991 VELCL:+00.050 ANGLE: 47.988 DELTA: 00145 NUMDEL: 00052

Figure 76

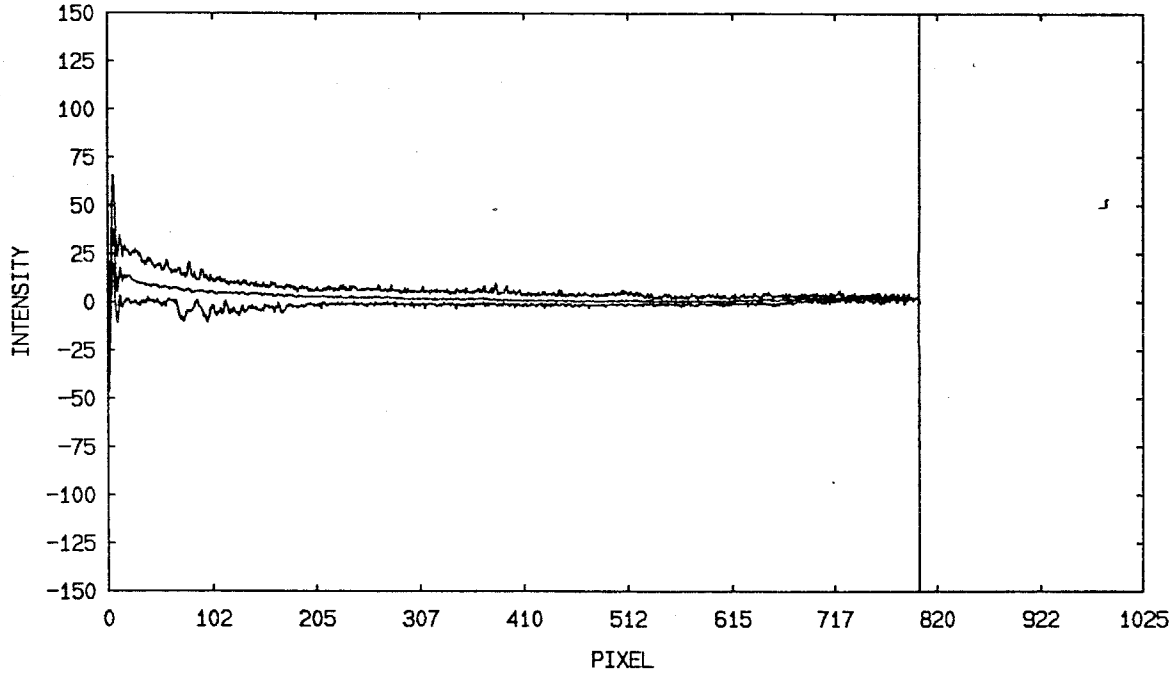

24,31 01-MAR-90 14:44:11 UPR: NONANE LWR: FRMIDE PLATE:29.900
38,39 MOTOR: V00.017 A010.000 D00211633 H- DELAY:00000
44,48 FILE: S01990 VELCL:-00.050 ANGLE: 47.988 DELTA: 00145 NUMDEL: 00052

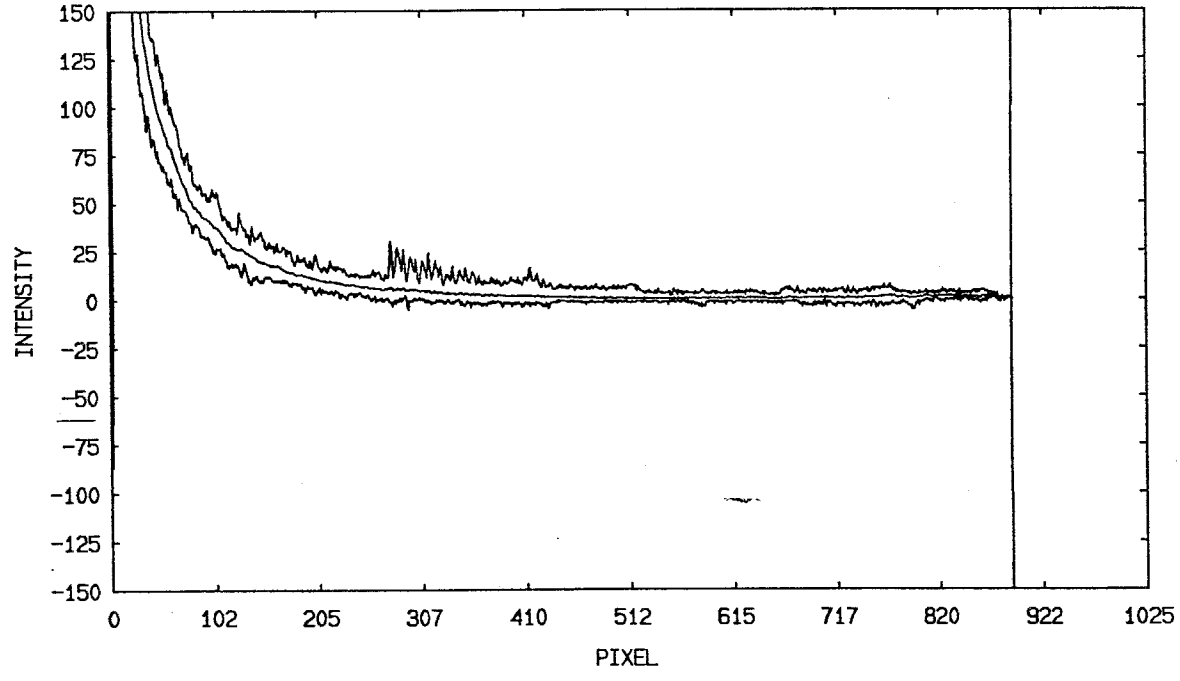

32,52 01-MAR-90 14:44:13 UPR: NONANE LWR: FRMIDE PLATE:29.900
0, 0 MOTOR: V00.017 A010.000 D00211633 H+ DELAY:00000
0, 0 FILE: S01991 VELCL:+00.050 ANGLE: 47.988 DELTA: 00145 NUMDEL: 00052

Figure 77

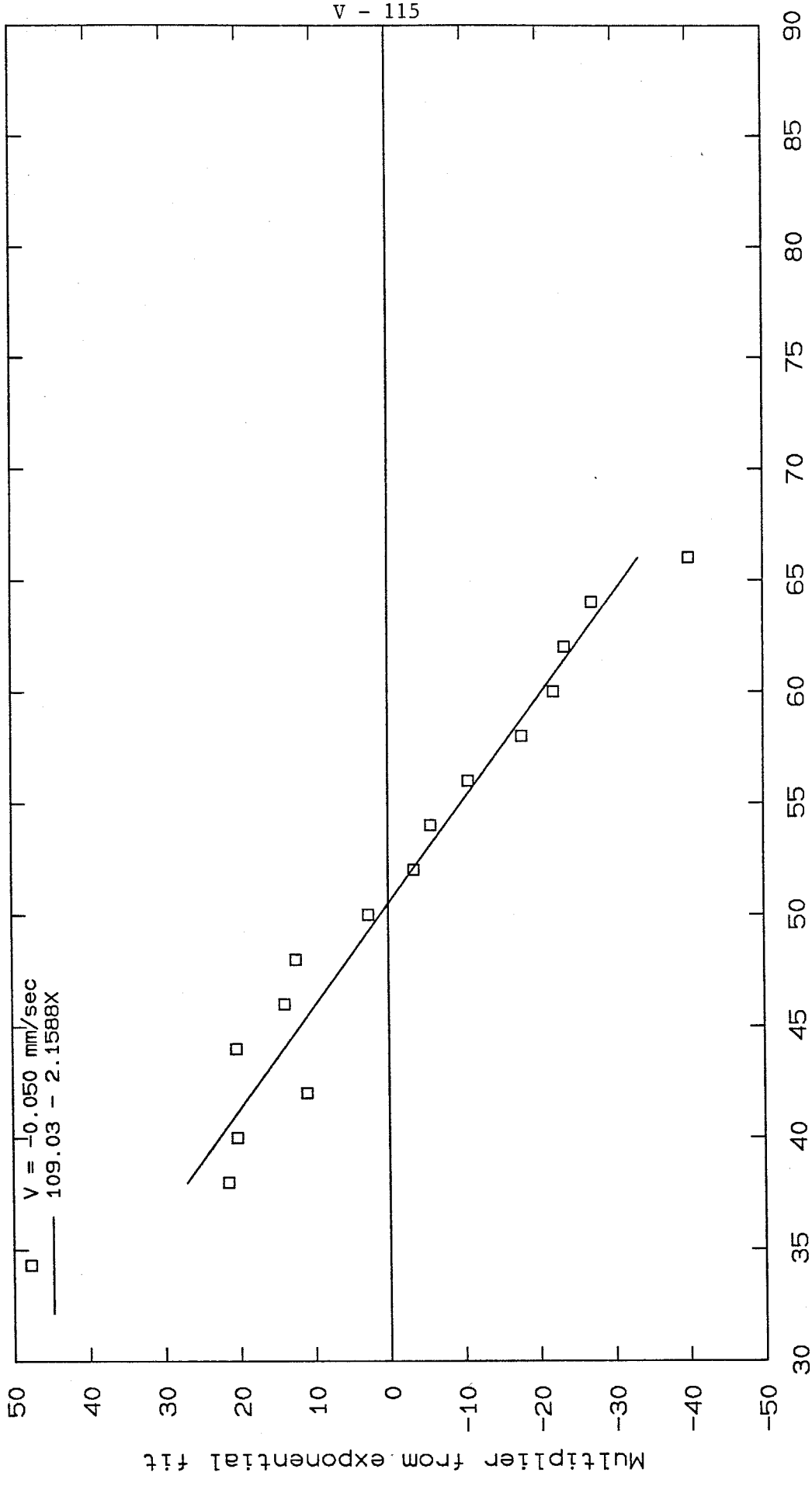

Figure 78 Multiplier from exponential fit vs. plate angle for receding velocities

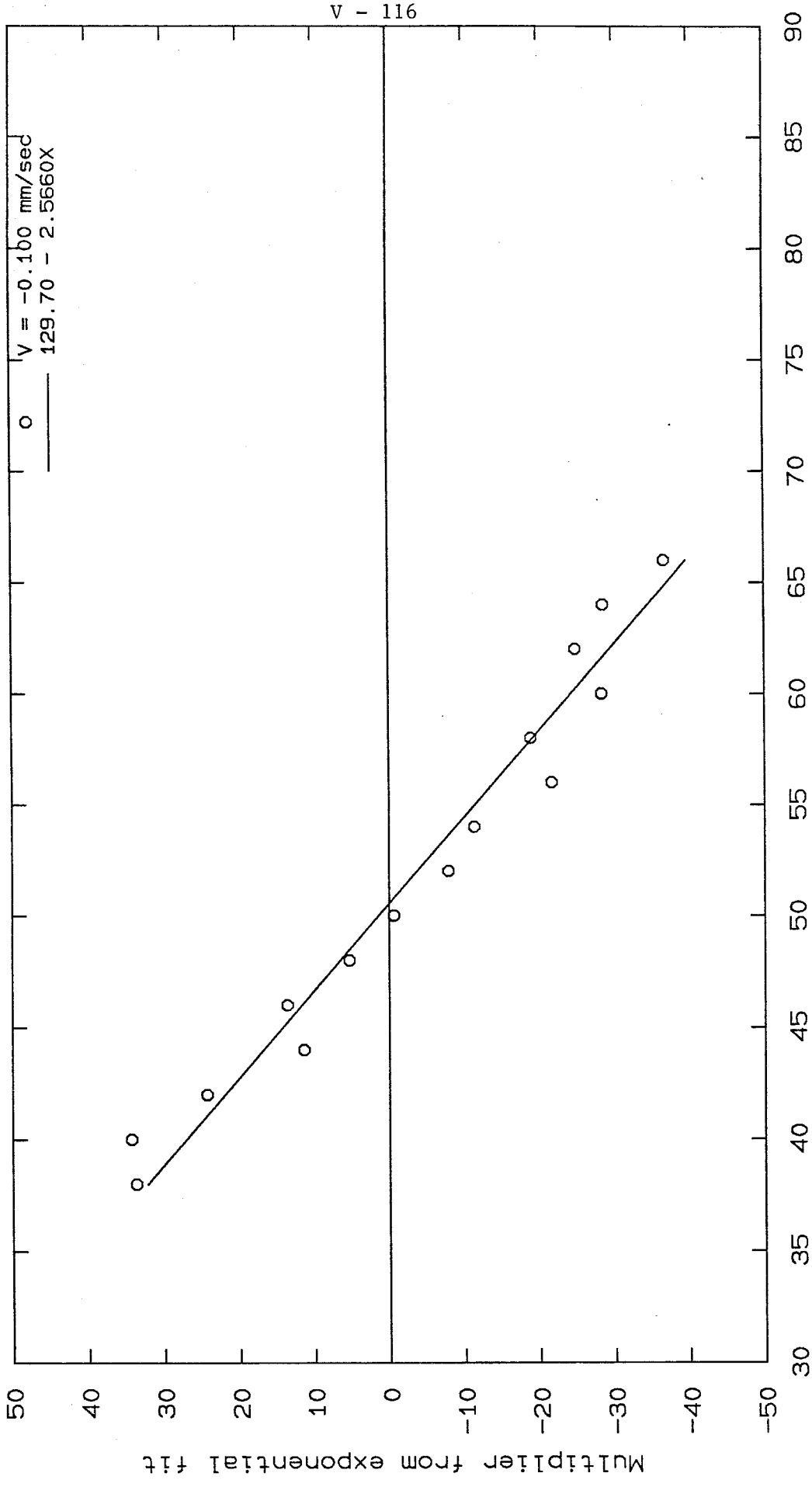

Figure 79 Multiplier from exponential fit vs. plate angle for receding velocities

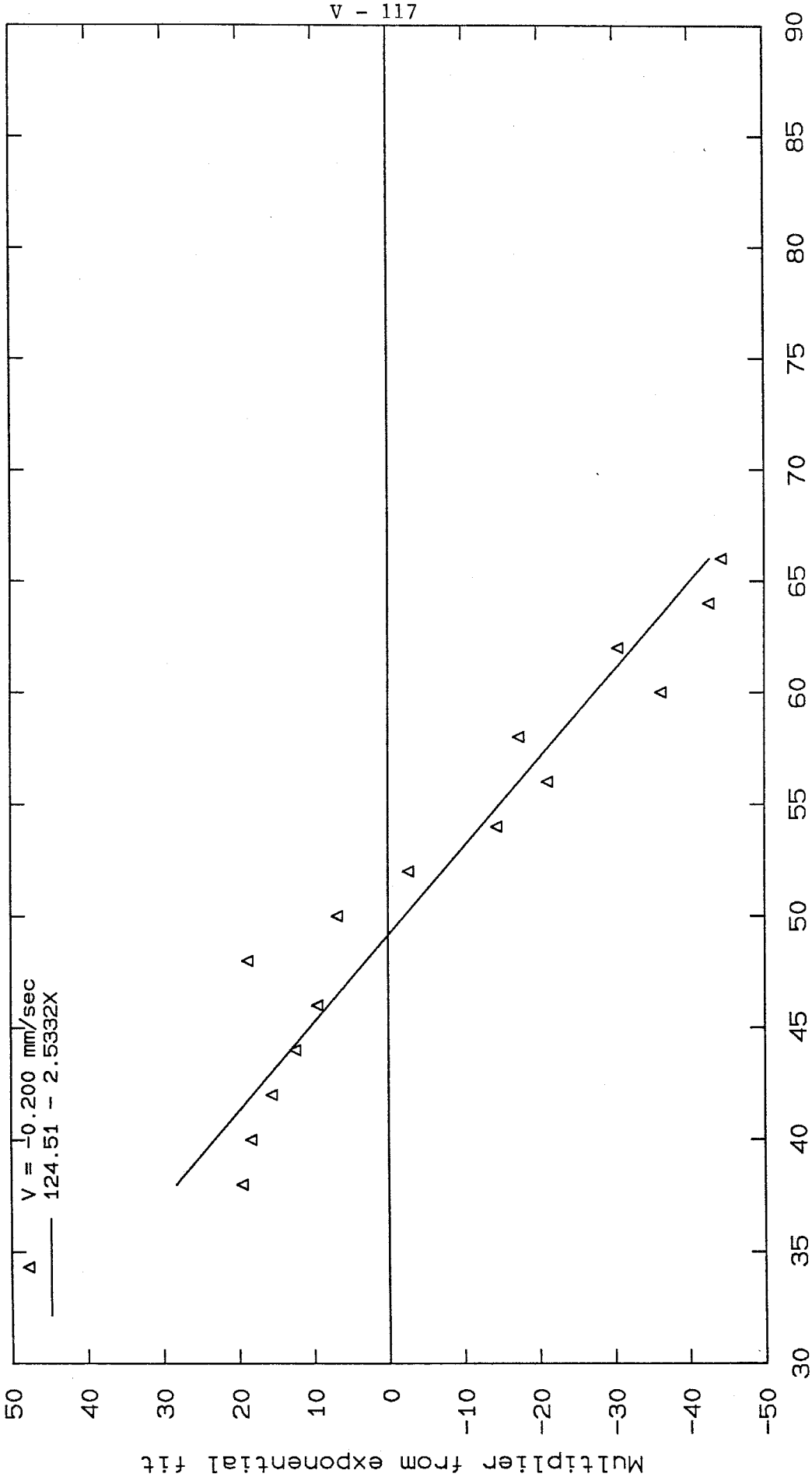

Figure 80 Multiplier from exponential fit vs. plate angle for receding velocities

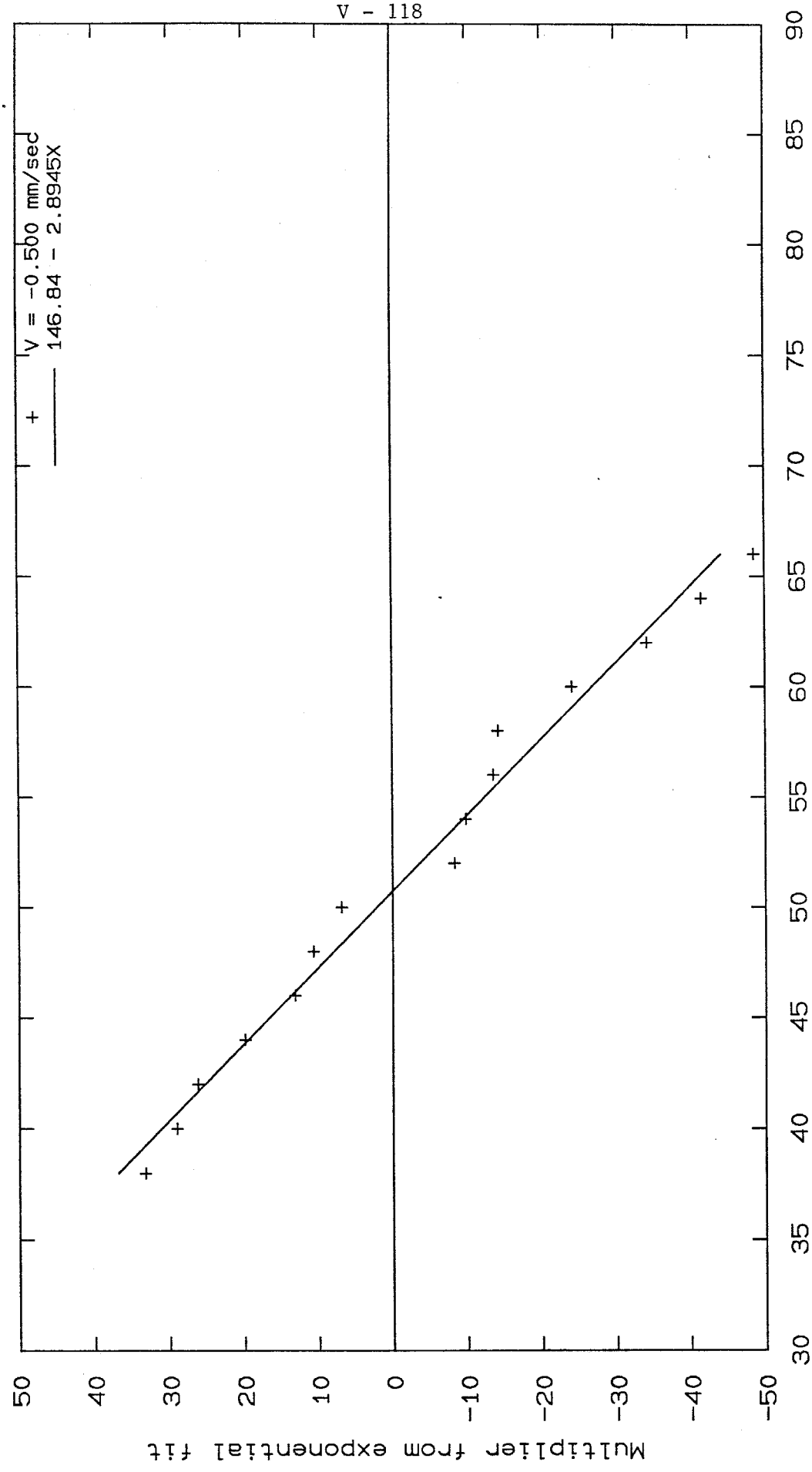

Figure 81 Multiplier from exponential fit vs. plate angle for receding velocities

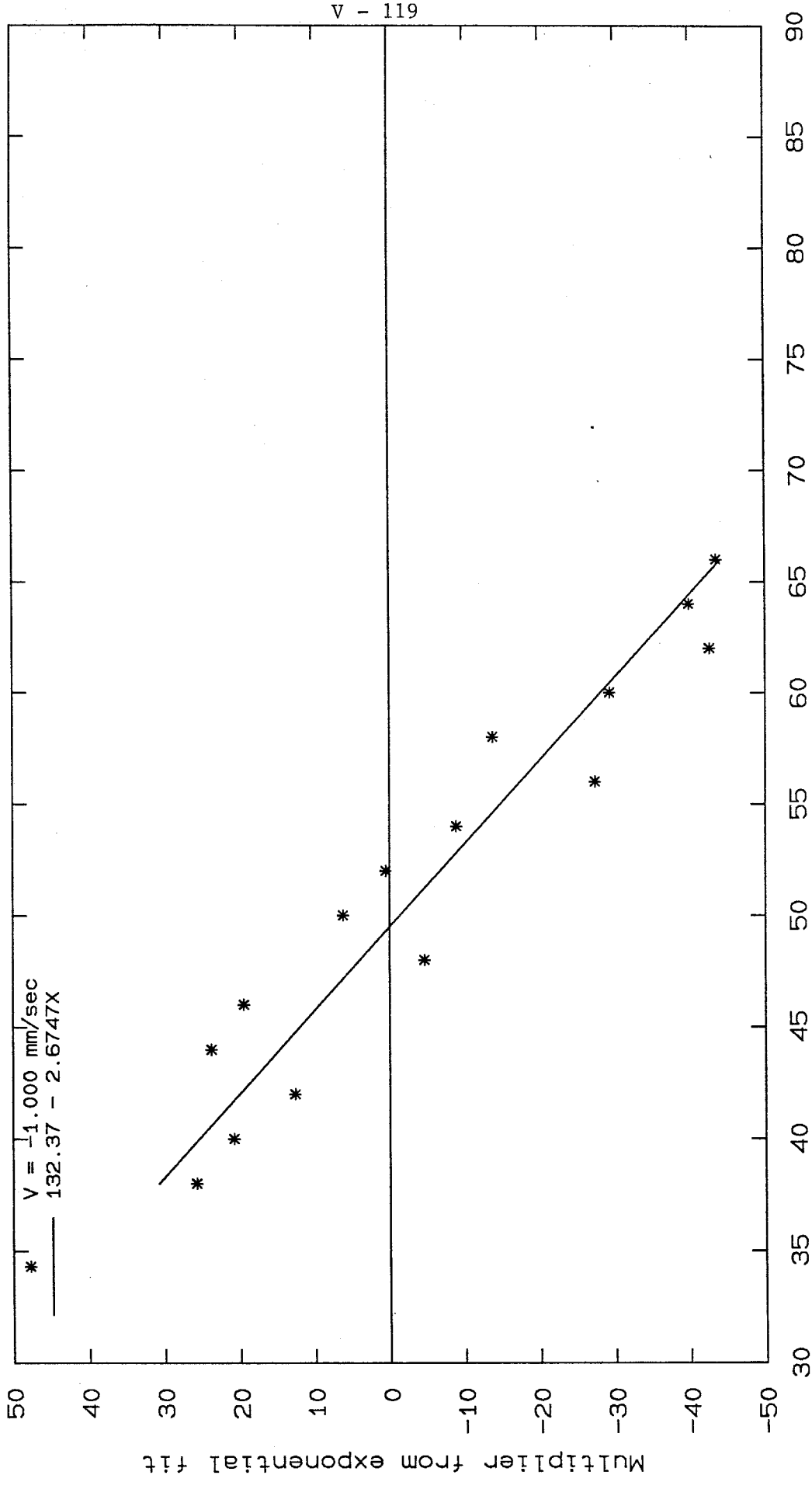

Figure 82 Multiplier from exponential fit vs. plate angle for receding velocities

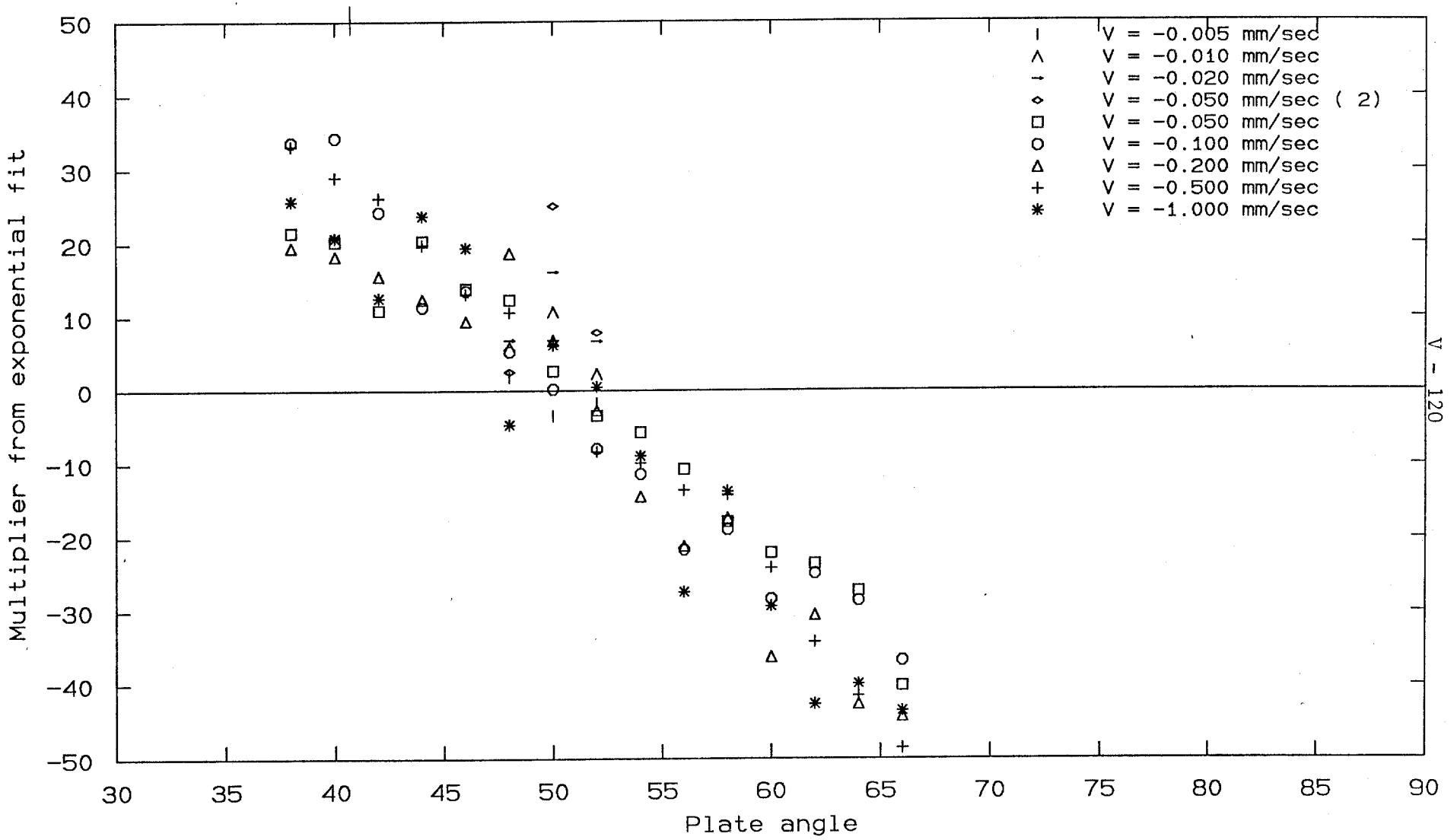

Figure 83 Multiplier from exponential fit vs. plate angle for receding velocities

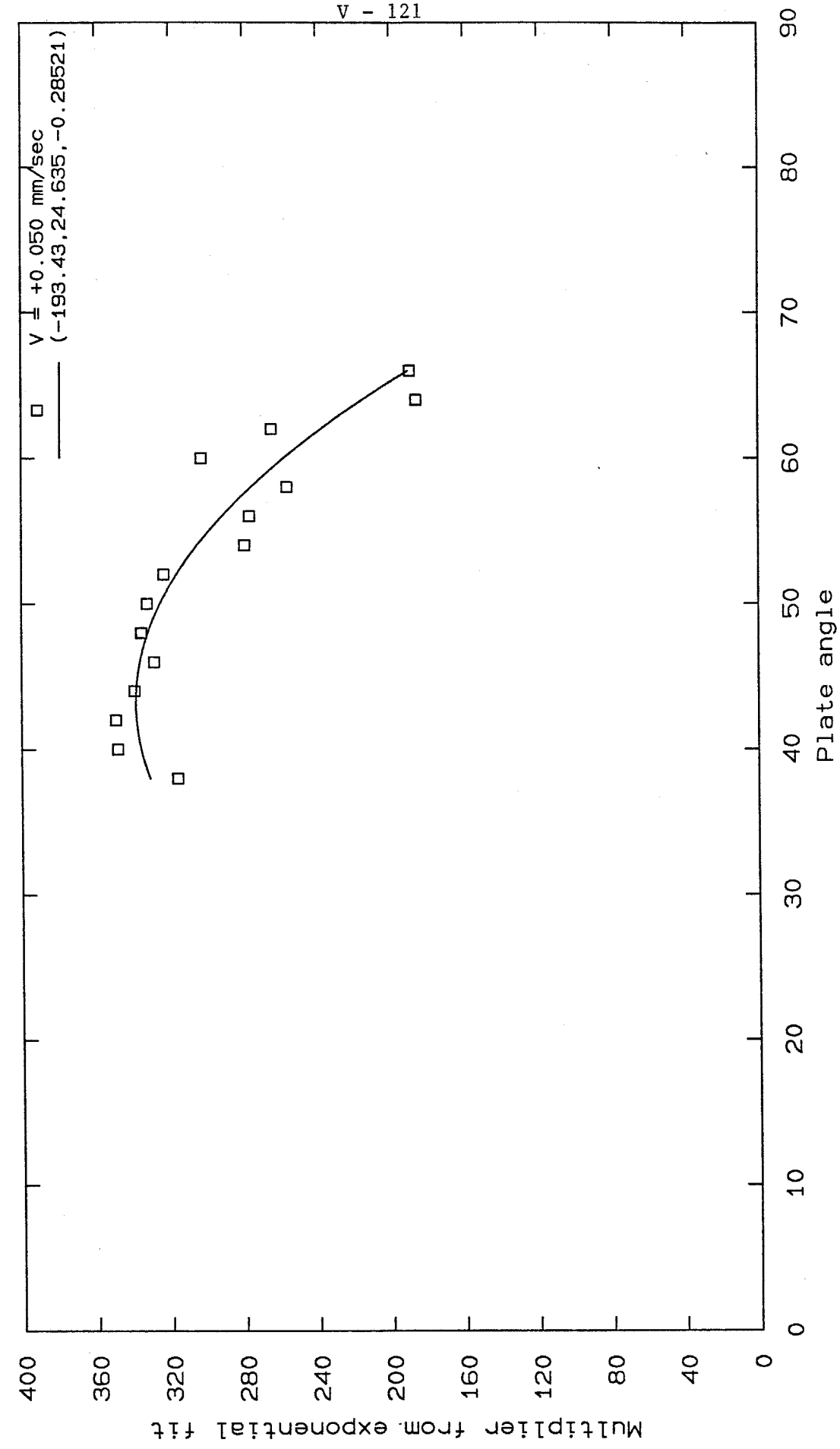

Figure 84 Multiplier from exponential fit vs. plate angle for advancing velocities

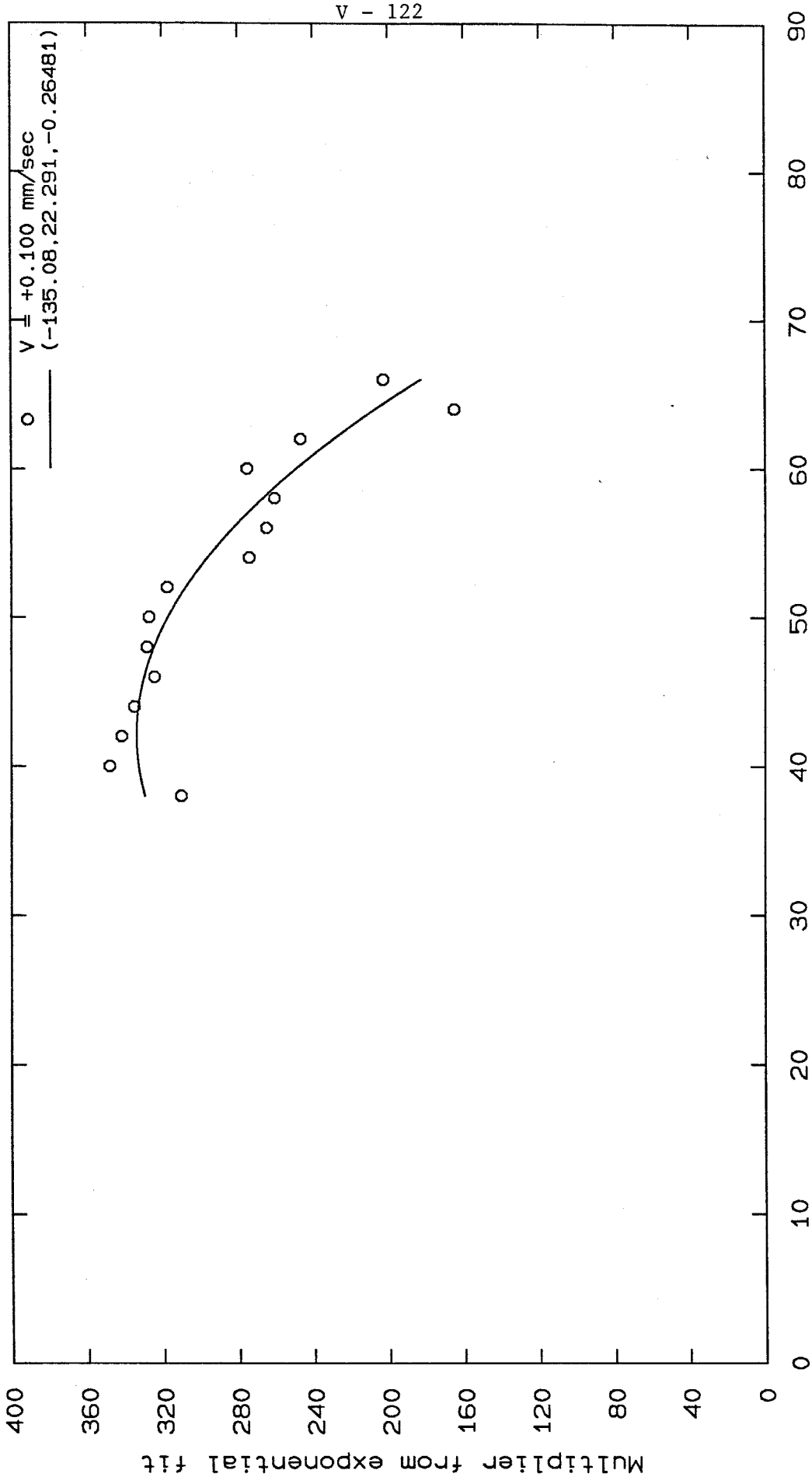

Figure 85 Multiplier from exponential fit vs. plate angle for advancing velocities

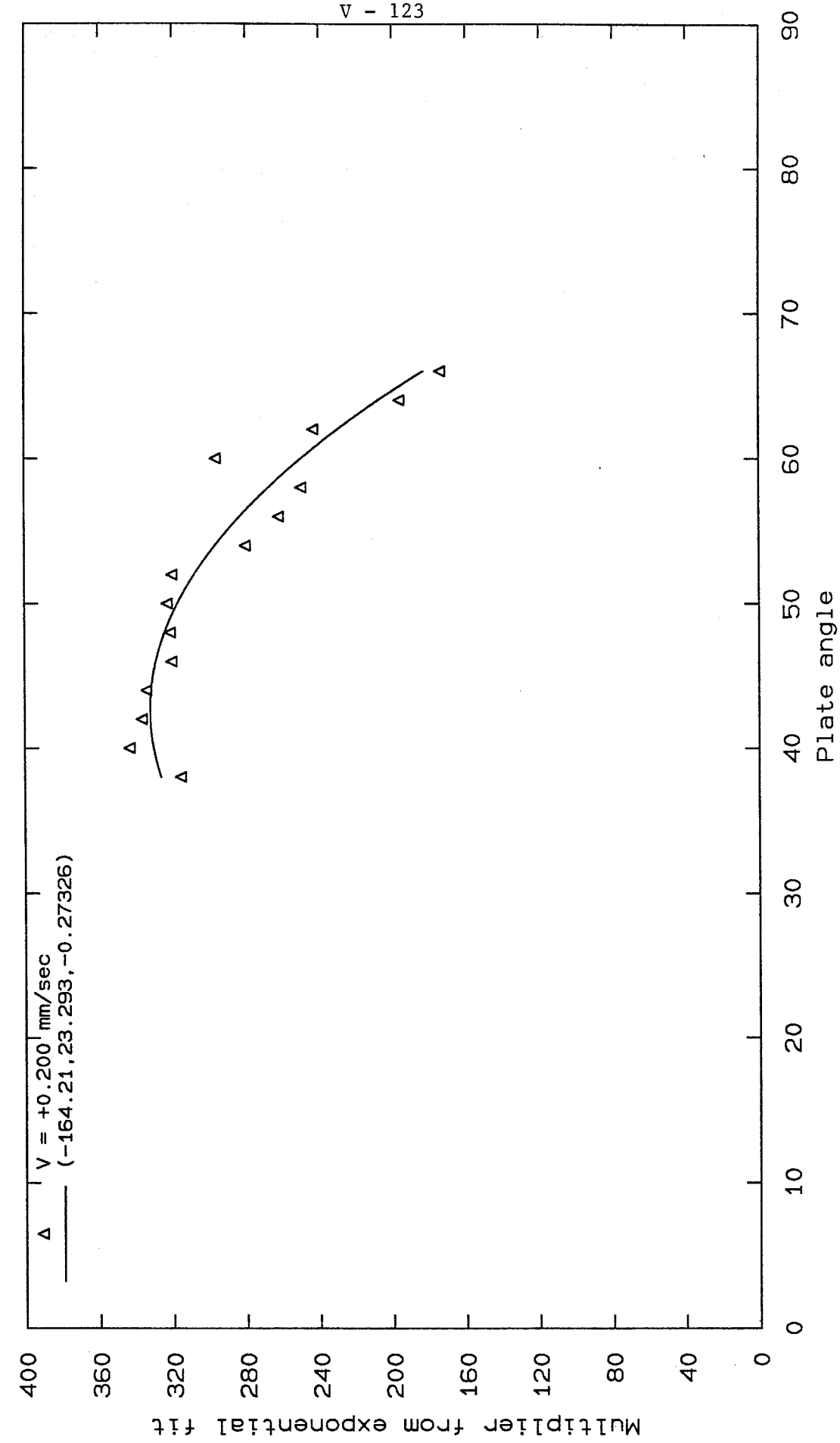

Figure 86 Multiplier from exponential fit vs. plate angle for advancing velocities

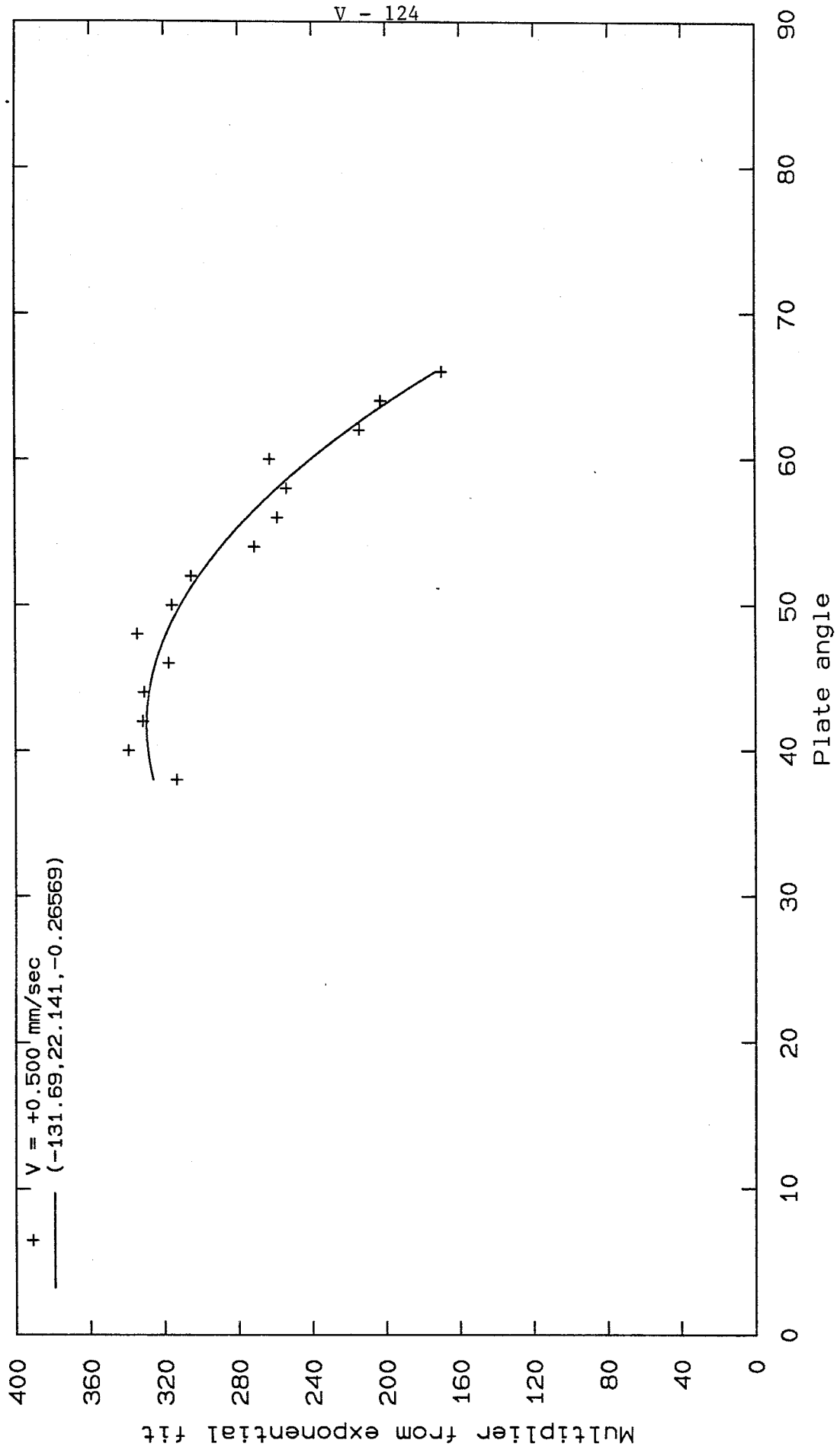

Figure 87 Multiplier from exponential fit vs. plate angle for advancing velocities

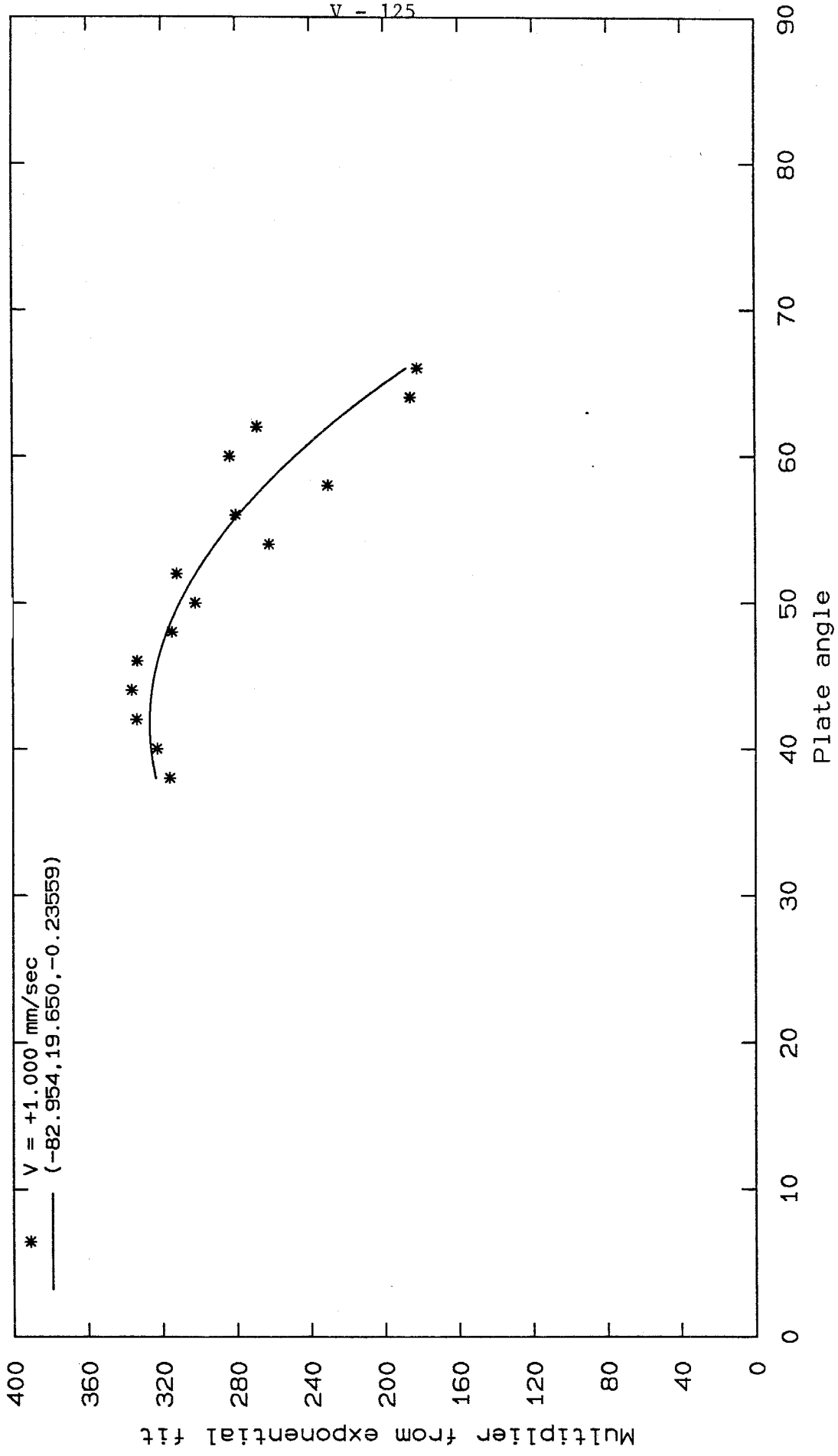

Figure 88 Multiplier from exponential fit vs. plate angle for advancing velocities

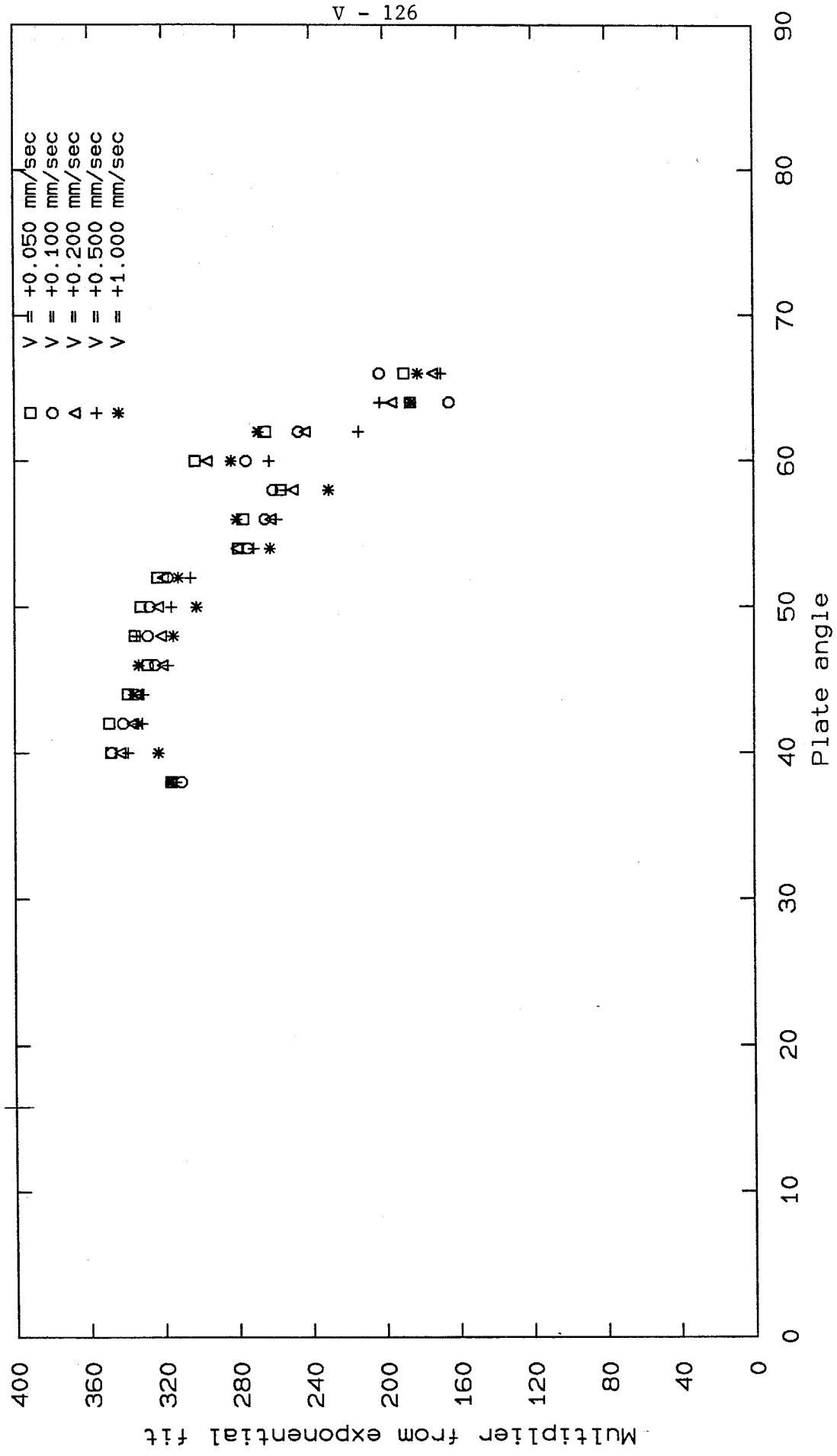

Figure 89 Multiplier from exponential fit vs. plate angle for advancing velocities

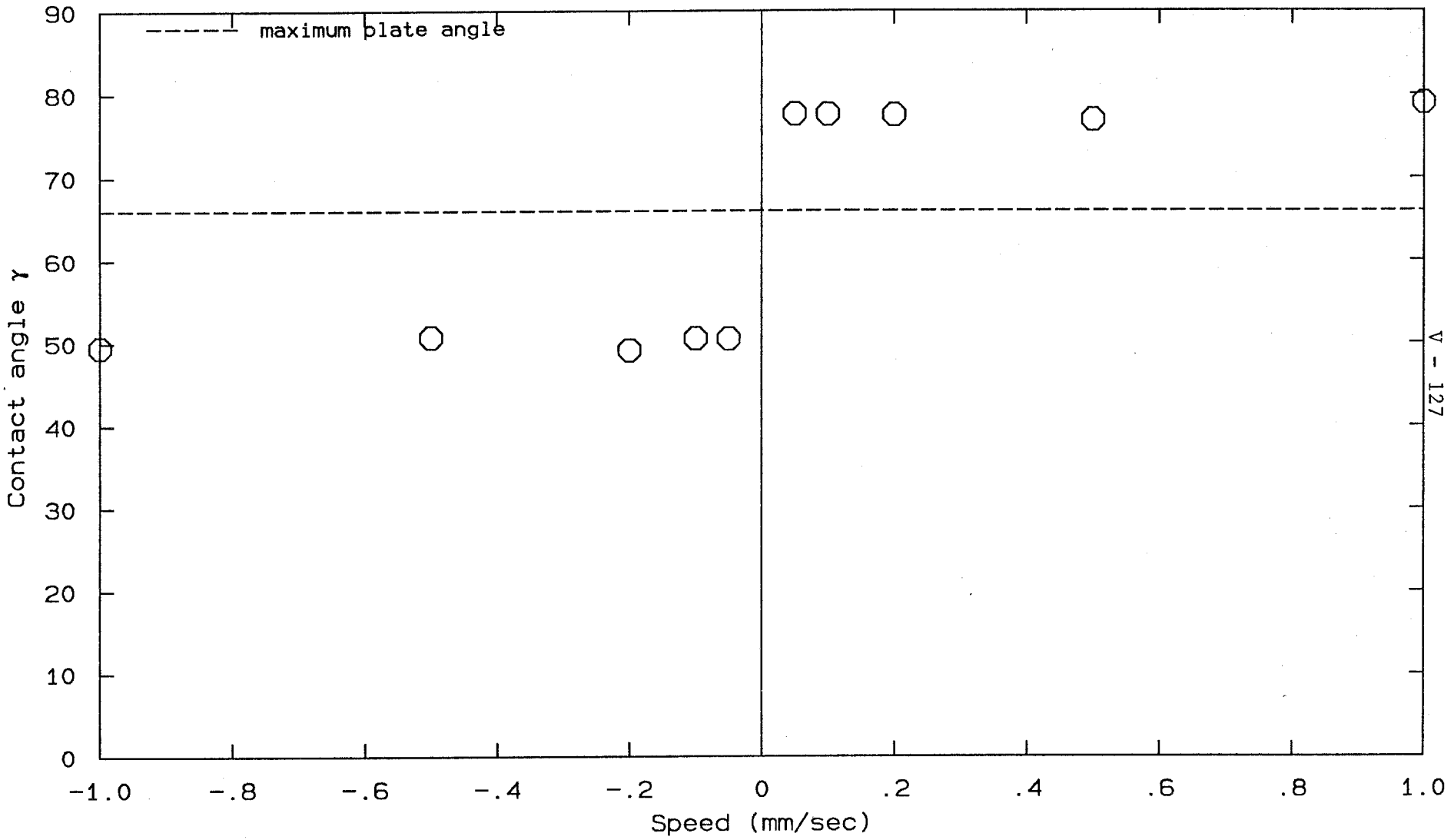

Figure 90
Contact angle vs. velocity for nonane/formamide (glass plate soaked in nonane)